PARTICLE IMAGE VELOCIMETRY APPLICATIONS IN COMPLEX FLOW SYSTEMS

DOCTORAL THESIS

Nihal Ertürk Düzgün

UNIVERSITAT ROVIRA I VIRGILI

2012

Nihal Ertürk Düzgün

PARTICLE IMAGE VELOCIMETRY APPLICATIONS IN COMPLEX FLOW SYSTEMS

DOCTORAL THESIS

Supervised by: Dr. Anton Vernet and Dr. Robert Castilla

Department of Mechanical Engineering

UNIVERSITAT ROVIRA I VIRGILI

Tarragona
2012

UNIVERSITAT ROVIRA I VIRGILI

Departament d'Enginyeria Mecànica
Escola Tècnica Superior d'Enginyeria Química
Universitat Rovira i Virgili
Av. Països Catalans, 26
43007 Tarragona
Tel. 977 55 96 02
Fax 977 55 96 91

Dr. Anton Vernet, Associate Professor in the Mechanical Engineering Department of Universitat Rovira i Virgili and Dr. Roberto Castilla, Associate Professor in the Fluid Mechanics Department of Universitat Politècnica de Catalunya

CERTIFY:

That the present study, entitled:

Particle image velocimetry applications in complex flow systems

presented by MSc. Nihal Ertürk Düzgün for the award of the degree of Doctor, has been developed under our supervision at the Department of Mechanical Engineering of this university and it is fully adequate in scope and quality as a dissertation for the degree of Doctor of Philosophy.

And, it fulfills all the requirements to be eligible for the European Doctorate Award, we sign this certification.

Tarragona, March 2012

Dr. Anton Vernet

Dr. Roberto Castilla

UNIVERSITAT ROVIRA I VIRGILI
PARTICLE IMAGE VELOCIMETRY APPLICATIONS IN COMPLEX FLOW SYSTEMS
Nihal Ertürk Düzgün
Dipòsit Legal: T. 881-2012

Dedicated to my family;

Kemal and Hilmiye Ertürk,

Gülizar, Hayri and Ece Köroglu,

Ali Düzgün

UNIVERSITAT ROVIRA I VIRGILI
PARTICLE IMAGE VELOCIMETRY APPLICATIONS IN COMPLEX FLOW SYSTEMS
Nihal Ertürk Düzgün
Dipòsit Legal: T. 881-2012

ABSTRACT

Recent technology advancements in Particle Image Velocimetry (PIV) technique offer new possibilities to study complex turbulent flows over a wide range of scales. Understanding the interactions between mechanical elements and the fluid flow, predictability and controllability of vortex-dominated and unsteady turbulent flows are important in enhancement of the performance of the these complex flow systems. The main objective of this PhD thesis is the improvement and application of the PIV technique to analyse different complex fluid flows in systems that contain solid moving or stationary parts.

The principles and basic set-up of the PIV technique have been described, giving some details about the tracer particles. The details about the time-resolved PIV technique has been explained to get accurate velocity vectors from the PIV images by discussing tracer particles, image pre-processing, interrogation area, estimation of displacement and data validation method implemented. Briefly, the particle images have been pre-processed using a clean-up mask to remove or to reduce undesired light reflections and to homogenize the median illumination. The triple image correlation method with the implementation of Local Field Correction (LFC) method has been used to obtain the average displacement of the ensemble particles from the particle image series. The triple image correlation algorithm has improved the peak correlation in moving parts that appear in the image. The technique for boundary treatment has been implemented with the use of the weighting function in order to achieve an appropriate resolution for the calculation of the velocity fields and to obtain the same level of accuracy available at inner locations of the flow system. In order to detect and remove spurious vectors, a validation algorithm has been implemented for the post processing of the images. The procedure to estimate the turbulent scales of the flows in complex systems that contain rotating parts has been explained. Special attention has been given to the study of assumptions needed to estimate the dissipation rate from the two-dimensional PIV

images to the influence of the measurement of the spatial and temporal resolution of the PIV data. Besides, the error estimations in measurement of the velocity vectors and the dissipation rate have been explained by considering the effect of number of samples employed in the ensemble-averaging of the velocities.

The alginate particles with/without fluorescein compound imbedded have been developed as a new alternative flow seeding elements for PIV applications. The alginate micro particles have been efficiently used in PIV as tracer particles for different experiment facilities and different fluids such as water, air, and oil to analyse the complex flows. It has been found that the alginate micro particles have many advantages over traditional ones used in PIV systems.

A comprehensive study on the three-dimensional flow analysis of the external gear pump has been done by time-resolved PIV technique to investigate its turbulent flow dynamics and statistics. The applied experimental techniques have established a method that allows visualizing the flow inside the gear pump with a high rotational velocity system. In order to investigate the three dimensionality of the flow, the experiments have been done in three horizontal and vertical planes considering the suction and impulse chambers of the pump. The results have displayed the periodical behaviour of the flow corresponding with periodical movement of the gears. Instantaneous and conditional (phase-locked) ensemble average velocity field data for a single phase of the gear position have been obtained in different planes. In addition to this, phase-locked ensemble average values have been computed at different phases of the gear position. Time evolution of the average motion has showed that the direction of the velocity patterns changes as a function of the movement of the gearwheel. The influence of the rotating gears has been observed in the variation of back flows from the phase-locked ensemble averages profiles. Furthermore, the flow rate through the pump and its relationship with the gear position has been obtained from the phase-locked ensemble average profiles. Vorticity and high turbulent kinetic energy areas have been identified inside the external gear pump.

The PIV technique has been efficiently applied to analyse an engine bypass flow heat exchanger in a low speed wind tunnel. The heat exchanger used in this thesis has been specifically designed for the turbofan engines to improve the thermal management of future aircraft power plants. It has been placed into the low speed wind tunnel to obtain the prior knowledge on the effects of the heat exchanger in the bypass flow. Two different tracer particles; the glass particles and the fluorescent particles have been used in the experiments in order to improve substantially the PIV image quality and further analysing the small-scale structures of the flow. The appropriate set-up conditions of the PIV technique have led to obtain the PIV data collection for the incompressible turbulent study on bypass flow over the heat exchanger.

UNIVERSITAT ROVIRA I VIRGILI
PARTICLE IMAGE VELOCIMETRY APPLICATIONS IN COMPLEX FLOW SYSTEMS
Nihal Ertürk Düzgün
Dipòsit Legal: T. 881-2012

RESUMEN

Los avances tecnológicos recientes en la técnica velocimetría por imágenes de partículas (PIV) ofrecen nuevas posibilidades para el estudio de flujos complejos turbulentos en un amplio rango de escalas. La comprensión de las interacciones entre los elementos mecánicos y el flujo de fluidos, la previsibilidad y capacidad de control de flujos turbulentos vórtice-dominado e inestable es importante en mejorar del rendimiento de estos sistemas de flujos complejos. El objetivo principal de esta tesis doctoral es la mejora y aplicación de la técnica PIV para analizar diferentes flujos de fluidos complejos en los sistemas que contienen partes sólidos móviles o estacionarias.

Los principios y establecido básico de la técnica PIV se han descrito, dando algunos detalles sobre las partículas trazadoras. Los detalles sobre la técnica tiempo-resuelva PIV se ha explicado para obtener los vectores de velocidad exactas de las imágenes PIV hablando de partículas trazadoras, pre-procesamiento de la imagen, área de interrogatorios, la estimación de los desplazamientos y método de validación de datos implementado. En pocas palabras, las imágenes de partículas han sido procesadas utilizando una máscara de limpieza para eliminar o reducir los reflejos no deseados de la luz y para homogeneizar la iluminación mediana. El método de triple correlación de imagen con la implementación del método (Local Field Correction) LFC ha sido utilizado para obtener el desplazamiento medio de las partículas del conjunto de la serie de imágenes de partículas. El algoritmo de triple correlación de imágenes ha mejorado la correlación de pico en las partes móviles que aparecen en la imagen. La técnica para el tratamiento de límites se ha aplicado con el uso de la función de ponderación a fin de lograr una resolución adecuada para el cálculo de los campos de velocidad y para obtener el mismo grado de precisión necesaria en los lugares interiores del sistema de flujo. Con el fin de detectar y eliminar vectores espurios, un algoritmo de validación se ha aplicado para el procesamiento posterior de las imágenes. El procedimiento para estimar las

escalas de los flujos turbulentos en sistemas complejos que contienen las piezas giratorias se ha explicado. Se ha prestado especial atención al estudio de los supuestos necesarios para calcular la tasa de disipación de las imágenes de dos dimensiones de PIV a la influencia de la medida de la resolución espacial y temporal de los datos del PIV. Además, las estimaciones de errores en la medición de los vectores de velocidad y la capacidad de disipación se han explicado al considerar el efecto del número de muestras empleadas en el conjunto del promedio de las velocidades.

Las partículas de alginato con/sin compuesto de fluoresceína incrustada se han desarrollado como una serie de elementos alternativos de siembra de nuevas aplicaciones de flujo para el PIV. Las micro-partículas de alginato se han utilizado eficientemente en PIV como partículas trazadoras para instalaciones experimentales diferentes y fluidos diferentes, tales como agua, aire y aceite para analizar los flujos complejos. Se ha encontrado que las micro-partículas de alginato tienen muchas ventajas sobre los tradicionales utilizados en sistemas de PIV.

Un estudio amplio sobre el análisis del flujo en tres dimensiones de la bomba de engranajes externa se ha hecho por la técnica tiempo-resuelva PIV para investigar la dinámica y las estadísticas de flujo turbulento. Las técnicas aplicadas experimentales han establecido un método que permite visualizar el flujo dentro de la bomba de engranajes con un sistema de rotación de alta velocidad. Con el fin de investigar la tridimensionalidad del flujo, los experimentos se han realizado en tres planos horizontales y verticales considerando las cámaras de aspiración e impulsión de la bomba. Los resultados han mostrado el comportamiento periódico del flujo correspondiente con el movimiento periódico de los engranajes. Datos conjunto de campo promedio de velocidad instantáneo y condicional (enganche de fase) para una sola fase de la posición de la marcha se han obtenido en diferentes planos. Además de esto, los valores de enganche de fase conjuntos medios se han calculado en diferentes fases de la posición de engranaje. Evolución temporal del movimiento promedio ha mostrado que la dirección de los patrones de velocidad cambia como función del movimiento de la rueda dentada. La influencia de los engranajes giratorios se ha observado en la variación de los flujos detrás de la posición de enganche de fase perfiles conjuntos medios. Además, la tasa de flujo a

través de la bomba y su relación con la posición del engranaje se ha obtenido de enganche de fase perfiles conjuntos medios. Vorticidad y zonas turbulentas de alta energía cinética se han identificado dentro de la bomba de engranajes externa.

La técnica PIV se ha aplicado de manera eficiente para analizar un intercambiador de calor de motor de flujo de bypass en un túnel del viento de bajo velocidad. El intercambiador de calor utilizado en esta tesis ha sido diseñado específicamente para los motores de turboventilador para mejorar la gestión térmica de las futuras plantas de energía de aeronaves. Se ha colocado en el túnel del viento de bajo velocidad para obtener el conocimiento previo sobre los efectos del intercambiador de calor en el flujo de bypass. Dos partículas trazadoras diferentes; las partículas de vidrio y las partículas fluorescentes se han utilizado en los experimentos con el fin de mejorar sustancialmente la calidad de la imagen PIV y aún más el análisis de las estructuras de pequeña escala del flujo. Las condiciones adecuadas de configuración de la técnica PIV han llevado a obtener la colección de datos del PIV para el estudio incompresible turbulento en el flujo de bypass sobre el intercambiador de calor.

Dipòsit Legal: T. 881-2012

ACKNOWLEDGEMENTS

It is a pleasure for me to thank my thesis supervisor Dr. Anton Vernet for his guidance throughout this thesis and for having confidence in me. Both his scientific and personal teachings have been really important in my personal development.

I would like to give my sincere thanks to Robert Castilla, my second supervisor, who gave me all the necessary support during my studies in Barcelona.

I would also like to acknowledge the members of my jury for giving me the honor to examine my thesis research: Dr. Francesc Xavier Grau i Vidal, Dr. Guillermo Paniagua, and Dr. Pedro Javier Gamez-Montero.

My sincere thanks also go to our beloved technician, Jordi Polo and all my office friends who were always there when I need them.

I want to specially thank to Dr. Rukan Genc who I made several valuable discussions about science and life for being a really precious friend. Also to Laura Villafañe and my other colleagues (especially Dario Iannetti, Alessandro Mazzetti and Alex Alvarez Lake) who helped me a lot during my research stay at Von Karman Institute, Belgium.

I also would like to thank to our Turkish community in Tarragona which have been valuable friends and helped a lot in not forgetting Turkish.

I thank to my father and mother, my dear sister Gülizar and lovely niece Ece for their support throughout my life.

Lastly, but mostly my biggest thanks go to my husband (soon Dr.) Ali Düzgün, who was always with me even in most difficult times.

This work was made possible by financial support of projects DPI2006-02477, DPI2006-14476, DPI2009-11204 and DPI2010-17212 from the Dirección General de Investigación of the Ministerio de Ciencia e Innovación and FEDER founds.

I will also like to thank the economic support received from the Universitat Rovira i Virgili through a pre-doctoral grant.

List of Publications and Contributions to Conferences

Journal papers

- Ertürk N, Vernet A, Castilla R, Gamez-Montero PJ, Ferre JA, Experimental analysis of the flow dynamics in the suction chamber of an external gear pump, International Journal of Mechanical Sciences, 53; 135-144, 2011.

- Ertürk N, Vernet A, Pallares J, Castilla R, Raush G, Small-scale characteristics and turbulent statistics of the flow in an external gear pump by Time-Resolved PIV, Flow measurement and instrumentation, 2012, submitted.

- Castilla R, Gamez-Montero PJ, Ertürk N, Vernet A, Coussirat M, Codina E, Numerical simulation of turbulent flow in the suction chamber of a gearpump using deforming mesh and mesh replacement, International Journal of Mechanical Sciences, 52; 1334-1342, 2010.

- Gamez-Montero PJ, Castilla R, Campo D, Ertürk N, Raush G, Codina E, Influence of the interteeth clearances on the flow ripple in a gerotor pump for engine lubrication, Proceedings of the Institution of Mechanical Engineers, Part D: Journal of Automobile Engineering, 2012, doi: 10.1177/0954407011431545

Patents

- Ertürk N, Vernet A, Uso de alginatos en velocimetría por imágenes de partículas y procedimiento para medir la velocidad de un fluido, Oficina Española de Patentes y Marcas (OEPM), Número de solicitud: P201132029, 2011.

International congress presentations

- Nihal Ertürk, Anton Vernet, Robert Castilla, Analysis of the Turbulent Flow Dynamics of an External Gear Pump by Time Resolved Particle Image Velocimetry, 7th Internacional Conference on Heat Transfer, Fluid Mechanics and Thermodynamics, Antalya-Turkey, 19 – 21 July 2010

- Nihal Ertürk, Anton Vernet, Robert Castilla, Pedro J. Gamez-Montero, Josep A. Ferre, Application of Time Resolved Particle Image Velocimetry to Analyze the Flow in an External Gear Pump, Conference on Modeling Fluid Flow (CMFF'09), The 14th International Conference on Fluid Flow Technologies, Budapest-Hungary, 9 – 12 September 2009

- Nihal Ertürk, Anton Vernet, Josep A. Ferre, Robert Castilla, Esteve Codina, Analysis of the Turbulent Flow of an External Gear Pump by Time Resolved Particle Image Velocimetry, 14th International Symposium on Applications of Laser Techniques to Fluid Mechanics, Lisboa-Portugal, 7 – 10 July 2008

- Nihal Ertürk, Anton Vernet, Josep A. Ferre, Analysis of the Turbulent Flow of an External Gear Pump by Time Resolved Particle Image Velocimetry, 6th Poster Exhibition day in Chemical, Environmental and Process Engineering, University of Rovira i Virgili (ETSEQ), Tarragona-Spain, 30 November 2007.

CONTENTS

LIST OF TABLES

LIST OF FIGURES

LIST OF SYMBOLS

C_v theoretical volumetric capacity (m^3/rev)
D gear diameter (m)
f frequency rate (fps, frames per second)
k_{2D} turbulent kinetic energy (m^2/s^2)
L length of the test section
P total pressure (Pa)
Q flow rate (m^3/s)
Q_t theoretical flow rate (m^3/s)
Re Reynolds number ($\omega\rho D^2/\mu$)
T_g gearing period (s)
U_p particle velocity
U fluid velocity
d_p particle diameter
x, y, z Cartesian co-ordinates
u, v velocity components with respect to x, y
u', v' fluctuating of the velocity components with respect to x, y
$\langle u \rangle$, $\langle v \rangle$ mean velocity components with respect to x, y
$F(v)$ frequency spectrum of velocity fluctuations
e velocity measurement error
v_{rise} bubble rise velocity
w_m mean velocity
e_b mean-bias error
w_a actual particle velocity
e_{RMS} RMS error
e_{TOT} sum of the mean-bias error and the RMS error
T_I integral timescale
$R_{ii}(r)$ autocorrelation function
R_{yy} two point autocorrelation function
r distance between two points in the flow

Δt interval time
$\Re$ truncation error
ε dissipation rate
η Kolmogorov length
v kinematic viscosity
τ_s relaxation time
λ_T Taylor micro scale
ρ density (kg/m^3)
ρ_p particle density
ρ_f fluid density
μ dynamic viscosity (Pa.s)
t time (s)
ω rotational velocity(rad/s)
ωD reference velocity (m/s)

CHAPTER I
INTRODUCTION

1.1 State of the art

The first concept of particle image velocimetry (PIV) is traced back over 100 years by Ludwig Prandtl who designed and used flow measurements techniques with a suspension of mica particles in a water channel (Raffel et al. 1998). Although it only provided a qualitative description of the flow field, recent advances in the flow measurements techniques have made it possible to extract quantitative information inside complex flows. In 1977, feasibility of laser speckle velocimetry (LSV) was demonstrated in laminar tube flow (Barker and Fourney 1977; Dudderar and Simpkins 1977; Grousson and Mallick 1977). Practical measurements of LSV were applied to analyze the flow of liquids and gases (Meynart 1982; Meynart 1983). The name "particle image velocimetry" was proposed in 1984 (Adrian 1984) and it was used in a scientific paper that stated that the low seeding density mode of LSV should be more appropriately classified as PIV (Pickering and Halliwell 1984). The technique became popular since it offered a new and highly promising way to study the structure of the fluid flow. PIV was developed by many researchers with respect to better performance of the optical and digital methods in the evaluation of PIV recordings (Adrian and Yao 1985; Adrian 1986). The major milestone for the PIV was the use of a cross-correlation CCD camera in synchronization with a double oscillator Nd:YAG laser source (Keane and Adrian 1992). The principle and fundamentals of digital PIV was presented in several papers (Willert and Gharib 1991; Westerweel 1993). Briefly, PIV can be defined as an optical experimental

technique that measures the velocity of the tracer particles in the flow of interest over a plane using the captured images of those particles. When the tracer particles in the flow measurement area are illuminated by the laser flashes at two short time duration, a double-exposure of the flow field is recorded with a CCD camera. Then, the velocity vector field is extracted from the two separate recorded frames by means of a cross-correlation analysis between small portions of the recorded image called interrogation areas. The size of these interrogations areas determine the resolution of the velocity field obtained. However, the PIV technique is still being continuously developed. Recent advancements in cross-correlation digital PIV methodologies deliver higher accuracy sub-pixel velocity measurements (Lourenco and Krothapalli 1995; Westerweel et al. 1997; Huang et al. 1997; Nogueira et al. 1999; Hart 2000; Werely and Meinhart 2001; McKenna and McGillis 2002). In addition, the technical improvements of the available instrumentation allow resolution of a wider range of scales in the flow.

1.1.1 Seeding particles

When using PIV, a large image size that is enough to capture the large scales and an interrogation area small enough to capture small scales should be selected carefully if all the turbulent scales of interest are to be evaluated accurately. To minimize the number of spurious velocity vectors (vectors obtained from the PIV process that have incorrect values), appropriate number of seeding particles should be supplied to each interrogation area. It is desirable that tracer particles should be non-toxic, non-corrosive, non-volatile, non-abrasive and chemically inert. A wide variety of tracer particles is available for PIV experiments. Polyamide seeding particles have been used in many applications (Skudarnov et al. 2002; Hjertager et al. 2003; Naterer et al. 2005; Ammourah et al. 2004; Schröder et al. 2010). These particles does not have exact spherical shapes, but made of a porous media that allows the continuum fluid to fill in and then become buoyant and faithfully follow the continuous medium flow pattern particularly in water flows. Besides, hollow glass sphere particles that have spherical shape and smooth surface are alternatively used as tracer particles in liquid flow applications (Meyer et al. 2011; Hopkins et al. 2000; Techet and McDonald 2005; Wong and Soria 2007). These particles

can follow the flow of water and can remain suspended in the flow for a long time due to their specific gravity being close to that of water.

Another kind of tracer particle used are the fluorescent particles that are known to improve the quality of vector maps and the signal to noise characteristics of the raw images from PIV measurements (Deschênes et al. 2010; Monji and Sato 2010; Lai and Menon 2004). The cost of the commercially available fluorescent particles is too high for the large-scale experiments. Generally, Rhodamine dye compounds are used as fluorescent dye in the production process of the fluorescent particles. The use of these particles can be prohibiting in large-scale experiments due to their toxic property and high cost. The fluorescent particles show high efficiency and detectability at almost every flow velocity and water depth (Angarita-Jaimes et al. 2008; Meselhe et al. 2004). Fluorescent polymer microspheres have been used to study near-wall fluid motion (Jin et al. 2004) and mixing processes and multiphase fluid systems (Angarita-Jaimes et al. 2008). Despite their promise, the use of fluorescent particles is forbidden to flow studies in large-scale laboratory experiments. The only example of fluorescent particles designed for large-scale PIV measurements is reported by Pedocchi et al. (2008). It is therein shown that the reduction of reflections due to the presence of free surfaces, sediments, and interfaces is a remarkable advantage of fluorescent particles in large-scale hydraulic experiments. In particular, a novel particle tracer is synthesized by mixing Rhodamine Water Tracer a low toxicity fluorescent dye, with commercial grade liquid polyester resin. The tracer is detected through common PIV and, due to the properties of the fluorescent material; good images are obtained in the vicinity of laser-reflective surfaces. However, use of these particles in underwater operations may be limited by the porosity of the resin material. Indeed, after their release, particles may absorb water and rapidly increase their density, as reported by Weitsman and Elahi (2000) for polymer-based composites. Therefore, in the long run, beads may lose their natural buoyancy and precipitate. All these difficulties (toxicity, size, shape, buoyancy, price, etc.) found in the selection of the appropriate particles for the PIV application has ended with the development of a new particle type based on alginate. These particles developed during this Doctoral Thesis are in the process of patent, and they characteristics and properties can be found in chapter 3.

1.1.2 Turbulent flow in complex systems contain rotating elements

Analysing turbulent flow systems in complex geometries and obtaining experimental data in such flows is always complicated. A wide amount of industrial machineries contains rotating parts that interact with fluid flow. Engineers who design equipment with rotating components need to analyse and understand the behaviour of those components in order to improve performance. The knowledge of the interactions between the moving mechanical parts and the fluid flow can provide improvements in the design of the industrial machines. Usually this kind of systems implies a turbulent flow. By its nature, turbulence occurs in a wide range of physical scales: from the largest scales down to the Kolmogorov scale. Hence a good measurement technique must be able to measure over a wide range of scales. Several different approaches can be used to study in and around rotating equipment. PIV provides instantaneous velocity information over a whole flow field, and hence it is advantages to use this technique for instantaneous and unsteady/turbulent flow events such as flows in wind turbine blades, jets, and rotor blades in the majority of the rotating machinery fluid-flow analyses. The study of Lang et al. (2002) is a good example of PIV application in an axial transonic turbine. They have investigated the flow at different stator-rotor positions and observed the vortex shedding in the rotor. PIV has been applied to analyse a Francis turbine with constant pitch blades that cause complex unstable cavitating flow in the diffuser cone (Iliescu et al. 2008). They used fluorescent particles based on Rhodamine B that allows applying the ensemble averaging by phase technique to extract the both the periodic velocity components and the rope shape. Grant et al. (1991) described the flow over a simple commercial wind turbine in a wind tunnel using the PIV technique. The authors analyse both the characteristics of the tip vortices trailing from consecutive blades and the circulation around one individual blade. Sharp and Adrian (2001) investigate the flow in a Rushton turbine consisting in rotating blade tips with periodic components in a cylindrical chamber. The instantaneous velocity flow fields with the information for RMS velocities and vorticity of the small-scales were obtained at different spatial resolutions. They used two-dimensional PIV to study the flow field very near of the impeller. The phase-locked data in the radial-azimuthal plane provided insight into the dynamics of the tip vortices

(location, strength, etc.) as well as highly resolved maps of the mean and turbulent flow fields.

The ability to measure instantaneous planar velocity fields makes PIV attractive for investigating pumps and the complex flow conditions produced by the rotor-stator interactions. Some applications of the PIV studies to the pumps that contain rotating parts can be found in Wulff (2006) that analyses radial impeller pumps and axial pumps systems. One of the most common pumps is the external gear pumps that are used in industry for transferring and metering high viscosity fluids and power transfer usually at high pressure rates. The external gear pump has two cogwheels rotating against each other. The flow of the external gear pumps has been analysed by several authors. It is difficult to theoretically solve the instantaneous flow areas and volumes accurately due to the complexities of the geometry profiles of gear teeth and wear plates. Falfari and Pelloni (2007) have developed a parametric lumped model by considering teeth space volumes, links of meshing zone, leakage between casing and tooth head, and clearance between the lateral side of gears and bearing blocks. Flow dynamics of the gear pumps have also been addressed by theoretical researchers. Control volume method has been used to estimate the flow ripples of the gear pump with different numbers of driving and driven gears (Manring and Kasaragadda 2003). Huang et al. (2009) have studied the flow characteristics of external spur gear pumps using a flow rate formula derived in closed form. Numerically, the suction chamber of the external gear pump has been analysed by an arbitrary Lagrangian-Eulerian formulation with mesh deformation and local remeshing (Castilla et al. 2010). Furthermore, in the same study a mesh replacement strategy has been also adopted in order to avoid skewed meshes and allow for simulation of solid contact between gears. Wang et al. (2011) proposed a numerical method for the entire gear pumps using the generalized control volumes method. The earlier experiments on the gear pump have been done by mounting the pressure transducers in the root of the driver gear to measure the meshing pressures and flow visualization (Eaton et al. 2006). In another experimental study, a capacitive clearance transducer has been installed in the end-face of the gear teeth in the driven gears in order to determine the thickness of the fluid film separating the gear end and bush (Koç et al. 1997). Due to the high frequency response needed to monitor the clearance as the gear and transducer rotated, the standard

bridge output has been replaced by a computer-based demodulation system (Hooke and Kakoullis; 1979). For the first time a non-intrusive technique has been applied to observe the flow inside the external gear pump by Castilla et al. (2008). The turbulence at different diameter-based Reynolds numbers have been analysed by using air bubbles as tracer particles for the time-resolved PIV.

1.1.3 Spatial resolution effects on the analysis of the turbulent structures

As stated before, two-dimensional PIV provides an important tool for obtaining space and time resolved velocity data and these data lead to analyse for complex turbulent flows. Experimentally determined flow fields can be used to evaluate additional flow parameters, including vorticity (Luff et al. 1999; Nicolaides et al. 1998; Fouras and Soria 1998; Foucat and Stanislas 2002), shear stress (Etebari et al. 2004a and 2004b), and the dissipation rate (Saarenrinne and Piirto 2000). Quantification of these parameters and their spatial variations are essential to the understanding of unsteady and/or turbulent flows. However, the method chosen for estimating the velocity derivatives has significant effect on the accuracy of estimation of these quantities, which greatly depends on the length scales present in the flow and the velocity random error. Several methodologies on the turbulent kinetic energy and the local specific energy dissipation rates have been elucidated and compared for the characterization of the stirred baffled vessel using time-averaged and angle-resolved PIV (Gabriele et al. 2009). Sheng et al. (2000) reviewed the methods of the dissipation rate estimation, the large eddy approach and stirred vessel studies. The reviewed methods included the estimation of the dissipation rate for direct measurement of strain rate tensors, turbulent kinetic energy balance, turbulence power spectrum, Taylor's frozen turbulence hypothesis and dimensional analysis. Baldi et al. (1996) has used direct definition in order to estimate the turbulence energy dissipation by evaluating the instantaneous spatial gradients of the Reynolds stresses. Particular attention has given to the effects of spatial resolution over estimation of energy dissipation.

Although PIV technique offers various advantages, the ability to resolve all scales of interest for turbulence studies has not been established properly according to the spatial resolutions to estimate the dissipative ranges. The spatial and temporal variations of the dissipation of the turbulent energy have been quantified in a stirred vessel by using laser Doppler anemometry (LDA), computational fluid dynamics (CFD) and PIV (Micheletti et al. 2004). The angle-resolved LDA and CFD results have shown that the magnitude of dissipation rate varied by more than two orders of magnitude between the impeller region and the bulk of the vessel. From the results through LDA and PIV, estimates of dissipation rate based on dimensional methods and other approximations have been concluded that the dimensional method underestimates the dissipation rate everywhere except close to the impeller tip where it exhibits a local maximum. The flow in a vessel stirred with a down-pumping axial impeller has been studied by Delafosse et al. (2011) to estimate the dissipation rate particularly attempting on the necessary assumptions and on the influence of the measurement spatial resolution. The smallest spatial resolution ranges between 1.8 and 2.5 times the local Kolmogorov scales have been computed on the measurement plane and it has been concluded that the local dissipation rate values might still be slightly underestimated. Again in this study, the validity of the isotropic assumptions in the literature has been examined to estimate the velocity gradients which cannot be measured by 2D-PIV. The results have showed that the turbulence was far from isotropic in the impeller discharge. The dissipation rates estimated using the hypothesis of a fully isotropic turbulence has been found that they were significantly overestimated, especially in regions where the dissipation rate was high. The relation proposed by Sharp et al. (1998) based on an assumption of statistically isotropic turbulence has given the better results. Huchet et al. (2009) has proposed the dimensionless time-variation of dissipation rate recorded during three seconds to analyse the impeller stream of a Rushton turbine by time-resolved PIV. Baldi and Yianneskis (2004) have evaluated values of local specific energy dissipation rates directly from the measured fluctuating velocity gradients. A large-eddy PIV method has been used in order to approximate the dissipation of energy at scales below the resolution of the measurements since PIV can only resolve to a certain minimum length scale defined by the size of the interrogation area (Sheng et al. 2000). The obtained results vary from one

work to another due to the approximations made on the structure of the turbulence and limitations in terms of spatial and temporal resolutions. In order to obtain dissipation rate, several relationships based on isotropy assumptions are proposed in the literature despite an insufficient number of measured gradients. A method that considers the turbulence as non-homogenous but statistically isotropic, have been used in several studies (Ducci and Yianneskis 2005; Sharp et al. 1998). The method calculates the theoretical local dissipation rate from definitions (Hinze 1975) using two-dimensional definition. The assumption on the turbulence as homogenous would be inappropriate due to the inhomogeneity and periodicity of the phases of rotating impeller parts. In order to perform the calculations, it can be assumed as isotropic turbulence although it is difficult to meet in practice. The applicability of the isotropic assumptions has been assessed by comparing the magnitudes of the mean square gradients. Another significant point to consider in the estimation of the turbulence dissipation is the spatial resolution of the PIV measurements since the dissipation occurs mostly at the smallest turbulent scales as the Kolmogorov scale. Recently, there have been attempts to quantify the effect of the spatial resolution on the estimation of the turbulent scales in PIV. The velocity gradients have to be determined with a spatial resolution equal or smaller than the Kolmogorov scale in order to achieve accurately the computed dissipation rate (Saarenrinne and Piirto 2000). It has been demonstrated that the use of overlapping interrogation regions with low image density can lead to biased results (Poelma et al. 2006). The spatial resolution of the PIV interrogation techniques have been discussed from an analytical point of view and assessed with Monte Carlo numerical simulation of the particle image motion (Scarano 2003). A comparison of two measurement techniques, hot-wire anemometry (HWA) and PIV, have been performed in order to study the effect of the finite spatial resolution of PIV on turbulent statistics for low speed wind tunnel (Lavoie et al. 2007). Although the study has indicated the significance of HWA for studying turbulent flows, it highlights the advantages of PIV in the availability of simultaneous velocity measurements at numerous points in space.

1.1.4 High speed flows contain rotating elements

The PIV in high speed flows is related on the ability of tracer particles to follow the flow. Homogeneous seeding of the flow with suitable tracer particles with sufficient density is one of the major problems in high-speed air-flows. In order to minimize the velocity lag in regions with strong positive or negative accelerations of the flow across shocks in turbulent flow or in vortical flows, very small tracer particles with a diameter of 1 μm or smaller are required (Bryanston-Cross et al. 1995). A high acceleration or deceleration in the flow causes the particles to travel locally at a velocity significantly different from that of the surrounding fluid. This significantly causes the particles to be ejected towards regions with lower accelerations due to the integrated effect of particle slip as reported in many works (Lang 2000; Koike et al. 2007; Schrijer and Scarano 2007; Schrijer et al. 2008). The unsteady motion of small spherical particles in fluid flows has been previously determined (Mei 1996) and it has been provided a general mathematical review for a high-speed regime (Tedeschi et al. 1999). A numerical study has been done to analyse the problem of the particle motion in turbulent flow compressible shear layers (Samimy and Lele 1991). The effect of the compressibility has been found insignificant on the motion of the particles in the range of Mach number 0.2 to 0.6. Furthermore, an analysis of the scattering and size specifications for suitable tracer particles and on the application of seeding PIV materials in gaseous and liquids has been studied and quantified for several systems (Melling 1997). For liquids, a concentrated suspension of seeding particles has been suggested to be prepared before starting the experiments. Then this mixture is introduced to the analysing flow. This allows the particles mix through the circulating flow uniformly. It has been stated that the dilutions up to 1:50000 were feasible and mono-disperse suspensions such as latex particles have been suggested although they are too expensive for large quantities. Sufficient seeding particles and stable concentration with a spatially uniform distribution have been suggested to be introduced for the gas flows, while minimizing coagulation and deposition of the particles.

1.1.5 The unsteady complex flow analysis

The inherent unsteadiness of the flow field caused by stator-rotor interaction has a significant impact on efficiency and performance. Single point techniques such as Laser Doppler vibrometry (LDV) are usually used for the measurements of unsteady flows. These techniques measure the unsteady flow fluctuations of pressure and velocity in the flow field. However, these measurement techniques cannot directly provide information over the entire instantaneous flow field and flow structures in unsteady flows. One measurement technique that is able to provide instantaneous flow field data and reveals flow structures in unsteady flows is the PIV method (Adrian 1997; Liu et al. 1991; Willert et al. 1995). PIV has become a powerful tool to investigate these unsteady processes in turbomachinery flows in attaining the great advances to yield significant characteristics of the complex flow structures. PIV and stereo-PIV have been applied to flow studies in transonic compressors (Copenhaver et al. 2002; Estevadeordal et al. 2002; Sanders et al. 2002; Tisserant and Breugelmans 1997), subsonic turbine flows (Chow et al. 2002; Hill et al. 2000; Uzol et al. 2002; Wernet 2000) and transonic turbine flows (Lang et al. 2002). The PIV technique yields good results for the investigation of transonic and supersonic flows (Bryanston-Cross 1995; Bryanston-Cross et al. 1992; Kompenhans and Höcker 1998; Towers et al. 1991). Furthermore it has been successfully applied to investigate the rotor-stator interaction in turbomachines (Towers et al. 1991; Grant et al. 1994; Tisserant and Breugelmans 1995) and to the 3-D flow field of a radial pump impeller (Visser and Jonker 1995). Moreover there is a growing trend in use of PIV for the validation of CFD codes and experimental verification. Confidential measurement of PIV is an important factor for the verification purposes of the experiments.

1.2 Objectives

The main objective of this thesis is the improvement and application of the PIV technique to analyse different complex fluid flows in systems that contain solid moving parts. This general objective is detailed in a series of the following specific objectives:

1. Apply PIV technique to the study of complex flow systems. Focus in the interaction of fluid and moving solid parts and in low speed air flow systems.
2. Adjust the ECoMMFiT PIV software to be able to analyse flow in systems with moving solid parts.
3. Implementation of an efficient methodology for estimation of turbulent statistics from PIV experimental data.
4. Research among the different types of tracer particles to obtain those that better fits in the studied systems. This objective ends with the development of new tracer particles adding additional objectives (5 and 6) not defined at the beginning of this doctoral thesis.
5. Development and description of the production process of the alginate tracer particles.
6. Characterization of the alginate tracer particles and demonstration that they can be employed as efficient and economical way in all kind of PIV applications in liquid or gas flows
7. Experimental analysis of the flow in an external gear pump.
8. Experimental analysis of the bypass flow in a turbofan engine with a heat exchanger in low speed wind tunnel.

The main added value of this thesis is the realization of comprehensive flow analysis with the turbulent flow dynamic characterization in the external gear pump flow by using the PIV technique. This thesis also attempts for the first time to implement alginate micro particles as tracer particles for the PIV technique in the external gear pump flow, and the engine bypass flow heat exchanger.

1.3 Outline of thesis

In this doctoral thesis, the external gear pump model has been comprehensively investigated by the PIV technique. At the beginning of our research, in October 2007, the characteristics of the complex flow pattern of this pump have been studied with appropriate experimental techniques that allow visualizing the flow inside the gear pump at high rotational velocities. The information about the time evolution of the large-scale flow structures, the mean and instantaneous velocity fields inside the suction chamber have been obtained. Air micro bubbles had been used as tracer particles in order to investigate the flow inside the suction chamber (Ertürk et al. 2011; Castilla et al. 2010). Since, the use of solid particles could produce material erosion due to metal–metal contact between the gear teeth and damage the transparent surface of the system. In addition, the use of water drops could produce oxidation of the steel gears. In the middle period of our research, alginate particles with/without fluorescein compound imbedded have been developed as a new alternative for PIV applications. The alginate micro particles have been efficiently used in PIV as tracer particles for different experiment facilities that have been detailed in the following chapters. Then, the alginate particles have been started to be used in PIV to analyse this flow system (Ertürk et al. 2012). The PIV measurements have been performed for different spatial resolutions configurations and various interrogation areas to estimate the dissipation rate of the turbulent kinetic energy. The optimal result has been achieved if the interrogation area is neither too large (sampling phenomenon) nor too small (noise in the measurement data). The effect of number of samples employed in the ensemble-averaging was also considered. Furthermore, the alginate particles have been applied to different experimental facilities and different fluids such as water, air, and oil to analyse the complex flows by PIV as indicated in the following chapters of the thesis. It has been found that the alginate micro particles have many advantages over traditional ones in PIV systems. Furthermore, they are environmental friendly, nontoxic and cheap (Ertürk and Vernet 2011).

The reminder of this thesis consists of 8 Chapters. In the current chapter we have seen that PIV is a developing technique that is capable of investigating dynamics and statistics of complex turbulent flows. The literature survey has been done in order to include the

effective tracer particles for the complex flow fluids that contain solid moving or stationary parts. In Chapter 2, fundamentals of the PIV technique are explained in detail with the image data analysis methods applied to estimate the seeding particle displacement. In addition, a there is a review of the relation between tracer particles and their respective images and the estimations on the turbulent statistical parameters. The applications of the PIV technique starts with Chapter 3 that provides information on the production methods of alginate micro particles and the application of these tracer particles to the PIV technique with experimental verifications. Chapter 4 provides a comprehensive study on the three-dimensional flow analysis of the external gear pump, while chapter 5, is devoted to the experimental study of an engine bypass flow heat exchanger in a low speed wind tunnel. Chapter 6 points out a summary of the main results and conclusions from the preceding chapters. In addition, acquired skills and attributes have been explained by focusing on the possible future developments with respect to PIV through the implemented methods and used tracer particles in this thesis. Finally, the references are included at the end of the thesis.

INTRODUCTION

CHAPTER II
FUNDAMENTALS OF PIV IMAGE DATA ANALYSIS

2.1 Introduction

Many techniques have been developed for flow field diagnostic that are classified as conventional intrusive methods and non-intrusive optical methods. The intrusive methods such as hot-wire anemometry and vane anemometry are used to obtain the velocity information at the point where the sensor is placed (Brunn 1995; Lundgren and Ashurst 1989; Doolan et al. 1999). Alternatively the non-intrusive methods are optical flow measurement techniques such as Particle Image Velocimetry (PIV), Particle Tracking Velocimetry (PTV) and Laser Doppler Velocimetry (LDV). These techniques are used to obtain flow information from the detection of light scattered by small particles moving with the fluid (Raffel et al. 1998; Ohmi and Li 2000; Truax et al. 1984). The flow field is influenced by the probe that is used in the intrusive methods, whereas non-intrusive methods have the measurement equipment placed outside of the system having no effect on the flow behavior. High temporal and spatial resolution measurements can be obtained using non-intrusive methods according to fast scatter of light and advanced electronic data acquisition and signal processing techniques. PIV is a non-intrusive measurement technique that needs a recording medium, an illuminating light source and a computer for image processing. Small tracer particles that are introduced in a region of a fluid are illuminated by two consecutive short duration light pulses produced by a laser. The image

of the particles during two consecutive laser pulses is recorded by a CCD camera. Processing these consecutive images by means of cross-correlation methods allow obtaining the velocity vectors associated with the fluid flow.

Besides the standard PIV system, different configurations such as Stereoscopic PIV, Endoscopic PIV, Micro PIV and Holographic PIV are presented depending on the flow system requirements. Stereoscopic PIV is a technique that uses two cameras to view flow field from two perspectives in order to be able to measure instantaneously the three components of the velocity in one plane. Recently stereoscopic PIV has been intensively developed and many commercial systems are available (Prasad 2000). By using the advantage of using two views in stereoscopic PIV set-up, 3D vector information with high accuracy can be recovered from the planar PIV images (Lawson and Wu 1997; Yoon and Lee 2004; Zhengliang et al. 2006). However, some applications require very restricted optical access in high temperature and high pressure flows and fluids that have a biological importance. Advancements in optical fibres (Hand et al. 1999), endoscopic relay lenses and miniature light sheet optics have resulted in several studies to implement endoscopic PIV systems (Dierksheide et al. 2001; Geis et al. 2002). Micro PIV is a modification of PIV in order to access the small scales of the microfluidic devices. The Micro PIV system (Meinhart et al. 1999) uses a CCD camera, a microscope with fluorescent unit and two pulsed Nd:YAG lasers. Another novel extension of the PIV technique is the Holographic PIV that is able to capture the three-component measurements from an extended volume of fluid (Zhang et al. 1997; Coupland and Halliwell 1992; Barnhart et al. 1994). Holographic PIV uses correlation based techniques to extract three-dimensional displacement fields from double-exposure holograms (Barnhart et al. 1999; Barnhart et al. 2000).

Although PIV is still a developing technique, excellent review papers have been published describing its historical development, measurement techniques and applications (Lauterborn and Vogel 1984; Adrian 1986; Adrian 1991; Dudderar et al. 1988; Adrian 2005; Buchhave 1992; Grant 1997; Prasad 1997). Lauterborn and Vogel (1984) and Adrian (1986; 1991) have described a large number of the optically based, non-intrusive velocimetry techniques that provide flow information in 2D and 3D

regions. Dudderar et al. (1988) mainly focus on the comparison between the advantages and disadvantages of the velocimetry techniques applied in steady and unsteady flows. The development of PIV has been summarized with its current status and future advances by Adrian (2005). Comprehensive reviews of the PIV technique as a fluid mechanics tool are properly described by Buchhave (1992) and Grant (1997). Prasad (1997) has also studied the fundamentals of the PIV technique including PIV algorithms, optical considerations, tracer particles, illuminating lasers, recording hardware and processing of PIV images.

Internal fluid flow in systems with rotating passages such as external gear pumps, centrifugal pumps, stirred vessels, turbines is exceedingly complex as they involve rotation and turbulence effects. These types of flows are interesting from a fluid mechanical perspective as it is often influenced by rotor-stator interaction mechanisms. Several measurement techniques have been developed and applied to a large variety of industrial machines in the struggle for accurate quantitative flow descriptions. Experimental measurements have provided fundamental knowledge of the flow phenomena occurring in rotating machines (Wernet 2000; Pedersen et al. 2003; Day and McDaniel 2005). However, the quest that maintains high efficiencies and performances at a broader range of operating conditions raises the need for a more detailed knowledge of the local and instantaneous features of the rotating passages flow.

In the last decades, PIV technique has been applied to the studies of a large number of flow problems (Adrian 2005). Wernet (2000) has applied this technique as a quantitative measuring method for the flow in turbomachines. A general description of the technique in rotating machinery applications can be found in the work of Wulff (2006). The high image acquisition rate is necessary to capture the evolution of the flow in systems with considerable velocity changes that are encountered in pumps with large rotational velocities. Time- Resolved Particle Image Velocimetry (TRPIV) is the technique that is used to obtain the velocity time-series from the particle images (Lecordier and Trinite 1999). By applying this technique, the information about the time evolution of the large-scale flow structures, the mean and the instantaneous velocity fields inside the suction chamber can be obtained.

In this chapter the principles and basic set-up of the PIV technique are described, giving some details about the tracer particles. The pre-processing of the acquired images and the details about the procedure to compute the displacement of the tracer particles is explained. This displacement is to get the velocity vectors from those images. Section 2.2 describes the PIV technique by discussing tracer particles, interrogation area, image pre-processing, estimation of displacement and data validation method implemented. In section 2.3 the procedure to estimate the turbulent scales of the flows in complex systems that contain rotating parts is explained. The special attention is given to the study to assumptions needed to estimate the dissipation rate from two-dimensional PIV images and to the influence of the measurement of the spatial and temporal resolution of the PIV data. Besides, the error estimations in measurement of the velocity vectors and the dissipation rate are explained by considering the effect of number of samples employed in the ensemble-averaging of the velocities.

2.2 Principles of PIV and image analysis

To apply the PIV technique it is necessary to seed the fluid of interest with some kind of tracer particles. These particles will be illuminated by two consecutive short duration light pulses produced by a laser. The images of the particles are captured with a CCD camera as shown in figure 2.1. It is assumed that the motion of the tracer particles follows faithfully the movement of the fluid. Thus, the motion of the fluid can be determined by measuring the particle displacements through evaluation of the PIV recordings. The recorded images are divided into small interrogation areas and analyzed by means of a correlation method. With the aid of PIV technique quantitative two-dimensional information of the fluid velocity is obtained. Comprehensive descriptions and explanation on the principle of the PIV technique have been provided by Raffel et al. (1998).

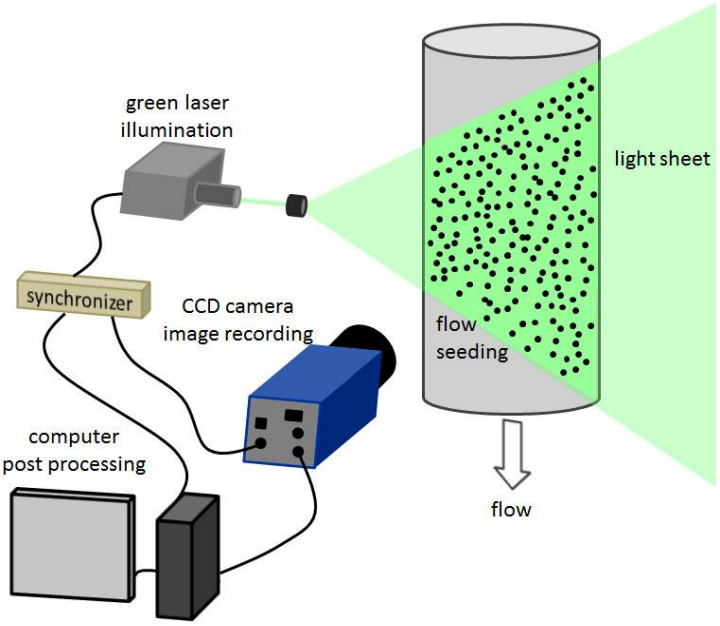

Figure 2.1. Principle of particle image velocimetry technique consisting on flow, flow seeding, laser, camera, synchronizer and computer.

2.2.1 Tracer particles

Flow seeding is a significant part in the experimental PIV set-up. This is achieved by adding small tracer particles into the flow. As explained before, it is assumed that the fluid and particles move as one. The images of the particles obtained when the region of interest is illumined twice by a laser allow computing the velocity of the flow field. The light scattered by the particles is recorded on a single frame or on a sequence of frames. The displacement of the particle images between the light pulses is then determined through evaluation of the PIV recordings. The principle of PIV is based on the direct determination of the two fundamental dimensions of the velocity as length and time. The technique measures the particle velocity which is determined instead of fluid velocity. Therefore, properties of the particles have to be checked in order to avoid significant discrepancies between fluid and particle motion (Raffel et al. 1998). The selection of the particles comprises a basis of the velocity measurements in PIV. These particles should be as small as possible in order to ensure good tracking of the fluid motion. On the other hand, they may not be too small, since they will not scatter enough light. If tracer

particles scatter light weakly, then more powerful lasers or more sensitive cameras that increase the costs and safety issues should be used. It is better to search ideal tracer particles that follow the flow faithfully and scatter enough light for the flow system in order to obtain accurate velocity field of the flow (Melling 1997).

The most commonly used tracer particles in liquid flows are polystyrene, aluminum, glass spheres as solid seeding, different types of oils as fluid seeding and oxygen bubbles as gaseous seeding. The obtained particle image intensity is directly proportional to the scattered light power. Therefore, it is more effective and economical to increase the image intensity by properly choosing the scattering particles than by increasing the power of the laser. The light scattered by small particles is a function of the ratio between the refractive index of the particles and that of the surrounding medium, the particles' size and their shape and orientation. There is a tendency for the scattered light intensity to increase with increasing particle diameter. However, increasing the size of the particles will affect tracking of the fluid motion. Moreover, difficulties arise in providing high quality seeding in gas flows compared to applications in liquid flows. The most commonly used tracer particles for PIV investigations of gaseous flows are polystyrene, aluminum, magnesium, glass micro-balloons as solid seeding and different oils as liquid seeding. Therefore, it is clear that a compromise to use tracer particles has to be found for liquid and gaseous flows.

Tracer particles should follow the flow without changing the pattern of the flow. Therefore, particle density (ρ_p) should closely match the density of the fluid (ρ_f). In addition, at zero-velocity condition, tracer particles should stay suspended in the fluid without sinking or floating up due to gravitational effects and buoyancy. For liquid flows, there are commercial particles that satisfy these conditions. For gas flows, finding suitable tracer particles requires more complex study and it is difficult to say any satisfactory requirements as said for liquid flows. Although the density of particle and the density of fluid do not match, it is neglected in many practical situations. Stokes' drag law can be applied in order to estimate the particle velocity as in Eq. 2.1 (Raffel et al. 1998). Here, it is assumed that tracer particles are spherical in viscous and low Re flow with continuous acceleration.

$$U_p(t) = U\left[1 - e^{-\frac{t}{\tau_s}}\right] \tag{2.1}$$

U_p is the velocity of the particle, U is the fluid velocity and τ_s is the relaxation time given by:

$$\tau_s = d_p^2 \frac{\rho_p}{18\mu} \tag{2.2}$$

where d_p is the diameter of the particle and μ is the dynamic viscosity of the fluid. τ_s is an indicator of the ability of a particle of certain size and density to respond to fluid acceleration. The particle velocity will lag behind the velocity of an accelerating fluid due to its inertia; the magnitude of this velocity lag can be calculated from Eq. 2.1. Figure 2.2 is illustrated for four different particle diameters in a water flow. It is shown that the particle response time decreases with particle diameter. A further constraint on particle size should be small in comparison to structures present in the flow, so that the fluid velocity does not change significantly across the tracer particle.

A new kind of tracer particles that can be named as alginate micro particles with diameter sizes approximately between 0.2 μm up to 30 μm has been developed and used in this thesis. This means that the errors due to velocity lag can therefore be negligible in the PIV applications that have been studied here. Details of the alginate micro particles as flow seeding in PIV can be found in Chapter 4.

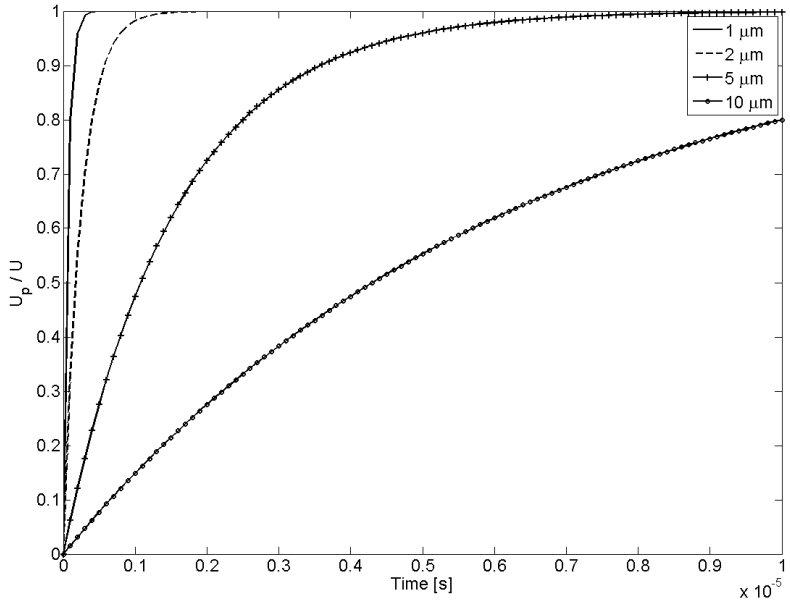

Figure 2.2. Particle response time to fluid acceleration for four different particle diameters; d_p = 1 μm, 2 μm, 5 μm, 10 μm (plot of Eq. 2.1)

2.2.2 Image pre-processing

First consideration on the processing of time series of PIV images can be introduced apart from the characteristics of the flow that is being measured. Since the time history of the illumination at each image location is available, statistical properties of the series can be analysed. In order to eliminate undesired light reflections and to homogenise the median illumination, the particle images are pre-processed before using them to calculate the velocities. The median value of the illumination at each point provides information that affects the detection of the actual displacement of the particles (Hart 1999). As the time history of the illumination at each particle image location is available, the mean value can be used in a clean-up mask process to remove and/or reduce the spurious permanent reflections. In order to eliminate undesired light reflections and to homogenize the median illumination, the particle images are pre-processed before using them to calculate the velocities. The fact that each experimental session implies a large number of individual images allows computing the median value of the illumination. This value

provides information that affects the detection of the actual displacement of the particles (Hart 1999). As the time history of the illumination at each particle image location is available, the mean value can be used in a clean-up mask process to remove and/or reduce the spurious permanent reflections. Figure 2.3 shows an original particle image by using air bubbles as tracer particles and the same image after applying the clean-up mask process. It can be seen that the filtered image shows a homogeneous illumination at the region of interest, and the high intensity reflections near the gears disappear.

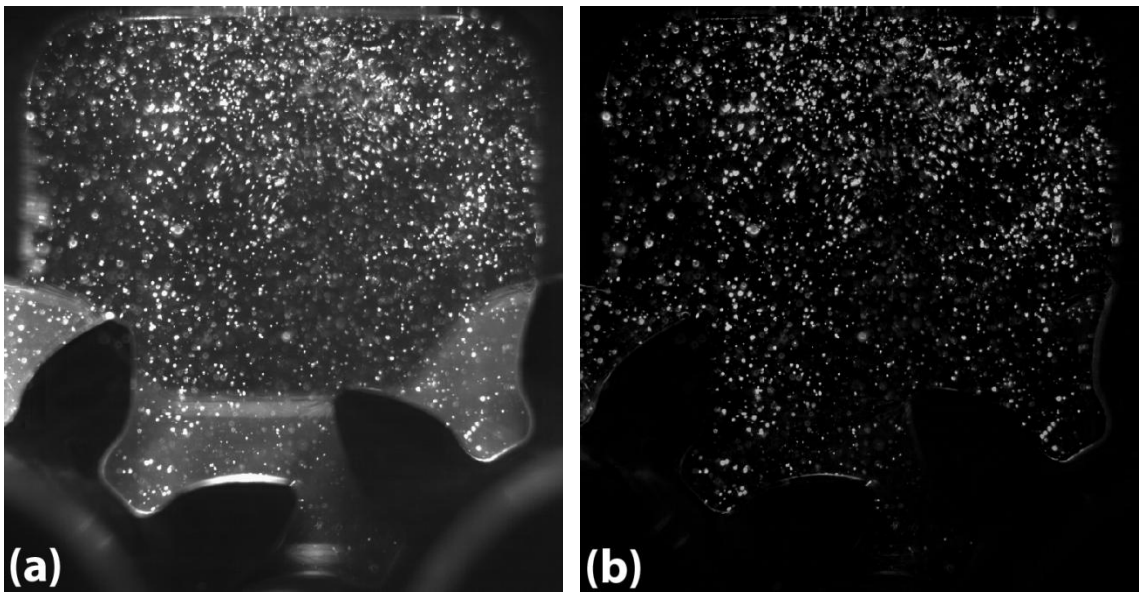

Figure 2.3. Application of clean-up mask process: (a) original particle image velocimetry and (b) the same image after clean-up mask process applied.

Figure 2.4 shows the original particle image by using alginate micro particles as tracer particles and the same image after applying the clean-up mask process. It can be seen that the filtered image shows a homogeneous illumination at the region of interest, and the high intensity reflections near the gears disappear. Furthermore, when recording the particle images by means of a CCD camera, there is always a certain amount of noise, owing to ambient light, bad focusing or alignment that can deteriorate the signal-to-noise ratio in portions of the image. The occurrence of the spurious vectors can be found in the

limitations of each technique and in the quality of the images, the lack of particles or out of plane displacement of the particles. Thus, a quality control must be applied to the velocity vectors that are obtained with the purpose of detecting and eliminating the spurious vectors.

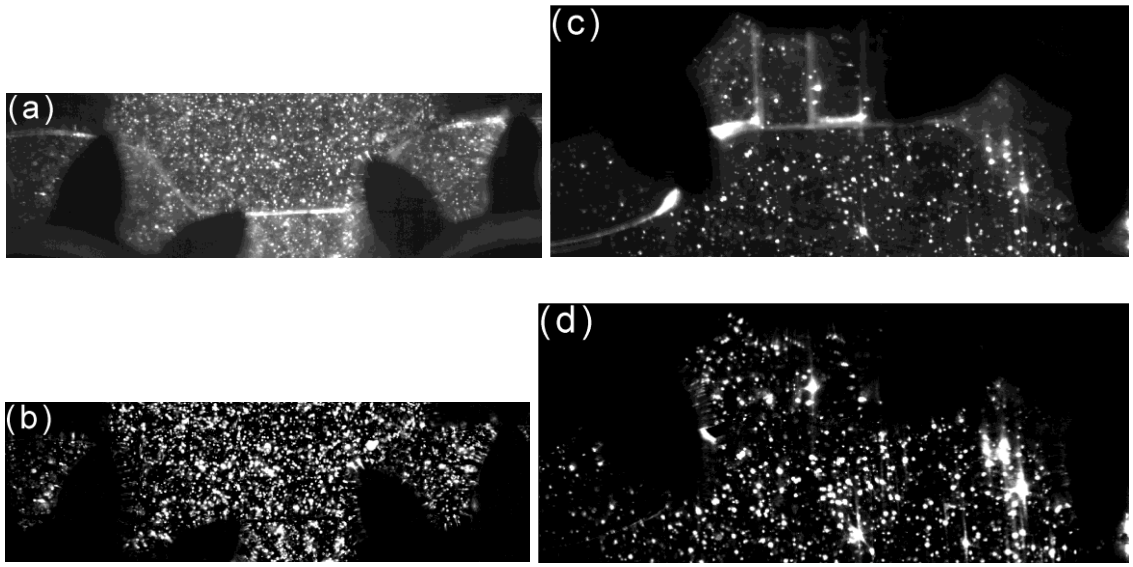

Figure 2.4. Application of clean-up mask process for the PIV images of the external gear pump: (a) original particle image in the suction chamber; (b) the same image of (a) after clean-up mask process applied; (c) original particle image in the impulse chamber; (d) the same image of (c) after clean-up mask process applied.

The alginate micro particles have been used to illustrate the PIV images in the figure 2.4. Approximately 60 phase averaged images have been used to apply the clean mask process. The figures 2.4a and 2.4b show the single instantaneous image and the same image after clean-up mask process applied, respectively, in the interest of the region in the suction chamber of the external gear pump. The figure 2.4c presents the impulse chamber of the field of region interest for a single instantaneous image, while figure 2.4d displays the differences between the original image and the median image from a time series of 60 images. The image pre-processing step has significantly reduced the spurious permanent reflections that could effect on the estimations of the displacement vectors.

2.2.3 Interrogation area

The main objective of the evaluation of PIV recordings is to determine the displacement of the particles between two light pulses. Initially, it is possible to think that the best option is to individually detect each particle and compute its own displacement. The main problem for this approach is how to detect the same particle in both images. This is the procedure applied in Particle Tracking Velocimetry, usually used when the particle density is very low. When PIV is used, a single image pair contains hundreds or thousands of particles, thus, it is nearly impossible to compute the velocity for each particle. Therefore, another approach is needed. The procedure used in PIV implies that the images are divided into small sub-areas called interrogation areas, as seen in Figure 2.5. In this figure, one of the interrogation areas has been shown at time t with its corresponding interrogation area at time $t = t+\Delta t$. The interrogation areas contain several particles that are used to obtain the mean velocity vector of all them by changing their displacement in an interval time, Δt.

It is assumed that all the tracer particles within an interrogation areas move homogenously between two laser pulses. The average of displacement is then calculated at each interrogation area by means of cross-correlation method to build up the complete 2D velocity vector map. Actually, this procedure acts like a filter of the velocity as the velocities of all the particles in an interrogation area are averaged. Typical dimensions of an interrogation area for PIV are between 16x16 to 128x128 pixels in power of two due to the use of standard FFT algorithm. In order to obtain a reliable estimator of the particle image displacement 10 to 15 particles in an interrogation area have to be present (Raffel et al. 1998). In this thesis, from 32x32 to 64x64 pixels interrogation areas have been used by considering the adequate particles density in each interrogation area.

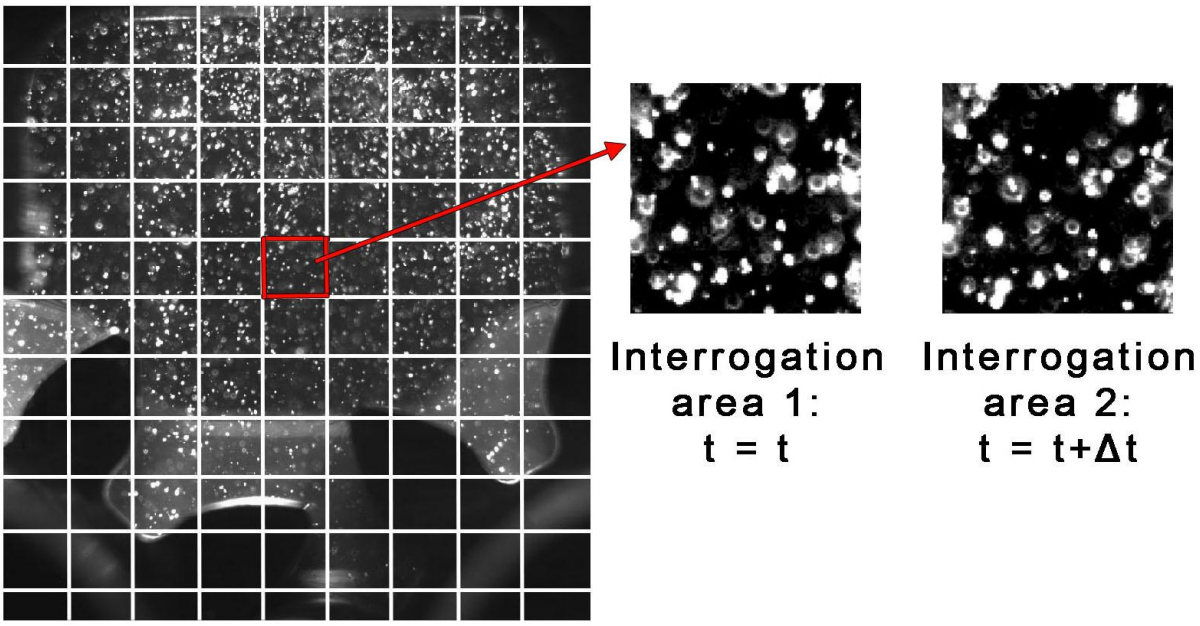

Figure 2.5. Illustration of the interrogation areas in a PIV image and the zoom image of the interrogation area at time t with its corresponding interrogation area at time $t = t+\Delta t$.

2.2.4 Evaluation of the particle displacement

Figure 2.6 illustrates the digital PIV cross-correlation procedure to estimate the mean displacement of the particles in an interrogation area. Computed cross-correlation values usually show a large peak that provide the best estimation for the displacement of the particle in the window. The information about the displacement and the time between two consecutive images allow computing the mean velocity in one interrogation area.

To calculate the cross-correlation between two corresponding interrogation areas from successive images (successive times), fast-Fourier transforms (FFT's) are used. Digital recording and computer analysis led to the application of a FFT in PIV image processing, which significantly decreased the time required for the necessary operations to produce a velocity measurement (Willert and Gharib 1991).

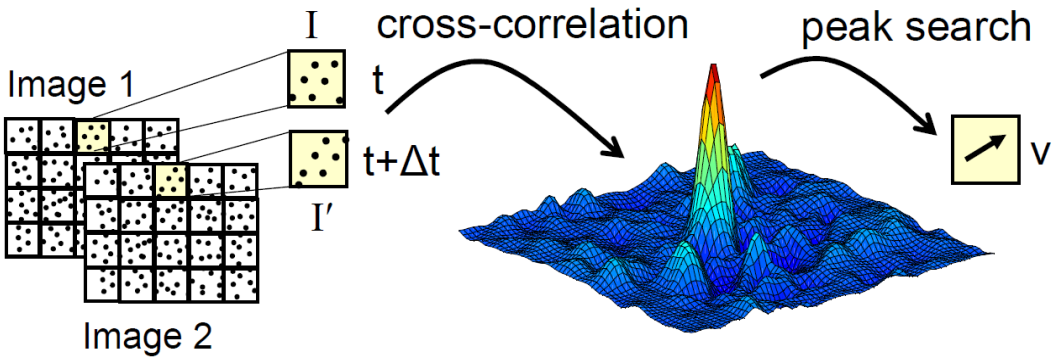

Figure 2.6. Cross-correlation procedure.

When recording the particle images by means of a CCD camera, there is always a certain amount of noise, owing to ambient light, bad focusing or alignment that can deteriorate the signal-to-noise ratio in portions of the image. The occurrence of the spurious velocity vectors can be found in the limitations of each technique and in the quality of the images, the lack of particles or out of plane displacement of the particles. Thus, a quality control must be applied to the velocity vectors that are obtained with the purpose of detecting and eliminating the spurious vectors. The number of spurious vectors could be reduced using the triple image correlation technique. Usually the PIV methodology requires two consecutive images to obtain one instantaneous velocity field. Alternatively, time-resolved analysis allows the use of a more robust procedure involving three consecutive images to obtain the velocity vectors associated to a specific time (Usera et al. 2004). A similar approach was proposed by Hart (Hart 1998; 1999), which uses the correlations obtained from adjacent regions to detect the error in the calculations of the velocity vectors. In this study, the correlations obtained at different times for the same interrogation window are used. The available experimental data is a set of particle images, which are uniformly spaced in time. The triple image correlation method uses three consecutive images to compute the velocity field. Thus, to calculate the velocity vectors at time t_i, the algorithm needs the particle images that are obtained at $t_{i-\Delta t}$, t_i and $t_{i+\Delta t}$. The correlation plane obtained from the particle images at time $t_{i-\Delta t}$ and t_i is multiplied by the correlation plane obtained from particle images at t_i and $t_{i+\Delta t}$ (Figure 2.7). The instantaneous velocity vectors of the double correlation and triple image

correlation have been illustrated in the figures 2.8a and 2.8b, respectively. The spurious vectors can be identified in the figure 2.8a more than the figure 2.8b. Triple image correlation scheme leads to the attenuation of the spurious correlation peaks that appear in only one of the correlation planes and increases the absolute height of the valid peak. This scheme is applied to each consecutive frame, thus each particle image (except the first and the last images of the series) is used in the calculation of three consecutive velocity planes. In this sense, the triple image correlation procedure does not modify the original sampling rate. The temporal resolution is the same for the computed velocity time history and the particle image series.

Obtaining the velocity field from the particle images has been done using domestic PIV software based on an iterative patterns deformation algorithm with regard to the Local Field Correction PIV method that is proposed by Nogueria et al. (2001). These authors found that this procedure has an enhanced behavior in strong gradient situations and the effective spatial resolution depends on the number of iterations. This means that the size of the interrogation area is not an absolute resolution limit in iterative PIV algorithms with image deformation. An appropriate weighting function eliminates the window size from the ensemble of spatial resolution (Nogueria et al. 2005).

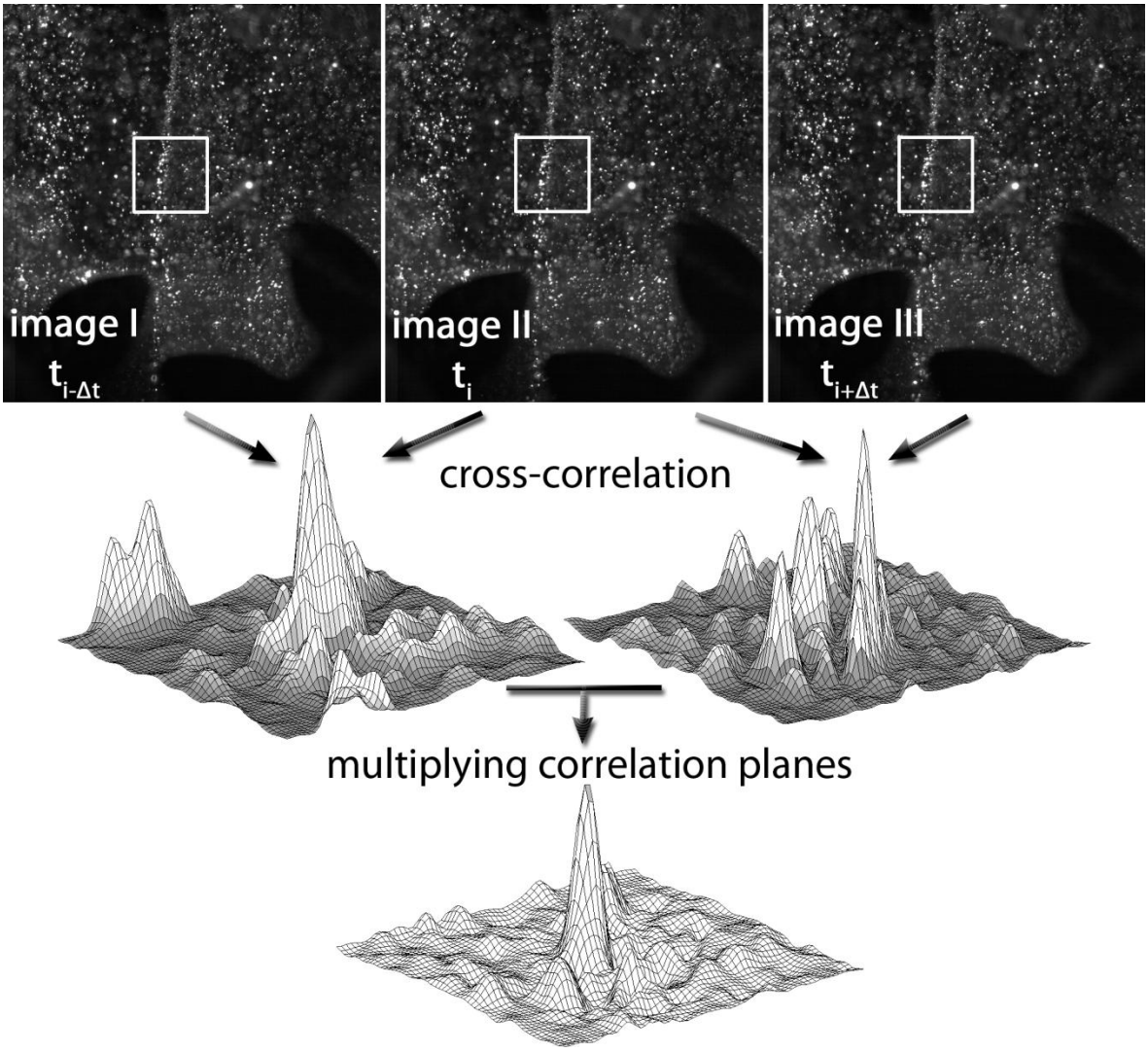

Figure 2.7. Triple image correlation scheme with correlation peak improvement. Two correlation planes are obtained from interrogation areas of image pairs at time ($t_{i-\Delta t}$, t_i) and (t_i, $t_{i+\Delta t}$). By multiplying the two correlation planes the correct displacement peak is enhanced.

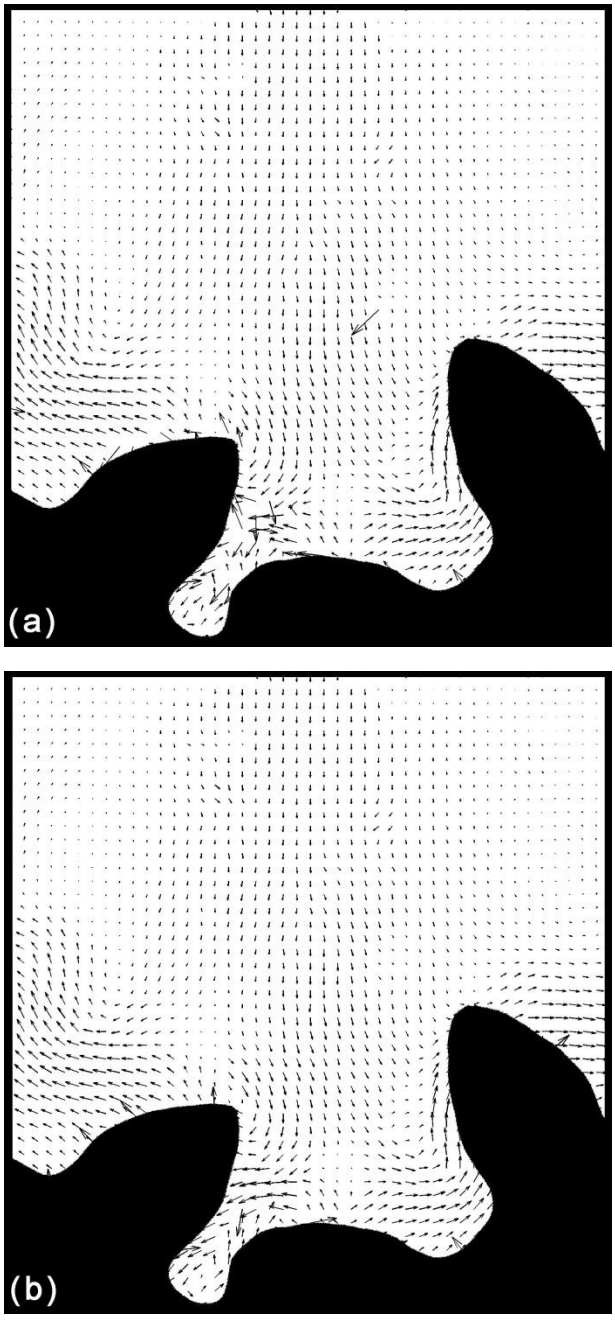

Figure 2.8. Instantaneous velocity fields by using 64x64 pixels interrogation area that is obtained after clean-up mask process: (a) double image correlation; (b) triple image correlation (see figure 2.7)

The 64x64 pixels interrogation area restricts the use of weighting functions in order to avoid resolution limits. Then, the resolution could be assumed to be between 8x8 and 16x16 pixels interrogation windows. The idea is to take the advantage of the LFCPIV method by combining the high spatial resolution with the robustness of a large window. On the other hand, iterative algorithms can introduce significant errors when the interrogation window is located near the image boundary. To avoid this issue, the boundary treatment method developed by Usera et al. (2004) has been used. This technique corrects the location of the computed velocity vector when the interrogation area overlaps the image boundary. Typically, the velocity estimation is obtained in the geometric center of the interrogation area. When the interrogation area overlaps the image boundary, the center could be placed out of the real boundaries of the image and this case leads to presence of erroneous vectors in the velocity field. The physical location of the velocity field is corrected by applying a weighting function that is able to adjust the real position of the vector (Usera et al. 2004; Lecuona et al. 2002).

In figure 2.8, 64x64 pixels interrogation area is used with a 75% overlapping to obtain the velocity field. This window size is selected after trying several possibilities and it was found to be the best value with the LFCPIV method to give enough information about the large-scale structures and to have an appropriate signal-to-noise ratio to minimize the number of spurious vectors. The oversampling process could affect the estimation of the differential quantities since adjacent velocity data are partially computed from the same particle images. For a 50% interrogation window overlap, the velocities can be considered as weakly correlated. For larger overlapping, special attention must be paid to the calculation of the differential quantities such as vorticity (Raffel et al. 1998). It is important to point out that the PIV technique uses the information from the interrogation area to obtain one velocity vector. In this sense, the value of the computed velocity is an average of the velocity of all the particles included in the interrogation area (Dudderar et al. 1998). Thus, the velocity field obtained is a filtered version of the real flow field. This filtering process results in a reduction of the measured turbulent kinetic energy and other second-order statistics of the velocity field (Spencer and Hollis 2005). In order to obtain a better resolution on the particle images, appropriate tracer particles should be used in the

PIV system. Smaller size tracer particles will allows using smaller size interrogation area such as 16x16 or 32x32 pixels that leads to determine the small-scale flow analysis.

2.2.5 Data Validation

Nogueira et al. (1997) proposed a validation algorithm that includes detection of false vectors, correction of these vectors and the calculation of derived flow magnitudes. The process starts by locating a zone where the vector field seems coherent by calculating how many vectors deviate from their neighbors. Then it proceeds scanning through the vector field, visually tracking the local gradient until a location is reached where the vectors clearly deviate from the previously scanned coherent ones. A coherence criterion is defined to decide whether a vector is coherent with its neighbors or not. The criterion is based on a series of comparisons between the candidate vector and predictions that are obtained from its neighbors. The permitted deviation between each prediction and the vector is limited by a user-given percentage of the average module of the vectors, which is involved in the calculations. The candidates that deviates less than a given amount with respect to the predictions are accepted as coherent vectors and incorporated into the current zone. As a post-processing step, this algorithm with a modification on the coherence criterion is applied to the velocity vectors obtained. The modified algorithm describes the coherence criterion as a parameter to define the maximum acceptable deviation of the candidate vector from the prediction. Instead of using a fixed value for controlling this parameter, an adaptive value is used. This value is derived from an estimation of the local gradient at each grid point. The local gradient estimation is made for each vector after it is incorporated into the current zone. This allows the algorithm to track the local gradient with the changes in the flow admitting larger deviations in the areas of the flow with stronger gradients. The instantaneous velocity field that has been shown in figure 2.8b is obtained without using this post-processing step. This velocity field with a small region of interest is shown in figure 2.9a. We see that there are some false or spurious vectors that can be identified from the vector map. They are different from the neighboring ones or outside the physically possible velocity range. Figure 2.9b

shows the result of applying the modified validation algorithm to the same instantaneous velocity vector map. It can be observed that false vectors are correctly validated.

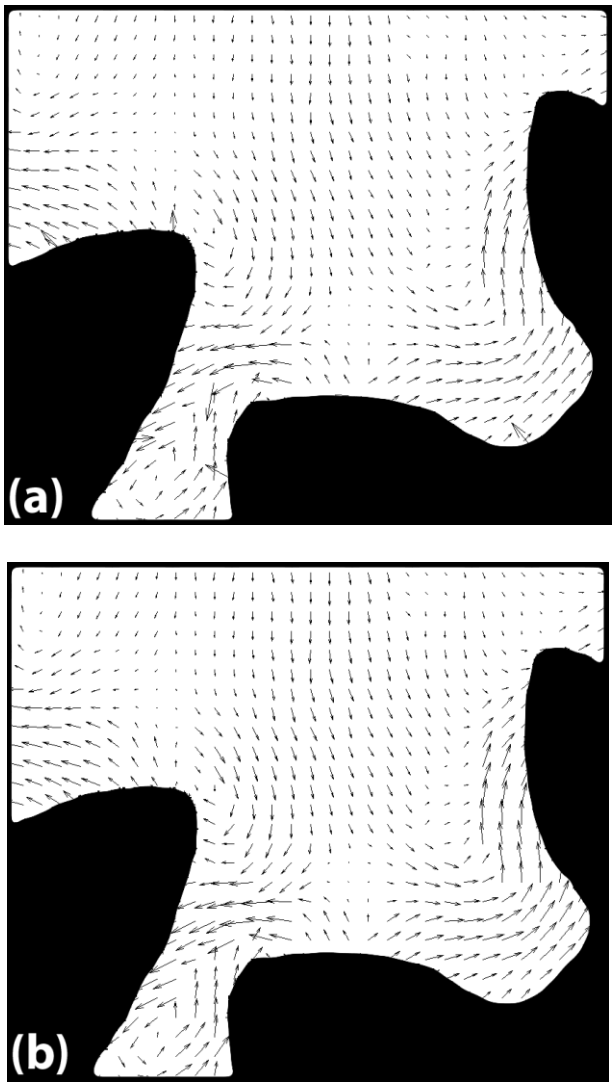

Figure 2.9. Instantaneous velocity fields: (a) with a region of interest to represent the detailed velocity vectors that are illustrated in Figure 2.8b and (b) the same region of interest after applying the modified validation algorithm.

2.3 Statistics of PIV images

2.3.1 Turbulent characteristics of the flow

This section clarifies some of the small-scale characteristics and turbulent structures in complex flow systems by performing two-dimensional field measurements using PIV. Besides, knowledge of viscous dissipation rate of turbulent kinetic energy, ε, may be required for the assessment of turbulence models employed in computational fluid dynamics (CFD) and turbulence models used to estimate the volumetric efficiency with effectiveness of different rotating part impeller profiles in the systems. Therefore, calculation of dissipation rate using experimental data is an open question.

PIV has been used to analyze the small-scale flow structures in system containing rotating parts. The flow in a Rushton turbine that consists of periodic rotating blade tips components in a cylindrical chamber has been investigated by Sharp and Adrian 2001. They obtained the instantaneous velocity flow fields with the information for RMS velocities and vorticity of the small-scales for different spatial resolutions. Several methods have been conducted in order to calculate the turbulent dissipation using PIV data. Moreover, the distribution of the turbulent dissipation across a stirred vessel in fully turbulent flow has been reported based on direct measurement of the instantaneous velocity gradients (Baldi et al. 1996). A wide amount of knowledge on the turbulent flow characteristics of stirred vessels that have rotating elements similarly to the external gear pump flow systems have been obtained through PIV technique in recent years (Sheng et al. 2000; Micheletti et al. 2004; Delafosse et al. 2011).

Besides, the PIV technique has been used in several studies in order to estimate the turbulent dissipation rate (Sharp and Adrian 2001; Sheng et al. 2000; Gabriele et al. 2009; Huchet et al. 2009). Despite all this work, the obtained results vary from one analysis to another due to the approximations made on the structure of the turbulence and limitations in terms of spatial and temporal resolutions. In order to obtain dissipation rate several relationships based on isotropy assumptions are proposed in the literature even though usually there is an insufficient number of measured velocity gradients. One of the

methods used implies considering the turbulence as non-homogenous, but statistically isotropic (Sharp et al. 1998; Ducci and Yianneskis 2005).

Although PIV technique offers various advantages, the ability to resolve all turbulent scales has not been established properly according to the spatial resolutions to estimate the dissipative ranges. Recently, there have been attempts to quantify the effect of the spatial resolution on the estimation of the turbulent scales using PIV (Saarenrinne and Piirto 2000; Scarano 2003; Poelma 2006). A comparison between measurements obtained from hot-wires anemometry (HWA) and PIV has been performed in order to study the effect of the finite spatial resolution of PIV on turbulent statistics (Lavoie et al. 2007). The advantages of PIV in the availability of simultaneous velocity measurements at numerous points in space have been significantly highlighted compare to HWA technique.

As stated before, to solve all turbulent scales of interest using PIV it is needed to select an image size large enough to capture the large scales and an interrogation area small enough to capture small scales. Additionally, to minimize the number of spurious vectors it is necessary to have an appropriate number of seeding particles in each interrogation area. To overcome this necessary spatial resolution issue, small solid particles (diameter sizes approximately 5-10 μm) have been used as flow seeding in this work. This particles leads to estimate turbulent scales effectively when compared with previous studies performed using air-micro bubbles as flow seeding (Ertürk et al. 2011). Moreover, the analysis of the spectrum and the time scale for the external gear pump flow with the use of air bubbles was done in the previous report (Castilla et al. 2008).

Some of the turbulent characteristics of the flow have been obtained using two point auto correlation functions. The autocorrelation function, $R_{ii}(r)$, of the velocity fluctuations, v', is defined as:

$$R_{ii}(x,r)=\frac{\langle v'_i(x)v'_i(x+r)\rangle}{\sqrt{\langle v'^2_i\rangle}} \tag{2.3}$$

where r refers to distance between two points in the flow and the symbol $\langle\ \rangle$ refers to the spatial average. The autocorrelation function is longitudinal if r is parallel to v_i, and crosswise if r is perpendicular to v_i, where v_i is the root-mean square velocity in the i-direction. The double-i subscript in R_{ii} indicates the autocorrelation function of a velocity component with itself. The calculations are done at an instant time t. For small values of the separation r, the autocorrelation coefficient is approximated by a parabolic function of r. Then, Taylor's length scale, λ_L, is estimated by:

$$\lambda_L^2 = \frac{r^2}{1 - R_{ii}(x, r)} \tag{2.4}$$

The integral length scale, I_L, of the velocity fluctuations is calculated by:

$$I_L = \int_0^\infty R_{ii}(x, r)dr \tag{2.5}$$

Length scale characteristics for different experimental cases are computed using the equations indicated above. The estimations can be done by using different number of instantaneous phase averages velocity vectors from the several image series of the PIV data. According to the energy-cascade model proposed by Kolmogorov (Hunt and Vassilicos 1991) energy is transported from the larger eddies to the smaller eddies and dissipated in the smallest scales. However, the existing rotating elements in the flow add energy at a scale that is in the middle of the energy spectrum. According to the Kolmogorov's hypothesis, the Kolmogorov length scale can be estimated by two parameters: dissipation rate (ε) and kinematic viscosity (ν). Several relationships based on isotropy assumptions are proposed in the literature in order to estimate the dissipation rate, but they calculation in any flow remains a challenge. Assuming homogeneous and fully isotropic turbulence, the dissipation rate can be estimated as follows:

$$\varepsilon = 15\nu\left\langle\left(\frac{\partial v'_i}{\partial x_i}\right)^2\right\rangle \tag{2.6}$$

However, when rotating elements exist in the flow such as in the external gear pump case, the flow is known to be highly anisotropic. It is considered that the turbulence as non-homogenous, but statistically isotropic (Sharp et al. 1998). External gear pump case is highly anisotropic but it is assumed as statically isotropic for the calculations of the PIV data. Then, dissipation rate can be estimated using the following relation (Delafosse et al. 2011):

$$\varepsilon = \nu\left\{2\left\langle\left(\frac{\partial u'}{\partial x}\right)^2\right\rangle + 2\left\langle\left(\frac{\partial v'}{\partial y}\right)^2\right\rangle + 3\left\langle\left(\frac{\partial u'}{\partial y}\right)^2\right\rangle + 3\left\langle\left(\frac{\partial v'}{\partial x}\right)^2\right\rangle + 2\left\langle\frac{\partial u'}{\partial y}\cdot\frac{\partial v'}{\partial x}\right\rangle\right\} \tag{2.7}$$

The important point here is that there are several factors in flows that have rotating parts such as anisotropy at large scales, inhomogeneity and periodicity due to the phases of rotating impeller parts. The assumptions used in estimating dissipation rate from the measurement techniques should be carefully assessed. In order to perform this calculation, assumption of local isotropy can be done, but in practice it is difficult to meet these conditions.

Moreover, integral length scale varies from region to region in complex flows. Eq. 2.7 is recommended for estimation of ε for lack of a more generally applicable alternative (Kresta and Wood 1993). Furthermore, this method that applies Eq. 2.7 has been used in several studies (Sharp and Adrian 2001; Sharp et al. 1998) and gives better estimation of the turbulent dissipation rate than Eq. 2.6.

It is assumed that the measurement techniques must be able to resolve velocities, smaller than the Kolmogorov length scale in order to fully resolve the velocity scales in turbulent flow. Kolmogorov length, η, and time, τ_η, scales can be estimated by:

$$\eta \approx \left(\frac{\nu^3}{\varepsilon}\right)^{1/4} \tag{2.8}$$

$$\tau_\eta \approx \left(\frac{\nu}{\varepsilon}\right)^{1/2} \tag{2.9}$$

Based upon the mean dissipation in the flow, the average Kolmogorov length scale along the defined place is estimated by using Eq. 2.6 and Eq. 2.8 and by using Eq. 2.7 and Eq. 2.8. In the calculations, smaller interrogation areas such as 32x32 pixels should be used in order to reach a high spatial resolution of particle images. The local dissipation is known to be considerably larger than the mean dissipation in the rotating parts area, so in order to be fully resolved, the spatial resolution should be smaller than average of Kolmogorov length scale. The spatial resolution of the present PIV experiments is found enough to estimate the dissipation rate for the turbulent analysis.

The turbulent time scale of the flow can be calculated in a selected spatial point in one phase rotation. Then, the average Kolmogorov time scale, τ_η, in the selected point can be calculated by using Eq. 2.6 and Eq. 2.9 and by using Eq. 2.7 and Eq. 2.9. The temporal resolution of the experimental images should be larger than the Kolmogorov time scale that is estimated using Eq. 2.7 and Eq. 2.9 in the selected point for a one phase rotation time.

Eddies and hence velocity fluctuations exist on various time and length scales. For eddies much smaller than the energy containing eddies (from the movement of the solid parts in the flow) and much larger than dissipative eddies (of the order of Kolmogorov scales), turbulence is controlled solely by the dissipation rate and the size of the eddy. In this sub-range, frequency spectrum of velocity fluctuations is calculated from Fourier transform and inverse transform:

$$F(v) = \int_{-\infty}^{\infty} v'(t) \cdot e^{-2\pi i v t} dt \tag{2.10}$$

$$v'(t) = \int_{-\infty}^{\infty} F(v) \cdot e^{-2\pi i v t} dv \tag{2.11}$$

The spectral energy density is then determined from the PIV measurements in the selected point for the experimental cases. The straight line with a slope of -5/3 corresponding to Kolmogorov's law fits the data well on a log-log plot (see example figure 2.10).

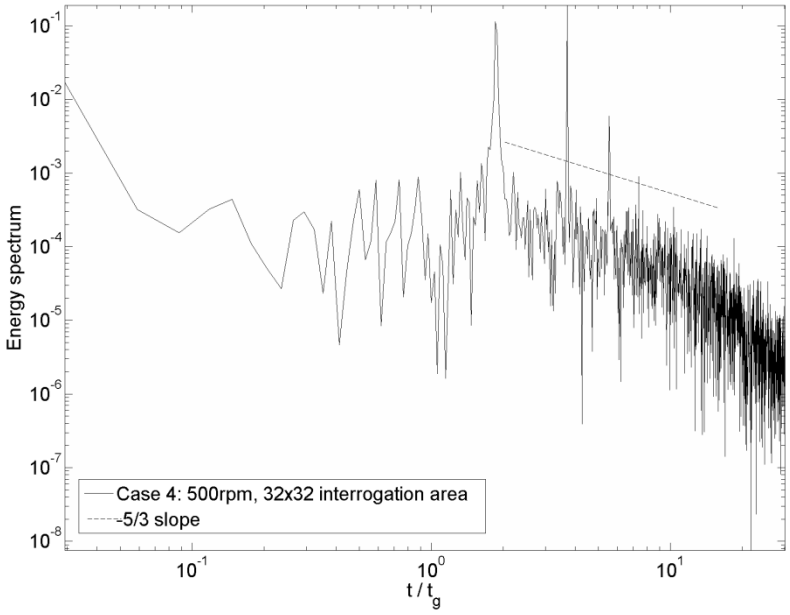

Figure 2.10. Energy spectrum versus frequency in the point P for a case study with 32x32 pixels interrogation area, frequency has been normalized by the frequency of one phase gear rotation.

2.3.2 Estimations of total measurement error

The error of the velocity vectors obtained from PIV can be estimated by studying mean-bias error and RMS error. In the case of the external gear pump, the velocity of the fluid close to one of the rotating impeller is expected to be same as the rotational velocity of the system. In order to calculate the total error of the measurements, 10 or more points can be defined around one impeller, or gear tooth, by considering that velocity of the flow in these points is the same as the rotational velocity of the system. Suppose that w_a

(a = 1, 2… N) is the actual particle velocity and w_i (i = 1, 2… N) is the N measured velocities. The mean velocity, w_m, is calculated as,

$$w_m = \frac{1}{N}\sum_{i=1}^{N} w_i \tag{2.12}$$

The difference between the actual particle velocity and the mean velocity gives the mean-bias error, e_b:

$$e_b = w_m - w_a \tag{2.13}$$

The RMS error, e_{RMS} is defined as;

$$e_{RMS} = \left(\frac{\sum_{i=1}^{N} (w_i - w_m)^2}{N} \right)^{1/2} \tag{2.14}$$

In the present study, the total error of the measurements, e_{TOT}, is defined as the sum of the mean-bias error and the RMS error.

$$e_{TOT} = e_b - e_{RMS} \tag{2.15}$$

The total error of the measurements is estimated for different experimental cases by using image series as instantaneous and various numbers of phase-averaged images. The error estimates are embedded with different numbers of phase-averaged images whose magnitude affects the results importantly. The measurement error tends to decrease if more image series are used in the phase-averaged (ensemble) averaging process.

2.3.3 Error estimation in measurement of dissipation rate

The error in the computed dissipation rate is evaluated from the measured velocity components and the values of their error. Two components of the error are evaluated, the truncation error, $\Re$, and the velocity measurement error, e (Saarenrinne and Piirto 2000). For a two dimensional region of flow field the in-plane velocity components u and v were measured. The measured velocity components are $u^*=u+e$ and $v^*=v+e$. The error in the calculation of the different terms of Eq. 2.7 can be evaluated using backward finite differences:

$$\left(\frac{\partial u}{\partial y}\frac{\partial v}{\partial x}\right)=\left(\frac{\Delta u^*}{\Delta y}+\Delta y\Re+\frac{e}{\Delta y}\right)\times\left(\frac{\Delta v^*}{\Delta x}+\Delta x\Re+\frac{e}{\Delta x}\right)$$
$$=\frac{\Delta u^*\Delta v^*}{2\Delta y\Delta x}+\frac{\Delta u^* e}{\Delta y\Delta x}+\frac{e^2}{\Delta x\Delta y}+\frac{\Delta v^* e}{\Delta y\Delta x} \qquad (2.16)$$

where $\Delta x = \Delta y$ and $\Re=\Delta x^2$. The accuracy of the estimated dissipation rate depends on the number of images used and the velocity measurement error is an important factor in the estimation of the dissipation rate.

2.4 Summary

The time-resolved PIV is a powerful technique to analyze the complex flow structures of the fluid flows as well those contain rotating elements inside the working fluid. The PIV data analysis techniques can be used to obtain detailed information of the instantaneous velocity fields, in systems with moving elements, which are not the part of the fluid flow.

The particle images are pre-processed using a clean-up mask to remove or to reduce undesired light reflections and to homogenize the median illumination. The ability to separate particles from the reflection and to clean/remove the spots allows improving the peak detection in the cross-correlation coefficient matrix, used for the particle displacement calculations.

The triple image correlation method with the implementation of LFC method is used to obtain the average displacement of the ensemble particles from the particle image series. The triple image correlation algorithm can improve the peak correlation in rather moving parts that appear in the image. The technique for boundary treatment is implemented with the use of the weighting function in order to achieve an appropriate resolution for the calculation of the velocity fields and to obtain the same level of accuracy available at inner locations of the flow system. In order to detect and remove spurious vectors, a validation algorithm is implemented for the post processing of the images.

The periodic behavior of the flow is determined by computing the autocorrelation of the velocities at selected points. This characteristic is used to obtain conditional (phase-locked) ensemble average velocity field of the flow since each phase of the impeller or gear tooth is associated with different flow structures in the flow system. Then phase-locked ensemble average is obtained for the fixed positions of the rotating elements that allow an average time evolution of the flow structures in the flow systems. This leads to obtain a better understanding of the dynamic behavior of the flow.

Turbulent structures and small-scale characteristics of the flow are determined by time-resolved PIV technique. Different spatial resolution levels of the interrogation areas can be studied in the dissipation rate estimations. Turbulent length and time scale characteristics are computed using autocorrelation function from the PIV data. Kolmogorov length scale is estimated with two different relationships based on isotropy assumptions for dissipation rate. The effect of the assumptions, turbulence as non-homogenous but statistically isotropic and turbulence as homogenous and fully isotropic, in the estimation of dissipation rate can be compared then.

The total error of the measurements can be estimated for different experimental cases by considering the effect of number of samples employed in the ensemble-averaging of the velocities. The measurement error decreases if more image series are used in the ensemble averaging process. The error in dissipation rate estimations is evaluated from the measured PIV data. It can be said that the accuracy of the estimated dissipation rate

significantly depends on the velocity measurement error and on the number of the used images.

FUNDAMENTALS OF PIV IMAGEDATA ANALYSIS

CHAPTER III
ALGINATE MICRO PARTICLES FOR FLOW SEEDING

As stated in the chapter before, PIV is a widely used technique. It needs the use of seeding particles in a fluid (liquid or gas) for directly measuring the displacement of those particles and thus assessing the velocity of the fluid. The selection of the particles is a critical point in all the process. They should be as small as possible in order to ensure good tracking of the fluid motion. Additionally, they may not be too small, since they will not scatter enough light. Particles that follow the flow accordingly and scatter enough light must be used in order to obtain accurate velocity field of the flow. Optimal tracers must have spherical shape for the tracing ability due to aero dynamical characteristics of particles and the continuous medium. To have good results when applying PIV it is also critical to have a uniform particle seeding with a homogenous diameter size. Concentration of the particles is also an important item, it is necessary to have about 15 particles per interrogation area to get high quality PIV images (Tropea et al. 2007). The particles should provide no agglomeration effect and mix well in the fluid flow. Furthermore, it is important to note that proper tracer particles must be non-toxic, non-corrosive, non-volatile, non-abrasive and chemically inert (Wang et al. 2007). Health considerations are important since the experimentalists may inhale the particles mostly in the open wind tunnel flow systems.

3.1 Commonly used tracer particles

The most commonly used seeding particles for PIV investigations in systems where the fluid of interest is liquid are polystyrene, aluminum oxide (Al_2O_3), titanium oxide (TiO_2), glass spheres as solid seeding, water and different oils as solid/liquid seeding and oxygen bubbles as gas seeding. The use of solid particles in wind tunnels has been described in a number of recent papers (Scarano and Oudheusden 2002; Hou et al. 2003). These authors report the use of polystyrene particles that have posed a minor fire hazard passing through the compressor of a closed-circuit supersonic wind tunnel by exceeding temperature 250^{o}C. A problem arises at this temperature since the polystyrene particles have a melting point of 250^{o}C causing agglomeration (Wernet et al. 1995). Moreover, traditional solid particles including polystyrene particles coat quickly the experimental model surfaces and windows that lead to disturb the optical accesses (Sabroske 1993; Liu and Sullivan 2004) and can corrode or damage the components of the tunnel or model (McNiel et al. 2007). The fluorescently labelled tracer particles are also commonly used in the PIV technique. They end with a better quality vector maps since they improve the signal to noise ratio of the raw images (Deschênes et al. 2010; Monji and Sato 2010; Lai and Menon 2004). However, the cost of the commercially available fluorescent particles is too high for large-scale experiments. The use of Rhodamine dye compounds based particles can be prohibiting in large-scale experiments due to their toxic property and high cost. However, the fluorescent particles show high efficiency and detectability at almost every flow conditions. Despite their promise, the use of fluorescent particles is largely limited to flow studies in small-scale laboratory experiments. Water and oils particles as flow seeding are incorporated with many smoke generators. The particles composed of glycol-water mixtures have been investigated for a closed-circuit transonic wind tunnel (Parobek et al. 1986). This practice resulted in an accumulation of an oily residue on the model, tunnel windows, and throughout the tunnel circuit.

3.2 The need of new particles

The particle image intensity obtained in a PIV experiment is directly proportional to the scattered light power. Therefore, it is more effective and economical to increase the image intensity by properly choosing the scattering particles than by increasing the power of the laser (Melling and Whitelaw 1973). The light scattered by small particles is a function of the ration of the refractive index of the particles to that of the surrounding medium, the particles' size, their shape and orientation. There is a tendency for the scattered light intensity to increase with increasing particle diameter. However, increasing the size of the particles will affect tracking of the fluid motion. Moreover, difficulties arise in providing high quality seeding in gas flows compared to applications in liquid flows. Therefore, it is clear that a compromise to use seeding particles has to be found for liquid and gaseous flows. The size specifications of the tracer particles with respect to their flow tracking capability for PIV have been described for several examples (Melling 1997; Hunter and Nichols 1985). Furthermore, it has reported a review of a wide variety of appropriately sized tracer materials used in the PIV experiments in liquids and gases.

Some microscopic particles containing imbedded fluorescent dyes to use in PIV applications are disclosed in a patent application (Katz 1992). These particles comprise an acrylic resin (Methacrylate) and have diameters between 10 and 30 microns. A special particle generation chamber is needed for generating these particles, and thus, their production is cumbersome. Furthermore, these particles may not be suitable for particular applications, such as systems that contain contacting metal parts, as they would damage the system due to interaction of the rigid particles into metal-metal contact. This problem can be solved using the alginate particles developed during this PhD research. A particular procedure is proposed for measuring the velocity of a fluid by seeding it with particles and detecting the scattered light at two different times wherein the seeding particles are alginate particles. These spherical particles offer the advantage of not being toxic and their production process is more easy and economic. Additionally, characterization of these particles is mostly appropriate in order to fulfill the needs of seeding particles in PIV technique. The particles ensure good tracking of the fluid motion

in the liquid and gas flow measurements. When fluid of interest is liquid there is not too much difference in density between the fluid and the particles since their porous structures absorb the analyzing fluid. The diameter size of the particles is increased when they are in the analyzing fluid with the porous property of the particles. Moreover, the particles can be obtained as small as possible while increasing its scattering behavior by attaching fluorescent dye molecules into the alginate micro particles. They have preferably a diameter between 0.2 and 30 microns and are optionally embedded with fluorescent dyes such as fluorescein. The use of alginate particles containing fluorescent dye is to enhance their contrast with any fluid for applications where a green laser is used for illuminating the particles and producing the scattered light. Furthermore, the fluorescent dye provides temperature sensitivity by absorbing the blue laser light.

On the other side, the softness of the alginate particles can be controlled by changing the parameters in the production process. The PIV technique takes advantage of the properties these particles and uses them efficiently in the flow systems to obtain accurate digital images.

3.3 Production method of alginate micro particles

Alginate is the most popular material that is used for preparation of gel beads among the wide range materials (Veliky and Mclean 1994; Mattiason 1983). Alginate is a natural, non-toxic polysaccharide found in all species of brown algae (Aslani and Kennedy 1996). Chemically alginate is a linear 1, 4 linked copolymer of β-D-mannuronic acid (M) and α-L-guluronic acid (G). Alginates are widely used in the food and pharmaceutical industries and have been employed as a matrix for the entrapment of drugs (Tomida et al. 1993), macromolecules (Kim and Lee 1992; Mumper et al. 1994) and biological cells (Lim and Sun 1980; Lee and Palsson 1993)

.

Alginate microspheres are generally prepared by two alternative methods; (i) by droping aqueous alginate into a solution of calcium salt (Salib et al. 1978; Matsumoto et al. 1986; Kazushi et al. 1995) or (ii) by emulsification method under gentle stirring (Wan et al.

1990; Poncelet et al. 1995).The particles that are produced by (i) are generally larger (more than 1 mm in diameter) and the attempts to obtain smaller particles requires special device that can have the disadvantage of the high cost and possible clogging (Skjâk-Braek and Martinsen 1991). The (ii) method has recently been extended to the field of nanotechnology. Experimental evidence shows that alginate nanoparticles have been successfully prepared using this method by creating the ideal conditions for the formulation (Reis et al. 2004). Some formulation and process parameters have been adjusted to produce smaller particles. In this present study, alginate microspheres are used as tracer particles in PIV and these particles should be small enough. The emulsification/internal gelation procedure provides appropriate way to produce the alginate microspheres with a preferable diameter sizes.

Entrapment within alginate spheres is considered as safe and simple system with good mechanical stability (Esquisabel et al. 2000). By controlling the production conditions, size can be easily controlled from a few nanometers to millimeters in diameter (Poncelet 2001). In internal gelation, calcium ions are homogeneously distributed in the alginate solution, thus diffusion of protons into the pre-gel droplets will induce gelation starting at the surface, giving rise to homogenous droplets (Quong et al. 1998). Also, the low shear involved in internal gelation protects fragile encapsulants (Poncelet et al. 1992). In addition, since toxic reagents and solvents are not used, biological and food applications may be considered. This method permits the efficient production of large quantities of small and controlled diameter alginate micro- and nanospheres. The alginate particles that are produced by this method have some disadvantages depending on their application process. Internally gelled particles are more porous than externally gelled particles. This disadvantage can be reversed to an advantage with an application of these particles to PIV system.

In the present study, the alginate gel microspheres are prepared by the emulsification/internal gelation method adapted from previous reports (Wan et al. 1992, 1993, 1994 and 2003) for encapsulation of macromolecules. This is possible due to the formation of a water-in-oil type emulsion, whose droplets are stabilized by the use of surfactants. Experimental evidence shows that alginate nanoparticles have been

successfully prepared using this method by creating the ideal conditions for the formulation. In order to obtain smaller particles, typically with a diameter of less than 10 μm, an ultrasonic probe is used to agitate and crumble the particles. The process to produce de alginate particles embedded with fluorescein and they use in PIV applications has been accurately developed during this PhD research and has ended with a patent application.

3.4 Characterization of alginate micro particles

Transmission Electron Microscopy (TEM), Environmental Scanning Electron Microscopy (ESEM) and Confocal laser electron microscopy have been used to characterize the alginate particles and the fluorescently labelled alginate particles. Figure 3.1 shows pictures of the alginate particles that were taken with TEM. The particles are obtained in black and white since the dense alginate particles do not allow the transmission of the electrons. It has been calibrated and the diameter size of the particles is obtained around 85nm on average.

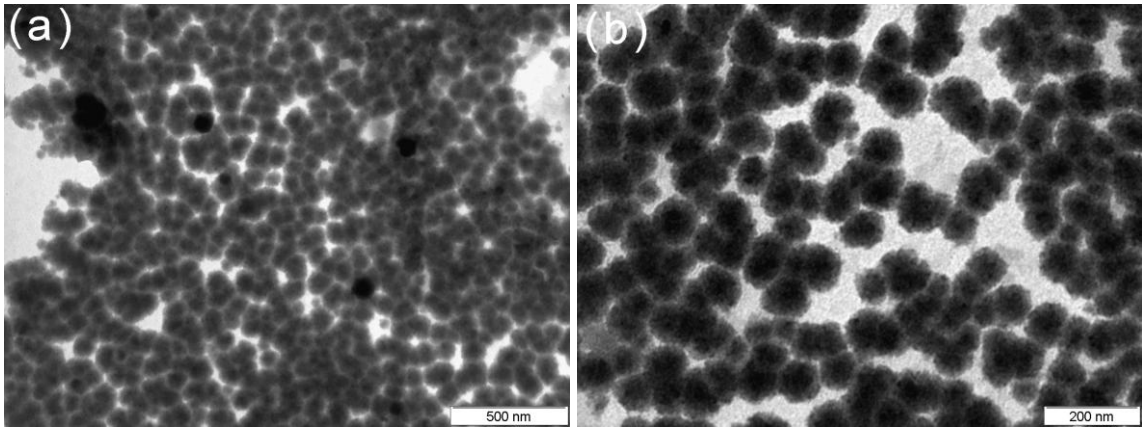

Figure 3.1. Visualization of the alginate particles at a scale of: (a) 1000nm; (b) 200nm.

Figure 3.2 shows a picture of the alginate particle that was taken with TEM. It can be observed that alginate particle consists of porous structure. This leads to have the particles jelly and soft structure. The porous structure leads particles to have the density of the particles as the same as density of liquid by absorbing the analyzing liquid. This property is significantly important in PIV technique. The desired seeding particles for PIV should have almost the same density or very similar density with the analyzing liquid. In this point of view, alginate particles are the adequate tracer particles for PIV.

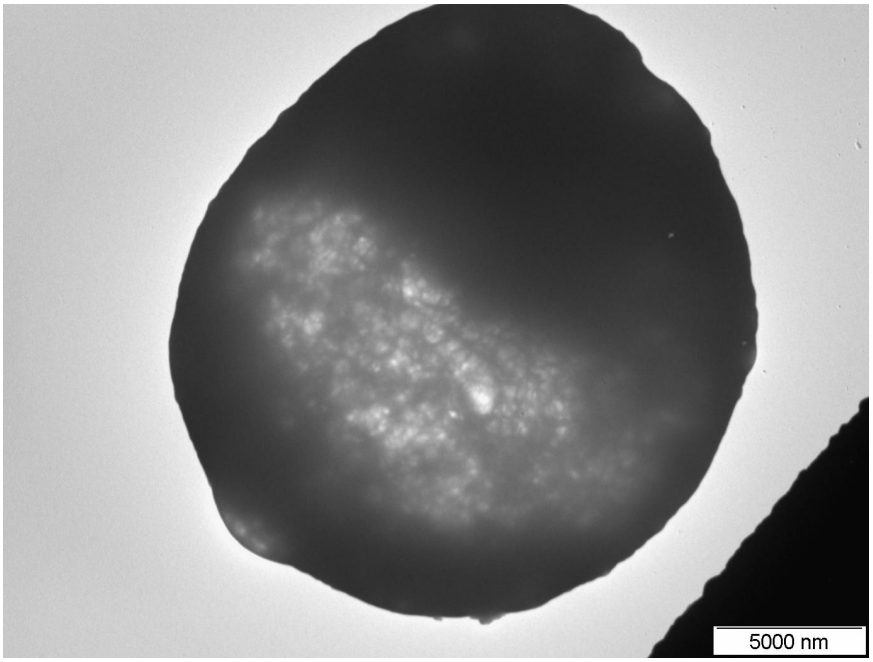

Figure 3.2. Visualization of the alginate particle at 5000nm scale.

In figure 3.3, a bunch of larger alginate particles have been imaged using ESEM. The particles have three dimensional spherical shapes with different size distribution varying 0.2 to 30 micrometer. In this case, the filtration process has not been yet applied to segregate the particles by size. So, with an appropriate filtration procedure we can easily generate similar sized particles. PIV technique also takes the advantage of the spherical shape of the alginate particles with similar diameter size.

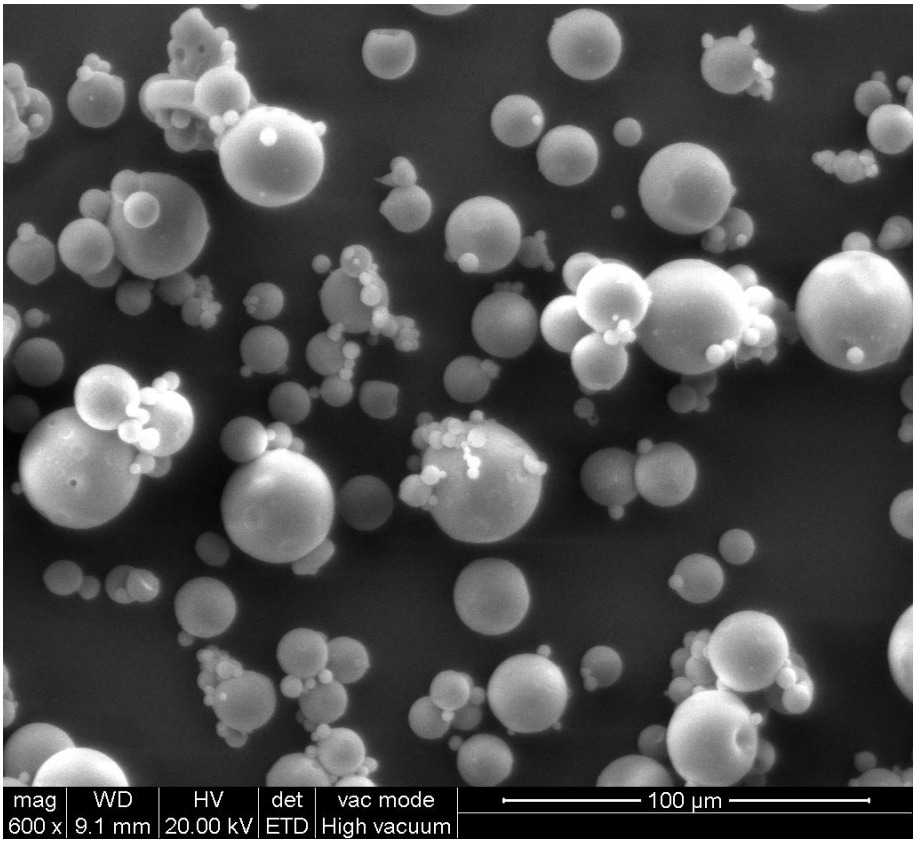

Figure 3.3. Visualization of the alginate particle at 100µm scale.

Confocal laser electron microscopy has been also used to characterize fluorescein containing alginate particles. Figure 3.4 illustrates confocal picture by using a blue laser emission at 488nm wavelength that is excited in green. The figure illustrates a scale bar of 30µm that means the particles diameter much lesser than 30 µm. Fluorescein that is appended to the alginate particles leads to the PIV system's tracer particles a highly scatter light property. It can be seen that a high amount of fluorescein is gathered and attached to the particles and particle shape is rounded. Three-dimensional confocal pictures at 488nm wavelength using different filters to excite the particles in green, red and blue lights has been illustrated in figure 3.5. The maximum absorption of fluorescein occurs at 496 nm, which is closest to the emission wavelength of the blue light-emitting diode (LED) of 470 nm. The process of shining different colored LEDs through the

fluorescein, red, 630 nm: orange, 605 nm; yellow, 592 nm; green, 525 nm; blue, 470 nm; and violet, 405 nm, is reminiscent of scanning spectroscopy. The observed fluorescence emission is greatest at the wavelength of maximum absorption. It is just by coincidence that the wavelength of the emitted light for fluorescence of fluorescein is also 520 nm. However, in PIV experiments, blue and green light can be used as light source in order to illuminate the alginate microparticles as flow seeding. Furthermore, due to the blue light emission property of the fluorescein, the particles could be used for the temperature analyses of the fluids.

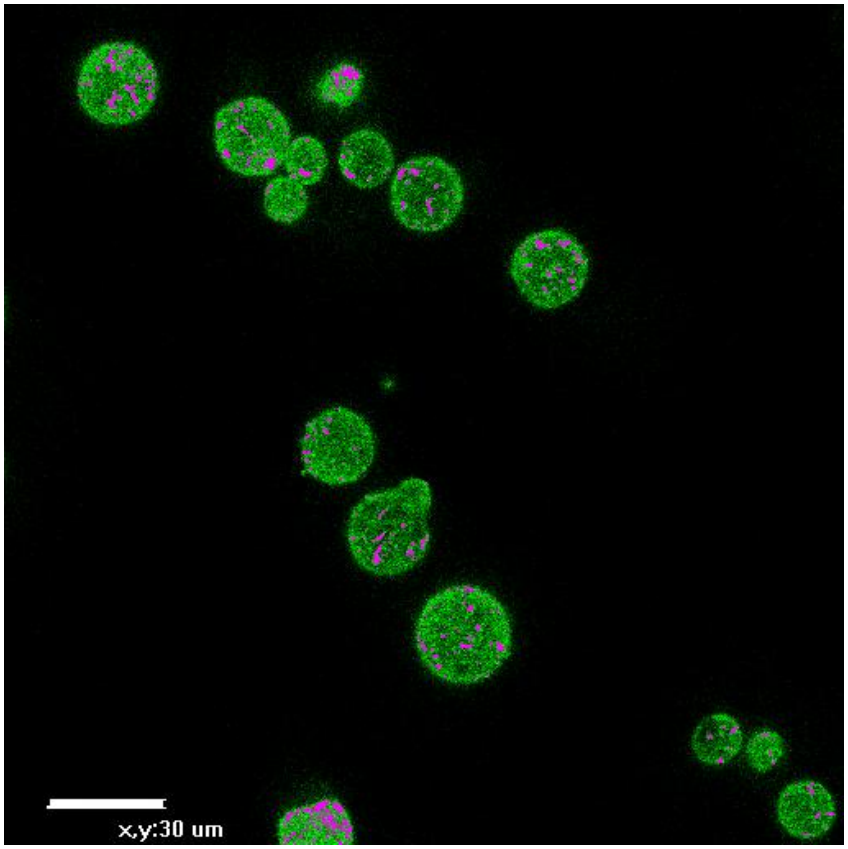

Figure 3.4. Visualization of the alginate particles that contain fluorescein by Confocal laser electron microscopy at 488nm wavelength with a scale bar 30 μm.

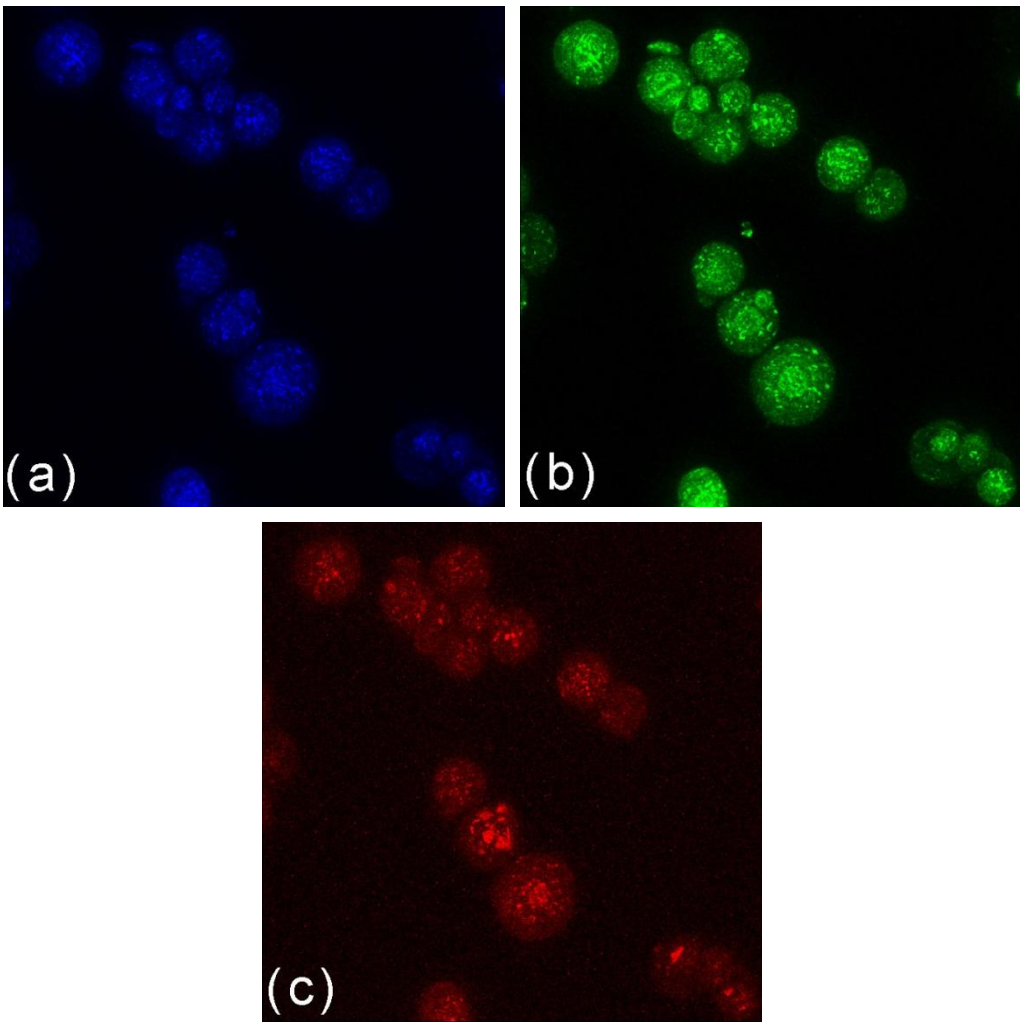

Figure 3.5. Visualization of the alginate particles that contain fluorescein by Confocal laser electron microscopy under (a) blue, (b) green and (c) red light at 488nm wavelength.

3.5 Application of the alginate particles in the PIV technique

The new alginate particles have been tested in several case studies. In this section, some of these cases are described. The first one corresponds to the analysis of the behavior of

the particles used with different working fluids and lasers. The second case study is the preliminary revision of the flow in an external gear pump.

3.5.1 Case study I

The first test case deals with the behavior of the particles in different fluids. Small-scale experiments have been made in order to identify if they scatter enough light by different lasers, infrared and green lasers. Figure 3.6 has been illustrated to show that the particles have enough light to scatter when a pulsed infrared diode laser with a wavelength of 800 nm has been used as illumination. The alginate particles not containing fluorescein are very sensitive to the infrared laser. For this type of particles (without fluorescein) it was not possible to obtain a proper image by using a green laser.

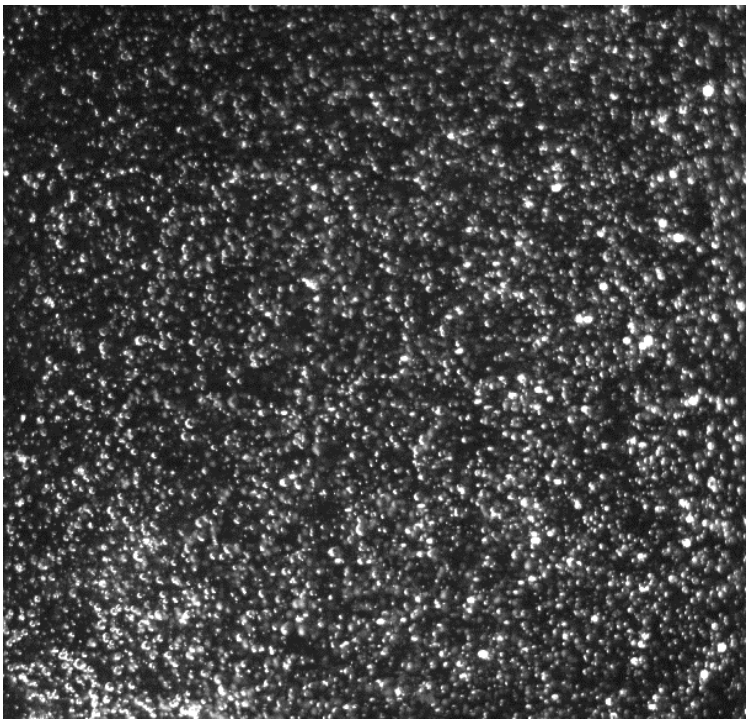

Figure 3.6. PIV image of the alginate microparticles, engine oil with density of 885kg/m^3 and viscosity of 0.028 Pa.s has been used as liquid and pulsed infrared diode laser with a wavelength of 800 nm has been used as illumination.

In order to increase light scatter quality of the particles by using green laser, very small amount of fluorescein has been added in the production process of the alginate particles. Fluorescein absorbs blue light with peak excitation occurring at wavelengths between 465-490nm. The resulting fluorescein occurs at the green wavelengths of 520-530nm (Bennett 2011). This wavelength range can be given by a green Nd-Yag laser. This means that the alginate particles that contain fluorescein can be used as tracer particles for green lasers. Figure 3.7 shows an example of PIV images where the alginate particles containing fluorescein have been illuminated by a green laser. 600ml of distilled water as analyzing fluid has been used and 0.06g of the alginate particles contain fluorescein. The image in figure 3.7a has been recorded when the rotational speed of the stirrer was at 200rpm, the laser current was set to 30mA, the frequency rate at 1130Hz and the exposure time was 881µs. To obtain the figure 3.7b, the magnetic stirrer has been stopped and after 30 minutes the image has been recorded using the same laser current. This second image demonstrates that the particles are suspended in water for a long time.

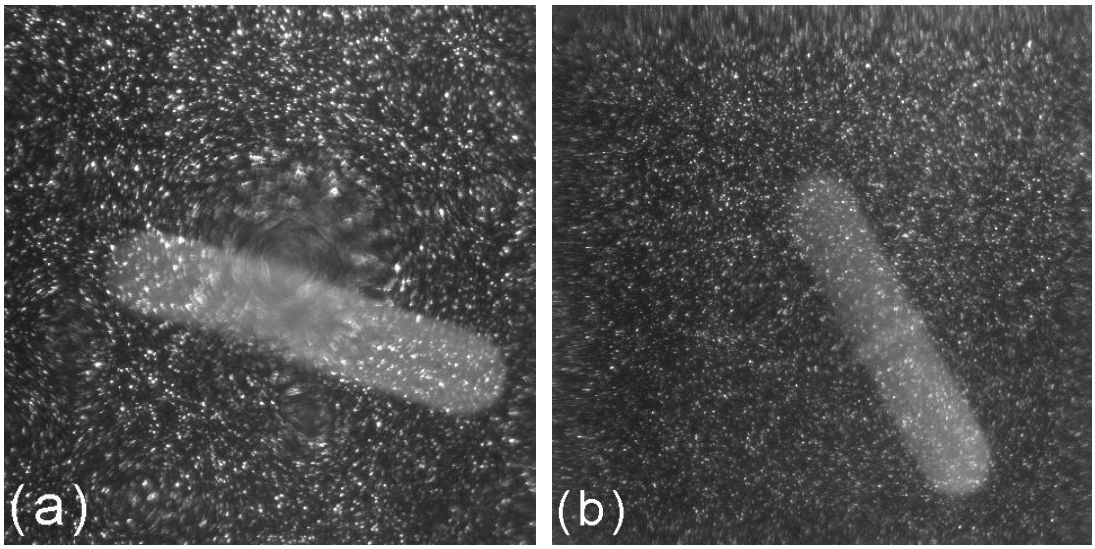

Figure 3.7. Illumination of alginate microparticles containing fluorescein in distilled water by using NdYAG green laser with a wavelength of 532 nm (a) Rotational speed of the stirrer is at 200rpm, laser current about 30mA, frequency rate 1130Hz, exposure time 881µs; (b) the stirrer is stopped and recorded 30min later.

The same alginate particles containing fluorescein have been tested as well in oil as working fluid using green laser. It has been used 95 ml of sunflower oil as analyzing fluid and 0.04g of the alginate particles contain fluorescein. Figure 3.8 has been recorded when the rotational speed of the stirrer was at 200rpm, setting the laser current about 30mA, the frequency rate to 1130Hz and the exposure time to 881μs.

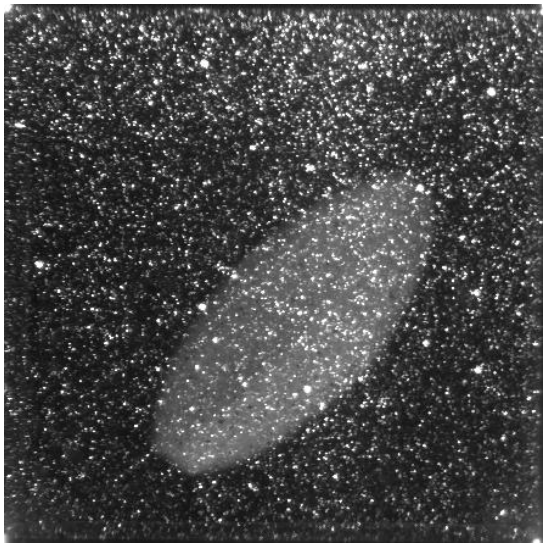

Figure 3.8. PIV image of the alginate particles containing fluorescein, sunflower oil has been used as liquid and green Nd-YAG laser with a wavelength of 532 nm as illumination.

The figures 3.6, 3.7 and 3.8 above show a homogenous distribution of the particles in the flow area. It can be stated that the alginate microparticles contains fluorescein can be used with green lasers and alginate microparticles can be used with infrared diode lasers. It should be noted that very few amount of particles have been used to obtain the images. The alginate particles containing fluorescein have also been tested also in air flow systems using a green laser as light source (figure 3.9). Figure 3.9a illustrates the engine bypass flow seeded with glass particles (diameter size approximately 30-35 μm) and figure 3.9b the same flow seed with the alginate particles with fluorescein (diameter size approximately 1 μm). The fluorescein particles have shown high reflectivity to the green laser light even though the size of the particles is small. Furthermore, it can be clearly

observed that the alginate particles display more homogenous distribution than the glass particles in the flow area. The details of the engine bypass flow analysis can be found in Chapter 5.

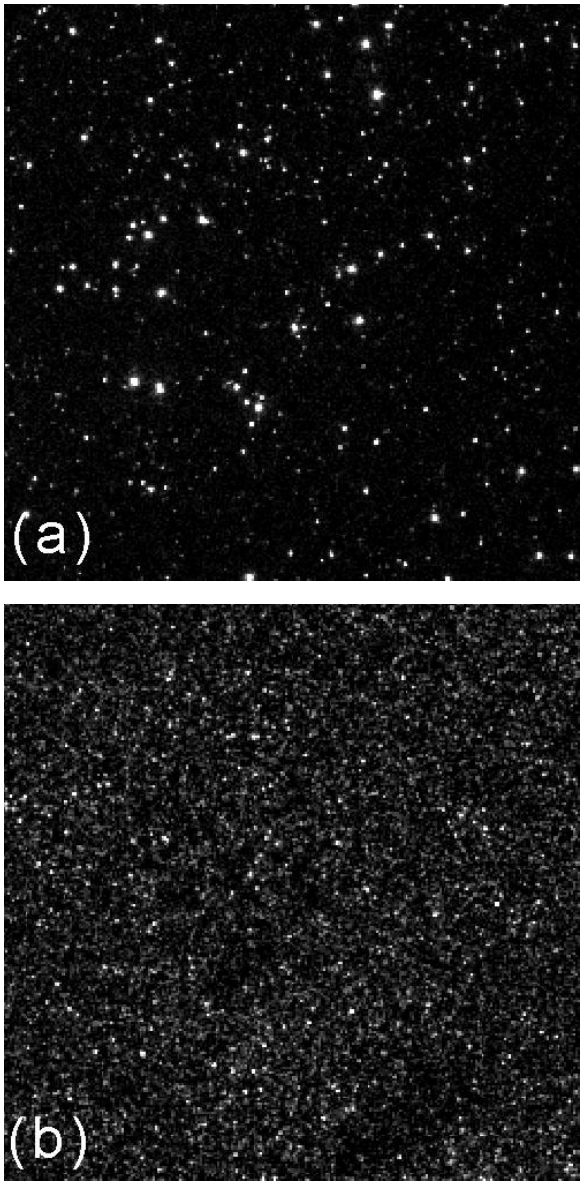

Figure 3.9. Illuminations of particles in the engine bypass flow analysis (a) glass particles (b) alginate particles containing fluorescein.

3.5.2 Case study II

The second test case analyzes the use of the alginate particles in the study of the flow in an external gear pump. Air bubbles have been used before as flow seeding in this analysis to minimize to possible damages to the gear (Castilla et al. 2008; Ertürk et al. 2010). However controlling the diameter size of the air bubbles was quite difficult. Alginate micro particles as flow seeding fulfill the demand of PIV requirements for this specific gear pump system, as they swell the analyzing liquid and do not give damage the gear.

One PIV image with air bubbles as flow seeding and one with alginate particles have been recorded using the same experimental conditions in an external gear pump system (figure 3.10a and 3.10b, respectively). The mean size of the alginate particles used was 10 μm while it was not possible to generate air bubbles smaller than 100 μm. The recorded PIV images shown here have the same size area of 290x280 pixels. It can be observed that the spatial distribution of the alginate particles is significantly different from the distribution of the air bubbles. More homogenous distribution is for the alginate particles used with industrial oil (density of 885kg/m^3 and viscosity of 0.028 Pa·s) as fluid system.

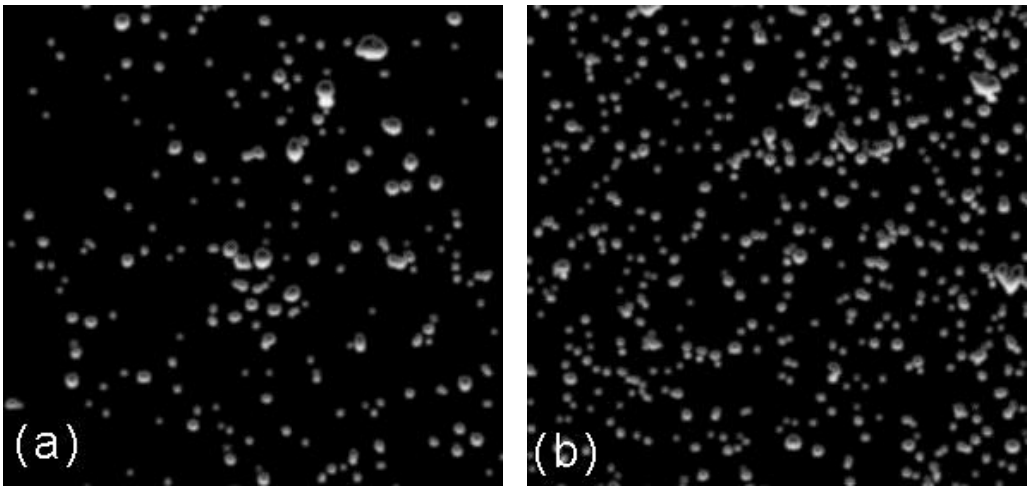

Figure 3.10. Recorded PIV images in the same area and the same image size of the flow field in an external gear pump: (a) air bubbles as flow seeding; (b) alginate particles as flow seeding.

Both PIV images were analyzed to measure the particle size distribution (PSD) (Figure 3.11). In agreement with the initial estimated size of the particles it has been found that the theoretical optimum particle size for alginate is approximately 10 µm while the size for the air bubbles is 100 μm. A small percentage of alginate particles larger than 10 μm were also detected in the analysis. In the case of air bubbles, 32% of them were 100 μm. Thus, under the same conditions, it is found that the alginate particles size distribution is narrower and better suited for PIV analysis. The production process and filtering could be optimized to increase the percentage of the 10 µm alginate particles.

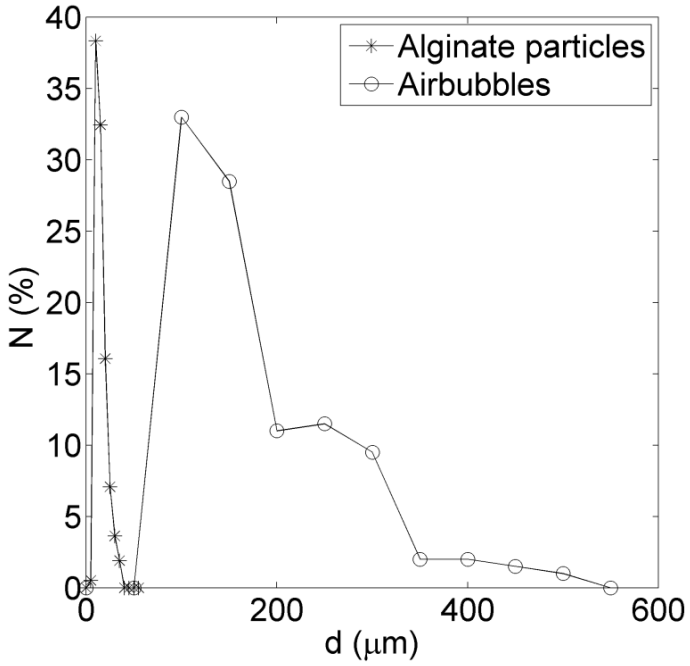

Figure 3.11. Particle size distribution of the alginate and air bubble particles from the recorded PIV images that have the same area and the same image size of the flow field in an external gear pump.

Another aspect to consider is the influence of the gravitational forces where the densities of the working fluid and the tracer particles do not match. Even though it can be neglected in many practical situations, the particle's behavior under acceleration can be derived from Stoke's drag law as shown in Eq. 3.1 (Raffel et al. 2007).

$$U_p(t) = U\left[1 - e^{-\frac{t}{\tau_s}}\right] \tag{3.1}$$

U_p is the velocity of the particle, U is the fluid velocity and τ_s is the relaxation time given by:

$$\tau_s = d_p^2 \frac{\rho_p}{18\mu} \tag{3.2}$$

where d_p is the diameter of the particle and μ is the dynamic viscosity of the fluid. The relaxation time, τ_s, is an indicator of the ability of a particle of certain size and density to respond to fluid acceleration. Step response of a particle measures conveniently the tendency of a particle to attain velocity equilibrium with the fluid. In figure 3.12, the result of the time response of different particles with a constant diameter size of 5 μm is shown for a strong acceleration in a water flow. Even that the difference is not too large, the alginate particles are the fastest among the three particle types at a given time. Therefore, it seems that the alginate particles have the highest cooperation with the fluid motion in the regarding fluid.

The images shown in figure 3.13 are part of two experimental series, one using air bubbles and another using the alginate particles. Both series have been used to analyze the flow in an external gear pump in order to compare the performance of both seeding material. They have been recorded at the same conditions of the flow using the same PIV devices (infrared laser and a CCD camera). In the case of the air bubbles some big particles can be observed in the flow (figure 3.13a). Those big particles cause distortion of the images that significantly prevent to obtain precise information of the PIV data. The alginate particles are homogenously distributed in all the region of the interest (figure 3.13b).

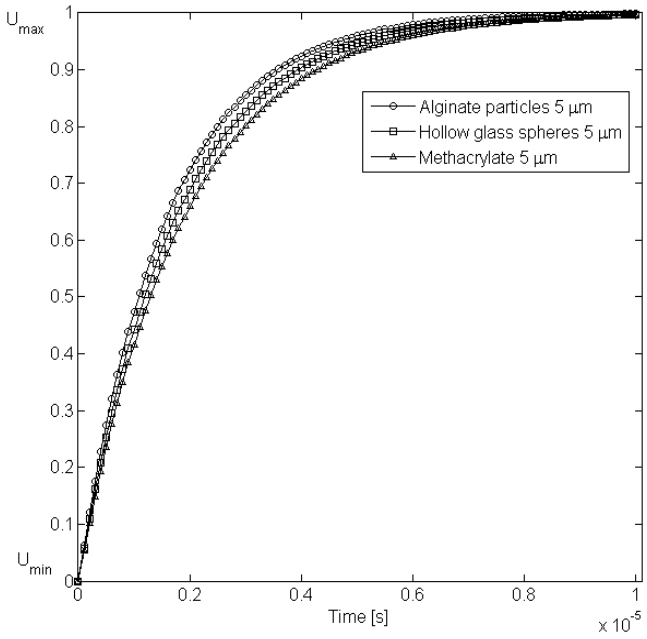

Figure 3.12. Time responses of different particles with a constant diameter size of 5 μm for a strong acceleration in a water flow.

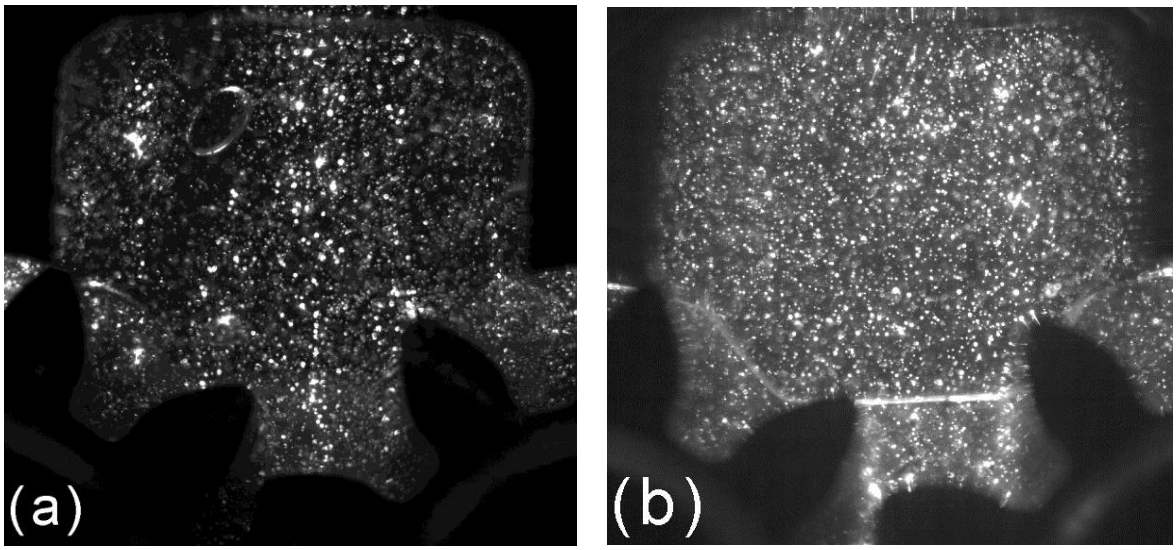

Figure 3.13. The recorded PIV images at the same conditions of the external gear pump flow of: (a) air bubbles and (b) alginate particles.

A comparison of the total error (sum of the mean-bias and the RMS errors) between alginate and air bubbles particles is shown in figure 3.14. The errors are displacement errors that can be observed in the PIV data analysis of the gear pump model. The PIV data analysis is done via cross-correlation method in 32x32 pixel interrogation areas of the images. To be able to analyse the flow in detail, we went down up to 32x32 pixel interrogation area due to the fact that it is the most appropriate size for small-scale turbulent flow analysis. The displacement error is shown by comparing various numbers of phase-averaged images to the displacement error by pixels. It can be observed that the error found when the alginate particles are used is one order of magnitude smaller than in the case where the air bubbles are used. Thus, it seems that there are more accurate displacement measurements when alginate particles are used. One of the reasons for this improvement in the measurements is that the alginate particles have smaller diameter hence the number of the particles in the same image area is bigger.

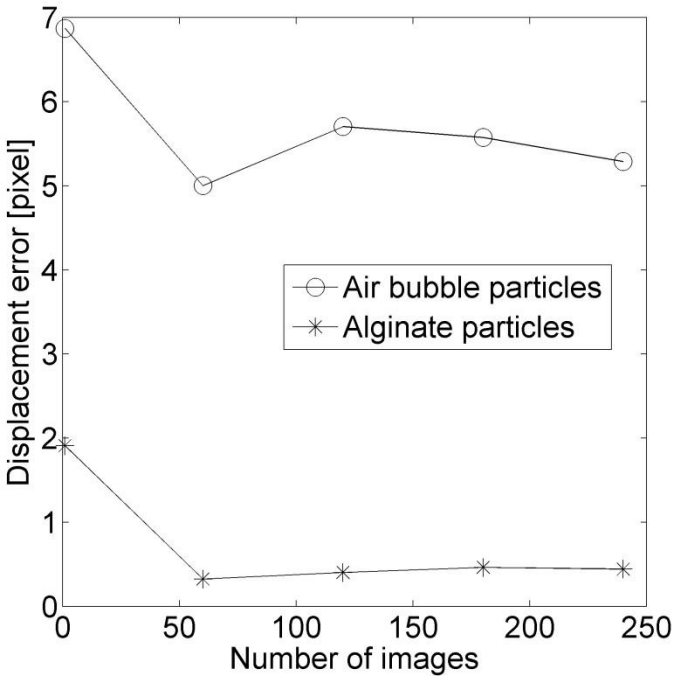

Figure 3.14. Comparison of the total error (sum of the mean-bias and the RMS errors) between alginate and air bubbles particles.

3.6 Summary

In this chapter there is a description of the particles used in PIV and the need of a new kind of particles is discussed. Production and the characteristics of the alginate seeding particles are presented.

In some biological and food application areas, the porous structure of the alginate microspheres produced by the emulsification method is regarded as a disadvantage. In the case of PIV applications this disadvantage is considered an advantage. For PIV experiments, the porous structure leads to obtain a density which is almost the same as the density of the analyzing fluid.
Addition of fluorescein has been into the alginate particles has been also analyzed. This compound enhances the light scattering property of the particles when using green laser as light source. Furthermore, alginate particles with fluorescein can be used as flow seeding in PIV technique for liquid and gas flows analysis.

Alginate particles have soft, jelly like structure. Thus they do not cause any damage to the inner contact surface of the machines. So that the particles are very appropriate for industrial machinery applications in PIV. The particles are spherical and furthermore non-toxic and environmentally friendly.

CHAPTER IV
FLOW IN AN EXTERNAL GEAR PUMP

4.1 Introduction

There are a great number of industrial machineries that contain rotating elements interacting with fluid flow. Most of this machinery is responsible for the fluid movement. This is the case of a large number of pump types. Knowledge of the interactions between the mechanical elements and the fluid flow can provide improvements in the pump design. A variety of measurement techniques have been applied to several industrial machines in the struggle for accurate quantitative flow descriptions (Ivantysyn and Ivantysynova 2001). This chapter is focused on the analysis of fluid flow through an external gear pump (Figure 4.1). These pumps are the most common hydraulic pumping devices for industrial machineries usually used for transferring and metering high viscosity fluids and power transfer typically at high pressure rates. They are also favourably used as lubrication pumps and oil pumps to provide circulation of the internal lubricants in the car and the aircraft engines. An external gear pump is a positive displacement pump that has two cogwheels rotating against each other. It transfers the fluid from a suction chamber to an impulse chamber increasing the fluid pressure as well. The fluid in the suction chamber is trapped between the teeth of the gears and the body of the pump. As the gears rotate, the fluid is transported to the impulse chamber under pressure. The external gear pumps are commonly preferred on the industrial scale for metering polymers, mixing and blending the chemicals due to their high capacity to work with precise viscous fluids. Although they have excellent performance features that make

them to be preferably used in the industry, the generation of significant vibration can occur due to flow rate fluctuation during the delivery process of the fluid. In order to detect where the fluctuations may occur in the flow for a specific external gear pump model, experimental analysis is needed to identify the highly turbulent characteristics of the flow field. This analysis is significantly important due to the optimization of the fluid transportation process, reducing the vibration excitation and continuous concern in the design of the pump.

The flow rate depends on the rotational velocity of the gears. Recently there is a trend to increase the pump performance by reducing its size and increasing the pressure as well as the rotational velocity (Dearn 2001; Wood 2006). Thus, the pumps are designed to be smaller and provide more power to the fluid. The current designs of the suction and impulse chambers involve a decrease of the volumetric efficiency of the pump when rotational velocity increases (Roquet 1998; Castilla et al. 2005). This means that the real flow rate could substantially decrease due to backflow through the gaps between the gear and the compensating plates or the pump body. Consequently, it is necessary to increase the knowledge of the flow characteristics on the suction and impulse chambers to improve their design. Furthermore, gear pumps can produce high frequency pressure pulsations, increasing the fluctuations of the delivered flow, which tends to damage pressure gauges. To reduce the fluctuations, geometric design of the gear tooth profile and the body of the pump are needed to be improved. As the gear tooth profiles are mainly comprised of complicated curves, significant parameters have to be determined in their design. Houzeaux and Codina (2007) developed a numerical strategy for the simulation of rotary positive displacement pumps that can help in the understanding of the flow phenomena occurring in the suction and impulse chambers. In another study, the flow characteristics of external spur-gear pumps have been investigated using the flow rate formula derived in closed form (Huang and Lian 2009). The control volume method has been applied to estimate the flow ripples of the gear pump with different numbers of driving and driven gears (Manring and Kasaragadda 2003). Iyoi and Ishimura (1983) have shown that it is not possible to get external gear pumps with no delivery fluctuation but it can be minimized. The efficiency of the pump is directly related with the

relationship between the moving parts and clearance factors. Moreover, the results that are obtained by these numerical studies need experimental validation.

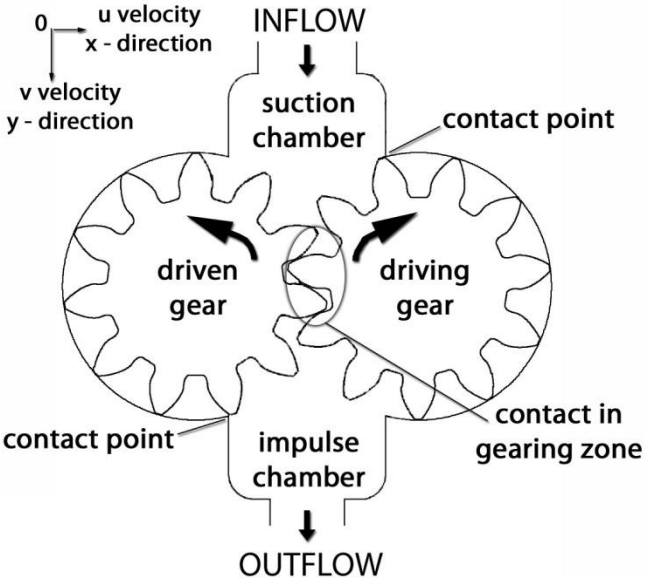

Figure 4.1. Schematic view of an external gear pump.

Additionally, the rotation of the gears produces the positive displacement that the carried fluid cannot return to the inlet due to the meshed portion of the gears between the gear teeth. The gear teeth of the pump should run in close fitting tolerances to ensure the sufficient fluid pressure and to prevent the fluid from the leaking back to the inlet. The controlling the tip leakage flow rate in the external gear pump is essential for the efficient fuel metering. An analytical prediction technique has been proposed to control the tip leakage flow rate at the different inlet/outlet pressure differences (Wahab 2009). The results of this proposed method have been found favourably with the experimental results.

Many aero-engines use external gear pumps in the high pressure part of the fuel system. The performance criterion for the high-pressure positive displacement stage of the external gear pump is to be capable of delivering the volumetric flow rate required by the engine operating conditions. The overall volumetric performance of the pump is depending on the input speed and the pressure rise operating range. The operating

characteristic of this pump is critical with respect to the performance. The design of the external gear pumps have been considered in various studies to obtain the effective and the optimal model of the gear pump by meshing pressure measurement and flow visualization methods (Eaton et al. 2006; Wang et al. 2011).

Even that several studies have been done about the external gear pumps it is difficult to obtain analytically the instantaneous flow areas and volumes accurately due to its complex geometry profiles of the gear teeth and wear plates. The use of lumped parametric models has been proposed and validated experimentally to predict the transient flow and pressure. Particularly they have been applied in the meshing area and to study the entire gear pump using the generalized control volumes method for the fluid dynamics and pump performance (Edge et al. 2001; Borghi et al. 2005; Borghi et al. 2006; Falfari and Pelloni 2007; Wang et al. 2011; Casoli et al. 2008). The dynamic model of the gears has been applied to the analysis of the trapped-oil stiffness by using an iterative operation based on Runge-Kutta method (Yulong et al. 2011). The experimental measurements of the clearances between the end-faces of the gears and the bushes have been obtained in the high pressure gear pumps (Koc et al. 1997). The design of the gears and wear plates have also been investigated experimentally for the performance and the volumetric efficiency of the gear pumps (Koc and Hooke 1997; Nagamura et al. 2004; Borghi et al. 2008).

PIV is a developing technique that is capable of investigating dynamics and statistics of complex turbulent flow structures with the improvement of digital cameras and lasers. Internal flow in systems which consists of the rotating passages is exceedingly complex, involving rotation and turbulence effects. Various measurement techniques have provided the fundamental knowledge of the flow phenomena occurring in rotating machines (Wernet 2000; Pedersen et al. 2003; Day and McDaniel 2005). However, the quest that maintains high efficiencies and performances at a broader range of operating conditions raises the need for a more detailed knowledge of the local and instantaneous features of the rotating passages flow (Wulff 2006). The high image acquisition rate is necessary to capture the evolution of the flow in systems with considerable velocity changes that are encountered in pumps with large rotational velocities. The flow characteristics of the

suction chamber of the external gear pump have been experimentally studied through PIV technique (Castilla et al. 2008; Ertürk et al. 2011) and numerically (Castilla et al. 2010). Instantaneous and phase-locked average fluid motions have been obtained with the accurate results of the PIV data. Furthermore, a basis for the experimental analysis of the flow inside of an external gear pump has been established for future analysis to investigate the three-dimensionality of the flow and the importance of the gearing contact point.

In this chapter, the fluid flow in an external gear pump has been analyzed experimentally for different rotational velocities. Obtaining the mean and the instantaneous velocity fields in the suction and impulse chambers can help to identify internal fluid flow system in order to improve the performance and the design of the pump (Castilla et al. 2008). The instantaneous 2D velocity measurements inside the chambers have been obtained using the PIV and information about the three-dimensional flow structures has been inferred. The volumetric flow rate through the pump has been estimated and its relationship with the gear positions from the phase-locked ensemble averages has been analysed. In this study, the velocity and vorticity field were obtained in the spatial resolution level of 32x32 pixel interrogation area size that leads to analyse the small scale turbulent flow structures in the gear pump.

In the last decades, this nonintrusive technique has been applied to the studies of a large number of flow problems (Adrian 2005). Wernet (2000) has applied PIV as a quantitative measuring method for the flow in turbomachines. A general description of the technique in rotating machinery applications can be found in the work of Wulff (2006). High speed digital cameras allow acquiring high frequency time-series of particle images. The high image acquisition rate is necessary to capture the evolution of the flow in systems with considerable velocity changes that are encountered in pumps with large rotational velocities. Thus time-Resolved Particle Image Velocimetry (TRPIV) can be applied (Lecordier and Trinite 1999). By using this technique, the information about the time evolution of the large-scale flow structures, the mean and the instantaneous velocity fields inside the pump chambers can be obtained.

Furthermore, the analysis done clarifies some of the small-scale characteristics and turbulent structures. Besides, knowledge of viscous dissipation rate of turbulent kinetic energy (ε) may be required for the assessment of turbulence models employed in computational fluid dynamics (CFD) and turbulence models used to estimate the volumetric efficiency with effectiveness of different gear tooth profiles in the external gear pump system. Therefore, calculation of dissipation rate using experimental data is an open question. Several experimental studies have been done to analyse the small-scales structures with the flow systems that contain rotating parts in fluid flow by using PIV technique (Sharp and Adrian 2001; Baldi et al. 1996). Two-dimensional PIV provides an important tool for obtaining space- and time resolved velocity data and these data can help to analyse complex turbulent flows. A wide amount of knowledge on the turbulent flow characteristics of stirred vessels that have rotating elements similarly to the external gear pump flow systems have been obtained through PIV technique in recent years (Sheng et al. 2000; Micheletti et al. 2004; Delafosse et al. 2011). Besides, the PIV technique has been used in several studies in order to estimate the turbulent dissipation rate (Sharp and Adrian 2001; Gabriele et al. 2009; Huchet et al. 2009). The obtained results vary from one work to another due to the approximations made on the structure of the turbulence and limitations in terms of spatial and temporal resolutions. In order to obtain dissipation rate several relationships based on isotropy assumptions are proposed in the literature despite an insufficient number of measured gradients. A method that considers the turbulence as non-homogenous, but statistically isotropic has been used in several studies (Sharp et al. 1998; Ducci and Yianneskis 2005). Although PIV technique offers various advantages, the ability to resolve all scales of interest for turbulence studies has not been established properly according to the spatial resolutions to estimate the dissipative ranges. Recently, there have been attempts to quantify the effect of the spatial resolution on the estimation of the turbulent scales in PIV (Saarenrinne and Piirto 2000; Scarano 2003; Poelma et al. 2006). A comparison of measurements techniques, hot-wire anemometry (HWA) and PIV, has been performed in order to study the effect of the finite spatial resolution of PIV on turbulent statistics (Lavoie et al. 2007). An image size large enough to capture the large scales and an interrogation area small enough to capture small scales should be selected carefully if all the turbulent scales of interest are to be evaluated accurately.

4.2 Experimental set up

4.2.1 External gear pump

The external gear pump that is used in this study has two identical cogwheels with eleven teeth each. The diameter of the gear is 53.6 mm and the depth is 36 mm. The theoretical volumetric capacity of this model is C_v = 4.4x10^{-}5 m^3/rev thus the flow rate in m^3/s is $Q = Cv\omega/2\pi$, where ω is the rotational velocity in rad/s. The used fluid in the experiments is a commercial oil with a density of ρ = 885 kg/m^3 and viscosity of μ = 0.028 Pa·s. The main body of the test pump is completely made of transparent Plexiglas in order to allow image acquisition (Figure 4.2). The cogwheels are made of metal and they are in contact with each other. The intake of the suction chamber is located in horizontal plane of symmetry of the pump. Impulse and suction chambers have a size of 31.8x16.8 mm^2 with 36 mm depth (Figure 4.2b). First, the fluid enters into the relaxation chamber through two opposite lateral pipes coming from an elevated tank. This chamber is designed to reduce the influence of the flow curvature at the entrance of the pump. Then fluid enters to the suction chamber from a pipe that is connected to the relaxation chamber. This setup allows illumination of the horizontal plane of symmetry of the pump with the laser sheet.

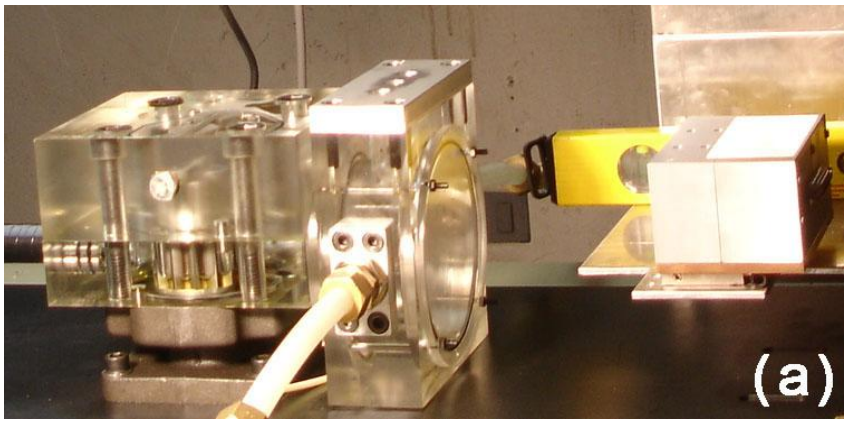

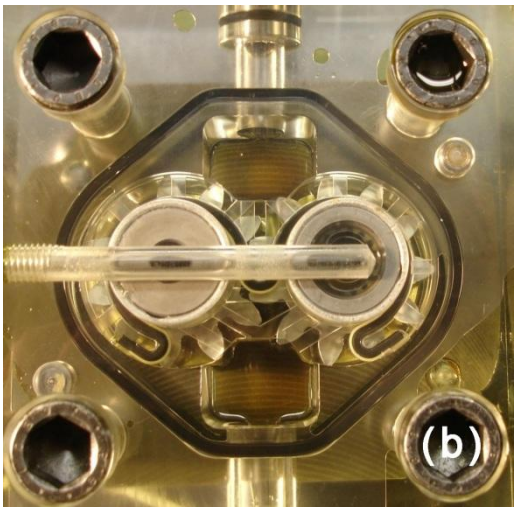

Figure 4.2. External gear test pump: (a) lateral view and (b) top view.

4.2.2 PIV experimental set-up

The PIV experiments have been performed in the pump system located in the LABSON group of the Universitat Politecnica de Catalunya (UPC) using several configurations. The pump is installed in a test bench that is connected by two hydraulic circuits. The primary circuit contains the pump that intakes the moving fluid from an elevated tank and impulses it through a pressure fall of $5x10^5$ to $15x10^5$ Pa to the tank again. The secondary circuit contains an oleohyraulic motor that supplies power to the pump and controls its rotational velocity. This allows an easy change in the rotational velocity and the delivered flow rate by the pump. The time-resolved PIV technique is an effective solution for the detailed study of the internal flow since it is a quantitative measuring method. The PIV setup has been illustrated in figure 4.3 for the experiments that have been realized in the x-y and x-z planes. Independently from the gear pump test facility, an L-shaped setup has been established for the camera and the laser. The L-shaped setup enables to move the system easily from the x-y plane to the x-z plane. The camera and the laser can be moved easily together in the same amount without changing the focus on the field of view where the analysis is done. By using easy configuration of

the L-shaped facility, PIV experiments have been done in x-y plane with Δz=0.003m distance of the depth of the suction and impulse chambers and in x-z plane with Δy=0.003m distance of the wide of the suction chamber.

The particle images are obtained using a Photron Ultima APX-RS camera with the sigma 105mm f/2.8 EX DG macro lens. The camera can work at 3000 fps for a maximum resolution of 1024x1024 pixels. For these conditions the buffer memory of the camera allows to record up to 2048 images. The sampling rate and the number of recorded frames can be increased by reducing the resolution. The illumination system consists in a pulsed infrared diode laser of MONOCROM with a wavelength of 800nm. It allows variable pulse duration ranging from10 to100 μs and pulse energy of 2.5–25 mJ with a maximum working frequency of 5 kHz. The laser generates an output light sheet of 0.7mm thickness and a width enough to illuminate the whole suction chamber of the pump. In order to investigate the three dimensionality of the flow, the experiments have been done in different horizontal and vertical planes considering the suction and impulse chambers of the gear pump. Figure 4.4 illustrates the sketch of the horizontal (x-y) plane for the suction and impulse chambers. The fluid in the suction chamber, engine oil in this study, is trapped between the teeth of the gears and the body of the pump. As the gears rotate across to each other, the fluid is transported to the impulse chamber.

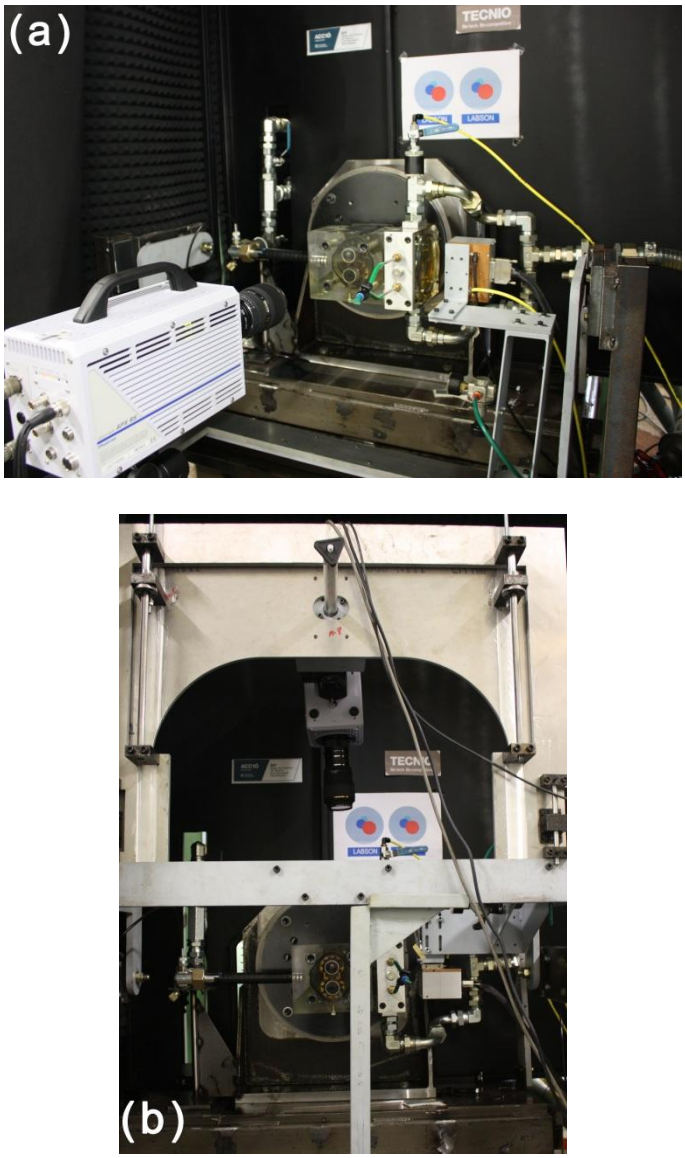

Figure 4.3. PIV experimental set-up to record: (a) x-y planes; (b) x-z planes (the x-y and x-z planes have been illustrated in figure 4.4).

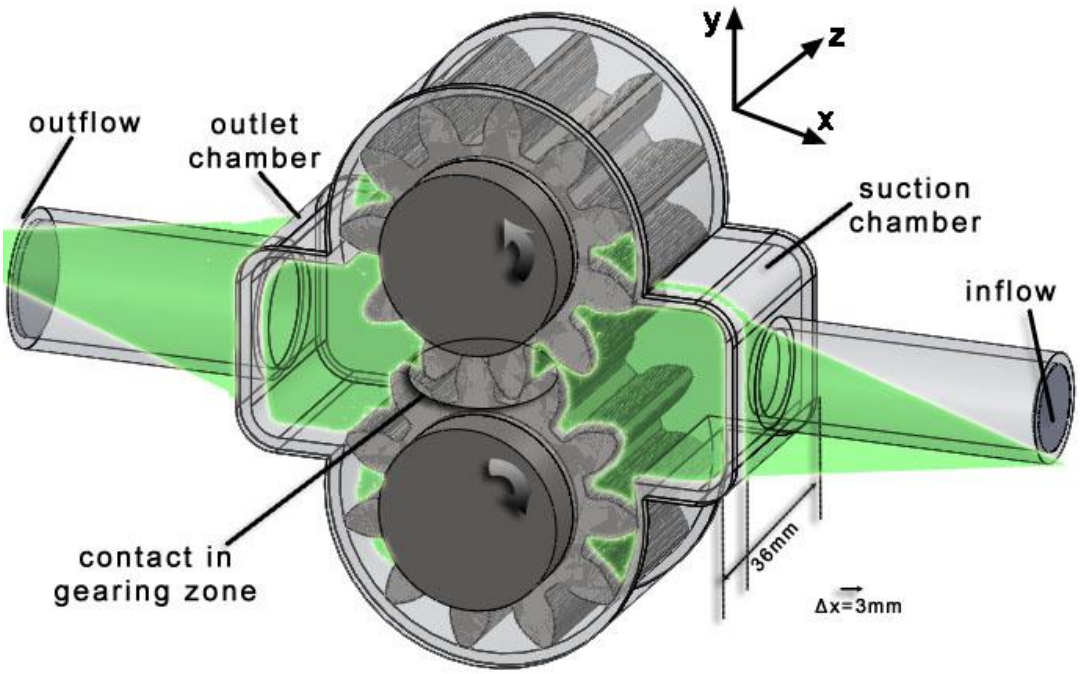

Figure 4.4. Sketch of the external gear pump test system with the horizontal (x-y) plane illustrations for the PIV flow analysis.

Table 4.1 shows the details for the experiments that have been performed in this study. Mainly, the experiments have been carried out for six different experimental cases considering the air bubbles and alginate particles as flow seeding and the analysing area of the gear pump flow. However, different rotational velocities of the external gear pump have been employed for each experimental case study. Furthermore, several planes of the suction and impulse chambers have been used in order to analyse the three-dimensional flow structures in the gear pump flow. Briefly, the experiments measure the velocity components in the horizontal and vertical plane of symmetry of the pump. The images are acquired by the CCD camera and stored in its buffer memory. When all the buffer memory is filled, the information is transferred to a personal computer for later processing.

Table 4.1. Experimental parameters

Parameters	**Case 1**	**Case 2**	**Case 3**	**Case 4**	**Case 5**	**Case 6**
Analysing area	Suction chamber	Impulse chamber	Suction chamber	Suction chamber	Impulse chamber	Close to gears
Seeding particles	Air bubbles	Air bubbles	Alginate	Alginate	Alginate	Alginate
Analysing plane	(x-y)	(x-y)	(x-y)	(x-z)	(x-y)	(x-y)
Number of analysed planes	1	1	11	9	11	3
Number of recorded image series	21	1	214	54	34	18
Resolution (pixels)	1024x1024 896x784 768x816	1024x1024	1024x1024 896x784	1024x1024	1024x1024 896x784	1024x1024
ω_1(rad/s) **ω_2(rad/s)** **ω_3(rad/s)** **ω_4(rad/s)**	28.5 34 43.2 47.4	15.2	52.3 62.8 72.3 83.7	52.3 83.7	52.3 83.7	52.3 62.8
$\omega \cdot D$ (m/s)	1.53 1.82 2.32 2.54	0.82	2.8 3.4 3.9 4.5	2.8 4.5	2.8 4.5	2.8 3.4
f (fps)	2000 3000 4500 4900	2000	3000 4500	3000 4500	3000 4500	3000
Re ($\omega \rho D^2/\mu$)	2588 3087 3923 4304	1380	4750 5703 6565 7600	4750 7600	4750 7600	4750 5703

4.2.3 Seeding particles

Initially air bubbles have been considered as seeding particles for the PIV analysis although most PIV experiments suggest using small solid particles. Moreover, the use of solid materials can produce material erosion and damage the transparent surface of methacrylate. They can also cause problems in the contacting gearing zone (Figure 4.4)

particularly in this gear pump due to the metal-metal contact between the teeth. The use of water drops as particle seeding could also be considered but in this case they can produce problems of oxidation of the steel gears. Finally, small air bubbles have been used in spite of some disadvantages: (i) the size of the bubbles is not easily controllable and a large variability in its size can make difficulties to estimate the velocity lag (Raffel et al. 1998), (ii) the density ratio is very large and (iii) the presence of gas in a liquid can reduce the velocity of sound and hence it can make the flow becoming compressible at relatively low velocity (Brennen 2005). The size of the bubbles was controlled by using pressurized air flowing through a porous media that avoids the generation of large size bubbles. The control of the air flow also allows regulating the density of particles in the measurement area. Drag and buoyancy forces associated with acceleration are the main forces that could act on bubbles for their motion in fluid than the force of the fluid flowing. These forces can be optimized to allow bubbles to relocate rapidly to a desired area (Moore 2007). By combining the drag force and the buoyancy force, Stokes Law given in Eq. 4.1 can be formed based on gravity acceleration (g), bubble radius (r) and kinematic fluid viscosity (ν) to estimate the bubble rise velocity (v_{rise}).

$$v_{rise} = \frac{2}{9}\frac{r^2 g}{\nu} \qquad \text{Eq. 4.1}$$

Figure 4.5 show how the rise velocities have a strong dependence on the bubble radius for the commercial oil (ρ = 885 kg/m^3, μ =0.028 Pa·s) used as pumped fluid.

If the flow has a streamwise mean velocity, $\bar{v}_y$, (Figure 4.1) and when the particle reaches the end of the test section, it goes out of its path with a distance of H:

$$H = v_{rise}\frac{L}{\bar{v}_y} \qquad \text{Eq. 4.2}$$

where L is the length of the test section. In order to find the ratio and keep the bubbles in the laser sheet, the ratio of vertical deviation and horizontal length of the test section can be obtained from the equations 4.1 and 4.2.

$$\frac{H}{L} = \frac{2}{9}\frac{r^2 \rho}{\nu \bar{v}_y} \qquad \text{Eq. 4.3}$$

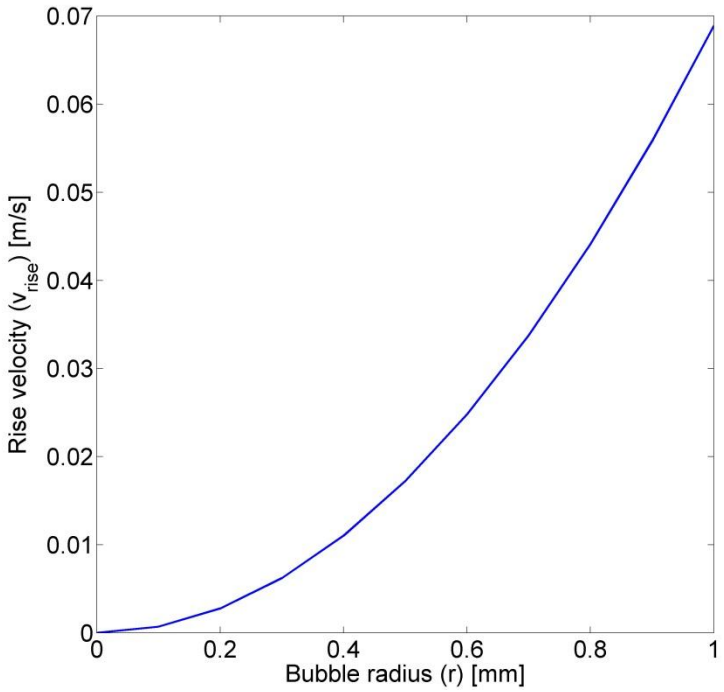

Figure 4.5. Rise velocities dependence on bubble radius.

In the experiments, the laser sheet has a 1 mm thickness and the test section has a length of 31.8 mm. In order to keep the bubbles in the laser sheet, *H*/*L* ratio needs to be approximately 0.03. The ratio of the vertical deviation and the horizontal length of the test section versus the streamwise mean velocity is plotted in the figure 4.6 for the various bubble diameters in the analysing oil.

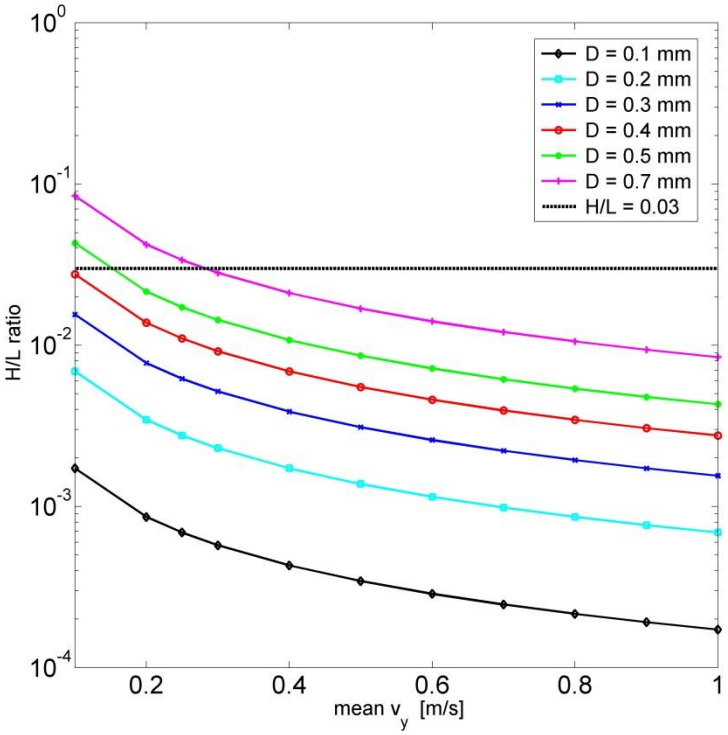

Figure 4.6. For several bubble diameters, the ratio of vertical deviation and test section length in function of mean horizontal velocity. The limit value, H/L ≈ 0.03 has been indicated as a straight horizontal line.

The effect of gas-liquid mixture on the sonic speed of the flow has also been considered. A sufficiently high volume fraction of air can reduce the sonic speed below to 20 m/s (Brennen 2005). In the present case, the gas maintains its temperature constant and the pressure of the pump system is quite low. When 64x64 pixels interrogation area with sufficient density of air bubble particles is used for low velocities, the flow shows reasonably far away from compressibility characteristics. In the worst situation which is the sonic speed is approximately 20 m/s, the rotational speed of the pump should be around 105 rad/s (5.6 m/s) in order to have a Mach number of the order of 0.3 (Castilla et al. 2008). In the present configuration of the experimental setup, the rotational velocity of the gear was working between 20.9-47.1 rad/s.

Although the air bubbles were practically used as flow seeding for the PIV system, there was a still demand to use solid seeding in the PIV system. One of the aims was to increase the efficiency of the recorded images such as obtaining homogenous seeding and high particle density in each interrogation area. Using smaller size particles would lead to analyse small-scale structures of the flow. Another point was to provide a practical way to perform the PIV experiments. Controlling the size of the air bubble particles was quite challenging even though the using a porous media to regulate their diameter size did not provide a continuous long term homogenous seeding. Furthermore, the density of the air bubbles (1.225 kg/m^3) and the density of analysing fluid (885 kg/m^3) were quite different. All the conditions that are considered above lead to seek for new tracer particles for the PIV analysis of the gear pump. Alginate particles as flow seeding fulfil the demand of PIV requirements for this specific gear pump system. The production and characterization of the particles have been given in the previous chapter 3. Particularly for the external gear pumps, the most important characteristics of the alginate particles are the small diameter sizes, excitation of the light property, the matching density and no damage on the gears. Due to the porous structure of the alginate particles, the particle density becomes almost the same as the analysing liquid. Besides, the particles are environmental friendly. The alginate particles are introduced from the oil supply tank of the external gear pump system and they recirculate in the flow system continuously.

4.3 Image data analysis

The particle images have been processed by ECoMMFiT PIV software based on Matlab program. The software uses the patterns deformation algorithm with regard to the Local Field Correction (LFC) PIV method (Nogueria et al. 2001; Nogueria et al. 2005). LFC PIV method leads an appropriate signal to noise ratio to minimise the number of spurious vectors (Ertürk et al. 2011). It has been tested different interrogation areas, 16x16, 24x24, 32x32, 48x48, 56x56, 64x64 pixels, with a 50% overlapping for the calculations of the velocity field and turbulent statistics. Enough seeding particles have been obtained in each interrogation area to extract the velocity data. However, the number of particles has been expected to be reduced close to the gear teeth area. In order to increase the

correlation peak in those areas to find the displacement accurately, the software applies triple image correlation and boundary treatment algorithms (Usera et al. 2004). In order to detect and remove spurious vectors, a validation algorithm has been introduced (Ertürk et al. 2011). Approximately 2.9% of the vectors have been considered erroneous and have been detected and corrected for the analysis of the external gear pump flow. The processing of the images can be found more details in chapter 2 of the present thesis.

Figure 4.7 has been illustrated to describe the studying areas and testing points where the image data analysis has been done for the analyses. The experimental conditions have been mainly identified in the suction and impulse chambers of the gear pump as indicated in table 4.1. The more emphasis has been done on the suction chamber due to the high influence on the flow structures of the gear pump flow. Some testing points have also been selected from the suction chamber since this chamber is designed to reduce the influence of the flow curvature at the entrance of the pump.

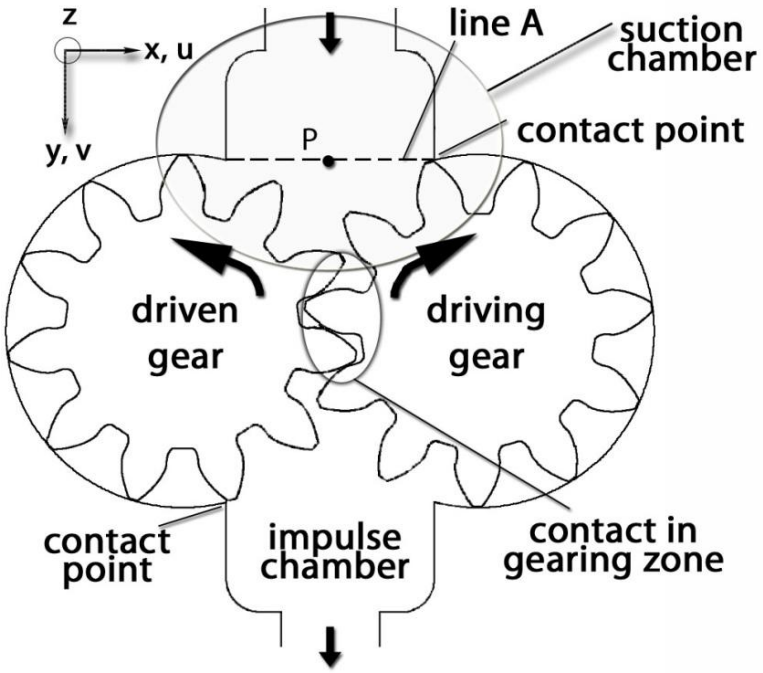

Figure 4.7. Schematic drawings of the external gear pump system. Testing points, Line A and point P, indicate the selected location where specific analyses have been done.

The statistical analysis of the velocity field has been done by considering the recorded number of images for each series. As indicated in table 4.1, several number of frequency rates have been applied to the different rotational velocities of the gear pump. 2048 PIV images have been obtained for the frequency rates of 2000 and 3000 fps. For 4500 and 4900 fps, 3009 and 3585 PIV images have been respectively recorded. Depending on the number of recorded PIV images, various phase-averaged images per each series can be evaluated. Furthermore, the number of phase averaged images can be increased using the several numbers of recorded series of the same conditional experiments. Obtaining several PIV image series lead to analyse the measurement error estimations and the statistical analysis of the turbulence in the external gear pump flow.

4.3.1 Conditional ensemble averages

In this section, the procedure used to analyse the evolution of the rotating elements interacting with fluid flow is introduced. The temporal evolution of the structures is obtained by using time-resolved PIV with a sufficient temporal resolution to capture the large scales. In this sense, time-series of PIV images can be considered as ‘time-resolved’ if the time step between measurements is smaller than the Taylor microscale of the flow. Thus, significant correlation exists between the large-scale structures that are presented in consecutive measurements, which allow analysis of its temporal evolution.

The available data from the experiments consist in a time history of particle images. After processing them, a set of velocity planes at a constant sampling rate is available for the analysis. The behaviour of the flow structures in the working flow can be observed from the velocity time history and analysed for each single time. This will imply to visualize and study more than 2000 velocity planes per each experimental series. This huge task can be applied to the analysis of the typical flow structures that periodically appear in the flow. Computing the autocorrelation of the velocity field can give an idea of the existence of periodic structures in the flow. Figure 4.8 shows the autocorrelation function computed from the velocity time history in the point P (Figure 4.7). It displays a cyclic behaviour corresponding to the periodical movements of a single tooth at a given position. This

indicates that similar flow structures appear in the flow for a fixed location of each tooth. Thus, averaging the velocity fields for a selected tooth location will provide a phase-locked ensemble average that shows the typical flow behaviour for a chosen wheel configuration. Usually, the phase-locked averaging are obtained using an external synchronization signal that indicates when the system displays a particular status. In this case there is no external signal that can be used for that purpose. Therefore, the condition for selecting the individual events to compute the phase-locked average is obtained directly from the time history of the particle images. Time elapsed between the passages of two consecutive teeth for the same physical location is used as a proper time scale (gearing period, T_g) due to the strong cyclic character of the flow.

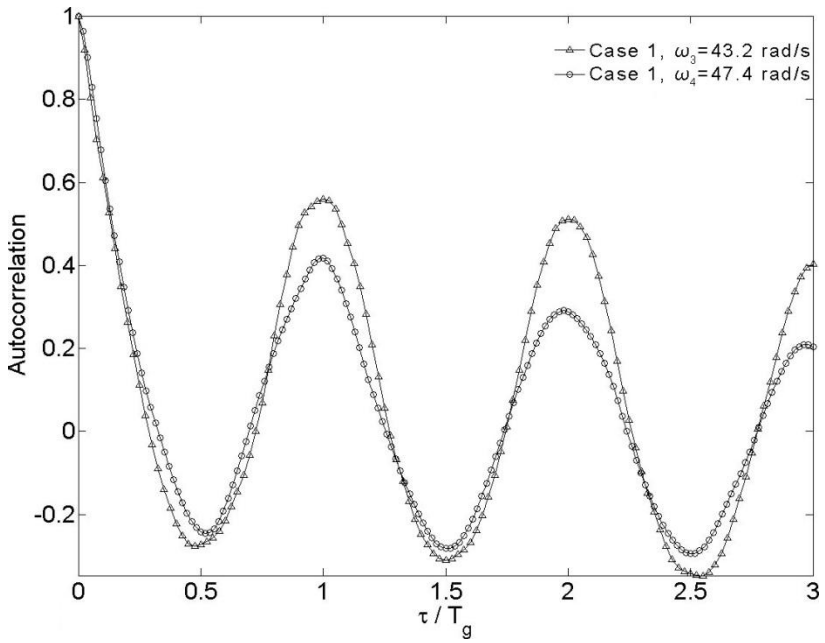

Figure 4.8. Autocorrelation function that is computed from the velocity time history at point P for case 1 at 43.2 and 47.4 rad/s, the plot shows the passages of three consecutive teeth for the same location.

The autocorrelations illustrated in figure 4.8 corresponds to the passages of three consecutive teeth for the same location. It shows that each gearing period corresponds to 54 and 40 particle images for case 1 and case 2 respectively. This means that for each

case 54 and 40 different tooth locations can be observed from the particle images. Only one of these locations has to be chosen in order to obtain the conditional (phase-locked) ensemble average of the velocity field. The process consists in selecting a single particle image with a defined teeth configuration and a region of interest that includes one gear tooth as shown in figure 4.9. Correlation coefficients between that single image and all the particle images are computed. The result is the cross-correlation function that is illustrated in figure 4.10. The peaks indicate the time events where the teeth are in the same phase. The mean of those events is computed to obtain the phase-locked ensemble average. A total of 53 and 50 are selected for averaging for experimental cases 1 and 2, respectively. These results agree with the fact that approximately 50 images are stored for each gearing period. The ensemble average at different phases can be obtained by simply averaging the instantaneous velocity planes at the selected time plus 1, 2, 3 … or 50. This procedure provides the time evolution of the ensemble average during one gearing period.

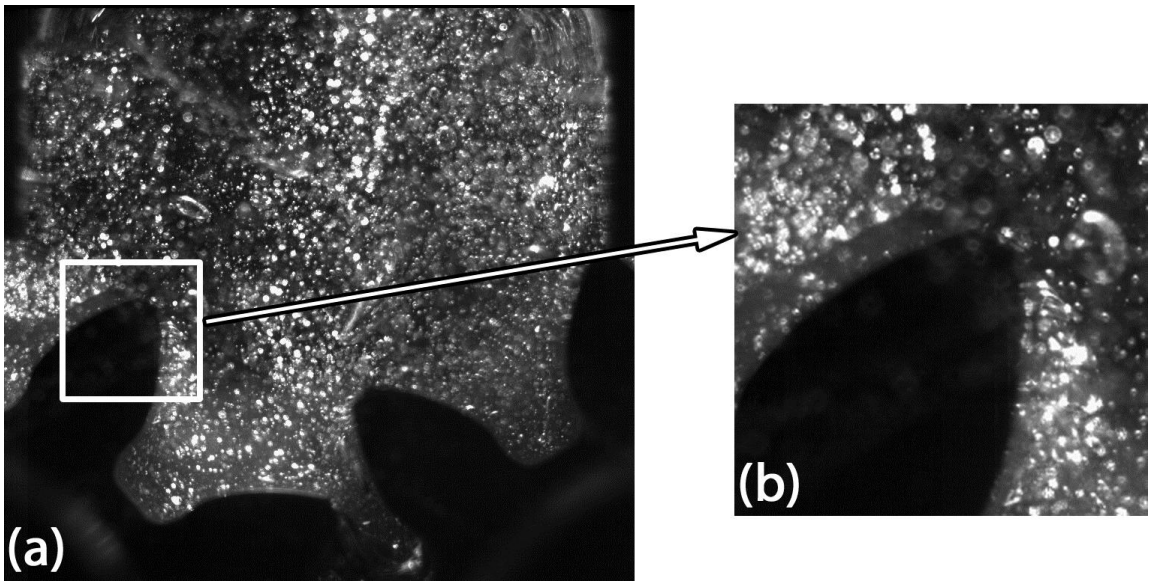

Figure 4.9. Representation of the selected image from the time-series: (a) selected single phase particle image and (b) selected region of interest; the selected image is used to find the location of the gears and the rotational velocity of the gear pump.

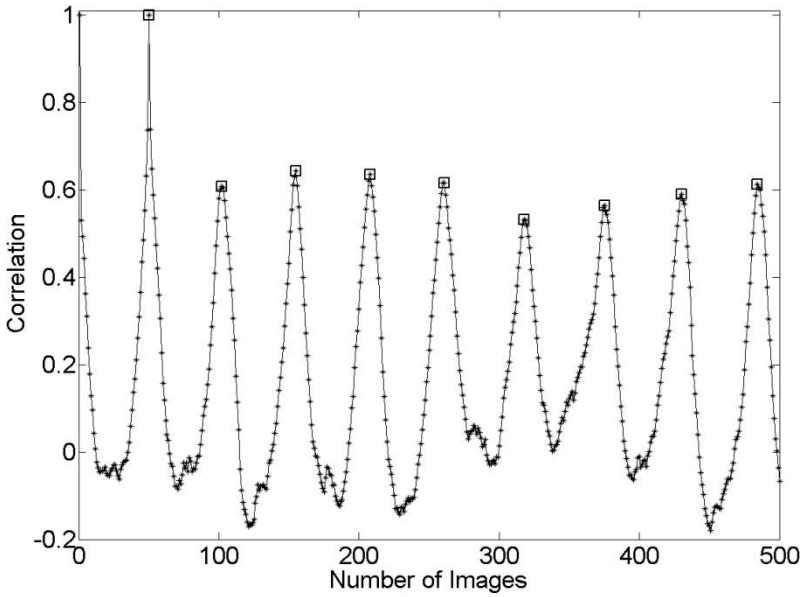

Figure 4.10. Cross-correlation function between the single image as shown in figure 2.10 and presently 500 particle images has been illustrated from 2048 images; the peaks indicate the time events where the teeth are in the same phase.

4.3.2 Accuracy and turbulent characteristics of the measurements

The accuracy of the measurements for phase-locked ensemble averages significantly depends on the number of the recorded particle images with the reference position where the gear tooth phase is locked. Several of the same phase-locked gear tooth PIV data have been considered in order to estimate the convergence of the total velocity measurement error. The sum of the mean bias-error and the RMS error of the velocity data can be used for the estimation of the total error measurement. The accuracy of the measurements can be obtained from the velocity data close to the gear tooth where the velocity of the flow is expected to be nearly the same as the rotational velocity of the pump. Thus, the total displacement error can be calculated in terms of the mean-bias and RMS errors (Huang et al. 1997) by considering the same several velocity data as a convergence function. The details of the estimation of the total measurement error have been indicated in chapter 2.

The error estimates are embedded with different numbers of phase-averaged images whose magnitude affects the results importantly. Furthermore, the convergence of the total displacement error measurements has been obtained by using the number of phase-locked ensemble average velocity data.

The small-scale characteristics and turbulent structures in an external gear pump flow have been investigated by performing two-dimensional field measurements using PIV. The time and length scales of the flow have been estimated at different spatial resolutions of the PIV data (Ertürk et al. 2012). Turbulence dissipation rate has been obtained for different rotating gear phase profiles. The calculation procedures have been given with details in the chapter 2.

4.4 Results

4.4.1 PIV measurements with air bubbles as flow seeding

The autocorrelation function (Figure 4.8) indicates the strong periodical behaviour of the flow inside the suction chamber. It is inferred that the large-scale structures must be very similar for each single gear tooth passage. This is the basis for using the passages of each gear tooth as a conditional signal to obtain the phase-locked average of the flow. Once the conditional ensemble averages are obtained, the characteristics of the flow can be analysed. Figure 4.11 compares the mean velocity profiles of the v-component compute in the line A (see figure 4.7) for two experimental cases (Case 1 with ω_3 and ω_4, see Table 4.1) and numerical simulation series where details of this numerical simulation can be found in Castilla et al. (2011). The velocity has been normalized with the reference velocity, ωD, and the position has been normalized with the width of the chamber, 31.8 mm.

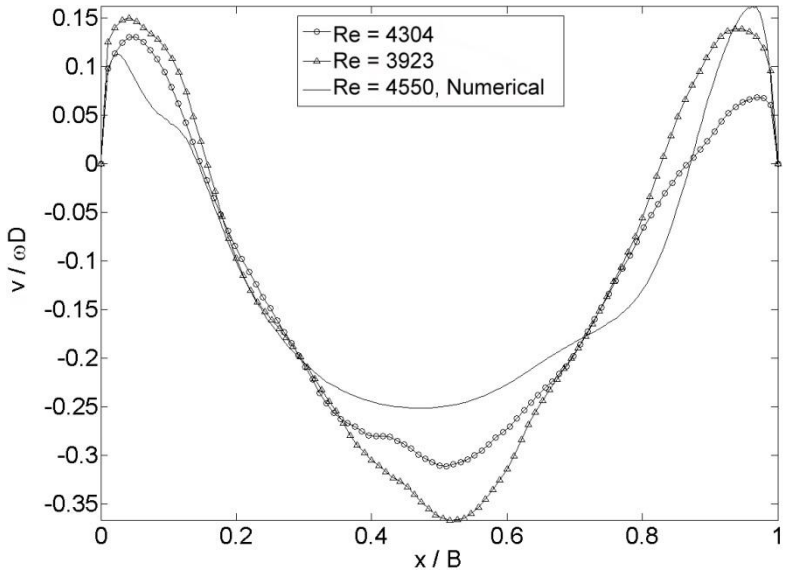

Figure 4.11. Mean velocity profiles of the v-component in the horizontal line A for case 1 with ω_3 and ω_4, the solid line shows the numerical result based on Castilla et al. (2010), the velocity has been normalized with the reference velocity, ωD, and the position has been normalized with the width of the chamber.

Negative values correspond to the flow from suction chamber to the gearing area and positive values correspond to the backflow which affect the overall performance of the gear pump. The larger negative velocity values are located at the centre of the suction chamber. It can also be observed that when the rotational velocity increases, the vertical mean velocity values decrease. The *v*-component velocity profile can be used to estimate the pump flow rates that are 3.3×10^{-4} and 3.7×10^{-4} m^3/s for case 1 with ω_3 and ω_4, respectively. These values agree with the theoretical flow rate values that are calculated as 3.03×10^{-4} and 3.32×10^{-4} m^3/s, respectively. Conditional velocity profiles have also been obtained by using the phase-locked averages. The conditional streamwise (*v*) and cross-stream (*u*) velocity profiles for case 1 with ω_4 at three different phases (Figure 4.12) have been illustrated in figure 4.13. The same behaviour of the conditional velocity profiles for case 1 with ω_3 is observed The direction of the flow with negative values of the streamwise velocity assembles in the centre zone of the suction chamber and backflows (positive velocities) are observed in the lateral zones (figure 4.13a). The flow in the right and left sides of the chamber are not completely symmetric. For the situation

corresponding to “Phase I” a tooth of the gear is closing the entrance of flow for the right side. Thus the backflow increases on the right side of the suction chamber, while it decreases on the left side. “Phase III” corresponds to an opposite situation where the left side is closed and the right side is open. Therefore, the backflow increases on the left side and decreases on the right side. For “Phase II”, right and left sides of the suction chamber are partially open and the profile is nearly symmetric.

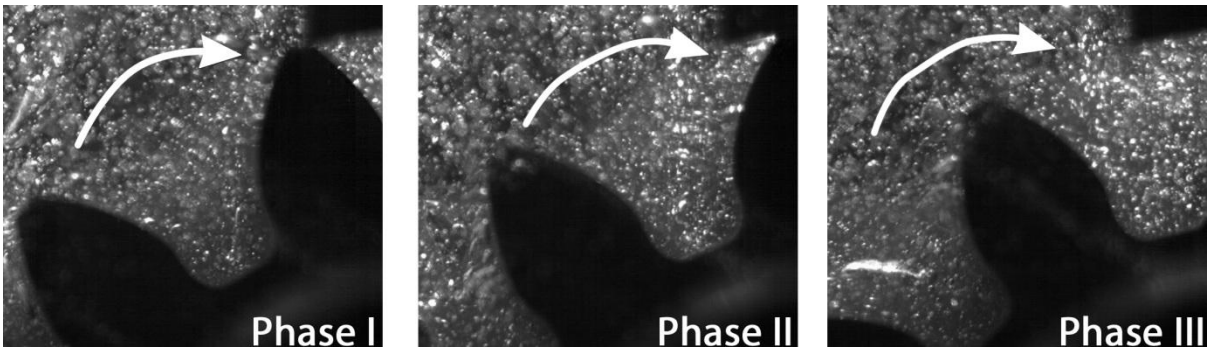

Figure 4.12. Illustration of three different phases of the gear tooth profile.

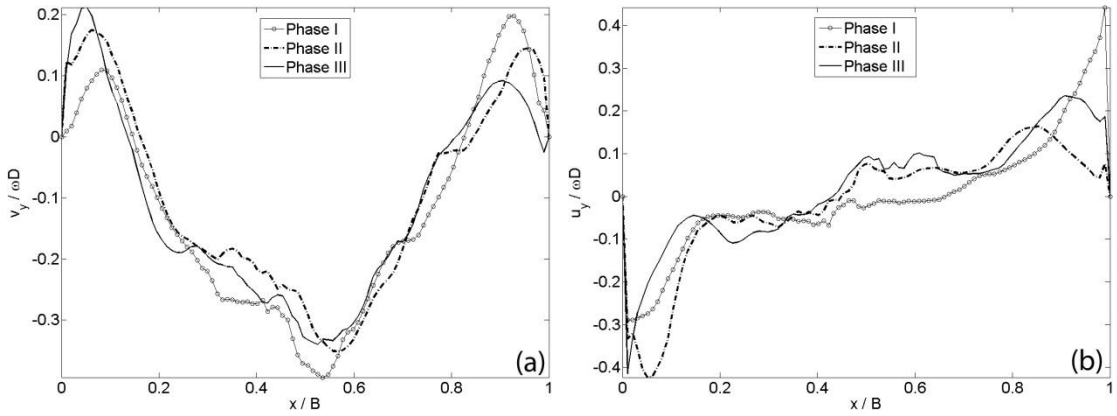

Figure 4.13. Conditional velocity profiles in the line A at three different phases (see figure 4.12) for case 1 with ω_4: (a) streamwise velocity (v), (b) cross-stream velocity (u).

On the other hand, the differences in the phase-locked velocity profiles agree with the fact that the flow rate in a gear pump is not constant along all gearing period as figure 4.14 illustrates. Each point in the flow rate function is estimated by integrating the corresponding phase-locked velocity profile. It is necessary to mention that the flow rate is computed from 2D information in a single plane of the suction chamber. Thus, some differences between the experimental results and the theoretical flow rate can be found mainly due to the three-dimensional character of the flow. To check that deviation the mean experimental flow rate is computed from the data in figure 4.14. Results show that the mean flow rate is about the 95% and 88% of Q_t for case 1 with ω_3 and ω_4, respectively. Figure 4.14 also shows the flow rate distribution that is obtained from a numerical simulation as detailed by Castilla et al. (2011). Experimental and numerical results are in qualitative agreement. However, significant differences are present between the two curves: the predicted step rise and the parabolic decay present in the numerical results are not well observed in the experimental measurements. In the numerical results, the fast growth of the flow rate and the bounce effect at the beginning of the cycle is caused by the sudden opening of the growing space between teeth when the contact point in the gearing zone (see figure 4.7) disappears. Basically the differences between experimental and numerical results could be attributed to the fact that the numerical simulation is done in 2D, thus any three dimensional effect is not presented in the numerical case.

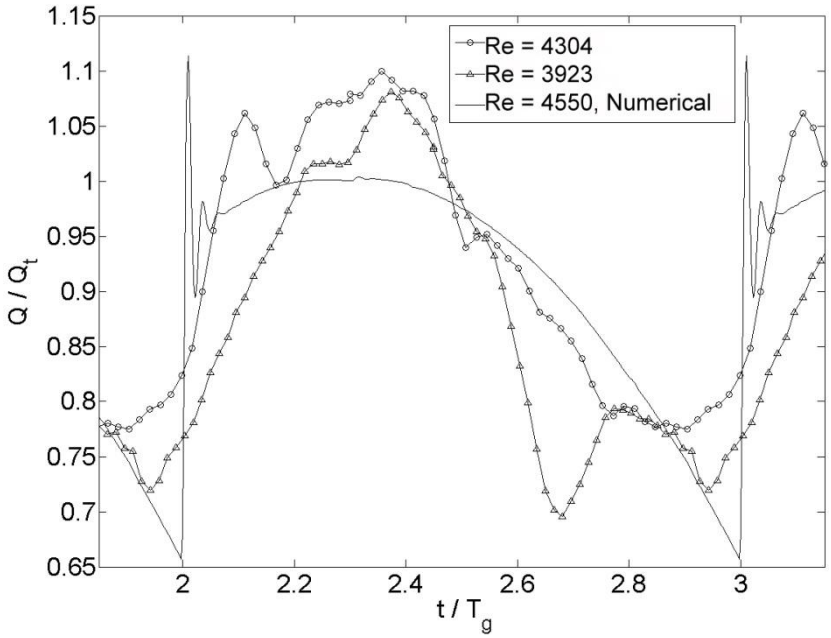

Figure 4.14. Flow rate history in the suction chamber in the line A, the flow rate is normalized with the theoretical flow rate (Q_t) and the time with the gearing period (T_g).

The ensemble average of the velocity field for case 1 with ω_4 is shown in figure 4.15. It is computed from 53 instantaneous vector maps for a single selected phase. The velocity vectors are larger in the centre of the suction chamber and around the gearing zone. Negative velocity vectors appear near the walls of the chamber and they are related with two big foci that are in the upper part of the suction chamber. These critical points and the magnitude of the velocity vectors point out to the three dimensionality of the flow. These two foci are present in the suctions chamber for all the phases of the gear. The location of the vortex centres is stable during a gear cycle. They are placed fully integrated into the suction chamber as it has been observed in the previous study for the impulse chamber of the same gear pump (Ertürk et al. 2008). A saddle point becomes visible in the centre of the figure near the gearing zone together with a focus that is attached to the right-side tooth. These two critical points move and evolve with the gear rotation.

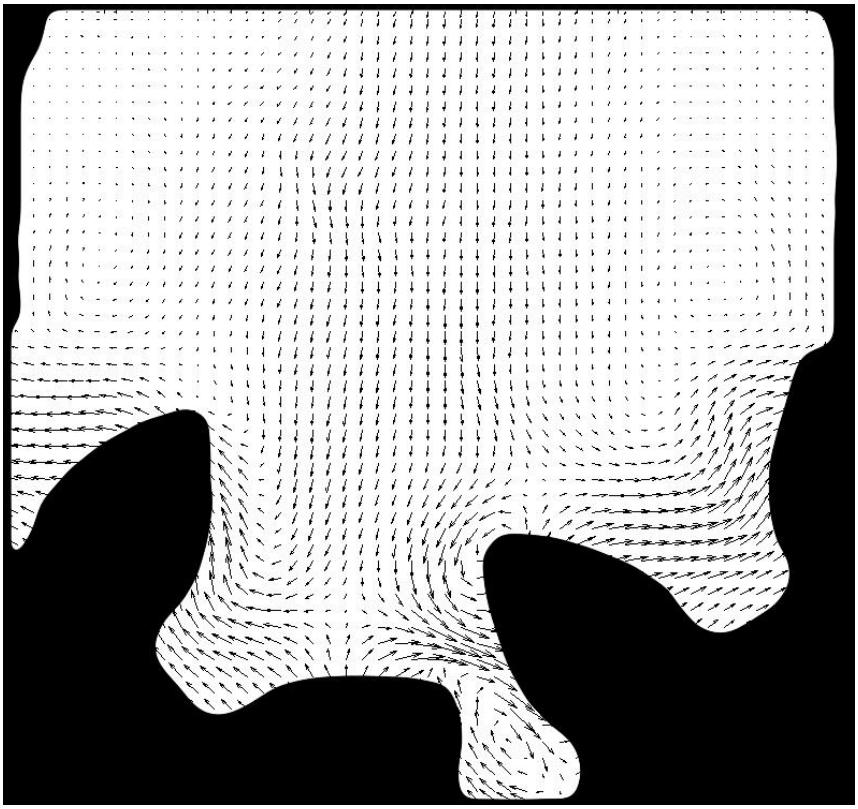

Figure 4.15. Conditional ensemble average velocity fields in the suction chamber for case 1 with ω_4, 53 instantaneous vector maps have been used to compute the velocity field.

Two dimensional streamlines are more suitable to visualize the flow structures and to follow their evolution. Figure 4.16 shows the 2D streamlines of consecutive phase-locked ensemble averages. The six ensembles that are shown in that figure represent the flow structures occurring in the suction chamber for one gearing period. The two foci that dominate the flow in the chamber are already present. The focus that appears in the centre of the gearing zone moves as the gear moves until it joins the big focus in the suction chamber. The dynamics of this focus is periodic. It appears when the gearwheel is opening the volume and suctioning the fluid and then moves consecutively to the right and to the left side of the suction chamber. For case 1 with ω_3, the results are found to be very close to case 1 with ω_4. The main direction of the flow in the centre of the suction chamber and the location of the foci has been found almost similar for both cases.

To analyse the turbulent behaviour of the flow in the suction chamber, a quantitative measure of the random unsteady velocity fluctuations is obtained from the velocity time history. An ensemble average of the two dimensional turbulent kinetic energy (k_{2D}) can be computed for each phase of the gear as:

$$k_{2D} = \frac{1}{2} \cdot \left[\left\langle u'^2 \right\rangle + \left\langle v'^2 \right\rangle \right] \qquad \text{Eq. 4.4}$$

where u and v are the velocity components, the primes denote the fluctuations and the brackets denote the conditional average. As it was pointed out before, the spatial filtering that is produced by the PIV technique ends with reduced values of the kinetic energy (Spencer and Hollis 2005). Thus, the obtained values for the k_{2D} have to be taken as an indication of the zones where the turbulent intensity is more intense. A contour plot of k_{2D} is illustrated in figure 4.17 and demonstrates a distribution of turbulent kinetic energy for case 1 with ω_4 and ω_3, respectively, by using the same gear phase. For both cases the distribution of the kinetic energy is similar. The higher levels of the turbulent kinetic energy are found around the gear tooth and appear in the centre of the gearing zone where the gearwheel is opening the volume and suctioning the fluid. The smaller values of the turbulent kinetic energy have been found in the backside of the gear tooth. The turbulent fluctuations do not reach until the top of the suction chamber where the large foci are located.

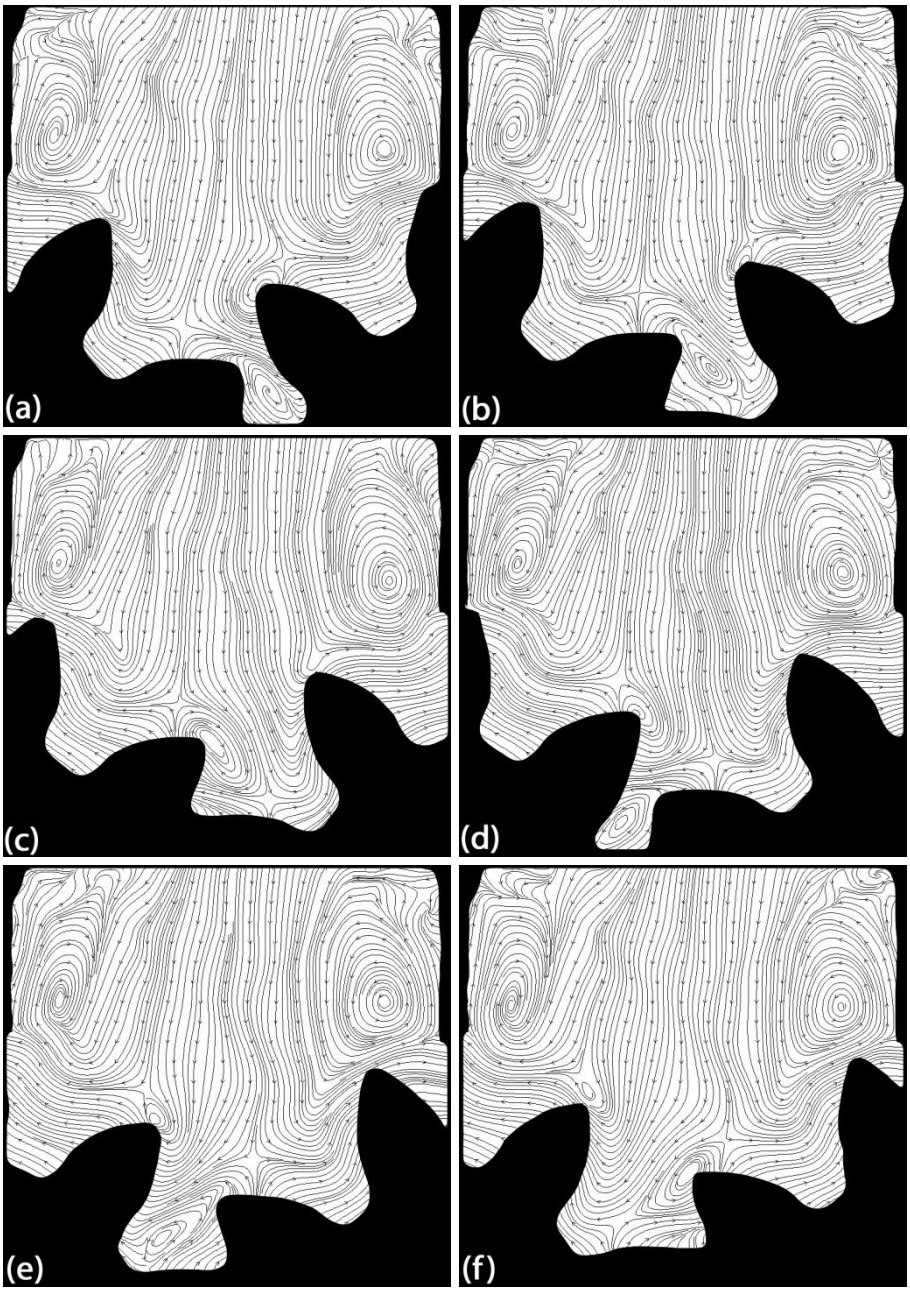

Figure 4.16. 2D streamlines corresponding to sample of six ensemble averages equally distributed in time spanning of one full gearing period for case 1 with ω_4, the averages at six consecutive times: (a) t_i, (b) $t_{i+\Delta t}$, (c) $t_{i+2\Delta t}$, (d) $t_{i+3\Delta t}$, (e) $t_{i+4\Delta t}$, (f) $t_{i+5\Delta t}$ where *i* refers to the initial sample.

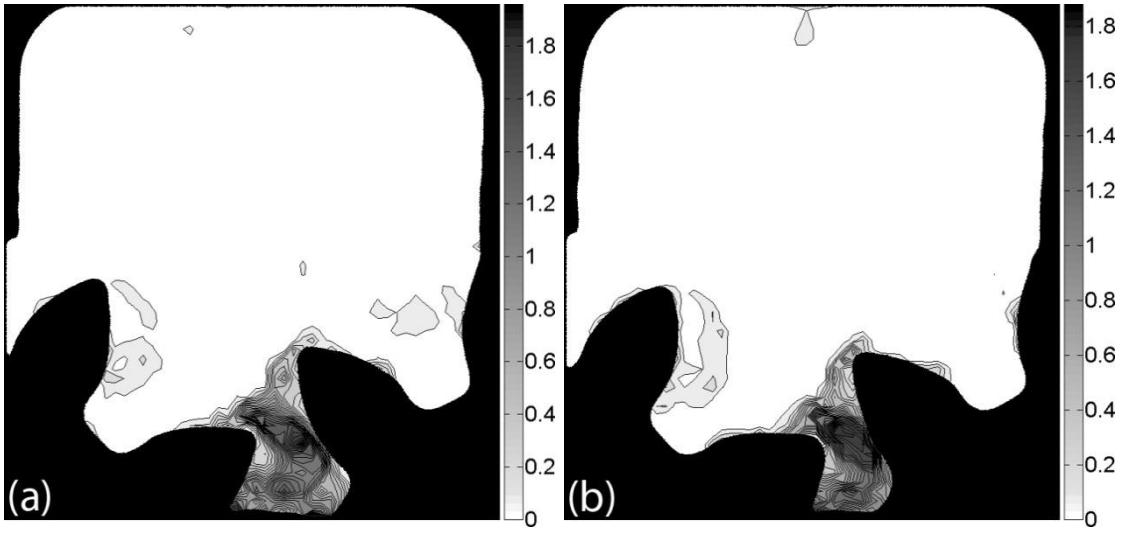

Figure 4.17. Contour plot of the k_{2D} of the turbulent kinetic energy inside the suction chamber by using the same gear phase for different experimental cases: (a) case 1 with ω_4, (b) case 1 with ω_3.

4.4.2 PIV measurements with alginate particles as flow seeding

4.4.2.1 Contour of velocity magnitude and streamlines

In this section, the results of the contour of velocity magnitude and streamlines in middle plane suction and impulse chambers are presented using different rotational velocities. The flow evolution in the suction and impulse chambers are studied. Furthermore, the vertical plane of the suction chamber has been analysed to identify the three dimensional structures of the flow system.

Figure 4.18 shows the velocity magnitude and the 2D streamlines of the consecutive phase-locked ensemble averages in the suction chamber for case 3 with ω_1, 52.3 rad/s (Table 4.1). The six ensembles that are shown in figure 4.18 represent the flow structures occurring in the suction chamber for one gearing period. The results are similar to those obtained for case 1 using air bubbles as tracers and different rotational velocities. Two

foci dominate the flow in the chamber and the focus that appears in the centre of the gearing zone moves as the gear. The dynamics of this focus is periodic. It appears when the gearwheel is opening the volume and suctioning the fluid and then moves consecutively to the right and to the left side of the suction chamber. The centres of the circular flow remain at the same position in all the images while the outer flow path of these two foci are usually bend except in figure 4.18b. The maximum velocity magnitude of the flow has been observed close to the gearing area of the suction chamber. Depending on the gear teeth positions, the velocity magnitude is changing with the movement of the gear teeth. The maximum velocity achieved is 1.4 m/s next to the gear teeth. Figures 20, 21 and 22 show the velocity magnitude and the 2D streamlines of the consecutive phase-locked ensemble averages in the suction chamber for case 3 with ω_2, ω_3 and ω_4, respectively, as indicted in the Table 4.1. In these cases, it has been observed that the two foci have been presented in the flow however the centres of the foci at the presented figures are not always stable in the right and left sides of the casing part of the suction chamber. Especially in the case 3 with ω_4 at 83.7 rad/s, the centres of the two foci are significantly changed, one of the centres of the focus is up and the other one is below, with the different phases of the gear teeth as shown in figures 22a and 22d. The magnitude of the velocity is increasing in the middle of the suction chamber by increasing the rotational velocity of the gear pump. Furthermore, the velocity is increased around gear teeth by increasing the rotational velocity while the area of increased velocity is expanding around the gear teeth.

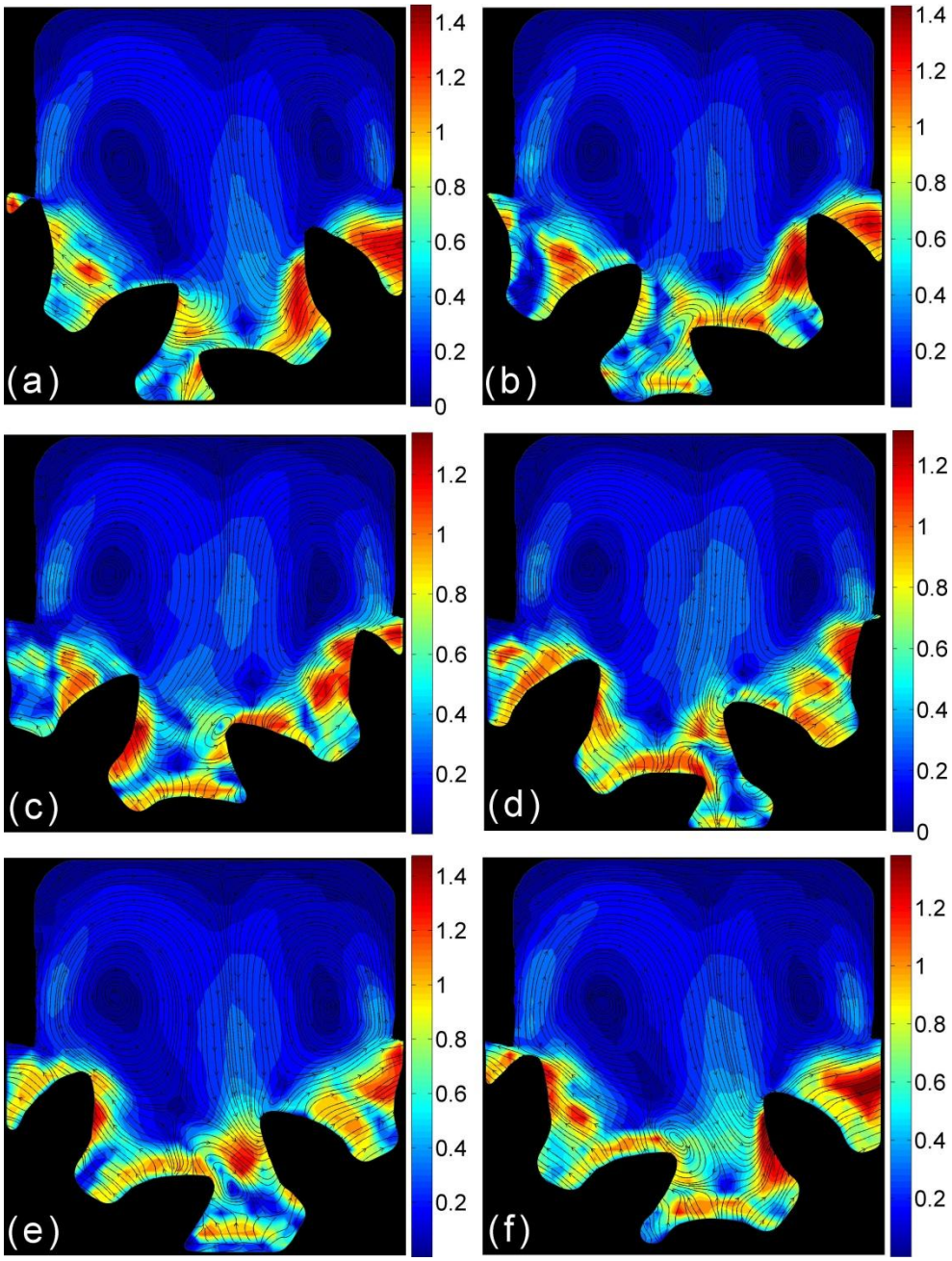

Figure 4.18. Velocity magnitude and 2D streamlines corresponding to sample of six ensemble averages equally distributed in time spanning of one full gearing period in the suction chamber for case 3 with ω_1, 52.3 rad/s, the averages at six consecutive times: (a) t_i, (b) $t_{i+\Delta t}$, (c) $t_{i+2\Delta t}$, (d) $t_{i+3\Delta t}$, (e) $t_{i+4\Delta t}$, (f) $t_{i+5\Delta t}$ where *i* refers to the initial sample.

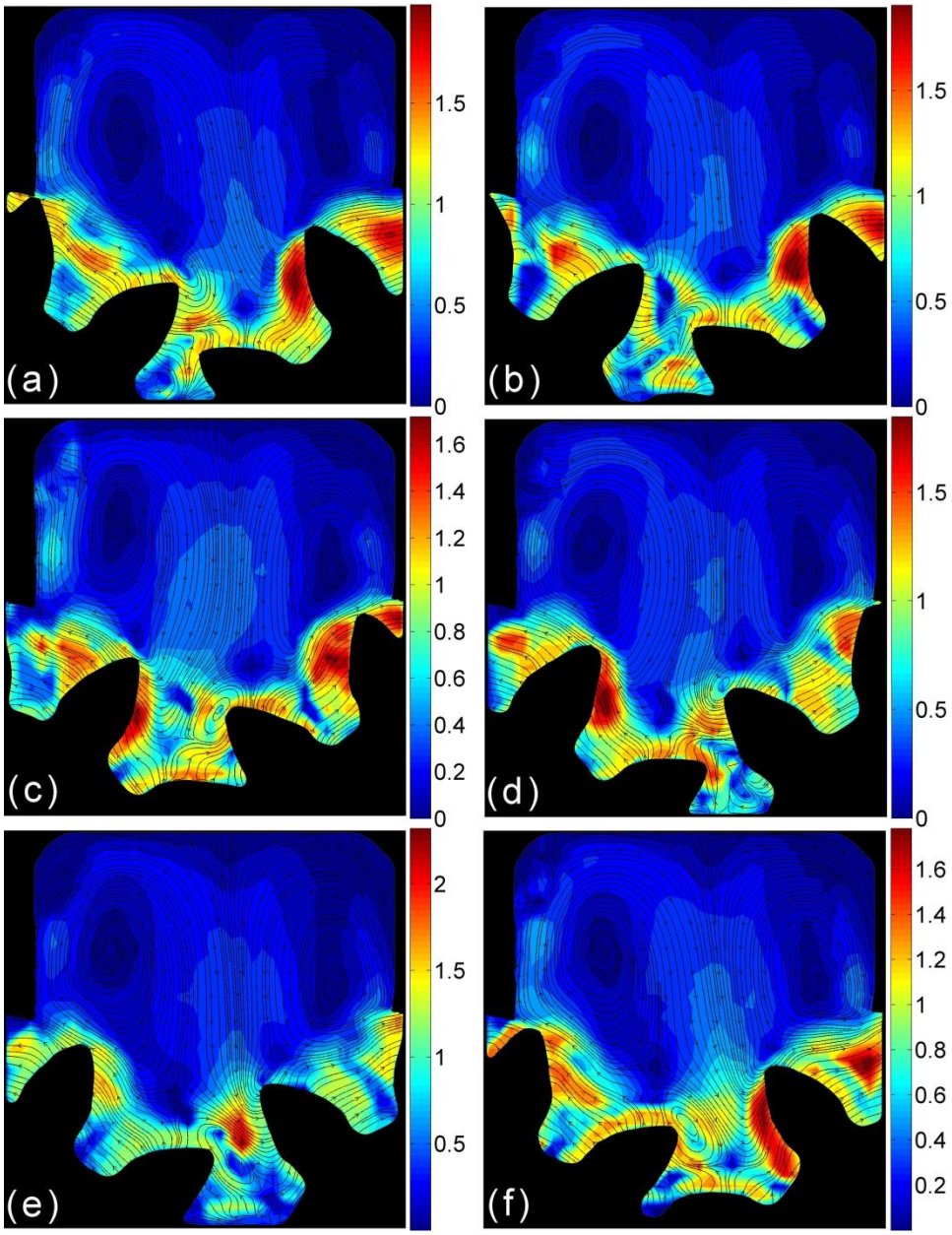

Figure 4.19. Velocity magnitude and 2D streamlines corresponding to sample of six ensemble averages equally distributed in time spanning of one full gearing period in the suction chamber for case 3 with ω_2, 62.8 rad/s, the averages at six consecutive times: (a) t_i, (b) $t_{i+\Delta t}$, (c) $t_{i+2\Delta t}$, (d) $t_{i+3\Delta t}$, (e) $t_{i+4\Delta t}$, (f) $t_{i+5\Delta t}$ where *i* refers to the initial sample.

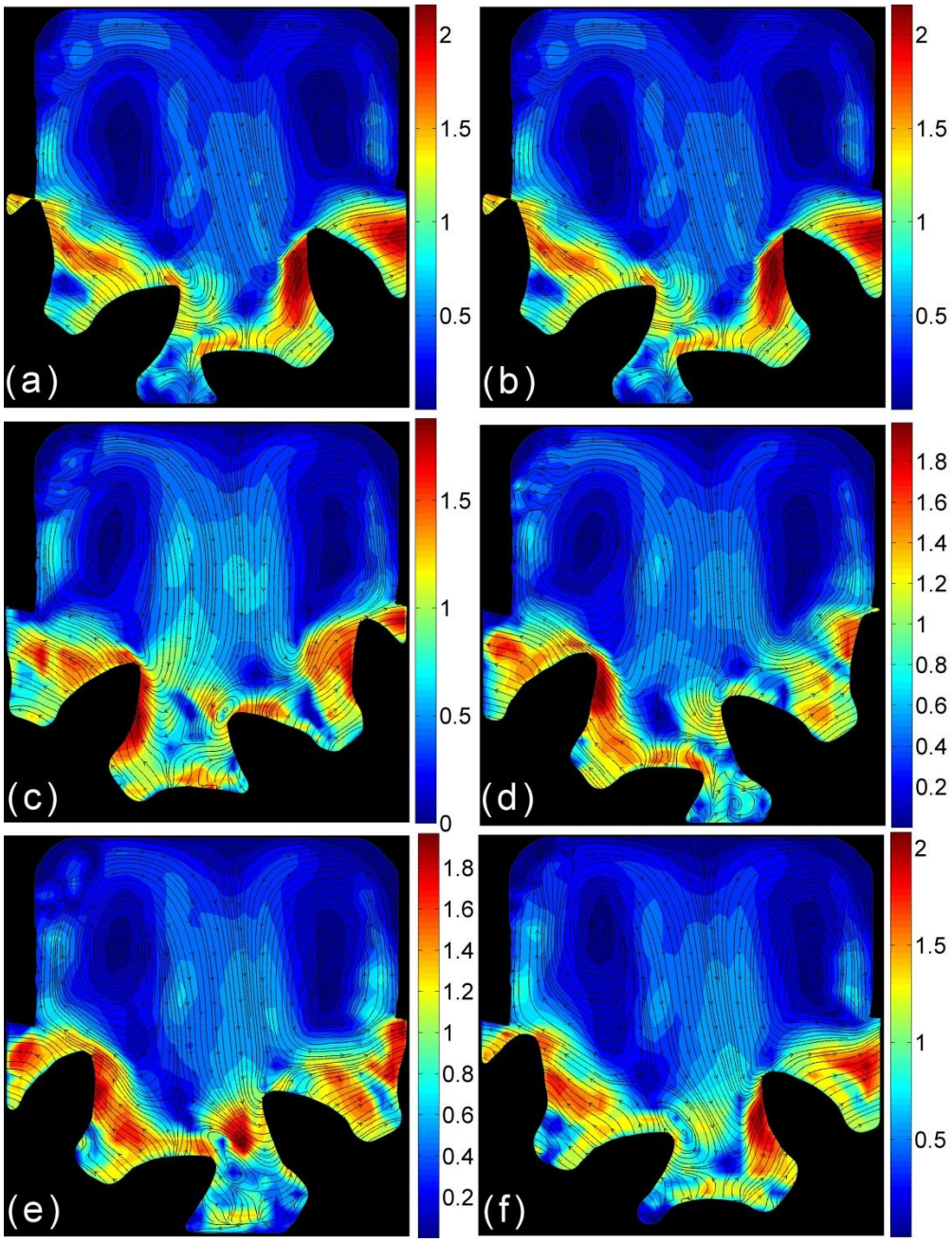

Figure 4.20. Velocity magnitude and 2D streamlines corresponding to sample of six ensemble averages equally distributed in time spanning of one full gearing period in the suction chamber for case 3 with ω_3, 72.3 rad/s, the averages at six consecutive times: (a) t_i, (b) $t_{i+\Delta t}$, (c) $t_{i+2\Delta t}$, (d) $t_{i+3\Delta t}$, (e) $t_{i+4\Delta t}$, (f) $t_{i+5\Delta t}$ where *i* refers to the initial sample.

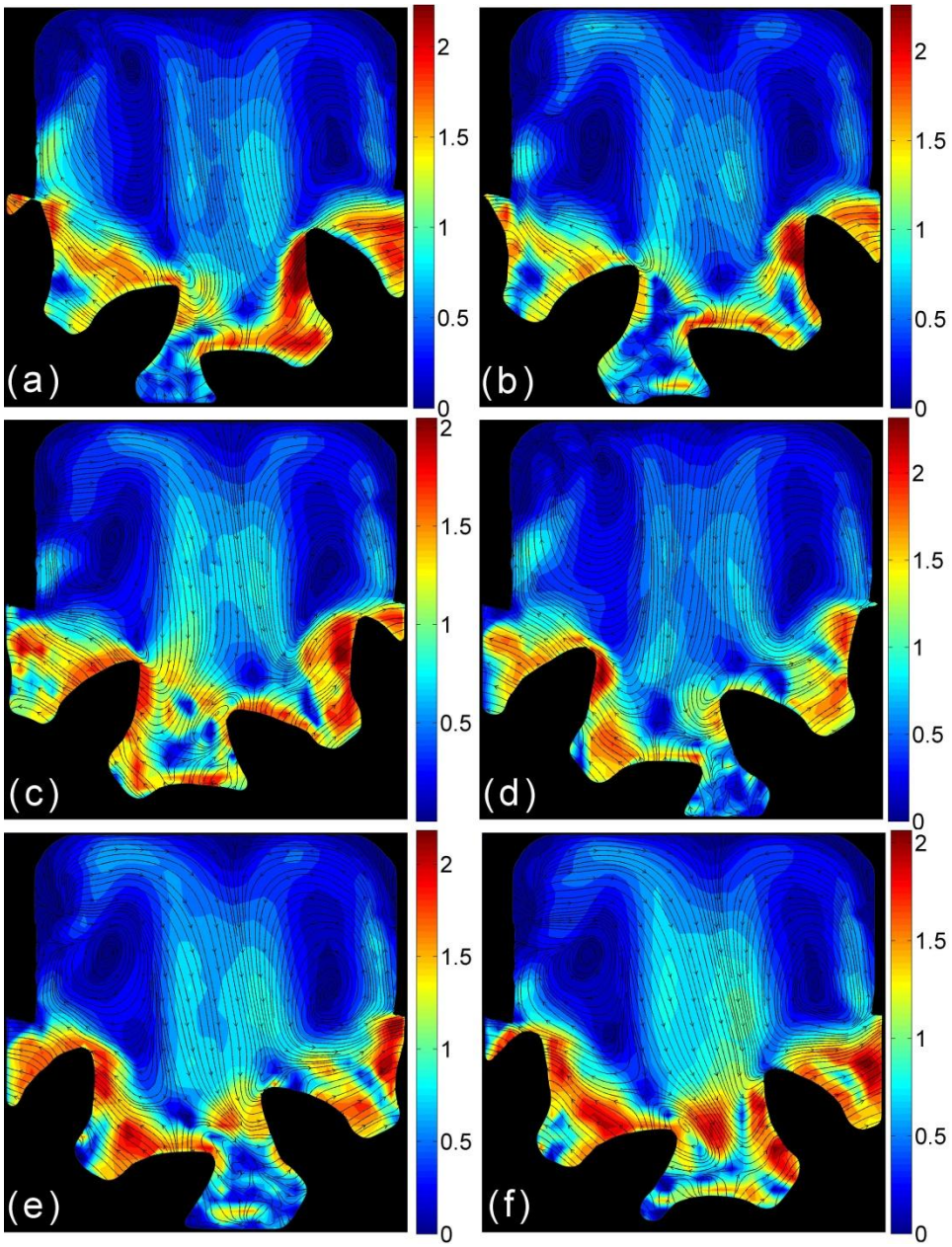

Figure 4.21. Velocity magnitude and 2D streamlines corresponding to sample of six ensemble averages equally distributed in time spanning of one full gearing period in the suction chamber for case 3 with ω_3, 83.7 rad/s, the averages at six consecutive times: (a) t_i, (b) $t_{i+\Delta t}$, (c) $t_{i+2\Delta t}$, (d) $t_{i+3\Delta t}$, (e) $t_{i+4\Delta t}$, (f) $t_{i+5\Delta t}$ where *i* refers to the initial sample.

Figures 4.22 and 4.23 show the velocity magnitude and the 2D streamlines of the consecutive phase-locked ensemble averages in the impulse chamber for case 5 with ω_1 52.3 and ω_2 83.7 rad/s, respectively as indicated in the Table 4.1. The ensembles represent the flow structures occurring in the impulse chamber for one gearing period. The two foci that dominate the flow in the suction chamber are not observed in the impulse chamber. The flow stacks on the corners of the below casing chamber through the outlet pipe where the flow carried out with high pressure. The two small foci that appear in the gearing zone move as the gear moves until they join the middle path of the right and left sides of the impulse chamber. They do not pass to the middle path of the impulse chamber. The dynamics of these foci are periodic. These two small foci appear when the gearwheel is opening the volume and impulsion the fluid (see the gear teeth positions in figure 4.7). One of the focus moves through the right and the other one moves to the left side of the impulse chamber. Then, they go out from the impulse chamber to the outlet pipe. The maximum velocity magnitude of the flow has been observed close to the gearing area and the middle right and left sides of the impulse chamber. Depending on the gear teeth positions, the velocity magnitude is changing with the movement of the gear teeth. The maximum velocity achieved is 1.6 m/s for the case 5 with ω_1 52.3 rad/s and 2.3 m/s for the case 5 with ω_2 83.7 rad/s as shown in figures 4.22 and 4.23, respectively. It has been observed that the fluid goes out through the pipe with more stable velocity magnitude in the figure 4.23 than the figure 4.22. This may be related to the time necessary to carry out of the small foci through the middle path in the impulse chamber to the outlet pipe.

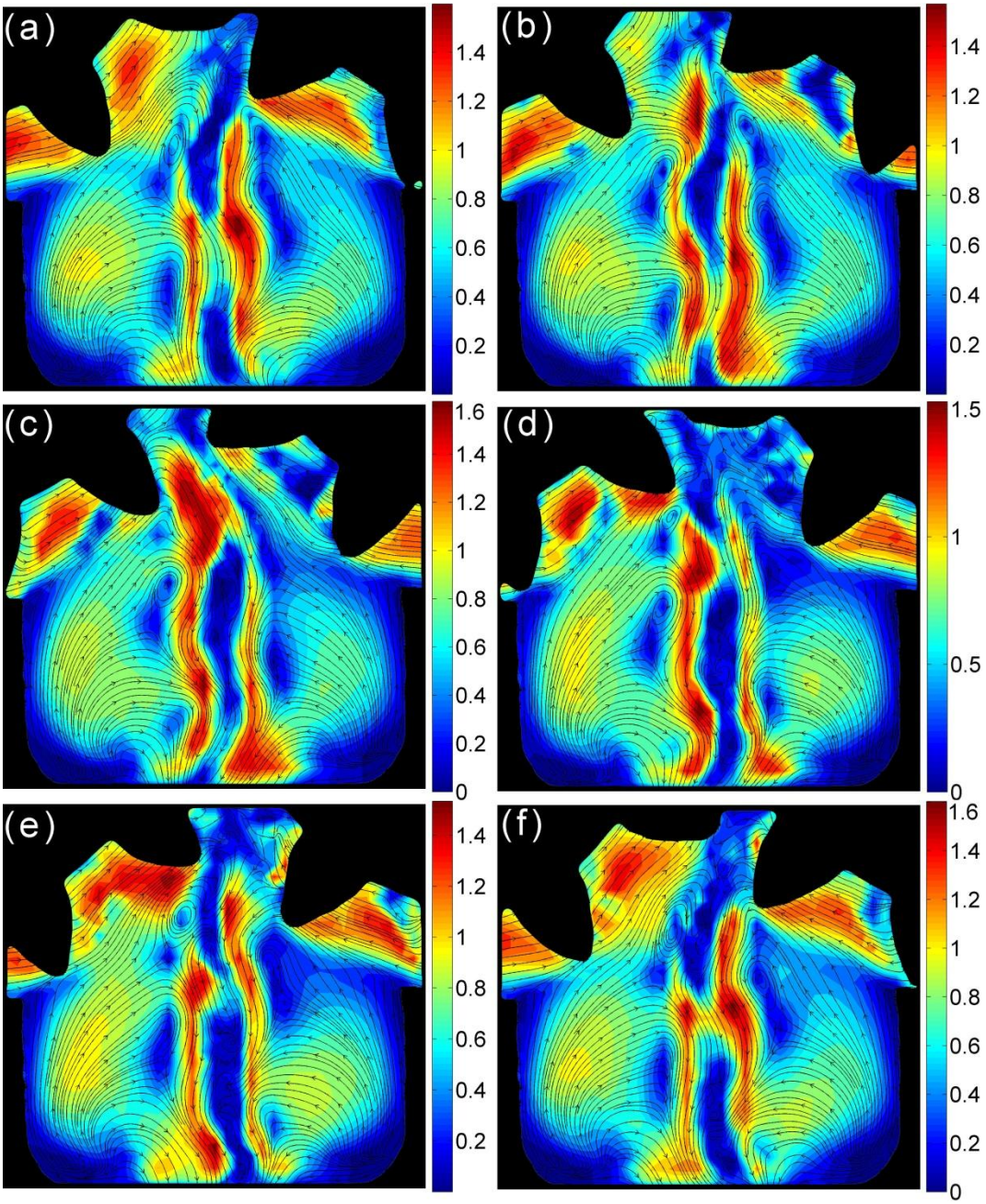

Figure 4.22. Velocity magnitude and 2D streamlines corresponding to sample of six ensemble averages equally distributed in time spanning of one full gearing period in the impulse chamber for case 5 with ω_1, 52.3 rad/s, the averages at six consecutive times: (a) t_i, (b) $t_{i+\Delta t}$, (c) $t_{i+2\Delta t}$, (d) $t_{i+3\Delta t}$, (e) $t_{i+4\Delta t}$, (f) $t_{i+5\Delta t}$ where *i* refers to the initial sample.

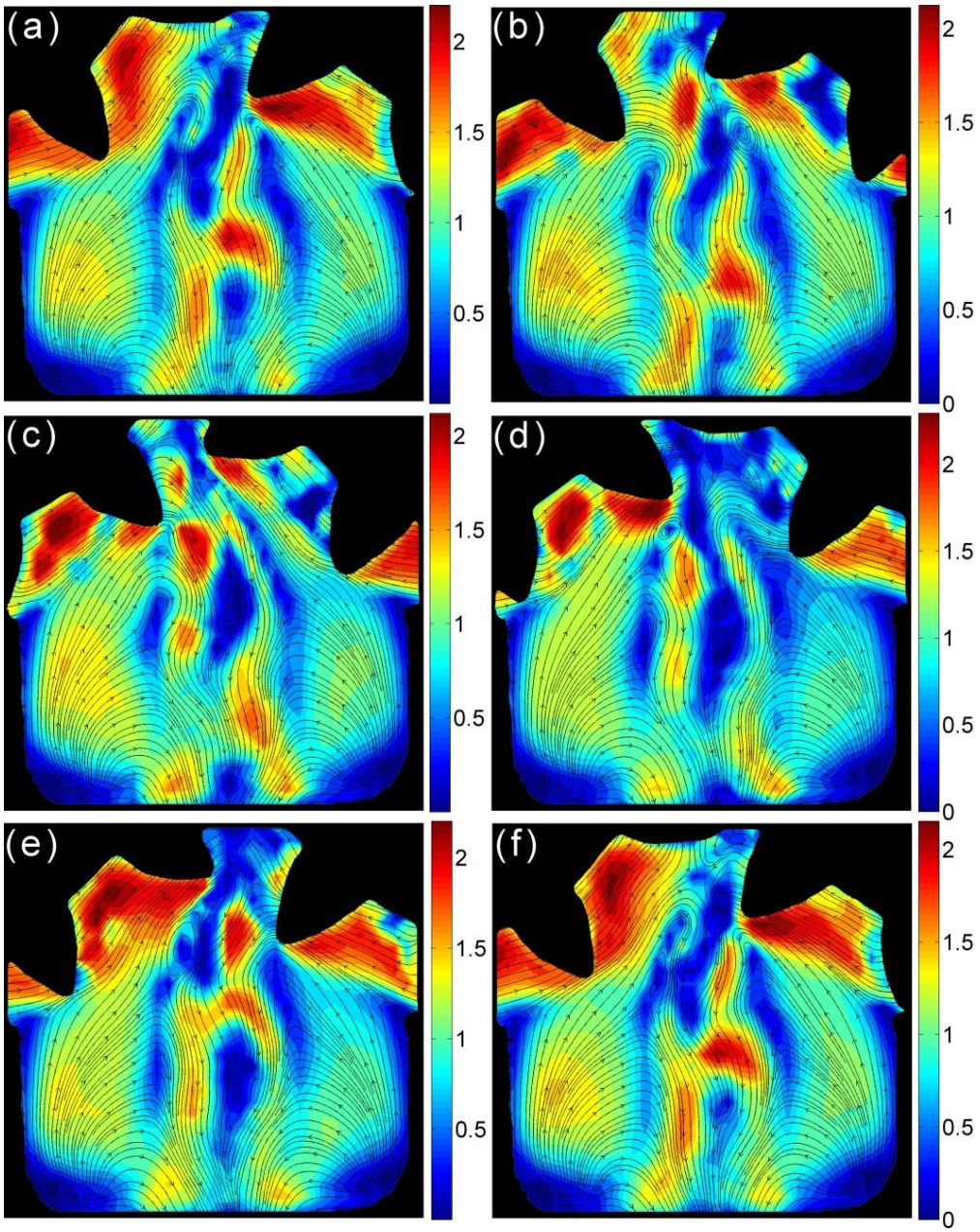

Figure 4.23. Velocity magnitude and 2D streamlines corresponding to sample of six ensemble averages equally distributed in time spanning of one full gearing period in the impulse chamber for case 5 with ω_2, 83.7 rad/s, the averages at six consecutive times: (a) t_i, (b) $t_{i+\Delta t}$, (c) $t_{i+2\Delta t}$, (d) $t_{i+3\Delta t}$, (e) $t_{i+4\Delta t}$, (f) $t_{i+5\Delta t}$ where *i* refers to the initial sample.

The vertical plane analysis in the suction chamber has been realized with different rotational velocities of the gear pump as indicated in Table 4.1 for the case 4 with ω_1 52.3 rad/s and ω_2 83.7 rad/s. Although the design of the gear pump has been arranged for the PIV analysis of the x-y plane of the suction chamber, some experiments have been realized in order to identify the flow structures in the vertical x-z plane. The original PIV image is shown in figure 4.24a. The PIV measurements were not able to record all the region of interest area of x-z plane due to the specific design of the suction chamber. For this reason, it has been considered only the flow area where the flow passing across to the gear teeth. The corresponding velocity vectors of the middle x-z plane for the case 4 with ω_1=52.3 and ω_2=83.7 rad/s are presented in the figures 25b and 25c, respectively. For the PIV analysis to extract the velocity displacement, it has been used 32x32 interrogation area for case 4 with ω_1 where the spatial resolution has been found enough to obtain the velocity field. On the other hand, at high speed of the gear pump, that is the case 4 with ω_2, 48x48 interrogation area has been found enough to obtain the velocity field.

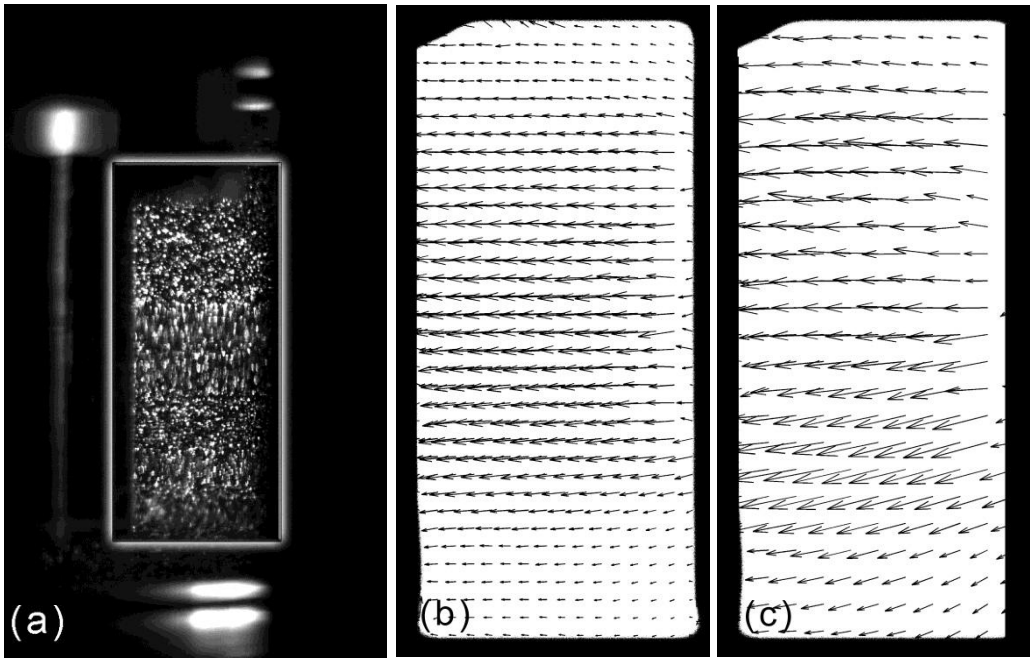

Figure 4.24. Middle vertical planes of the suction chamber of the velocity field results for different rotational velocity of the gear pump for case 4: (a) original PIV image; (b) ω_1=52.3, interrogation area 32x32 pixels; (c) ω_2=83.7, interrogation area 48x48 pixels.

Figures 4.25 and 4.26 show the velocity magnitude and the 2D streamlines of the consecutive phase-locked ensemble averages in the x-z plane of the suction chamber for case 4 with ω_1=52.3 and ω_2=83.7 rad/s, respectively as indicted in the Table 4.1. The six ensembles that are shown in that figure represent the flow structures occurring in the suction chamber for one gearing period. When the rotational velocity of the gear pump is at 52.3 rad/s, the maximum magnitude of the velocity is accumulated in the middle of the x-z plane of the suction chamber. However, the maximum velocity is dispersed on the right and left sides of the x-z plane of the suction chamber when the rotational velocity is 83.7 rad/s. The direction of the flow is the same for all cases and is straight on from the inlet to the gear teeth area. This flow direction corresponds to the two big foci that appeared in the x-y plane of the suction chamber.

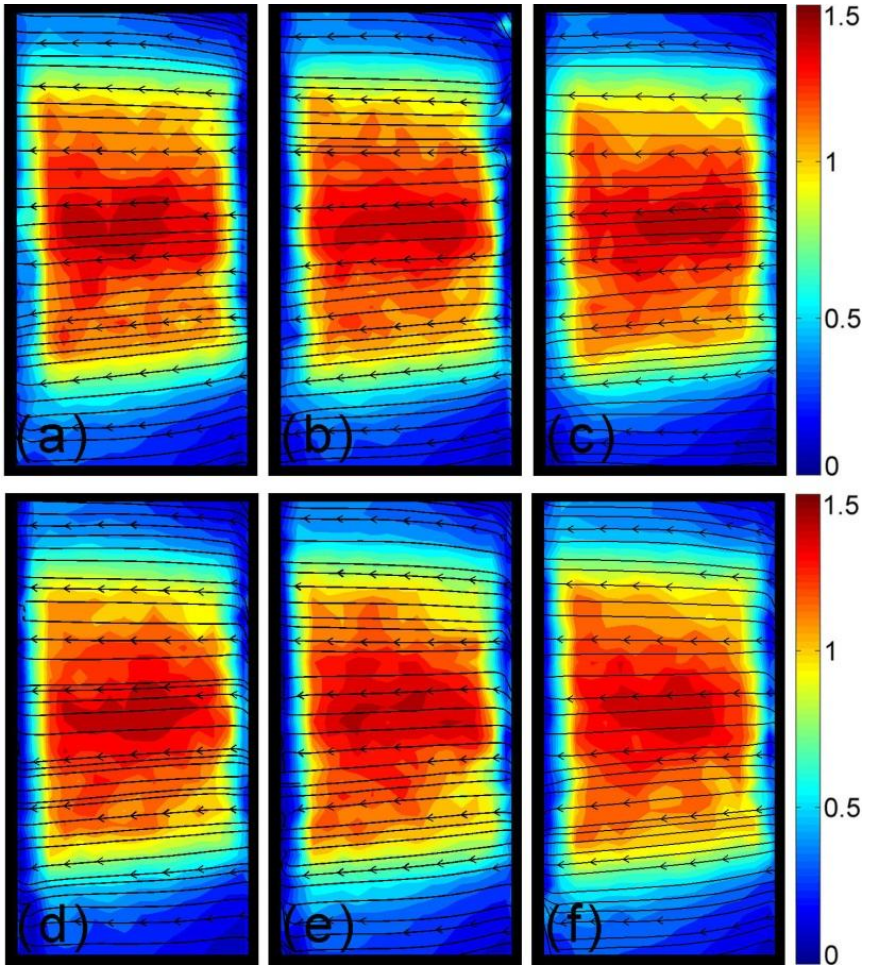

Figure 4.25. Velocity magnitude and 2D streamlines corresponding to sample of six ensemble averages equally distributed in time spanning of one full gearing period in the x-z plane of the suction chamber for case 4 with ω_1, 52.3 rad/s, the averages at six consecutive times: (a) t_i, (b) $t_{i+\Delta t}$, (c) $t_{i+2\Delta t}$, (d) $t_{i+3\Delta t}$, (e) $t_{i+4\Delta t}$, (f) $t_{i+5\Delta t}$ where *i* refers to the initial sample.

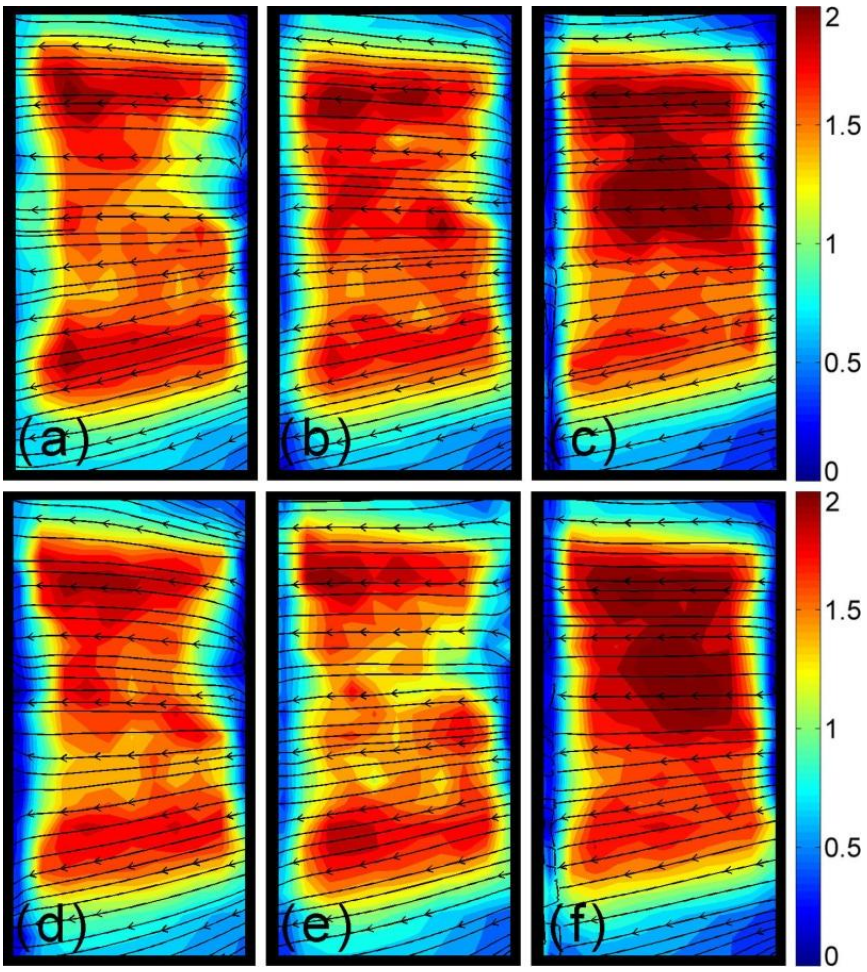

Figure 4.26. Velocity magnitude and 2D streamlines corresponding to sample of six ensemble averages equally distributed in time spanning of one full gearing period in the x-z plane of the suction chamber for case 4 with ω_2, 83.7 rad/s, the averages at six consecutive times: (a) t_i, (b) $t_{i+\Delta t}$, (c) $t_{i+2\Delta t}$, (d) $t_{i+3\Delta t}$, (e) $t_{i+4\Delta t}$, (f) $t_{i+5\Delta t}$ where *i* refers to the initial sample.

4.4.2.2 Vorticity and velocity fields

In this sub-section, experimental cases using the different rotational velocities of the gear pump and the different gear phases have been compared in order to identify the vortex in the flow field. The vorticity and velocity flow field has been obtained for the suction and impulse chambers. Figures 4.27 and 4.28 show the vorticity and velocity results of the suction chamber for case 3 with ω_1=52.3 rad/s and ω_4=83.7 rad/s. These flow fields correspond to those depicted in figures 4.19 and 4.22 respectively that show the streamlines. Even that the stream lines show the existence of two big foci in the suction chamber, the vorticity and velocity vectors show that they are not as strong as they seems. The vorticity is significantly larger close to the gear teeth. The absolute value of the vorticity is increased for the case 3 with ω_4=83.7 rad/s around the gear teeth.

Figures 4.29 and 4.30 show the vorticity and velocity results of the impulse chamber for case 5 with ω_1=52.3 rad/s and ω_2=83.7 rad/s. In the impulse chamber, it has been observed that the vorticity is significantly evident close to the gear teeth and additionally in the middle of the impulse chamber all the flow path through the direction of the outlet pipe. The same situation as case 3, the absolute value of the vorticity is increased for the case 5 with ω_4=83.7 rad/s around the gear teeth.

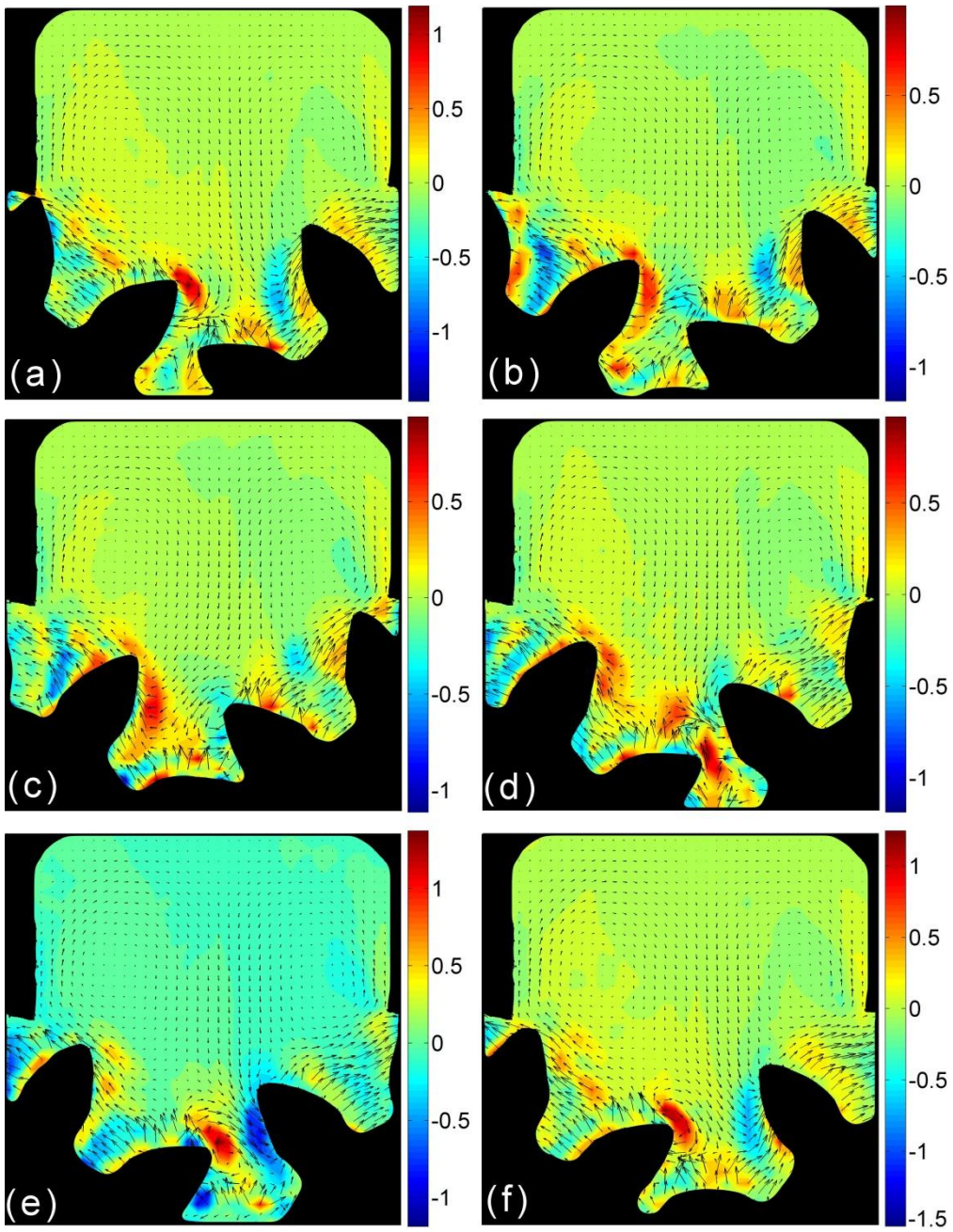

Figure 4.27. Vorticity and velocity fields corresponding to sample of six ensemble averages equally distributed in time spanning of one full gearing period in the suction chamber for case 3 with ω_1, 52.3 rad/s, the averages at six consecutive times: (a) t_i, (b) $t_{i+\Delta t}$, (c) $t_{i+2\Delta t}$, (d) $t_{i+3\Delta t}$, (e) $t_{i+4\Delta t}$, (f) $t_{i+5\Delta t}$ where *i* refers to the initial sample.

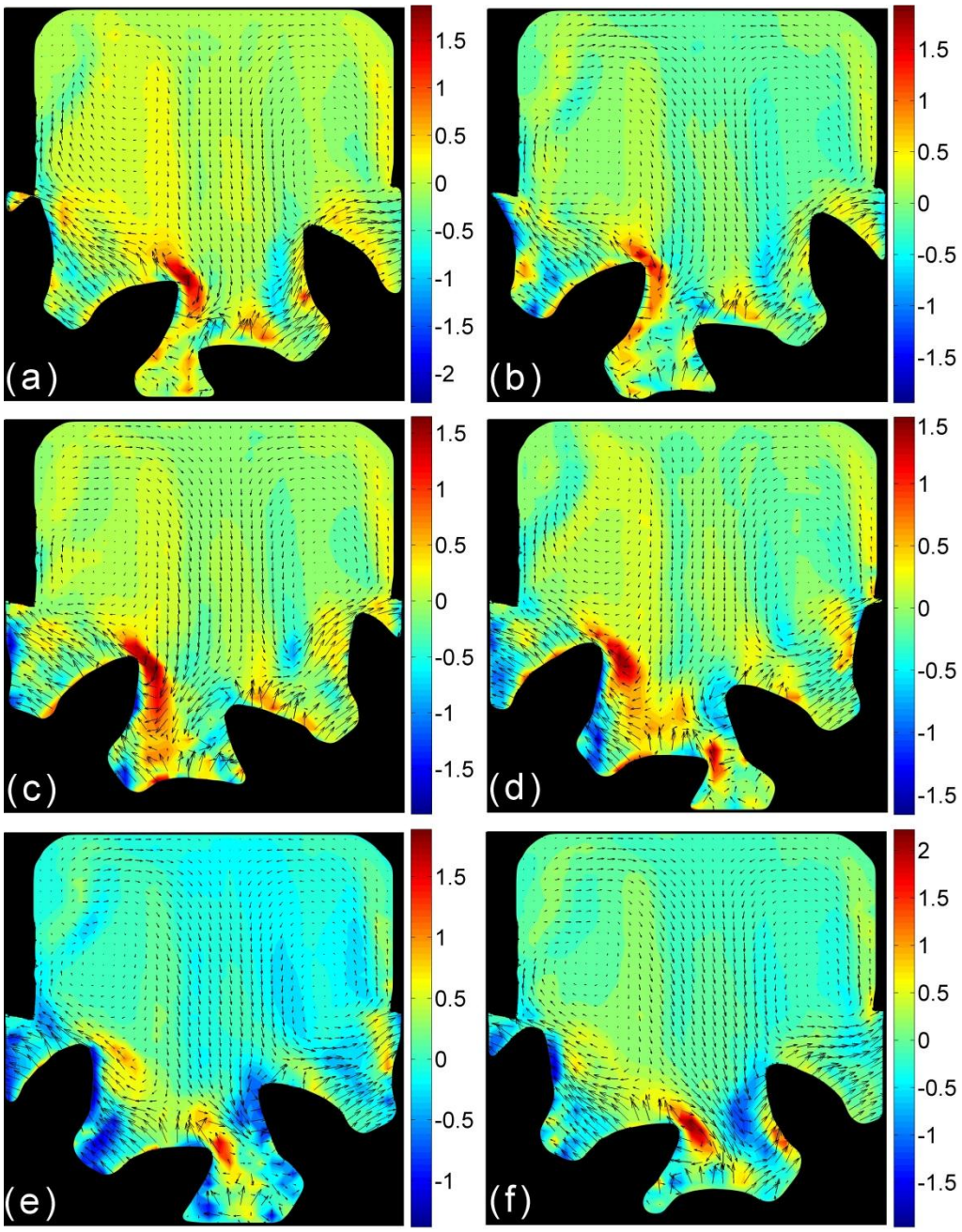

Figure 4.28. Vorticity and velocity fields corresponding to sample of six ensemble averages equally distributed in time spanning of one full gearing period in the suction chamber for case 3 with ω_4, 83.7 rad/s, the averages at six consecutive times: (a) t_i, (b) $t_{i+\Delta t}$, (c) $t_{i+2\Delta t}$, (d) $t_{i+3\Delta t}$, (e) $t_{i+4\Delta t}$, (f) $t_{i+5\Delta t}$ where *i* refers to the initial sample.

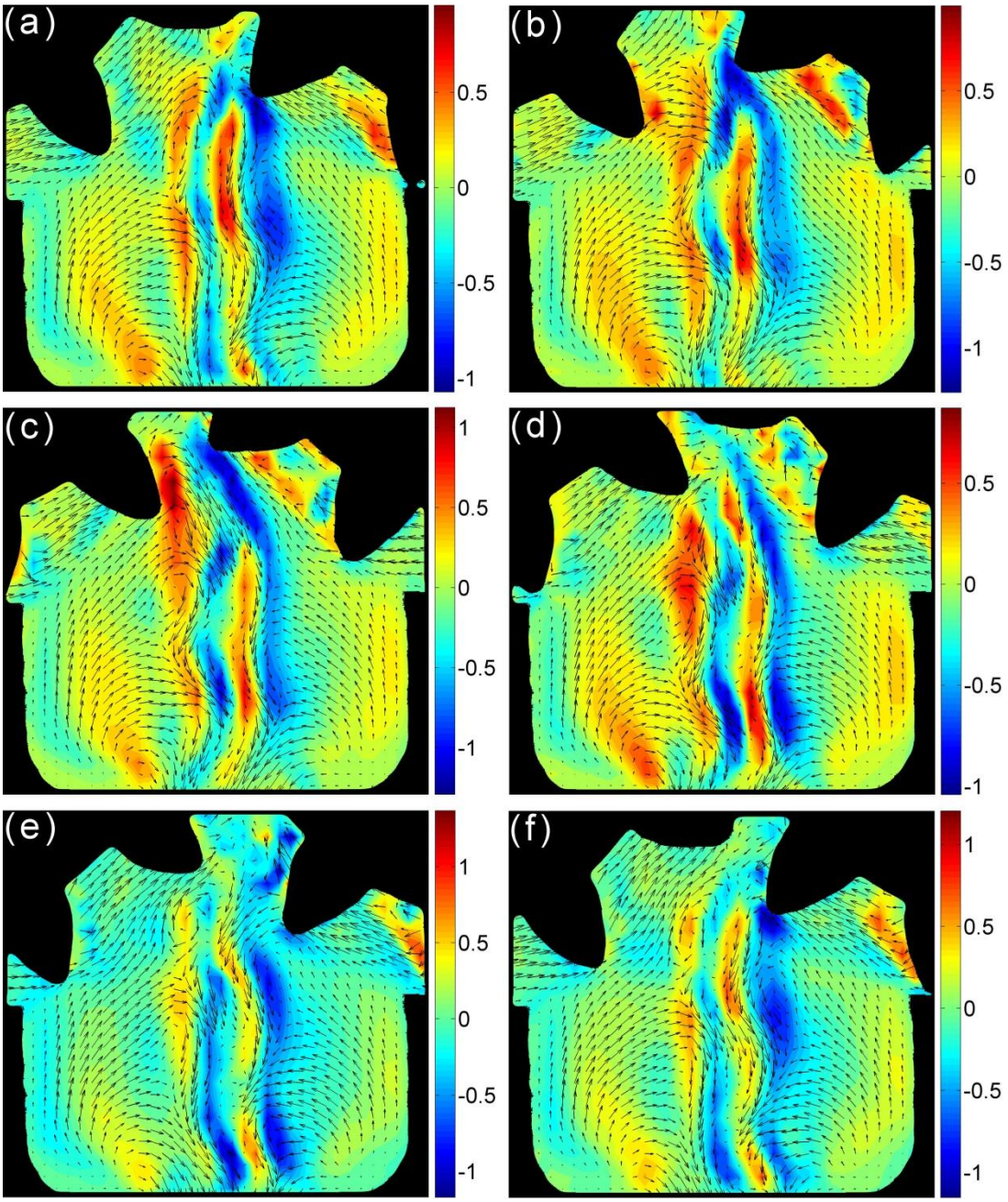

Figure 4.29. Vorticity and velocity fields corresponding to sample of six ensemble averages equally distributed in time spanning of one full gearing period in the impulse chamber for case 5 with ω_1, 52.3 rad/s, the averages at six consecutive times: (a) t_i, (b) $t_{i+\Delta t}$, (c) $t_{i+2\Delta t}$, (d) $t_{i+3\Delta t}$, (e) $t_{i+4\Delta t}$, (f) $t_{i+5\Delta t}$ where *i* refers to the initial sample.

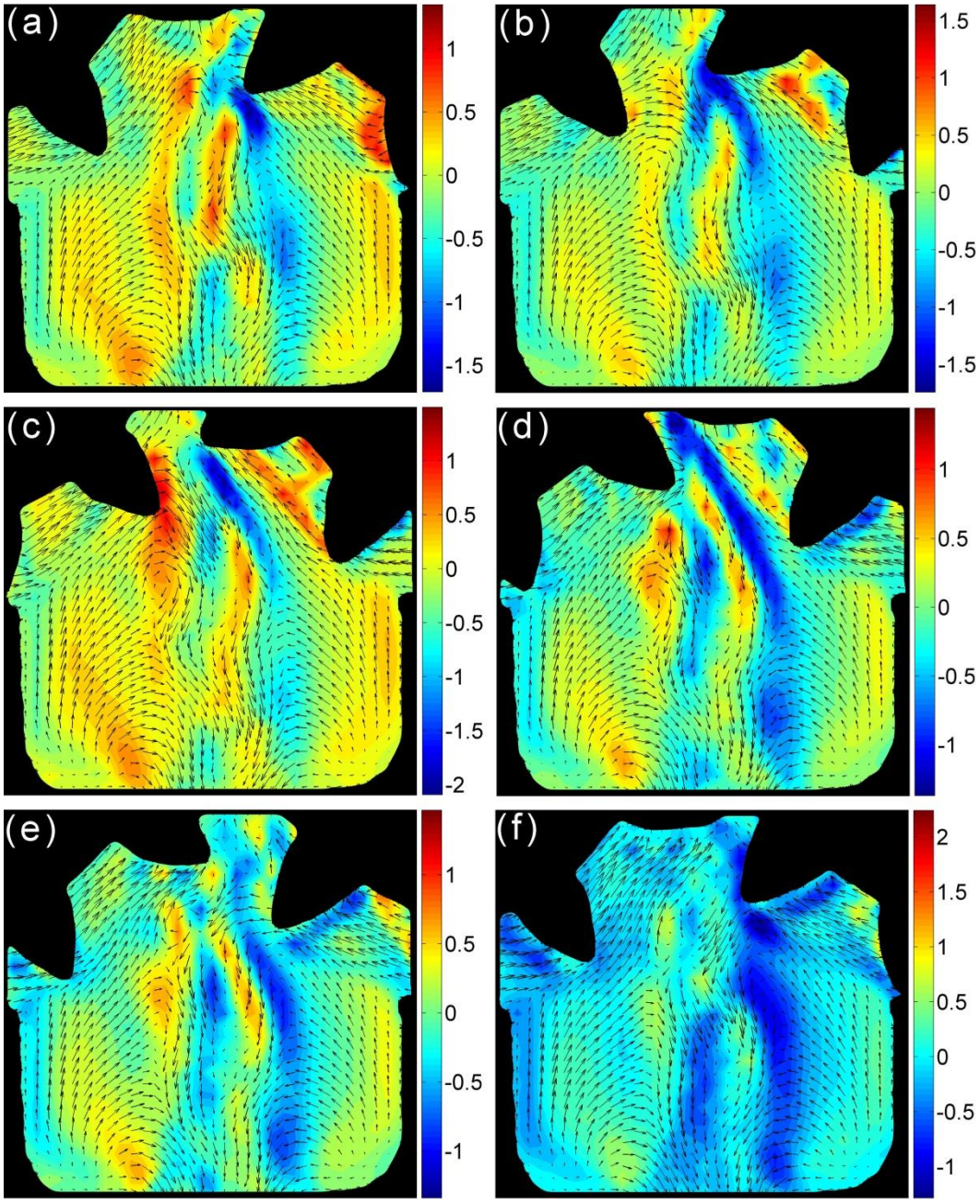

Figure 4.30. Vorticity and velocity fields corresponding to sample of six ensemble averages equally distributed in time spanning of one full gearing period in the impulse chamber for case 5 with ω_2, 83.7 rad/s, the averages at six consecutive times: (a) t_i, (b) $t_{i+\Delta t}$, (c) $t_{i+2\Delta t}$, (d) $t_{i+3\Delta t}$, (e) $t_{i+4\Delta t}$, (f) $t_{i+5\Delta t}$ where *i* refers to the initial sample.

4.4.2.3 Small-scale characteristics and turbulence statistics

The main objective of this section is to estimate the turbulent scales of the fluid flow in the suction chamber of the external gear pump. Special attention is given to the study of the assumptions needed to estimation the dissipation rate from two-dimensional PIV measurements and to the influence of the measurement of the spatial and temporal resolution of the PIV data.

In the present study, the spatial characteristics of the flow have been obtained by two point auto correlation functions as explained in detail in Chapter 2. The main experimental cases used in this sub-section are Case 3 and Case 6 with ω_1 (Table 4.1). The spatial resolution of the PIV data used is specified in Table 4.2 where the different sub-cases considered and their conditions are summarized. The aim is to analyze the changes in turbulent statistics by using different interrogation areas to establish the goodness of the PIV technique when scale parameters need to be evaluated. Table 4.2 shows the dimensions of the image, the spatial resolutions of the image, the six different interrogation areas. Sub-case 7 corresponds to the gearing area in the x-y plane with high spatial resolution.

Table 4.2. Experimental sub-case studies: size of the image and interrogation areas used and spatial resolution of the PIV measurements

Sub-case	Image area (mm)	Spatial resolution (mm/pixel)	Interrogation area (pixels)
1	55.1 × 46.1	0.066	64×64
2	55.1 × 46.1	0.066	56×56
3	55.1 × 46.1	0.066	48×48
4	55.1 × 46.1	0.066	32×32
5	55.1 × 46.1	0.066	24×24
6	55.1 × 46.1	0.066	16×16
7	24.6×24.46	0.023	64×64

Based upon the mean dissipation in the gear pump, the average Kolmogrov length scale along the line A (see figure 4.7) is estimated to be about 0.237 mm by using Eq. 2.6 and Eq. 2.8 and 0.250 by using Eq. 2.7 and Eq. 2.8 (see Chapter 2) by using a 32×32 pixel interrogation area. The dissipation in the gearing area is known to be considerably larger than the mean dissipation in the gear area, so in order to be fully resolved in the gearing area, the spatial resolution should be better than approximately 0.25 mm. Thus the resolution in this study is 3.78 times larger than the average Kolmogorov length scale η for experimental sub-cases. Thus, spatial resolution of the present PIV experiments has been found enough to estimate the dissipation rate for the turbulent analysis. However, different techniques can be applied to the external gear pump flow to estimate the dissipation rate for future studies.

Length scale characteristics for different experimental cases are indicated in Table 4.3. The values have been computed using the autocorrelation function, R_{yy}, along the Line A indicated in figure 4.7. It has been estimated by using approximately 240 instantaneous phase averages velocity vectors from a four series of the experiments. The turbulent length scales show that there is a relation between the length scales as *spatial resolution*< λ_T< l_L.

Table 4.3. Summary of turbulent length scale characteristic of the flow in the Line A for different experimental cases

Sub-case	λ_T (mm)	I_L (mm)
1	3.2	4.9
2	3.7	5.7
3	3.8	6.0
4	5.3	10.3
5	5.3	11.5
6	5.2	10.9

The turbulent time scale characteristic of the flow has been calculated in the point P (see figure 4.7) for a time of one gear phase rotation, Δt_{period} = 0.011 s. Necessary time

difference can be taken from the ensemble averages of the gear phases due to periodic flow. For all experimental sub-cases, frequency rate has been taken as 3000 fps. The average Kolmogorov time scale, τ_η, in the point P has been calculated nearly 0.018 s by using Eq. 2.6 and Eq. 2.9 and 0.022 by using Eq. 2.7 and Eq. 2.9 by using a 32×32 pixel interrogation area. Hence, the temporal resolution of the experimental images has been found 2 times larger than the Kolmogorov time scale that has been estimated using Eq. 2.7 and Eq. 2.9 in the point P for a one gear phase rotation time. The spectral density of energy is shown in figure 4.31 where the measurements have been done in the point P for the experiment sub-case 4 with 32x32 pixels interrogation area. The slope of -5/3 corresponding to Kolmogorov's law is shown for the purpose of comparison.

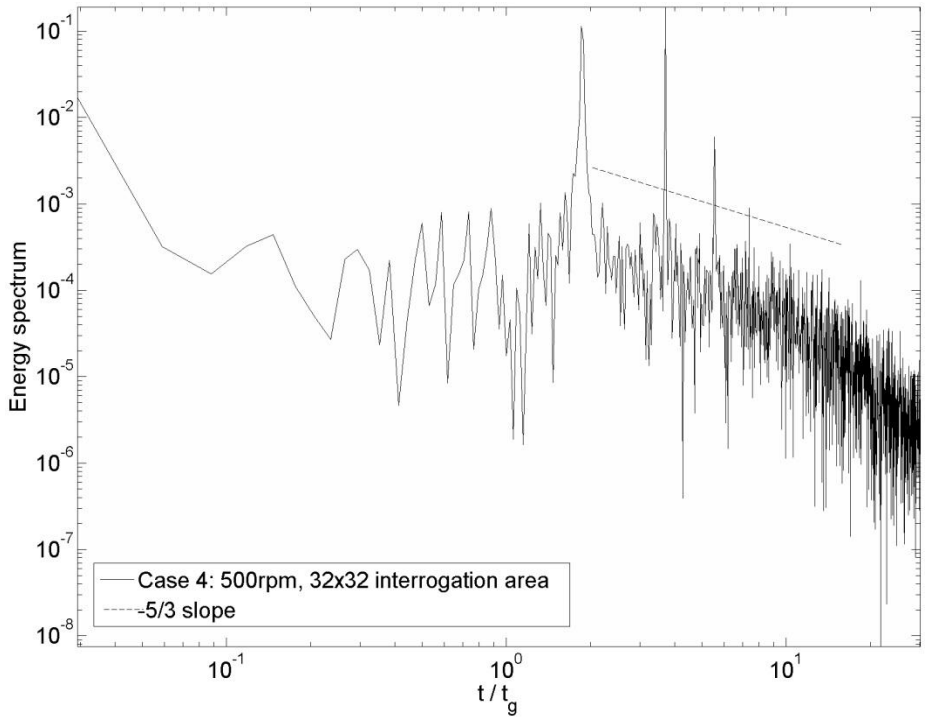

Figure 4.31. Energy spectrum versus frequency in the point P for sub-case 4 with 32x32 pixels interrogation area, frequency has been normalized by the frequency of one phase gear rotation.

The evolution of the predicted integral and Taylor length scales for the experiment sub-case 4 during one phase gear rotation is shown in figure 4.32. It can be seen that the turbulence length scales vary slowly during one gear phase rotation: when the volume of

the suction chamber is open (i.e. when the left gear tooth leaves the suction chamber), the Taylor and the integral length scales increase suddenly. After this increase λ_T and I_L fluctuate around large values to decrease back at the end of the phase.

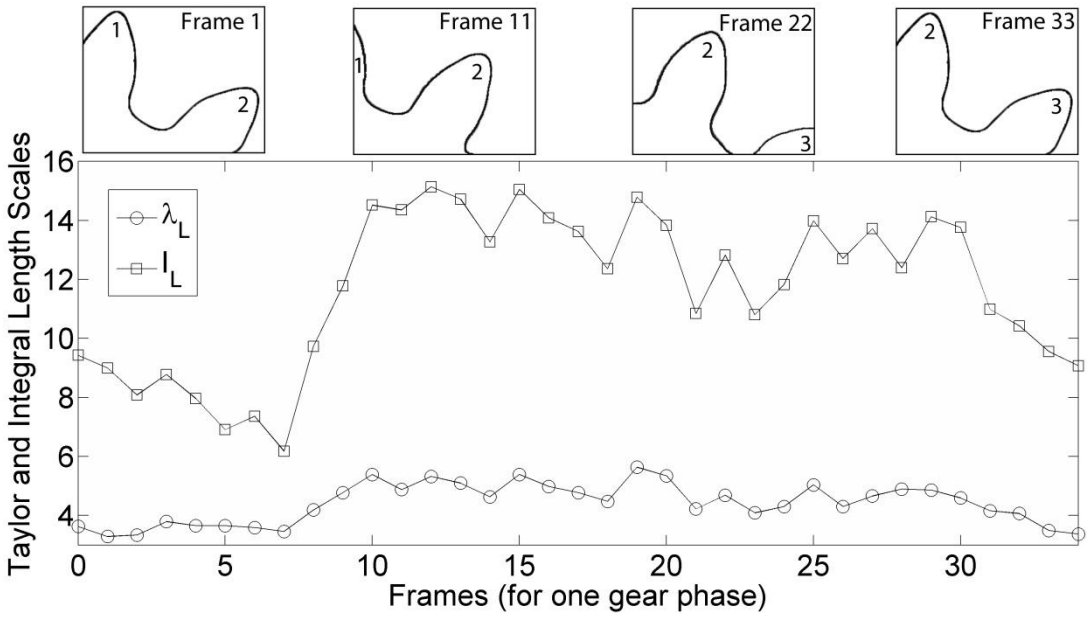

Figure 4.32. Evolution of the integral and Taylor length scales for sub-case 4 with 32x32 pixels interrogation area, time has been normalized by time of one gear phase rotation.

Experimental sub-cases using the same PIV images have been compared in order to identify any small-scale vortex in the flow field. LFC PIV method has been used with Triple Image Correlation for different spatial resolution levels. All the velocity vectors have been overlapped by 50% of interrogation area size for every spatial resolution level. Figure 4.33 shows the PIV results of the suction chamber of an external gear pump flow at four different spatial resolution levels from the same series of PIV images. Rotational velocity of the pump is 52.3 rad/s and ensemble averaged velocity fields have been obtained for a one phase gear position. Four spatial resolution levels of interrogation area sizes are defined as 64 × 64 pixels (Figure 4.33a), 56 × 56 pixels (Figure 4.33b), 48 × 48 pixels (Figure 4.33c) and 32 × 32 pixels (Figure 4.33d) respectively. The PIV result at the first spatial resolution level is very smooth and only big vortices (upside from the gearing

area on the left and right sides) can be seen in the flow field (see figure 4.33a). When the spatial resolution level is improved to the second level, some smaller vortices and turbulence structures which were filtered out in the first spatial resolution level can be found in the PIV velocity field (see Figure 4.33b). As the spatial resolution level is improved further to the third and fourth level (see figures 34c and 34d) more velocity vectors can be obtained and more small scale vertical and turbulent structures can be seen clearly in the PIV results. Especially, small vortices become clearer close to the gearing area.

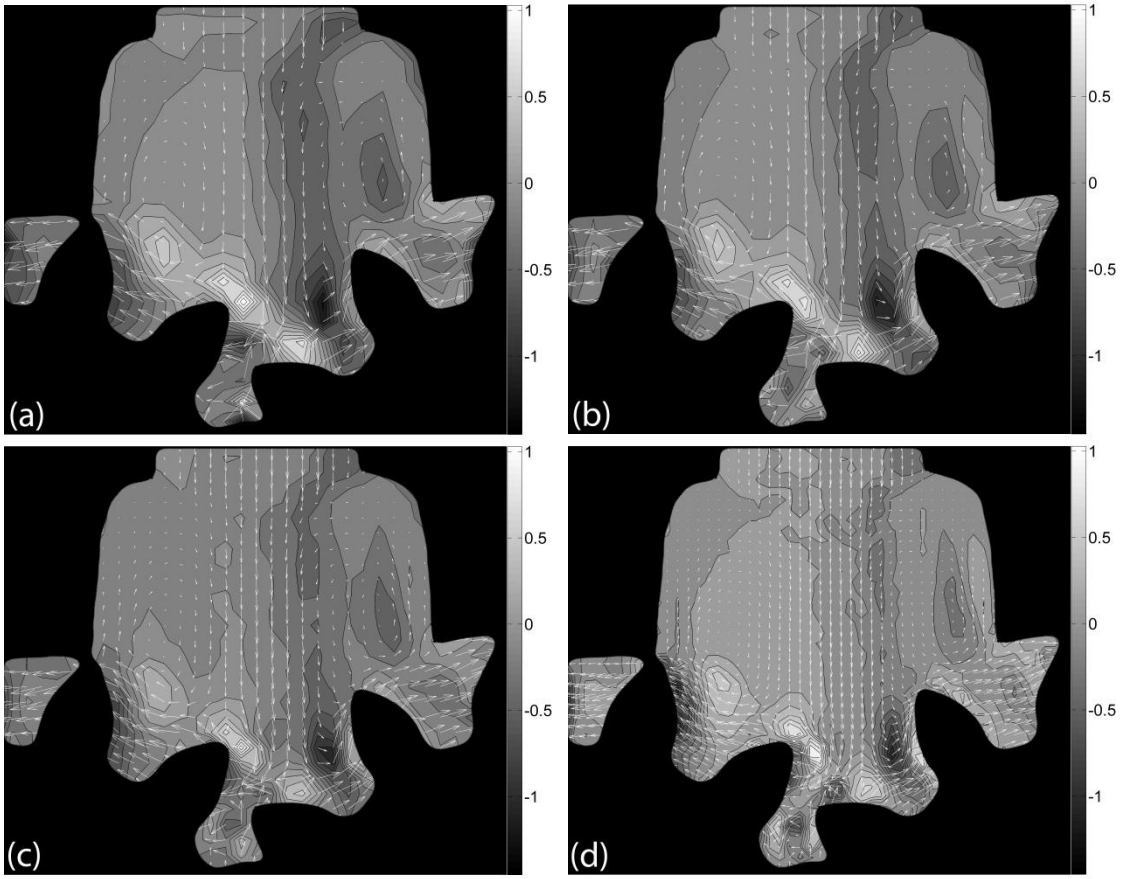

Figure 4.33. Velocity field with contours of vorticity of the suction chamber of the external gear pump with different spatial resolution levels at interrogation areas of: (a) 64 × 64 pixels; (b) 56 × 56 pixels; (c) 48 × 48 pixel; (d) 32 × 32 pixels.

A quantitative comparison of the PIV results at different spatial resolution levels has been shown in the figure 4.34, which are the streamwise and spanwise velocity profiles along line A. The velocity profile at the first spatial resolution level with 64x64 pixel interrogation area is found to be less resolution since turbulence components less than interrogation area sizes are filtered out.

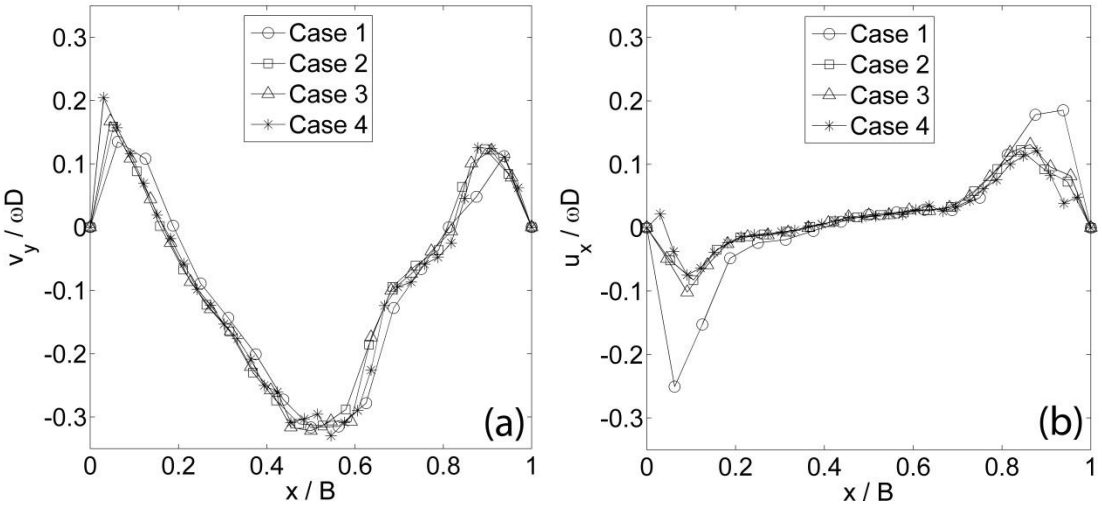

Figure 4.34. Velocity profiles in the suction chamber with different spatial resolution levels: (a) streamwise velocities; (b) spanwise velocities.

4.4.2.4 Flow structure near the gear teeth

In order to demonstrate the effect of the image resolution, PIV experiments have been done only focusing on the gearing area by using extension tubes (65 mm) attached to the high speed digital camera. In sub-case 7, higher image resolution has been used for the velocity field estimation. The original PIV image area is shown in figure 4.35a. PIV image analysis has been done by using LFC PIV method with triple image correlation for different spatial resolution levels in order to the estimate velocity and vorticity field. It has been found that as the interrogation area with a 64x64 pixels gives accurate results as shown in figure 4.35b. One of the reasons to use the 64x64 pixels interrogation area is the adequate number of particles for interrogation area. This can be overcome by using

smaller tracer particles; it is difficult to obtain a good homogeneity of the particles into the high viscosity flows. Another reason to use a relatively large interrogation area is due to the fact is that the smaller interrogation area produces more spurious vectors near the rotating gear teeth. The insufficient data of the gear tooth area causes too many noise peaks in the correlation space. However, using larger interrogation area size such as 64x64 prevents to obtain spurious vectors close to the gear teeth areas.

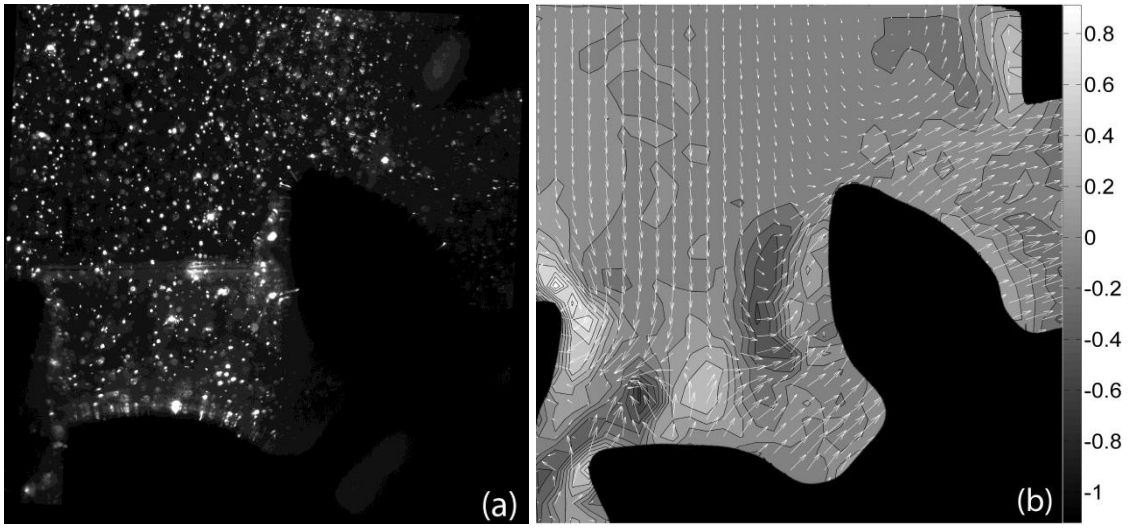

Figure 4.35. 1056x1048 pixels image resolution PIV experiments close to the gearing area for sub-case 7: (a) original PIV image; (b) velocity field with contours of vorticity by using 64x64 pixels interrogation area size.

The averaged Taylor length scale and the integral scale over the fluid region for sub-case 7 have been found about 5.06 and 10.92 mm, respectively. The average Kolmogorov length scale has been estimated as 0.47mm using the Eq. 2.6 and 0.53mm using the Eq. 2.7. The spatial resolution of the measurement, 0.023mm is approximately 23 times smaller than η value by Eq. 2.7 and 20 times smaller than η value by Eq. 2.6. Under these conditions, the velocity data allows the calculations of the dissipation rate of the flow field.

For the sub-case 4, 2048 instantaneous images have been obtained for each series. 60 phase-averaged images per each series have been evaluated. Figure 4.36 shows the magnitude of the velocity in the suction chamber by using 240 phase-averaged images from four PIV image series. The total measurement error can be estimated by studying mean-bias error and RMS error. The velocity of the flow close to gear tooth is expected to be same as the rotational velocity of the gear pump. In order to calculate the total error of the measurements, 10 points have been defined around one gear tooth (see figure 4.36) by considering that velocity of the flow in these points is the same as the rotational velocity of the gear pump, 1.4 m/s. In the present study, the total error of the measurements, e_{TOT}, is defined as the sum of the mean-bias error and the RMS error as explained in detailed in Chapter 2.

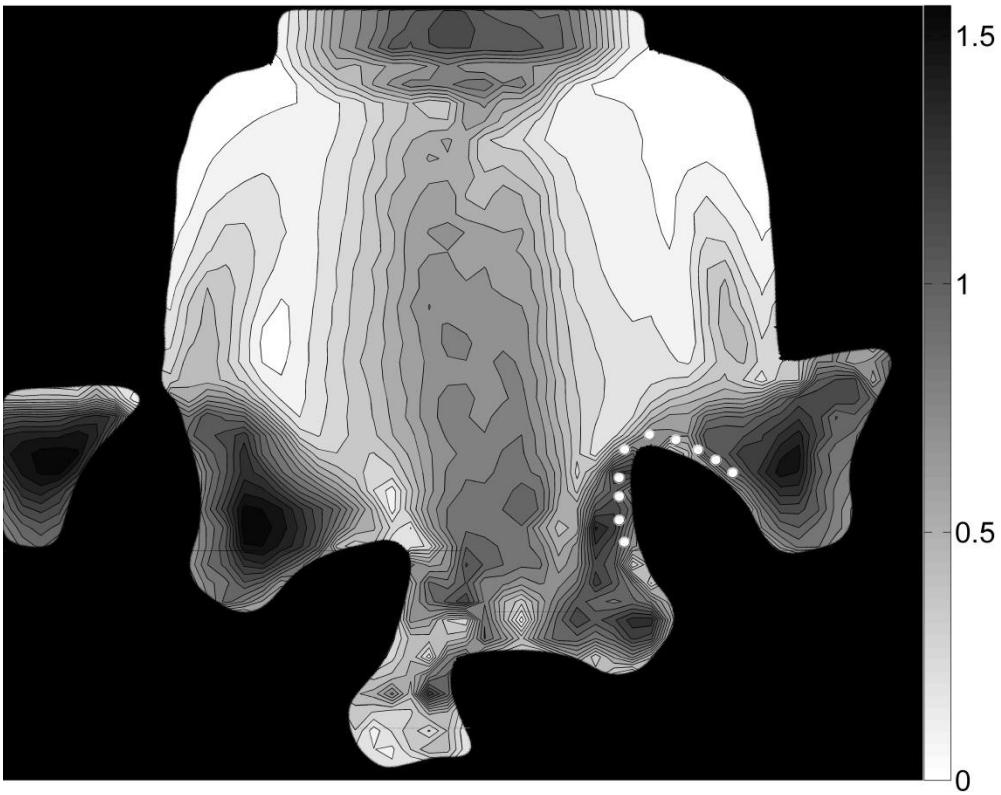

Figure 4.36. Magnitude of the velocity in the suction chamber for sub-case 4 by using 240 phase-averaged images, ● shows the analyzing points for the accuracy of the measurements.

The total error of the measurements has been estimated for different experimental cases by using image series as instantaneous, 60, 120, 180 and 240 phase-averaged. The result of error measurement data is shown in figure 4.37. The error estimates are embedded with different numbers of phase-averaged images whose magnitude affects the results importantly. The measurement error tends to decrease if more image series are used in the phase-averaged (ensemble) averaging process. If 240 phase averaged images are used, the total error of the measurements is found to be 0.5 pixels. This value corresponds to approximately 6% of the data for the different interrogation areas used. In addition, the total error has been estimated for sub-case 7 that has a high spatial resolution. In that case, the measurement error has been estimated from the instantaneous data, 60 and 120 phase-averaged image series. The total measurements error gives approximately 6.8% from the instantaneous velocity data, 16.5% from 60 phase-averaged image series data and 13.6% from 120 phase-averaged image series data.

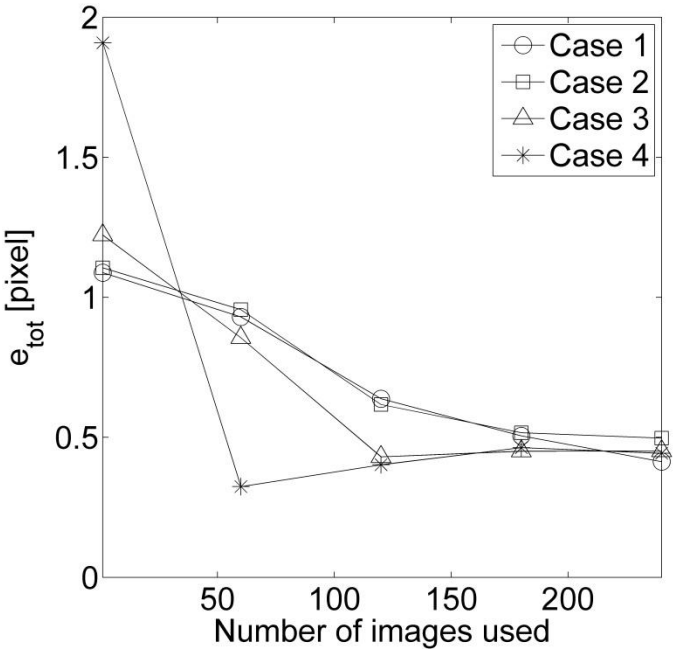

Figure 4.37. Errors in velocity measurements of the analysis for different experimental sub-cases with different number of phase-averaged images used (Note that displacement is obtained as a mean of the analyzing point's data that are shown in figure 4.36).

It has been required to keep the spatial distance between the adjacent vectors short for the estimation of turbulent kinetic energy dissipation rate. In this study, adjacent vectors in space have been found available from the PIV analysis that permits direct calculation of the turbulence energy dissipation through the definition of the velocity gradient (see Table 4.2).

The turbulence energy dissipation has been estimated using Eq. 2.7 considering turbulence as non-homogenous, but statistically isotropic and using Eq. 2.6 assuming homogeneous and fully isotropic turbulence. The effect of the estimates on the distribution of the calculated normalized mean ε values (ε / (N^3D^2) where N is the frequency and D is the diameter of gear) by using different equations near gear teeth is shown in figure 4.38. The ε contour plot obtained using Eq. 2.6 is shown in figure 4.38a. This is the simple assumption in order to estimate the dissipation rate. As reported on flows of stirred tanks, the estimated dissipation rate values obtained considering this assumption are overestimated (Sharp and Kim 2001 and Micheletti et al. 2000). Figure 4.38b shows the ε contour plot obtained using Eq. 2.7. The dissipation rate estimated by Eq. 2.6 and Eq. 2.7 that has the same spatial resolution, 0.06 mm, are slightly different. The energy dissipation obtained with Eq. 2.6 presents high values ($\varepsilon^* > 0.35$). On the other side, the energy dissipation obtained with Eq. 2.7 shows more regular distribution of ε^* with values decreasing with the distance from the gear teeth.

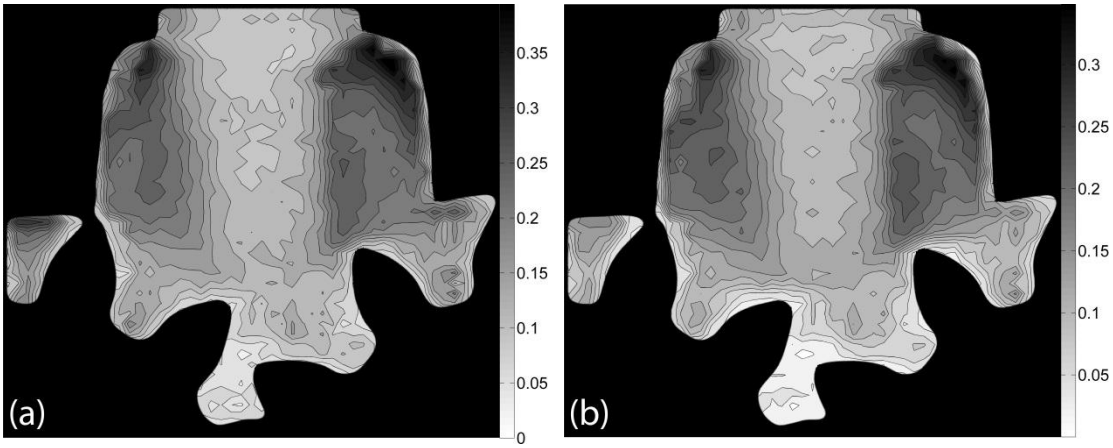

Figure 4.38. Contour plot of the normalized turbulence energy dissipation ($\varepsilon / (N^3D^2)$) using 240 phase-averaged images used for sub-case 4 and calculated by: (a) Eq. 2.6; (b) Eq. 2.7.

The measurements of ε^* obtained from sub-case 7 that has a higher spatial resolution (0.023mm) than the other cases are shown in figure 4.39. As shown in the previous case with a spatial resolution 0.06mm, the energy dissipation obtained with Eq. 2.6 (see figure 4.39a) presents higher values ($\varepsilon^* > 0.4$) than the energy dissipation obtained with Eq. 2.7 (see figure 4.39b) values ($\varepsilon^* > 0.25$). The values of dissipation calculated with Eq. 2.7 show more available data around the gear teeth. Considering the right gear tooth profile for the data of the figure 4.38b and figure 4.39b that have different spatial resolution, it can be noted that higher dissipation values are gathered in figure 4.39b.

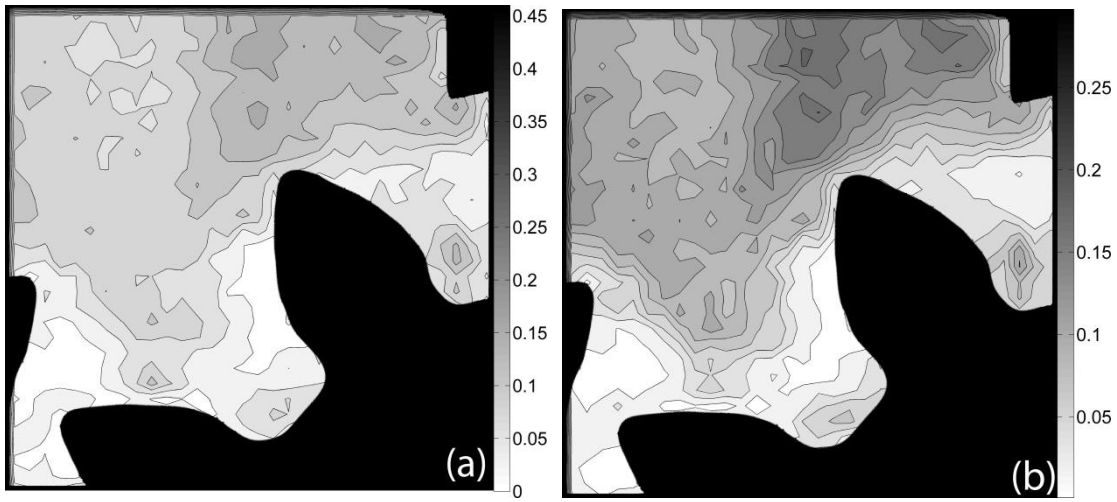

Figure 4.39. Contour plot of the normalized turbulence energy dissipation ($\varepsilon / (N^3D^2)$) using 100 phase-averaged images used for sub-case 7 and calculated by: (a) Eq. 2.6; (b) Eq. 2.7.

The error of the estimations of the dissipation rate has been evaluated from the measured velocity components and the values of their error. Two components of the error have been evaluated, the truncation error, $\Re$, and the velocity measurement error, e (Saarenrinne and Piirto 2000). For a two dimensional region of flow field the in-plane velocity components u and v were measured. The measured velocity components are $u^*=u+e$ and $v^*=v+e$. The dissipation rate error can be evaluated using backward finite differences (see Chapter 2). The error for sub-case 4 is shown in figure 4.40 for normalized dissipation rate for different numbers of images used as instantaneous data, 60, 120, 180 and 240 images used. The dissipation measurement error has been estimated from Eq. 2.7 for 1% and 8.5 % velocity measurements errors. The curves show a steady decrease from instantaneous velocity data up to 240 images used velocity data by considering the error terms or without considering the error terms in the Eq. 2.7. The results show that the accuracy of the estimated dissipation rate depends on the number of images used and the velocity measurement error is an important factor in the estimation of the dissipation rate. In the present study, 0.4 pixel velocity measurement error gives 8.5 % error in the dissipation rate estimations. For 0.023mm spatial resolution measurements as indicated for the experimental sub-case 7, the percentage of the error

has been found 6.4% that is smaller than the 0.06 mm spatial resolution measurements as indicated in sub-case 4.

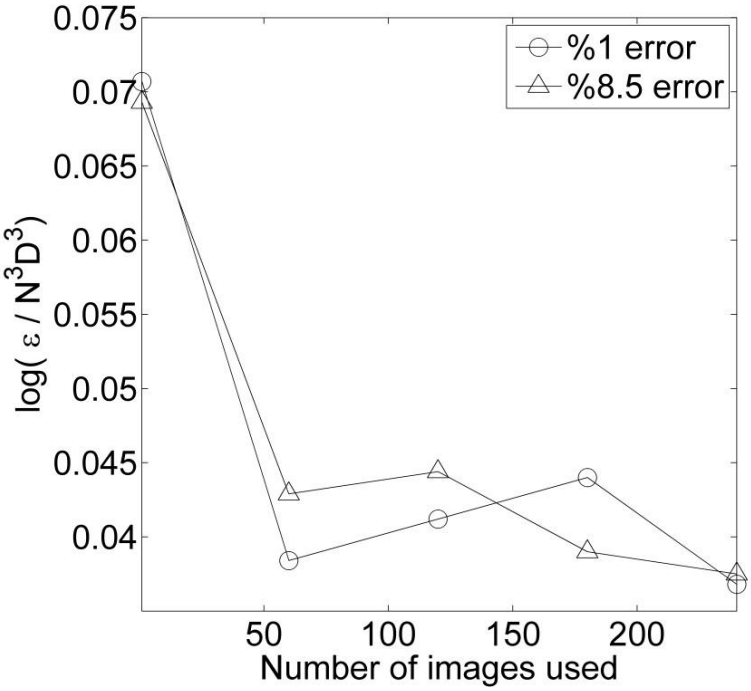

Figure 4.40. Errors in dissipation rate values calculated by Eq. 2.7 using different number of phase-averaged images used for sub-case 4.

4.4.2.5 Three-dimensional flow fields

The three-dimensional flow structure has been inferred from the 2D velocity maps obtained in the suction and impulse chambers in the x-y plane (see figure 4.4). The three-dimensional results have been presented by considering 6 mm difference between the planes. Figure 4.41 shows the velocity profiles in the line A of the suction chamber at different horizontal planes and different rotational velocities of the gear pump.

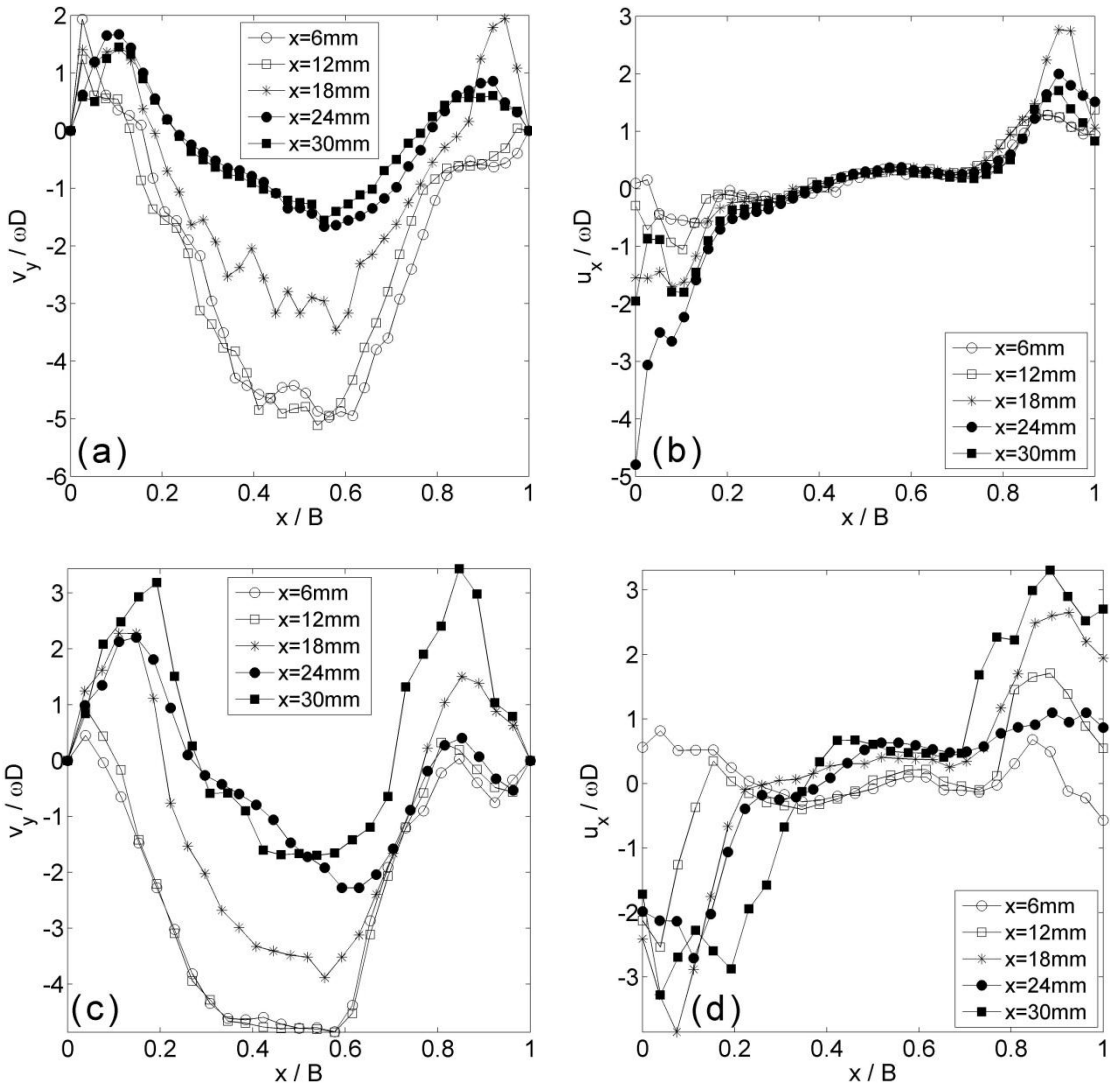

Figure 4.41. Velocity profiles in different horizontal planes for one gear phase: (a) spanwise velocity profile for case 3 with ω_1, 52.3 rad/s; (b) streamwise velocity profile for case 3 with ω_1, 52.3 rad/s; (c) spanwise velocity profile for case 3 with ω_4, 83.7 rad/s; (d) streamwise velocity profile for case 3 with ω_4, 83.7 rad/s.

Figures 4.42 and 4.43 show the velocity and vorticity fields at the same gear tooth phase and at different planes of the suction and impulse chambers of the gear pump at 52.3 and 83.7 rad/s, respectively. The figures have been illustrated up to below indicating the

different horizontal planes in the suction chamber. The upper figures show that the analysing plane is in the front side of the gear pump with a Δx = 6 mm as shown in figure 4.4. The following figures show the corresponding analysed planes by increasing 6 mm difference from the previous plane to the back side of the gear pump. The depth of the gear pump is 36 mm. The planes are generated by 6 mm division of the depth of the gear pump. The figures 4.42a and b are illustrated the plane of the measurements that is 6 mm away from the front side of the gear pump. The figures 4.42c and d show the plane that is 12 mm away from the front side of the gear pump. The middle plane of the gear pump is shown in the figures e and f. The figures 4.42g and h are illustrated the plane of the measurements that is 24 mm away from the front side of the gear pump that is the symmetric plane of the figures 4.42 c and d. The figures 4.42 j and j with a 30 mm far from the front side of the gear pump is the symmetric plane of the figures 4.42 a and b. In figure 4.42, the two big foci that dominate the suction chamber flow have observed in all the analysing planes. The positions of the two foci are the same for all the planes and they are fully integrated in the suction chamber. In the impulse chamber, the two foci have been observed in the most of the planes except in figure 4.42f that is the middle plane of the gear pump. The positions of the two foci in figures 4.42b and 4.42j are closer to the gears than in figures 4.42d and 4.42h. This demonstrates that the tow foci change direction from the lateral sides of the impulse chamber case to the middle side of the impulse chamber and exit from the middle of the impulse chamber through the outlet pipe. Likewise in figure 4.43, the two big foci that dominate the suction chamber flow have observed in all the analysing planes. Differently from the suction chamber of the figure 4.42, the positions of the foci are close to the lateral side of the suction chamber and they seem more irregular due to the high velocity of the gear pump. In the different planes of the impulse chamber of the figure 4.43, we have observed the same flow field as shown in the impulse chambers of the figure 4.42. The two big foci are close to the gears at the lateral planes of the gear pump as seen in figures 4.43b and 4.43j. The planes between the middle and the lateral sides of the gear pump, the two foci moves a little far from the gears as seen in figures 4.43d and 4.43h. In the middle plane of the gear pump, the two foci disappear through the outlet pipe of the gear pump.

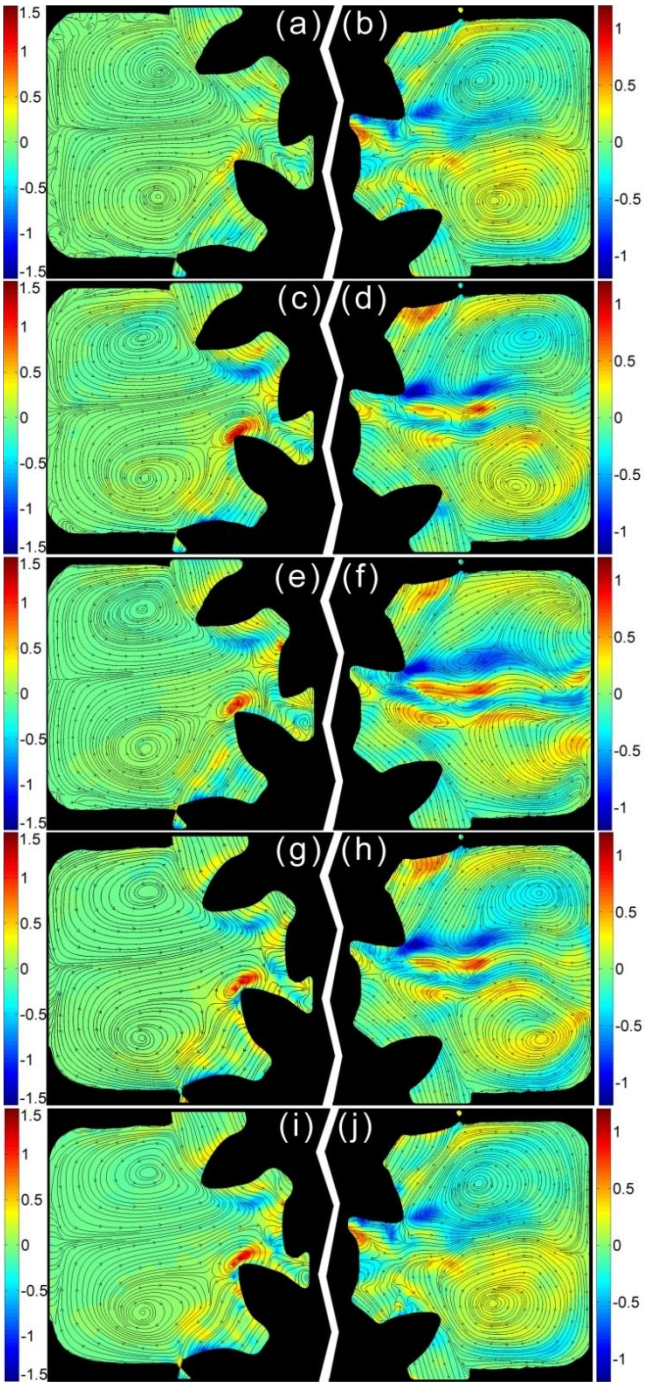

Figure 4.42. Velocity and vorticity fields in the different horizontal planes at 52.3 rad/s. Left set of the figures indicate the inlet chamber and the right set indicate the impulse chamber.

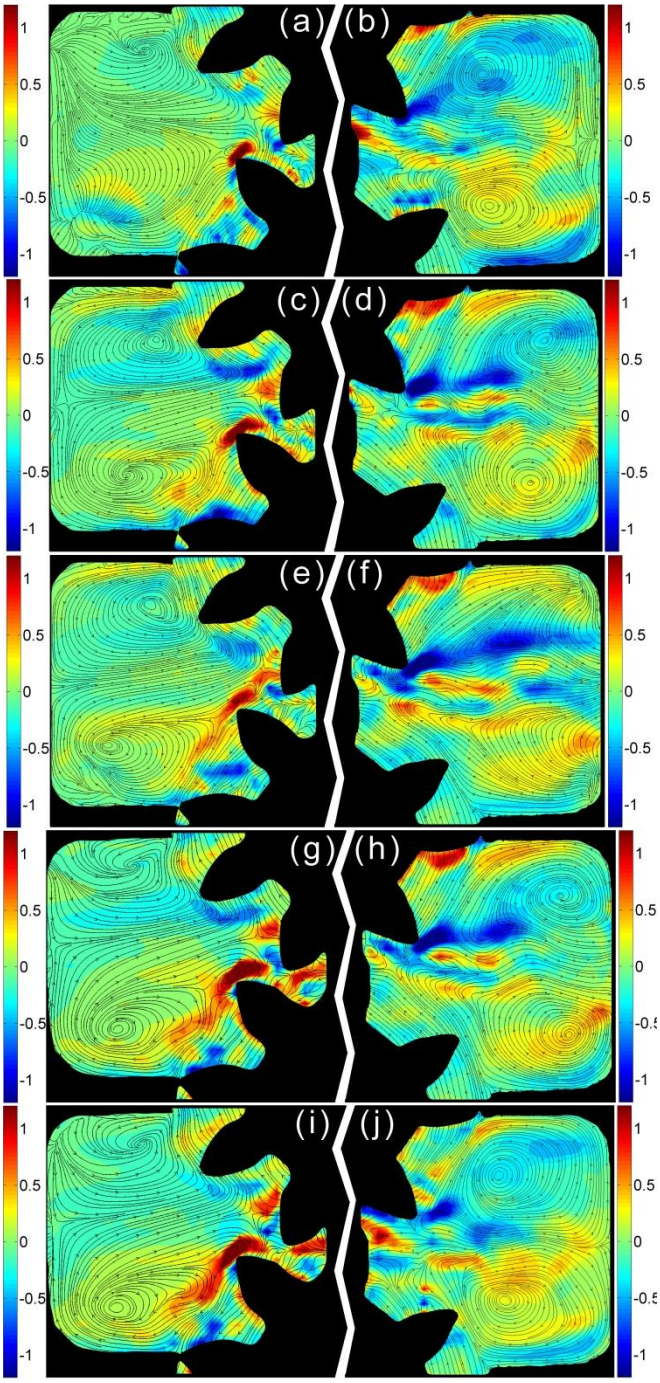

Figure 4.43. Velocity and vorticity fields in the different horizontal planes at 83.7 rad/s. Left set of the figures indicate the inlet chamber and the right set indicate the impulse chamber.

4.5 Summary and conclusions

The TRPIV technique has been successfully applied to the study of the flow structures in the suction and impulse chamber of an external gear pump. The particle images have been pre-processed using a clean- up mask to remove or to reduce undesired light reflections and to homogenise the median illumination. The Triple Image Correlation algorithm has been successfully applied to obtain the instantaneous velocity time history from the particle image series.

The computed autocorrelation of the velocity at one selected location of the suction chamber indicates a periodic behaviour of the flow inside the chamber. The periodicity has been found to be associated with the gearing period of the pump. This characteristic was used to obtain phase-locked averages of the flow field since each phase of the gear can be associated with different flow structures in the suction and impulse chambers. Several gear phases have been selected to compute conditional (phase-locked) ensemble average velocity fields for each case. Those results have been used to obtain an ensemble average time history of the flow inside the suction chamber. Experimental cases have displayed a very similar behaviour and a good agreement with theoretical mean results.

Turbulent structures and small-scale characteristics of the flow inside the external gear pump system have been analyzed by time-resolved PIV. Different spatial resolution levels of interrogation areas have been studied in the dissipation rate estimations.
Turbulent length and time scale characteristics have been computed using autocorrelation function from the PIV data. Kolmogorov length scale has been estimated with two different relationships based on isotropy assumptions for dissipation rate. The effect of the assumptions, turbulence as non-homogenous but statistically isotropic and turbulence as homogenous and fully isotropic, in the estimation of dissipation rate have been compared.

Total error of the measurements has been estimated for different experimental cases by considering the effect of number of samples employed in the ensemble-averaging of the velocities in the external gear pump. The measurement error decreases if more image

series are used in the ensemble averaging process. The error in dissipation rate estimations has been evaluated from the measured PIV data. It has been found that the accuracy of the estimated dissipation rate significantly depends on the velocity measurement error and on the number of the used images.

The three-dimensional flow structures have been obtained in the external gear pump for different rotational velocities of the pump. The influence of the flow structures at different planes has been observed in the variation of the vortexes appeared in suction and impulse chambers.

CHAPTER V
MEASUREMENTS IN AN ENGINE BYPASS FLOW HEAT EXCHANGER

5.1 Introduction

In turbofan engines the incoming air splits after passing the fan. The primary air flow moves through the compressor while the rest circulates through the bypass duct (Figure 5.1). The bypass air is used to cool the engine and to generate a large amount of bypass thrust that results in improvement of the fuel consumption and the propulsive efficiency of the engine. The hot flow path components, particularly, the lubrication of gears and the combustor must be cooled continuously in order to prevent problems for engine operation. Turbofan engines usually use a fuel-cooled cooler to refrigerate the lubricating oil due to the large heat absorption capacity of the fuel. Air could also be used to cool the oil. In this case the amount of cooling air is limited to keep the engine efficiency high (Linke-Diesinger 2008). In order to improve the oil cooling by air, a heat exchanger could be placed inside the bypass duct (Elovic 1981; Olver et al. 2008; Anderson et al. 2008; Wakeman 1980; Cornet 2009; Zyzman et al. 2008). Thus, the overall performance and the thermal management of the engine can be improved by reducing the cooling air required by the engine. Currently a new transonic wind tunnel has been designed to reproduce the bypass aero-engine flow in von Karman Institute (Villafañe et al. 2011a). Three-dimensional computations have been performed in order to investigate and optimize the interaction of the flow with the heat exchanger. Furthermore, different fins' array geometries of the heat exchanger have been characterized at the transonic flow

conditions (Villafañe et al. 2011b). The efficiency of the heat exchanger at different locations along the test section has been experimentally studied for the validation of the engine models.

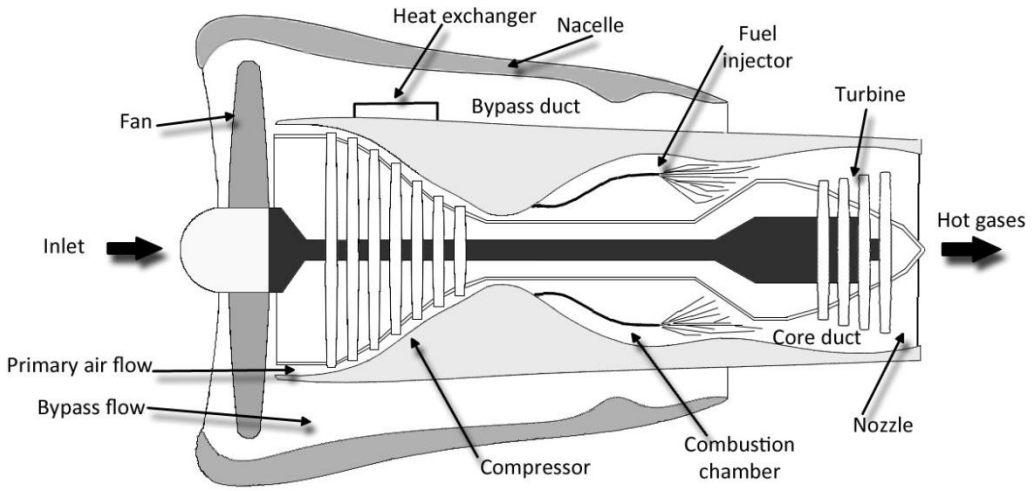

Figure 5.1. Schematic view of turbofan engine with a heat exchanger placed at the inner wall of the bypass duct.

Turbulent effects of the heat exchanger on the bypass air flow are significantly important. Therefore, an efficient heat exchanger type should be placed on the bypass duct in order to obtain less flow effects. The knowledge of the flow structures generated by the presence of the heat exchanger and the influence of its geometry may lead to the design of an efficient heat sink configuration for turbofan engines. In this work the Particle Image Velocimetry (PIV) technique has been used to experimentally analyse the flow behaviour in the bypass region. As in all the flow systems analysed by PIV in high speed flows the performance of the technique is related on the ability of tracer particles to follow the flow. Homogeneous seeding with suitable tracer particles and enough particle density is one of the major problems in high-speed air-flows. In order to minimize the velocity lag in regions with strong positive or negative accelerations across shocks in turbulent flow or in vortical flows, very small (<1 μm) tracer particles are required (Bryanston-Cross et al. 1995). A high acceleration variation causes the particles to travel locally at relative different velocity from that of the surrounding fluid. This causes the

particles to be ejected towards regions with lower accelerations due to the integrated effect of particle (Lang 2000; Koike et al. 2007; Schrijer and Scarano 2007; Schrijer et al. 2008). Selection of the particles used is one of the most important decisions before performing any PIV experiment. Spherical particles are one of the best possible choices. The unsteady motion of small spherical particles in fluid flows has been previously determined (Mei 1996) and it has been provided a general mathematical review in a specific study related with the high-speed regime (Tedeschi et al. 1999). On the other hand, the use of fluorescent tracer particles can also improve the PIV results. They end with a better quality of vector maps and the signal to noise characteristics of the raw images from PIV measurements (Deschênes et al. 2010; Monji and Sato 2010; Lai and Menon 2004). However, the cost of the commercially available fluorescent particles is too high for the large-scale experiments. The use of Rhodamine dye compounds based particles can be prohibiting in large-scale experiments due to their toxic property and high cost. However, the fluorescent particles show high efficiency and detectability at almost every flow conditions. Despite their promise, the use of fluorescent particles is largely limited to flow studies in large-scale laboratory experiments.

This chapter focuses on the use of PIV technique to analyse the flow structures of the heat exchanger. The heat exchanger is placed into the low speed wind tunnel to obtain the prior knowledge on the effects of the heat exchanger in the bypass flow. Two different tracer particles as the glass particles and the fluorescent particles are used in the experiments in order to improve substantially the PIV image quality and further analysing the small-scale structures of the flow. The increase in PIV image quality results in the improvements on the accuracy of the PIV measurements. This analysis for the flow structures of the interaction between the bypass flow and the heat exchanger may lead to use an efficient heat exchanger type for the further applications in the bypass engines.

5.2 Experimental setup

The PIV experiments have been performed in a closed-circuit low speed with tunnel located in the Von Karman Institute (see Figure 5.2). The closed circuit wind tunnel gives

the advantage to collect the seeding particles for further use in different experimental conditions. The wind tunnel has a 1.6m long test section with 0.1 x 0.3m cross section and the walls of the test section optically transparent. The settling chamber, fitted with a honeycomb, is followed by a 12.4 to 1 contraction. The centrifugal fan is driven by a PC-controlled variable-speed 8kW DC motor to achieve any specific speed-time history. The wind tunnel can reach a maximum flow velocity of 70 m/s and is suitable for optical measurements of surface wave motion and for general flow studies.

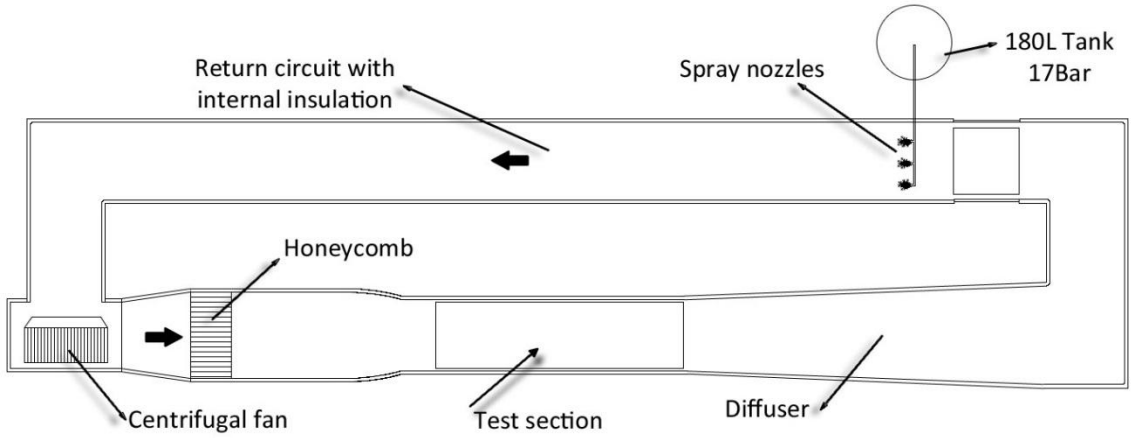

Figure 5.2. The schematic drawing of the closed-circuit low speed with tunnel system.

The specific type of the heat exchanger is used to analyse the turbulent flow effects done by the heat exchanger. The heat exchanger is established in the middle of the test section of the wind tunnel. The first experimental set-up is illustrated in figure 5.3. The heat exchanger is placed horizontally to the test section and across to the flow direction. The PIV measurements are taken using a double pulsed Nd-YAG green laser to illuminate the particles in the flow. The laser has a wavelength of 532nm and a variable frequency between 1 and 15Hz. A PCO Sensicam Camera with a CCD sensor and a resolution of 1280x832 pixels is used to record simultaneous images of the flow. The camera acquires 12 bit images resolves with 4096 grey levels between black and white. The camera is able to acquire two subsequent images very close in time. The time between the two images can be obtained 200ns in the double short exposure mode or 1 μs in the double long mode. In this study, the PIV experiments have been done by using two types of lenses for the camera, 35 mm lens and 200 mm lens.

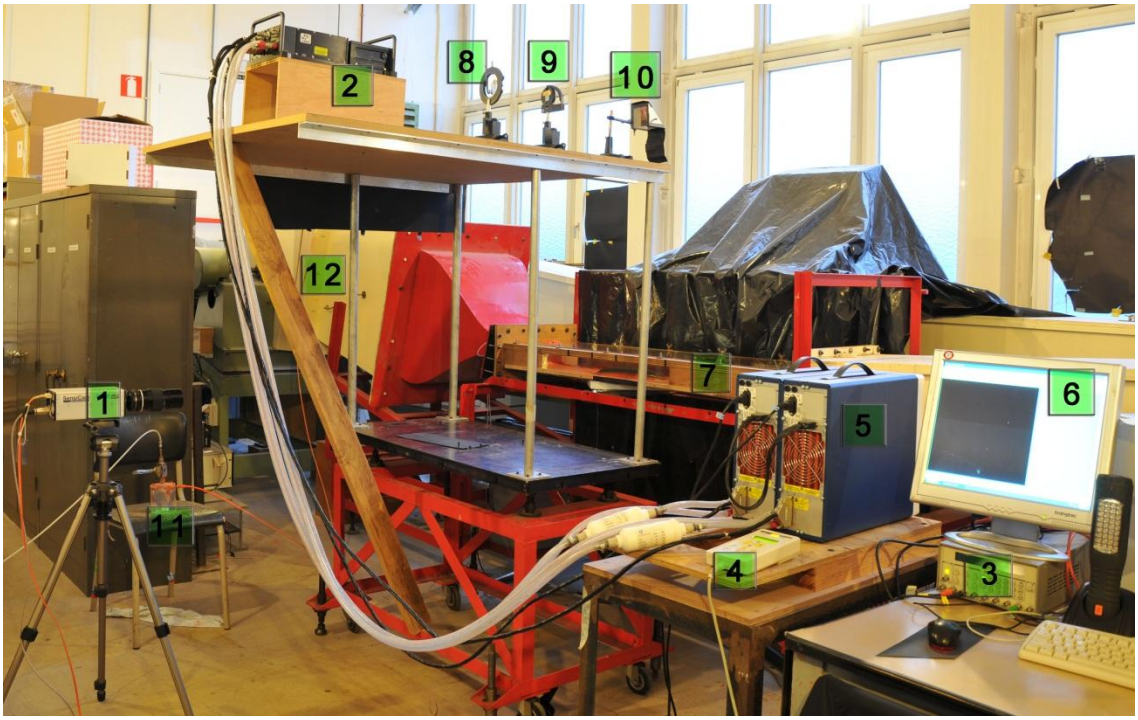

Figure 5.3. The first PIV experimental set-up: 1.Camera, 2.Nd-YAG green laser, 3.Synchroniser, 4.Wired remote control for laser, 5.Laser twins' box, 6.Computer, 7.Test section, 8.Focal lens, 9.Cylinder lens, 10.Prizm lens, 11.Cyclotron, 12.Particle introduction.

In the first experimental set up, the laser sheet is introduced vertically to the test section. The aim of this set up is to analyse the flow passing through the heat exchanger in the lateral sides. The PIV measurements are done in the different vertical planes of the surrounding the heat exchanger. In this configuration of the experiments, 200 mm lens has been used in order to extend the analysing area. In the second PIV experimental set up as shown in figure 5.4, the laser sheet is introduced to the test section horizontally. The images are captured from the top of the test section. In this case, the aim is to analyse the flow passing through the heat exchanger and the trailing vortexes occurring after the fins. In this configuration, 35 mm lens has been used for the camera. A tripod has been used to hold the camera for the top view of the analysing area. The PIV images that are captured by the camera are transferred via a high speed data transfer to computer. The only file format supported by the program of the camera is the b16 format. Then b16

format PIV images – taken by full CCD array- are converted to tif images for further image data analysis.

The solid particles have been introduced to the wind tunnel after the honeycomb section by a cyclone type seeder (see figure 5.3). The diameter size of 4 mm pipe has been used to connect the cyclone seeder and wind tunnel in order to seed particles. The velocity of the tunnel has been set to 40m/s and 50m/s to identify the flow characteristics at different speeds.

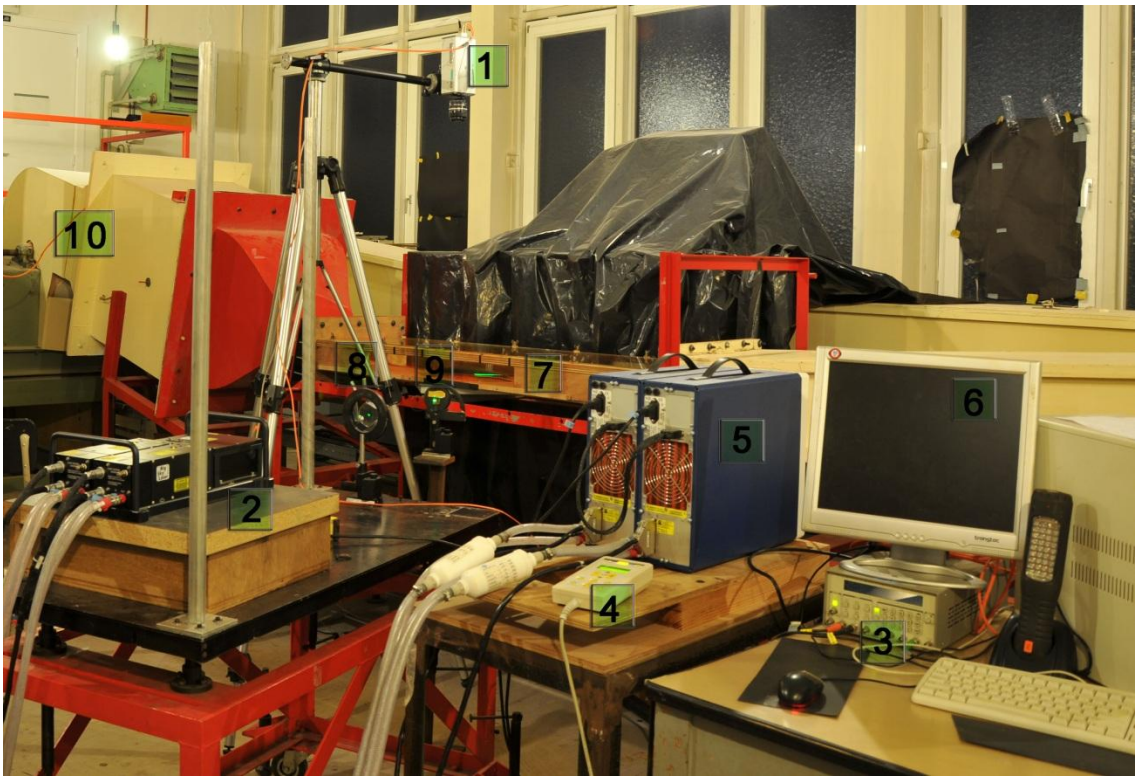

Figure 5.4. The second PIV experimental set-up: 1.Camera, 2.Nd-YAG green laser, 3.Synchroniser, 4.Wired remote control for laser, 5.Laser twins' box, 6.Computer, 7.Test section, 8.Focal lens, 9.Cylinder lens, 10.Particle introduction.

5.2.1 Heat exchanger

For the first time, we have conducted a basic flow analysis of a specific type heat exchanger via PIV technique. The specific type of the heat exchanger has been specially designed by Techspace Aero (http://www.techspace-aero.be/) in use of air cooled oil cooler to be integrated in the secondary flow of the engine. It is an additional cold surface for the lubrication oil cooling system in order to increase the efficiency of the engine. Recently, different designs of the air cooled oil coolers have been experimentally investigated for the comparisons of the aero-thermal performance of the heat exchangers by Techspace Aero and Université Libre de Bruxelles (ULB) (Heintz et al. 2011). The 3D geometry of the heat exchanger that has been used in this study is shown in Figure 5.5. The heat exchanger has 12 fins extending from its base with 1.5mm thickness. The height of fins is 14mm and there is a 5 mm distance between the fins.

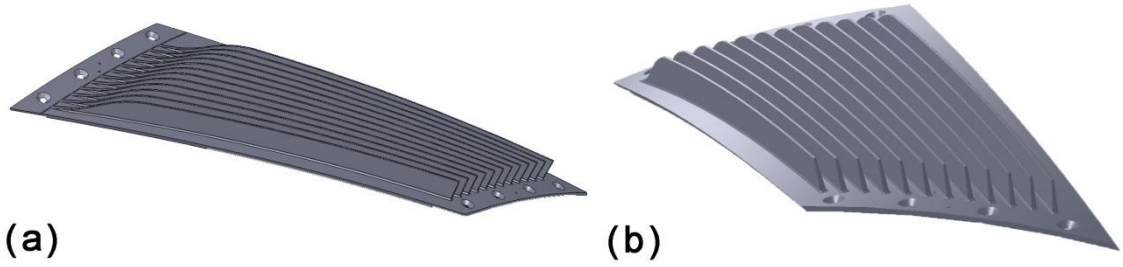

Figure 5.5. The 3D geometry of the heat exchanger (a) lateral view (b) front view.

In the PIV experiments, the heat exchanger is placed horizontally to the test section and across to the flow direction (see figure 5.6a). The flow direction is parallel to the fins of the heat exchanger. The entrance of the inlet flow to the heat exchanger is illustrated in the figure 5.6b. The shapes of the fins are skewed in this side of the heat exchanger. The flow passes through the fins and leaves the heat exchanger from the opposing side. In the outlet flow, the shapes of the fins are rectangular as shown in the figure 5.6c.

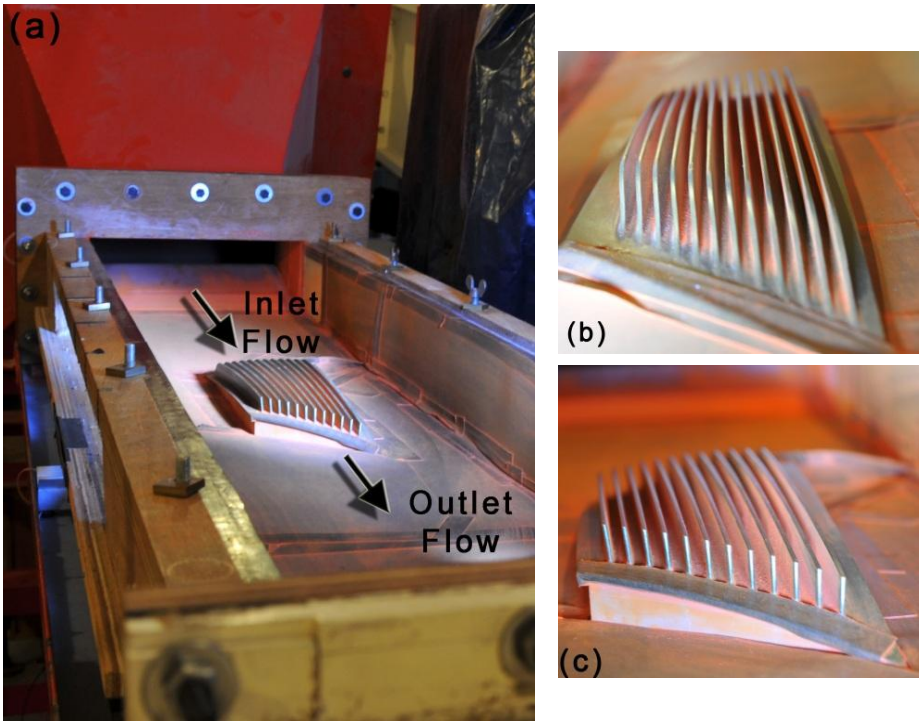

Figure 5.6. The position of the heat exchanger in the test section: (a) test section, heat exchanger and the flow direction; (b) detailed view of the heat exchanger at the inlet flow; (c) detailed view of the heat exchanger at the outlet flow.

The geometry of the heat exchanger is designed as totally skewed for the fins and the plate of the fins in order to fit the heat exchanger in the bypass duct section of the engine. Figure 5.7 shows the heat exchanger's position into the transonic wind tunnel application. The test section of this wind tunnel has been characterized by an annular sector-type test section with the unique 3D bypass flow conditions (Villafañe et al. 2011a). In order to reproduce engine radial and longitudinal gradients, the annular test section turning the axis at a constant reference radius was required. This configuration of the wind tunnel will be able to reach the flow with a Mach number approximately 0.8. Hence the shape of the heat exchanger is designed as skewed to be able to fit the annular test section of the transonic wind tunnel.

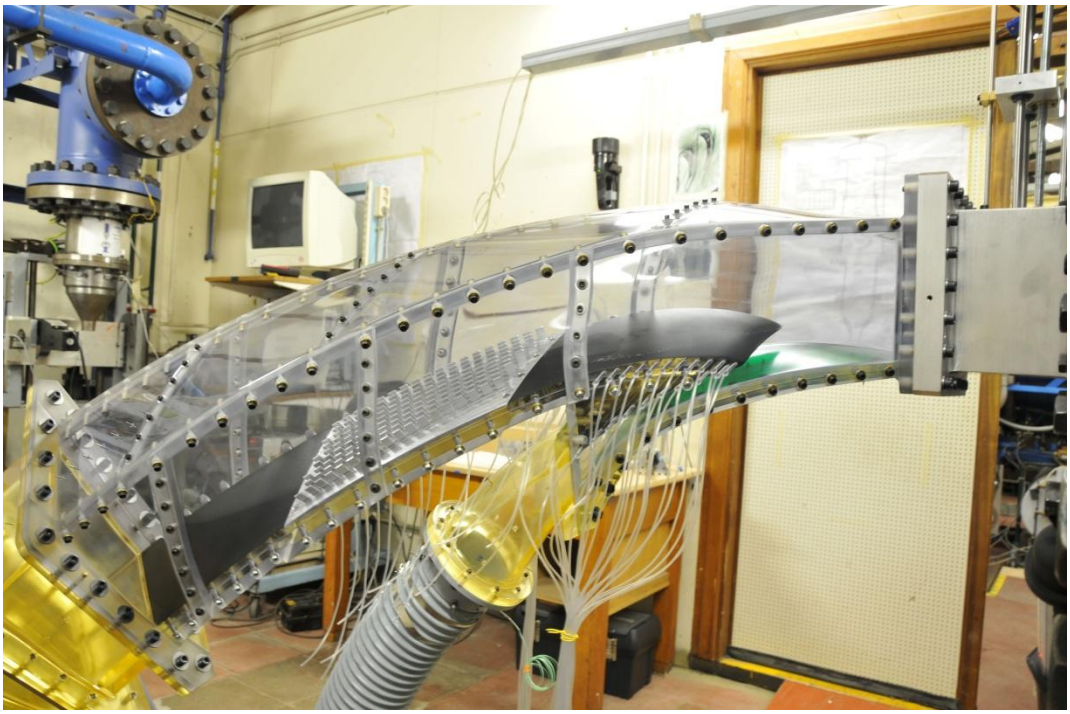

Figure 5.7. The place of the heat exchanger in the transonic wind tunnel.

5.2.2 Seeding particles

Different types of solid particles are used as tracer particles in the PIV system. The glass sphere particles with diameter sizes approximately 4 μm and approximately 30μm have been used for the flow analysis. Then, the fluorescent particles with diameter sizes approximately 1μm have been used to analyse the small-scale flows that are formed by the effects of the fins of the heat exchanger. The introduction of the solid particles into the wind tunnel has been done by using a cyclone type particle seeder (Figure 5.8) that is fulfilled with the solid particles. Air is introduced to the cyclotron by the help of a pipe and flow through the inside of the cyclotron. The particles are moved with the high pressure of the air and goes out from the cyclotron with the particles. Then the particles are introduced to the wind tunnel through the pipe. The cyclone type seeder has been

found enough to seed the wind tunnel for PIV experiments due the advantage of close loop wind tunnel.

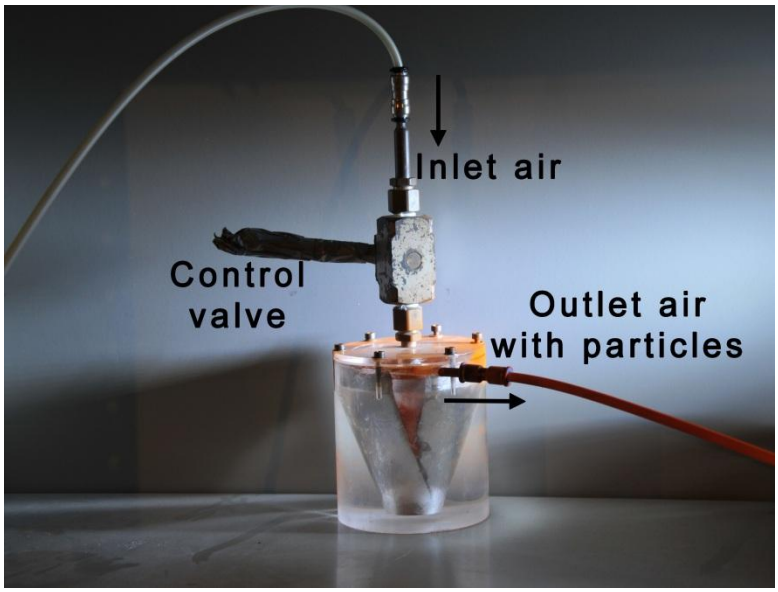

Figure 5.8. The cyclone type seeder.

5.2.3 Challenges in the experimental setup

The PIV studies have been realized in the Von Karman Institute for the 3 months short stage. In the experimental set-up, several challenges have been found to be solved for the future experiments that are going to be realized in the transonic flow wind tunnel (Villafañe 2011a and 2011b). This section clarifies the experimental set-up challenges in order to improve the PIV technique.

First of all, the wind tunnel is seeded with the solid particles to perform PIV. The reason to use the solid particles is to obtain a prior knowledge about particles for the application of the engine bypass flow heat exchanger in transonic flow. In the new design of the transonic wind tunnel with air cooled oil cooler heat exchanger (Villafañe 2011a) as

shown in the figure 5.9a and 9b, the working temperature will be very low. Hence using liquid particles such as water droplets cannot be used for PIV seeding. For this reason, glass and fluorescein particles have been used as solid flow seeding to perform PIV in this study. The introduction of the particles has been done by using a cyclone type seeder through a pipe to the wind tunnel. The cyclone type seeder has been found as an efficient way to seed the wind tunnel. However, the advantage of the closed wind tunnel leads to obtain homogenous seeding particles in the flow. For the design of the transonic wind tunnel (Figure 5.9), it is recommended to use a nozzle to introduce the solid particles since the new design is an open wind tunnel.

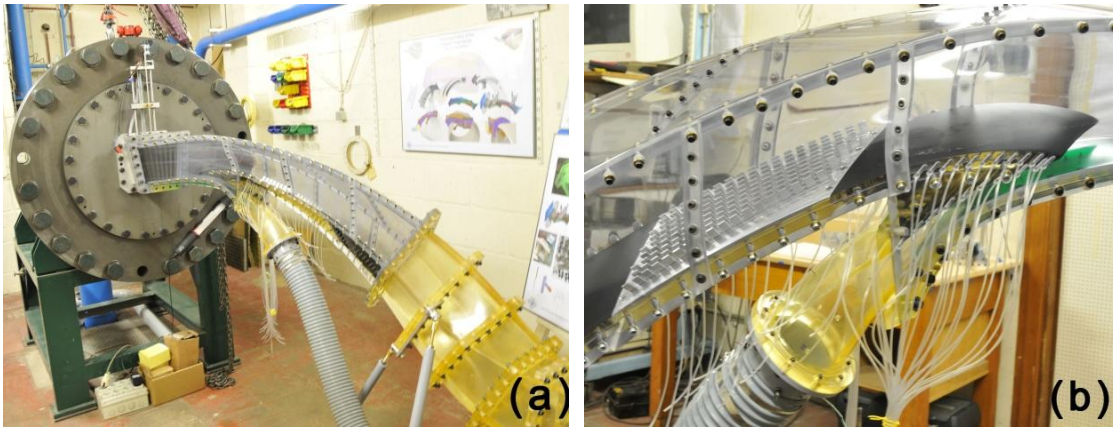

Figure 5.9. The design of the new transonic wind tunnel: (a) overall view; (b) test section view with the heat exchanger.

During the PIV experiments, it has been observed that the particles smaller than 30 μm diameter have stacked on the Plexiglas of the test section. It was impossible to realize the PIV experiments in this condition. Hence an antistatic liquid is used to clean the Plexiglas before starting the PIV experiments. Using the antistatic liquid cleaner improved to obtain clearer view of the particles in the images during the recording time. Furthermore, the test section must be able to open and close simply because for each series of PIV experiments, the Plexiglas must be cleaned. On the other hand, the glass particles did not stick on the Plexiglas due to the diameter sizes, approximately 30 μm.

In most PIV experiments, the difficulties come across when undertaking PIV experiments close to a wall was glare. In order to counteract this, the surface of the heat exchanger was painted with black paint that is able to resist to 750^{o}C. Nevertheless this did not remove the entire glare. In future, more efficient paint must be used in order to solve the glare problems. A simple paint is made of a synthetic resin in matt black colour should be used although its resistance temperature is not for high temperatures. The matt property in the black paint will significantly prevent the glare problems. However, an image mean for each PIV run helped to reduce the reflections and leads to improve the PIV data.

The Plexiglas that is used for the optical access for PIV must be clear enough to obtain adequate PIV images in the analysing area. In this study, some scratches have been found in the Plexiglas. However, the scratches did not affect the analysing area significantly.

5.3 Image data analysis and techniques

The motion of the fluid is determined by measuring the particle displacements through evaluation of the PIV recordings. As a single image pair contains hundreds or thousands of particles, the images are divided into small sub-areas called interrogation areas. It is assumed that all the tracer particles within each interrogation areas move homogenously between two laser pulses. The average of displacement is then calculated at each interrogation areas by means of cross-correlation method to build up the complete 2D velocity vector map. Typical dimensions of an interrogation area for PIV are between 16x16 to 128x128 pixels. In order to obtain a reliable estimator of the particle image displacement 10 to 15 particles in an interrogation area have to be present (Raffel et al. 1998).

In this study two different types of the PIV programs have been used. In the first PIV program, the PIV images are analysed using the ECoMMFiT PIV software that is being developed by ECoMMfit group in the University of Rovira i Virgili, Spain. In this chapter, the usual cross-correlations that are obtained at different times for the same interrogation window are used. The available experimental data is a set of particle

images, which are uniformly spaced in time. The cross-correlation method uses two consecutive images to compute the velocity field. The PIV software computes the velocity field with regard to the Local Field Correction PIV method that is proposed by Nogueria et al. (2001). The detail of the algorithms can be found in chapter 2.

In the second PIV program, the PIV images are analysed using the PIV software of the von Karman Institute (VKI), Rhode-Saint-Genèse, Belgium (Horvath 2011; Scarano and Riethmuller 2000a). For the image pre-processing, the program uses a subtraction method that creates a posterior background for the two consecutive image frames and then it subtracts these images from the relevant frame series respectively. This subtraction diminishes the background noise in the level of light intensity and enhances the signal-to-noise ratio and the number of validated vectors. The method is able to suppress the unwanted reflections as well without any artifact in the images (Scarano and Riethmuller 1999). The PIV technique, that is called as Windows Displacement Iterative Multigrid (WIDIM) performs iterative interrogation of the PIV recordings (Scarano and Riethmuller 2000b). The method is based on cross-correlation that uses the translation of the interrogation areas. The displacement is predicted and corrected by means of the iterative procedure. During the iterative procedure the size of the interrogation windows is gradually reduced yielding a finer resolution in space. Discrete window offset and deformation are applied for the local deformation of the fluid continuum [51].

5.4 Results

5.4.1 Image pre-processing results

In the PIV experiments, it has been observed glare by the reflection of the laser light on the heat exchanger. The surface of the heat exchanger was painted with matt black nevertheless this did not remove the entire glare. This situation has been appeared significantly in the first experimental set-up (Figure 5.3) in the vertical plane flow analysis of the heat exchanger. In order to reduce the reflections, an image mean for each

PIV series helped to reduce the reflections however it was not enough to extract the entire PIV data close to the heat exchanger's fins.

Figure 5.10 shows the results of the processed PIV images in the vertical plane analysis of the heat exchanger flow. The laser plane is in the middle of the heat exchanger and the significant glare is on the next first fin after the laser plane. The fluorescein particles have been used as flow seeding that is shown in the images. The recorded images contain an area of the flow as 1200x680 pixels that correspond to a 60 by 34 mm^2 area. The raw PIV images as shown in figure 5.10a contains the data of 16 bit format tif image that is shown as 8 bit format tif. Two image per-processing programs as explained in section 6.3 have been applied to the raw image to convert 8 bit format and reduce the reflections of the laser on the heat exchanger. Figure 5.10b is the pre-processed result of the VKI PIV algorithm and figure 5.10c is the ECommFiT PIV algorithm. The reflection by the laser on the heat exchanger has significant influence on the PIV data. Both applied algorithms could not able to remove the entire reflections on the fins, particularly the fin behind the laser plane on the heat exchanger (see figures 5.10b and 5.10c). However the particles can be identified clearly except the first fin that appears in the PIV images. Furthermore, the image pre-processing algorithm used in the VKI PIV program reduces the number of the particles in the images. As it can be seen from the zoom figures, figure 5.10c contains more particles than the figure 5.10b.

The quality of the recorded PIV images behind the fins' of the heat exchanger in the vertical plane of the laser is found considerably good when the fluorescein particles used as flow seeding. In that case, no reflection occurred by the heat exchanger. Moreover, in the second experimental set-up, laser plane horizontally in the heat exchanger, the reflections did not affect the PIV image view.

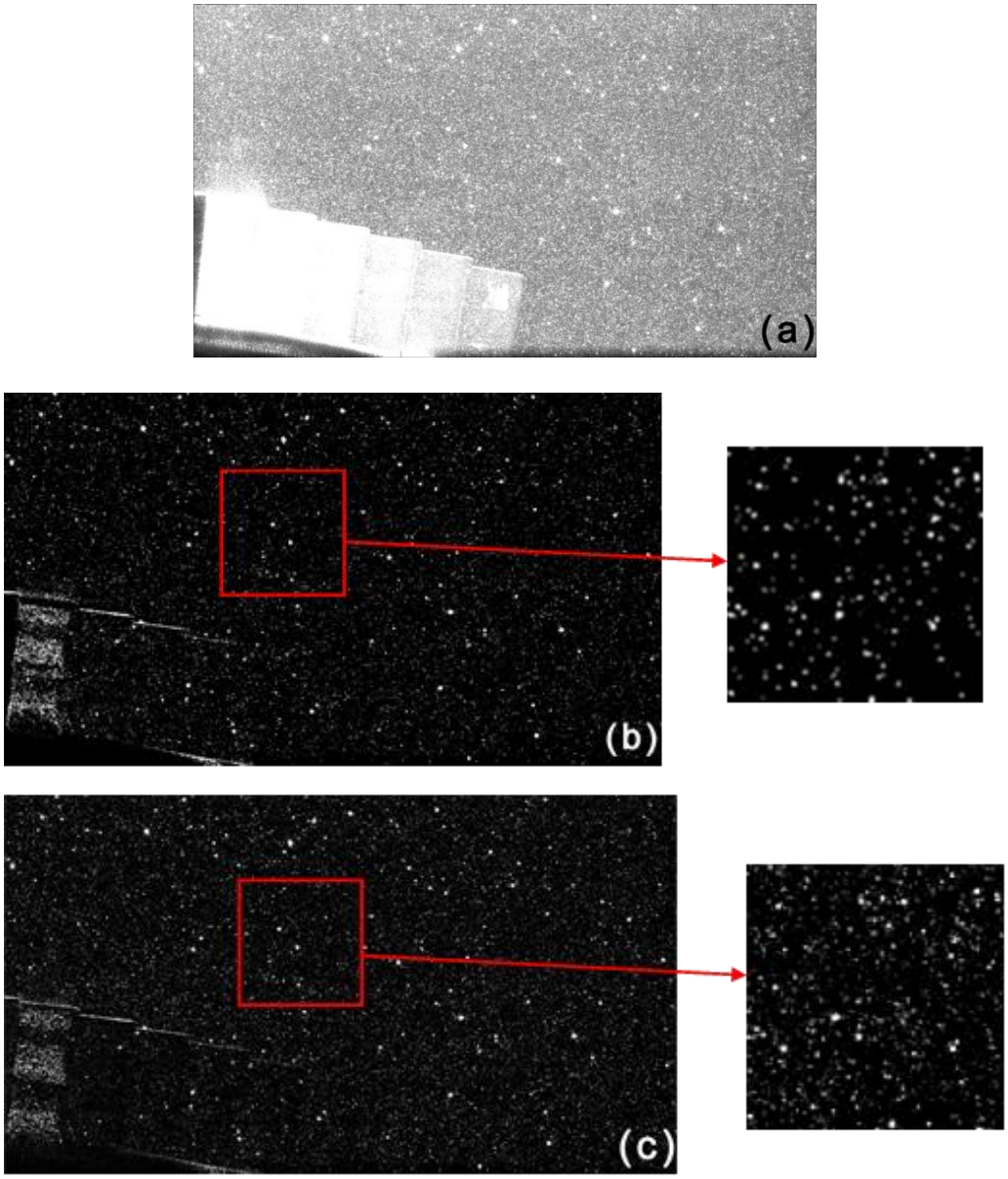

Figure 5.10. Image pre-processed results for the vertical plane analysis of the heat exchanger, laser sheet is in the middle of the heat exchanger and fluorescein particles are used as flow seeding: (a) raw image in 16 bit format as shown in 8 bit format tif; (b) VKI PIV image pre-processing algorithm; (c) ECommFiT PIV image pre-processing algorithm.

5.4.2 Different seeding particles

In this study, different tracer particles have been tested as flow seeding for this specific application of the engine bypass flow heat exchanger in order to apply PIV technique efficiently. Initially, the Nanoperl particles with the diameter size approximately 4 μm have been used as flow seeding. The particles are the new generation of the ultrafine glass beads. However, they exposed a bad reflectivity under the green light due to the smaller diameter size. Afterwards, it has been decided to use the glass beads, this time diameter ranges between 30-35 μm. The glass particles have a spherical shape and a smooth surface. They show a good reflectivity to the green laser. Nevertheless the diameter size of the particles must big enough to reflect the laser light. Lastly, the fluorescein particles with approximate diameter sizes 1 μm have been tested as flow seeding for the engine bypass flow heat exchanger. The fluorescein particles have shown high reflectivity to the green laser light even though the size of the particles is small. The properties of the fluorescein particles have been explained in detailed with the characterization in the chapter 3. The figure 5.11 is shown in order to compare the glass particles and fluorescein particles in the PIV images. It has been observed a significant difference between the PIV images as shown in figure 5.11a and 5.11b that have been captured in the same settings of the laser and camera. The dimension of the images is 656x352 pixels correspond to an area of 92x49 mm analyzing area. The fluorescein particles as flow seeding lead to obtain efficient PIV images for the air flow analysis. Eventually, the fluorescein particles have been decided to be used as flow seeding for the analysis of the engine bypass flow heat exchanger.

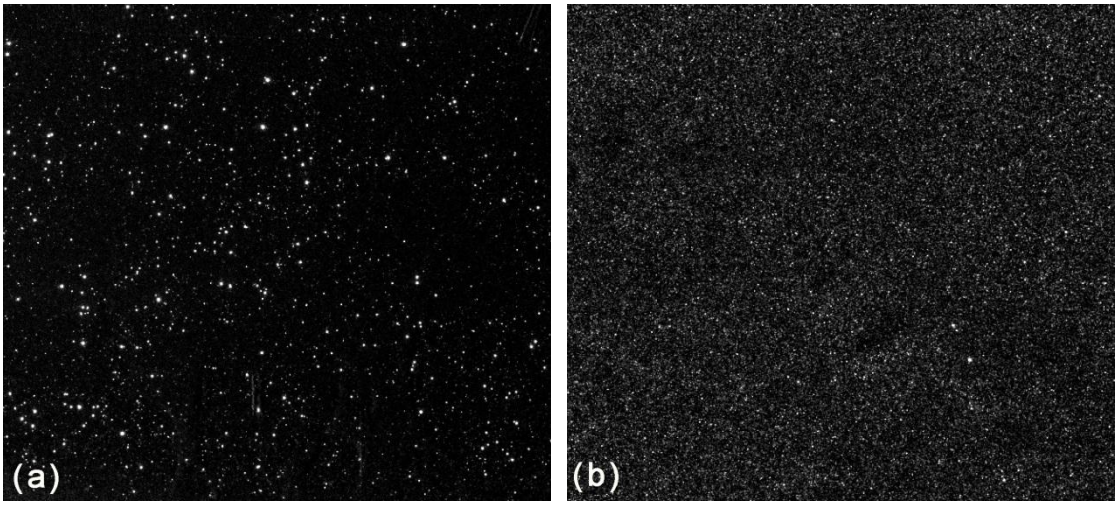

Figure 5.11. PIV images for the vertical plane analysis of the heat exchanger, laser sheet is behind the fins' of the heat exchanger: (a) Glass particles approximately 30-35 μm as flow seeding; (b) Fluorescein particles approximately 1 μm as flow seeding.

5.4.3 Vertical plane analysis of the engine bypass flow heat exchanger

The PIV technique has been applied to analyze the bypass flow heat exchanger in the vertical planes of the heat exchanger. The aim is to obtain the structures of the flow that passed all through the fins. Due to the complex 3D geometry of the heat exchanger, several vertical planes have been used to analyse the flow as shown in figure 5.12.

For the vertical PIV experiments, 1000 and 2000 particle images have been recorded for each series. The time difference between the two images has been set to 25μs when the velocity of the wind tunnel was 40m/s. The frame rate of the camera was 3Hz. 200mm focal length objective has been used for the camera. 500 instantaneous velocity fields with a 0.33s time difference have been obtained intermittently. When the velocity of the wind tunnel was 50m/s, the time difference between the two consecutive images has been set to 20μs with the frequency of 3Hz.

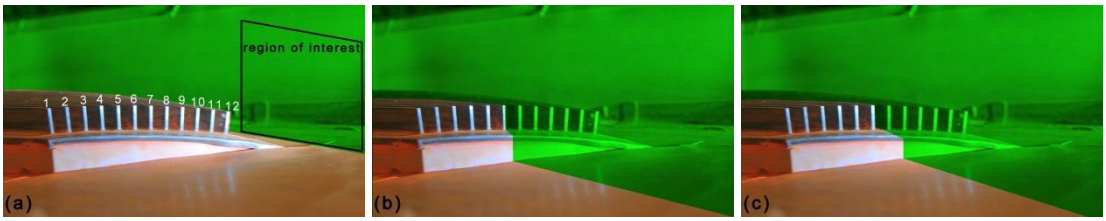

Figure 5.12. The laser sheet arrangements for the vertical plane analysis: (a) behind the heat exchanger; (b) on the 6th fin; (c) between the 6th and 7th fins, in the middle of the heat exchanger.

First of all, the PIV programs from VKI and ECoMMFiT has been tested in order to qualify the PIV data. For this purpose, the recorded PIV image series from the vertical plane behind the heat exchanger with the region of interest (Figure 5.12a) have been considered in order to compare the PIV data without reflection effects from the heat exchanger. On the Plexiglas, there was a scratch and a nail as shown in figure 5.13 as an example for the recorded PIV image. There was no information of the particles due to the nail in front of the Plexiglas. It is expected that the scratch should lead to reduce the velocity magnitude particularly on that area due to its glare effect. These situations could be used for the reference points on the comparisons of the programs on results of the mean velocity field. Furthermore, the flow is supposed to move in the x-direction (see figure 5.13) in the analyzing area because the laser plane is placed behind the heat exchanger. The mean velocity results with the streamlines and magnitude of the velocity have been illustrated in figure 5.14. The interrogation area has been used as 64x64 pixels and 32x32 pixels in order to compare the PIV program results. Figure 5.14a and figure 5.14b illustrate the results of the VKI and ECoMMFiT PIV programs, respectively, that are done by using 64x64 interrogation areas for comparison. The direction of the flow according to the streamlines is agreed well between the PIV programs. Likewise, the magnitude of the velocity is agreed between the programs except for the reference points. The magnitude of the velocity at the reference points cannot be identified in the VKI program when 64x64 interrogation area is used. On the other hand, the magnitude of the velocity at the reference points can be identified in the VKI program when 32x32 interrogation area is used (see figure 5.14c). In the case of the ECoMMFiT programs when 64x64 and 32x32 interrogation areas are used, the magnitude of the velocity at the reference points can be clearly identified as shown in figures 5.14b and 5.14d. In fact, we

can conclude from these figures that it is possible to identify small-scale structures with the ECoMMFiT PIV program at large interrogation areas. However, it is better to use VKI program with small interrogation areas such as 32x32 in order to extract the velocity results.

Figure 5.13. Illustration of the scratch and nail reference points on the raw PIV image.

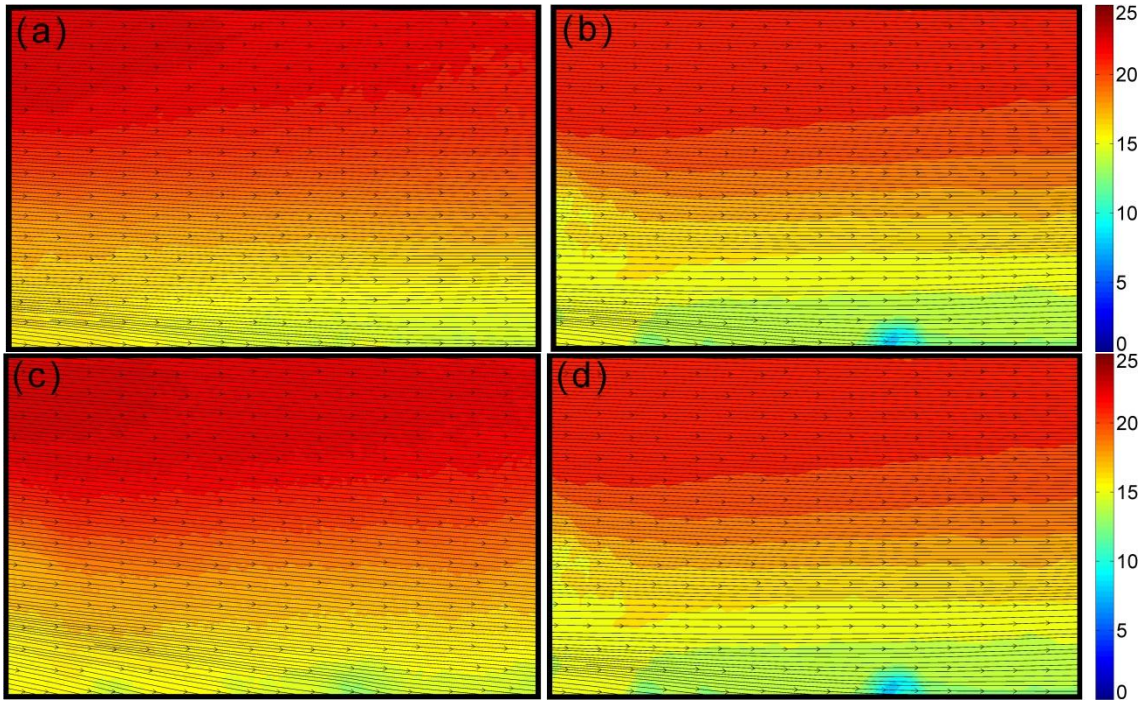

Figure 5.14. The mean velocity magnitude and the streamlines by using PIV programs of: (a) VKI by using 64x64 interrogation area; (b) ECoMMFiT by using 64x64 interrogation area; (c) VKI by using 32x32 interrogation area; (d) ECoMMFiT by using 32x32 interrogation area.

Figure 5.15 shows the vorticity and streamlines velocity fields of the planes over the 6th fin of the heat exchanger and its corresponding downstream at 40 m/s speed of the wind tunnel. The results of the measurements done over the 6th fin of the heat exchanger presented very complex structures over the heat exchanger. The effects of the complex structures can be still observed in the downstream of the 6th fin heat exchanger plane in figure 5.15b. It is clear that the effects of the complex structures in downstream of the heat exchanger are observed less than over the 6th fin. In order to identify the effects of the heat exchanger fins in the wind tunnel, the PIV measurements have been done at different speed of the wind tunnel. The laser sheet is arranged in the middle of the heat exchanger as shown in figure 5.12c. The vorticity and streamlines velocity fields of the planes in the middle of the heat exchanger have been illustrated in figure 5.16. It has been

observed that if the velocity of the wind tunnel is higher, less effect of the complex structures is occurred around the fins. However, the downstream of the fins have been found more complex when the speed of the wind tunnel is 50 m/s as shown in figure 5.16b.

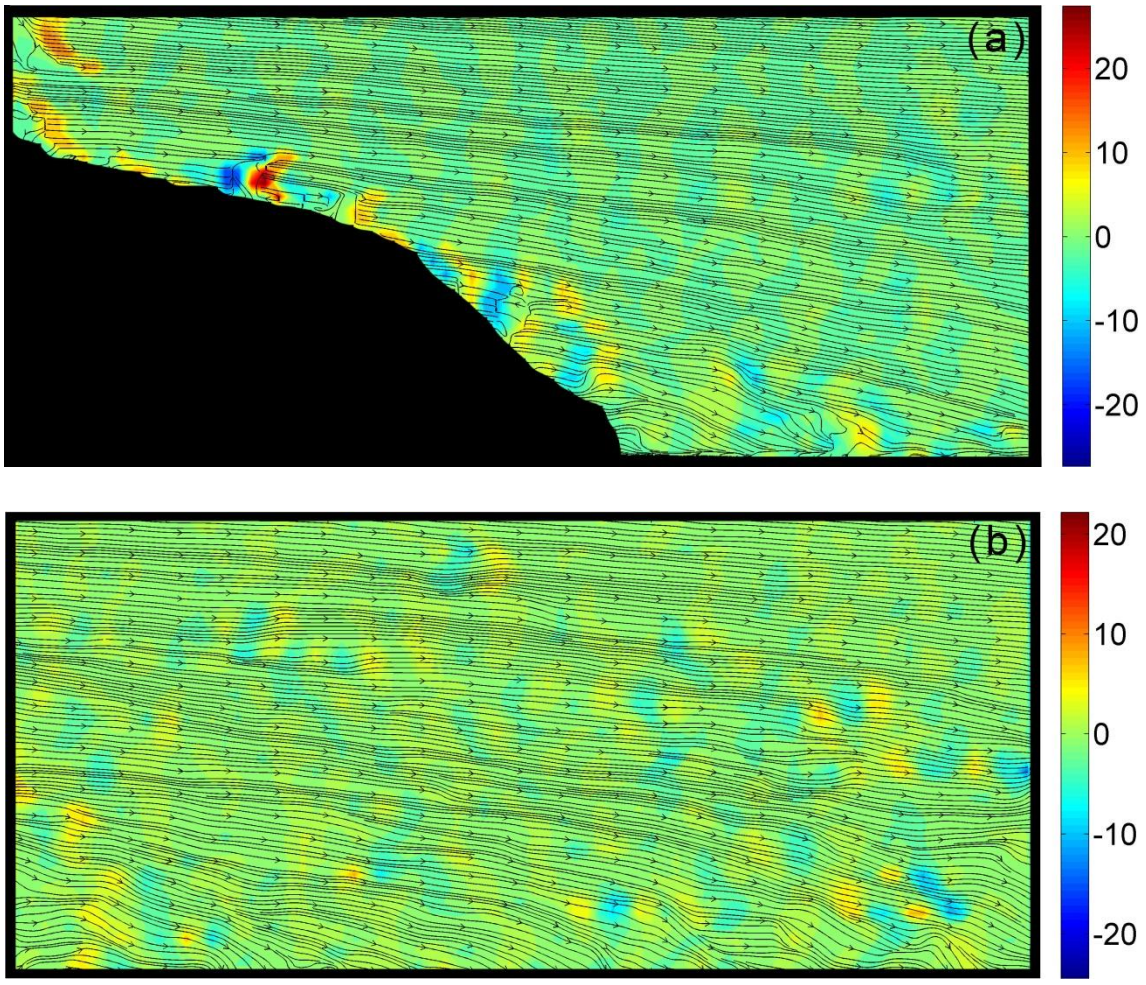

Figure 5.15. The vorticity and streamlines velocity fields in the planes of: (a) over the 6th fin of the heat exchanger; (b) over the 6th fin downstream of the heat exchanger.

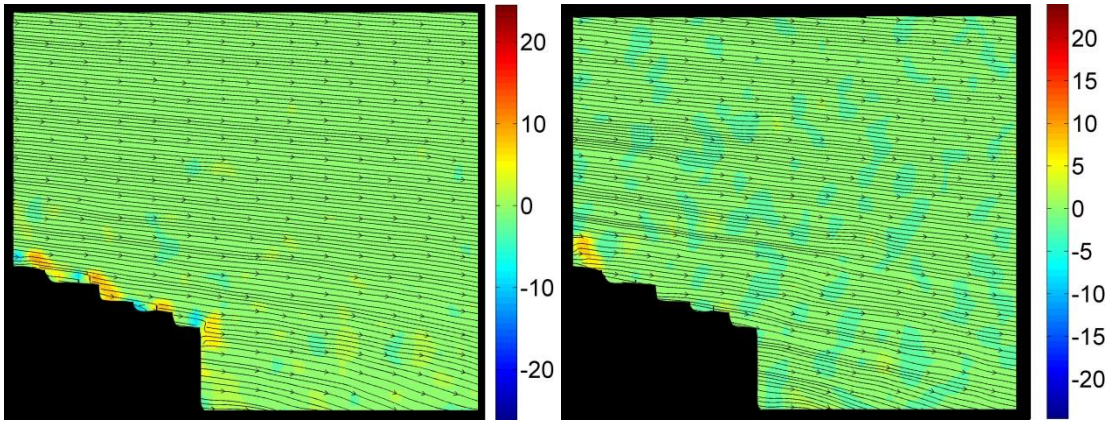

Figure 5.16. The vorticity and streamlines velocity fields in the middle plane of the heat exchanger at different velocity of the wind tunnel: (a) 40 m/s; (b) 50 m/s.

5.4.4 Horizontal plane analysis of the engine bypass flow heat exchanger

The PIV technique has been used to analyse the engine bypass flow heat exchanger in the horizontal plane. The aim is to obtain the trailing vortexes between the fins. As explained in section 6.2.1 the heat exchanger has a 3D skewed plate where the fins are placed on it annularly. The lengths of the fins, 25.5cm, are as long as the skewed plate thus it is interesting to find out the structures of the flow that passed all through the fins. Due to the complex 3D geometry of the heat exchanger, two different horizontal planes have been used to analyse the flow as shown in figure 5.17. The first horizontal plane of the laser has been arranged to the middle of the fin 1 (Figure 5.17a) and the second horizontal plane has been arranged to the middle of the fin 8 (Figure 5.17b). The purpose of the different arrangements of the laser is to identify the flow structures below and the lower sizes of the fins.

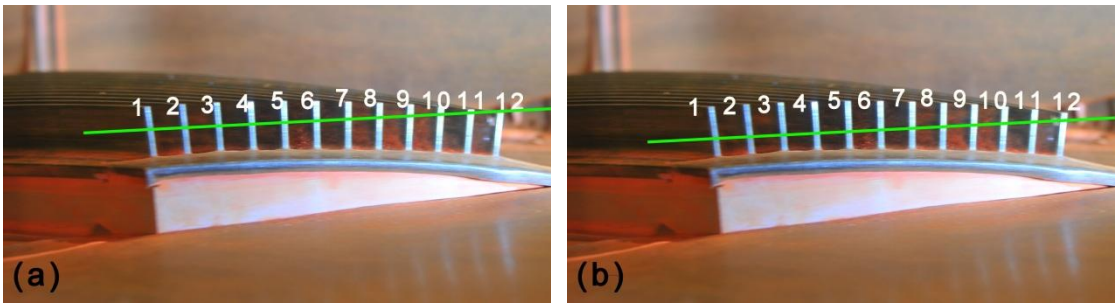

Figure 5.17. The laser sheet arrangements for the horizontal plane analysis: (a) the middle of the fin 1; (b) the middle of the fin 9.

In the PIV experiments, 600 particle images have been recorded for each series. The time difference between the two consecutive images has been set to 25μs when the velocity of the wind tunnel was 40m/s. The frame rate of the camera was 3Hz. 35mm focal length objective has been used for the camera. 300 instantaneous velocity fields with a 0.33s time difference have been obtained intermittently. When the velocity of the wind tunnel was 50m/s, the time difference between the two consecutive images has been set to 20μs with the frequency of 3Hz.

The global averaging of the flow field of the magnitude of the vertical velocity component and the streamlines of the horizontal planes are shown in figure 5.18 for the wind tunnel velocity 40 and 50 m/s. Figures 5.18a and 5.18b show the results of the 40 and 50m/s velocity of the wind tunnel respectively when the laser sheet as described in figure 5.17a. The mean flow field velocity results of the laser sheet as described in figure 5.17b has been illustrated in figures 5.18c and 5.18d for 40 and 50 m/s velocity of the wind tunnel, respectively. The size of the analyzing area is 82.3x84.6 mm^2. In the estimation of the velocity displacements 64x64 pixels interrogation area has been used with 75 % of the image overlapping. The flow from the wind tunnel comes across to the heat exchanger and passes between the fins to 25.5 cm. It has been observed that the magnitude of the velocity decreases significantly at the end of the fins. Due to the heat exchanger's skewed shape, the flow changes the direction to the left side of the heat exchanger far along the fins. The changes of the flow direction at the velocity of the wind tunnel 50m/s can be seen more distinct than at the velocity of the wind tunnel 40m/s.

When the laser sheet is in the middle of the 1st fin as shown in figure 5.17a, the flow changes the direction till the 8th fin. On the other case as shown in figure 5.17b, the changes of the flow direction is observed far away from the end of the fins. Furthermore, many saddle points have been observed in the results that infer the highly three dimensionality of the flow for the complex geometry of the heat exchanger. In this study, only two-dimensional flow analysis has been considered for the first time analysis of the engine bypass flow heat exchanger.

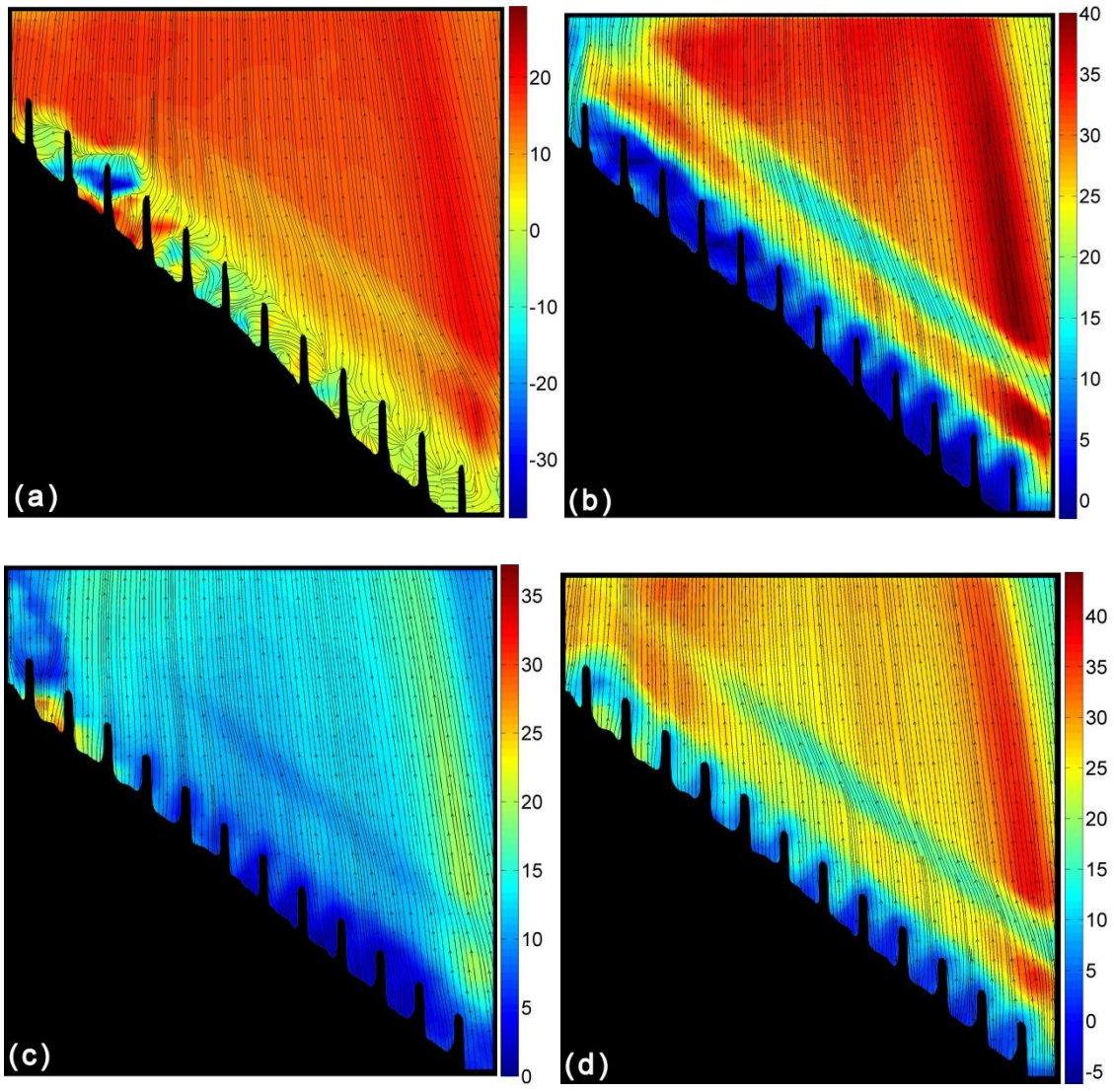

Figure 5.18. The mean flow field of the magnitude of the vertical velocity component and the streamlines of the horizontal planes for the different wind tunnel velocities: (a) at 40m/s and the laser sheet in the middle of the 1st fin (see figure 5.17a); (b) at 50m/s and the laser sheet in the middle of the 1st fin (see figure 5.17a); (c) at 40m/s and the laser sheet in the middle of the 8th fin (see figure 5.17b); (d) at 50m/s and the laser sheet in the middle of the 8th fin (see figure 5.17b).

Turbulent characteristics of the engine bypass flow heat exchanger have been evaluated by PIV data. In the velocity displacement estimations, 64x64 pixels interrogation area has been used by considering enough particles in each windows size. Table 5.1 indicates the experimental cases for the turbulent characteristics of the flow analysis. The spatial resolution of the each PIV experimental cases is 0.14mm/pixel. It has been used 600 recorded PIV images for each experimental case for the statistical analysis.

Table 5.1. Experimental case studies for the turbulent characteristic of the flow analysis.

Case	Horizontal plane sheet	Velocity (m/s)	Spatial resolution (mm/pixel)	Number of recorded images	Δt (μs)
1	middle of the 1st fin	40	0.14	600	25
2	middle of the 1st fin	50	0.14	600	20
3	middle of the 8th fin	40	0.14	600	25
4	middle of the 8th fin	50	0.14	600	20

The calculations have been done as explained in the chapter 2 in the section 2.3.2. The spatial characteristics of the flow have been obtained by two point autocorrelation function, R_{yy}, along the Line A as indicated in the figure 5.19. The length scale characteristics have been estimated by using 300 instantaneous velocity vectors for each experimental case as indicated in Table 5.2.

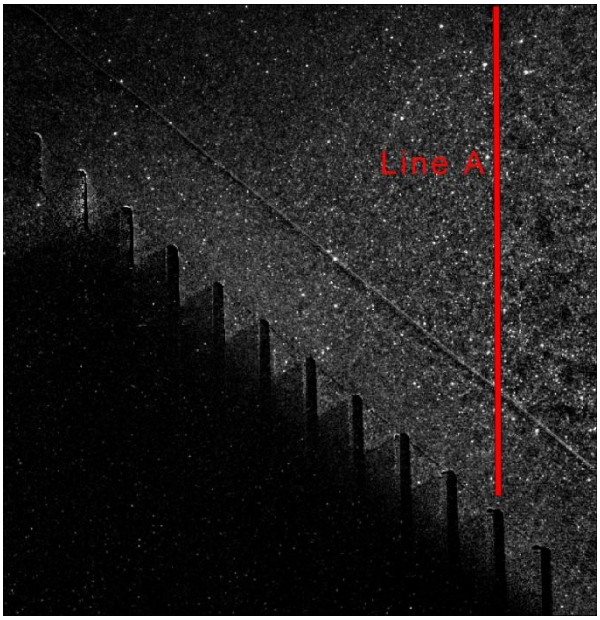

Figure 5.19. Sketch of Line A for the estimation of spatial characteristics.

Table 5.2. Summary of the turbulent length scale characteristic of the flow in the Line A for different experimental cases.

Case	λ_T (mm)	I_L (mm)	η (mm) by Eq. 2.6	η (mm) by Eq. 2.7
1	3.3	4.4	0.35	0.37
2	5.7	13.4	0.43	0.40
3	5.8	12.8	0.58	0.56
4	5.3	11.6	0.48	0.46

The turbulent length scales show that there is a relation between the length scales as spatial resolution$<\eta<\lambda_T<l_L$. According to the Kolmogorov's hypothesis, the Kolmogorov length scale can be estimated by two parameters: dissipation rate, ε, and kinematic viscosity, *v*. In this study, the kinematic viscosity of the air is calculated as 14.4x10-6 m2/s. The dissipation rate has been estimated by assuming homogeneous and fully

isotropic turbulence as indicated in Eq. 2.6 and by assuming non-homogenous, but statistically isotropic as indicated in Eq. 2.7. Then, the Kolmogorov length scale is estimated by using Eq. 2.8. As indicated in table 5.2, all the estimated η are larger than the spatial resolution of the PIV data. Thus, the spatial resolution of the present PIV experiments has been found enough to estimate the dissipation rate for the turbulent analysis.

The turbulence energy dissipation has been estimated using Eq. 2.6 assuming homogeneous and fully isotropic turbulence and using Eq. 2.7 considering turbulence as non-homogenous, but statistically isotropic as explained in chapter 2. The streamlines of the instantaneous velocity fields with the vertical component velocity of the experimental cases have been illustrated in figure 5.20. In the results of the instantaneous velocity fields, it has been observed more complex flow structures. The effects of the flow structures passed through the heat exchanger fins are clearly observed by dispersing the vortex structures at the exit of the heat exchanger. According to the instantaneous velocity fields of the experimental cases 1, 2, 3 and 4, the ε contour plots obtained by using Eq. 2.6 by assuming homogeneous and fully isotropic turbulence and Eq.2.7 by assuming non-homogenous, but statistically isotropic as presented in figures 5.21 and 5.22 respectively. In both figures, it has been obtained that the velocity fluctuation is not negligible very near the leading edge where very strong velocity gradient exists. Figure 5.21 shows the results calculated by the simple assumption in order to estimate the dissipation rate. The estimated dissipation rate values obtained considering this assumption are overestimated (Sharp and Kim 2001 and Micheletti et al. 2000). Figure 5.22 shows the ε contour plot obtained using Eq. 2.7. The dissipation rate estimated by Eq. 2.6 and Eq. 2.7 that has the same spatial resolution, 0.14 mm, are slightly different. The energy dissipation obtained with Eq. 2.6 presents high values ($\varepsilon > 2$). On the other side, the energy dissipation obtained with Eq. 2.7 shows more regular distribution and more available data of ε with values decreasing with the distance from the heat exchanger fins.

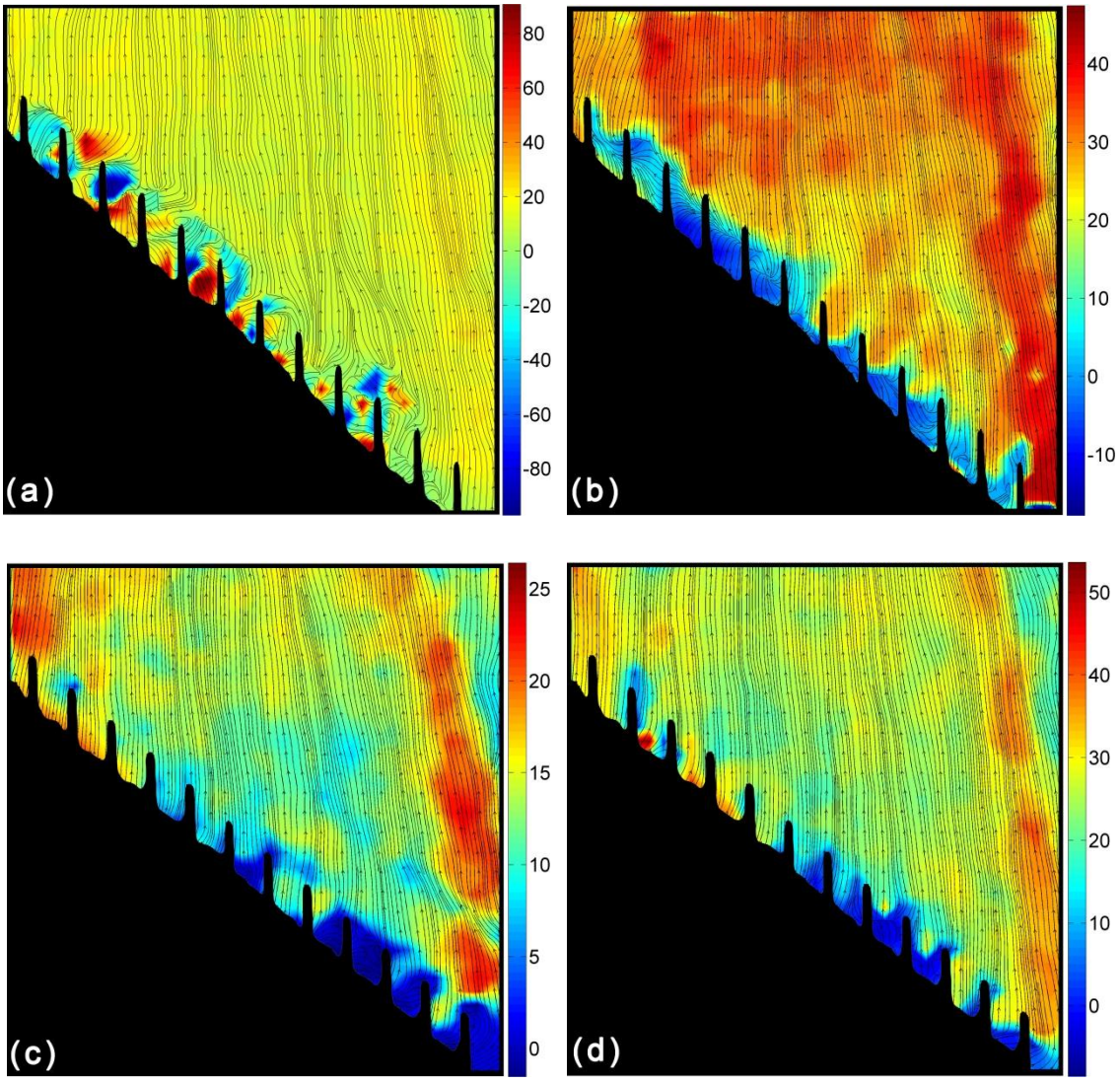

Figure 5.20. The instantaneous velocity field of the magnitude of the vertical velocity component and the streamlines for the different experimental cases: (a) Case 1; (b) Case 2; (c) Case 3; (d) Case 4.

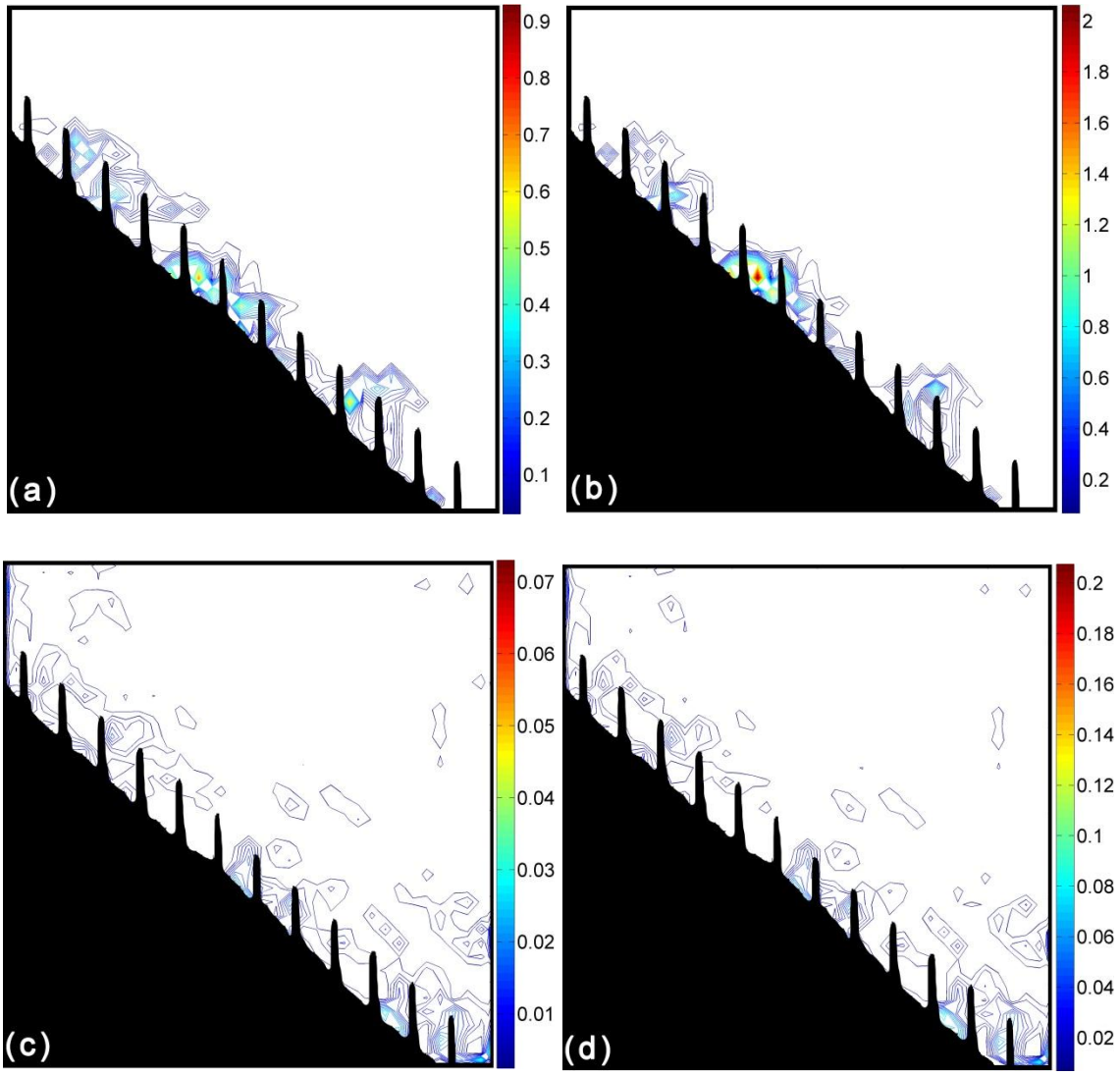

Figure 5.21. Contour plot of the turbulence energy dissipation, ε, using 250 phase-averaged images used for the different wind tunnel velocities and calculated by Eq. 2.6: (a) Case 1; (b) Case 2; (c) Case 3; (d) Case 4.

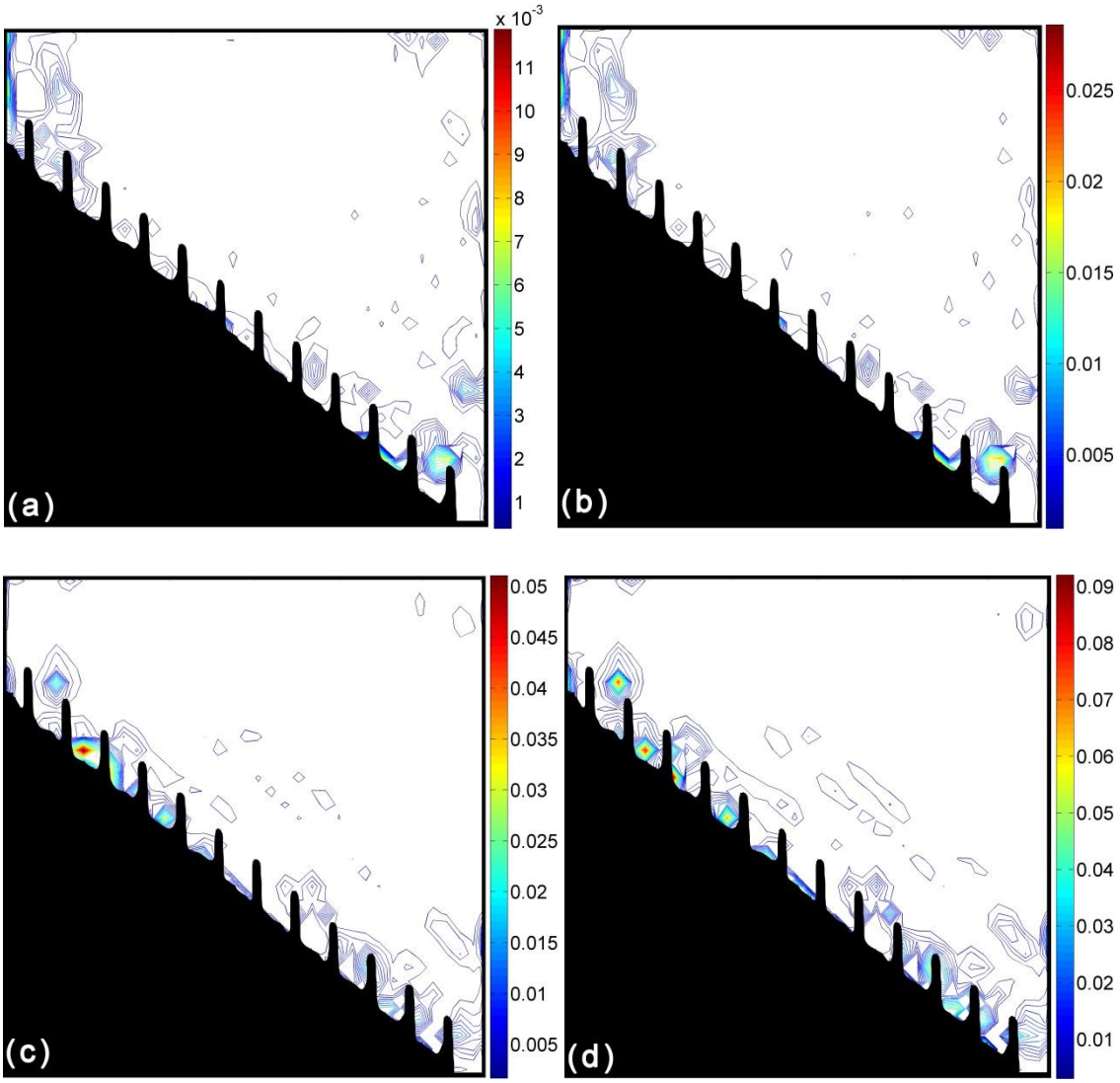

Figure 5.22. Contour plot of the turbulence energy dissipation, ε, using 250 phase-averaged images used for the different wind tunnel velocities and calculated by Eq. 2.7: (a) Case 1; (b) Case 2; (c) Case 3; (d) Case 4.

5.5 Summary and conclusions

The PIV technique with the different seeding particles has been efficiently used to analyse the bypass flow over the heat exchanger configuration. The heat exchangers used in this study were specifically design for the turbofan engines to improve the thermal management of future aircraft power plants. The heat exchanger was placed in the beginning of the bypass air flow section to provide an efficient air-cooled oil cooler for the lubricating system of the turbofan. However it was necessary to investigate the turbulence effects of the heat exchangers on the bypass air flow of the engine. The fluorescent particles and the glass sphere particles have been used as flow seeding for PIV technique to analyse the flow structures that exists the heat exchanger and determine the bypass flow surrounding the heat exchanger geometry.

The knowledge on the flow structures of the interaction between the bypass flow and the heat exchangers might lead to use an efficient heat exchanger type for the applications. To obtain a prior knowledge on the effects of the heat exchangers, the PIV measurements have been performed with the vertical and horizontal planes of the surrounding the heat exchangers in a low speed wind tunnel at the Von Karman Institute. The wind tunnel has the closed circuit that gives the advantage to collect the seeding particles for further use in different experimental conditions.

The velocity field of the flow has been extracted from the PIV data and collected for further comparisons. The turbulent analyses have been performed at different velocity of the wind tunnel in the horizontal plane analysis of the heat exchanger.

CHAPTER VI
CONCLUSIONS

The state of the art of the thesis explained in Chapter 1. The principles and basic set-up of the PIV technique have been described, giving some details about the tracer particles. The details about the time-resolved PIV technique has been explained to get accurate velocity vectors from the PIV images by discussing tracer particles, image pre-processing, interrogation area, estimation of displacement and data validation method implemented. Briefly, the particle images have been pre-processed using a clean-up mask to remove or to reduce undesired light reflections and to homogenize the median illumination. The triple image correlation method with the implementation of LFC method has been used to obtain the average displacement of the ensemble particles from the particle image series. The triple image correlation algorithm has improved the peak correlation in moving parts that appear in the image. In order to detect and remove spurious vectors, a validation algorithm has been implemented for the post processing of the images. The PIV technique has been successfully applied to the study of complex flow systems. The focus has been done in the interaction of fluid and the moving solid parts and in low speed air flow system. The ECommFiT PIV software has been adjusted to be able analyse flow systems with moving solid parts. An efficient methodology for estimation of turbulent statistics from PIV experimental data has been implemented to the software program. The procedure to estimate the turbulent scales of the flows in complex systems that contain rotating parts has been explained. It has been clarified some of the small-scale characteristics and turbulent structures in complex flow systems by performing two-dimensional field measurements using PIV. The error estimations in

measurement of the velocity vectors and the dissipation rate have been explained by considering the effect of number of samples employed in the ensemble-averaging of the velocities. The total error of the measurements has been estimated for different experimental cases by using image series as instantaneous and various numbers of phase-averaged images. It has been found that the measurement error tends to decrease if more image series are used in the phase-averaged (ensemble) averaging process.

The alginate particles with/without fluorescein compound imbedded have been developed as a new alternative flow seeding elements for PIV applications in Chapter 3. The alginate micro particles have been efficiently used in PIV as tracer particles for different experiment facilities and different fluids such as water, air, and oil to analyse the complex flows. The development and description of the production process of the alginate tracer particles have been explained briefly. It has been found that the alginate micro particles have many advantages over traditional ones used in PIV systems. Furthermore, it has been demonstrated that the alginate particles can be employed as efficient and economical way in all kind of PIV applications in liquid or gas flows. The PIV method with the alginate particles can be used in systems which have containing parts made of metal as they do not cause any damage. The particles are spherical and furthermore non-toxic and environmentally friendly, and as they are porous, their density can be easily matched to that of the fluid so that they follow the fluid efficiently.

A comprehensive study on the three-dimensional flow analysis of the external gear pump has been done by time-resolved PIV technique to investigate its turbulent flow dynamics and statistics in Chapter 4. The applied experimental techniques have established a method that allows visualizing the flow inside the gear pump with a high rotational velocity system. The results have displayed the periodical behaviour of the flow corresponding with periodical movement of the gears. Instantaneous and conditional (phase-locked) ensemble average velocity field data for a single phase of the gear position have been obtained in different planes. Phase-locked ensemble average values have been computed at different phases of the gear position. Time evolution of the average motion has showed that the direction of the velocity patterns changes as a function of the movement of the gearwheel. The influence of the rotating gears has been

observed in the variation of back flows from the phase-locked ensemble averages profiles. The flow rate through the pump and its relationship with the gear position has been obtained from the phase-locked ensemble average profiles. Vorticity and high turbulent kinetic energy areas have been identified inside the external gear pump.

The PIV technique has been efficiently applied to analyse an engine bypass flow heat exchanger in a low speed wind tunnel in Chapter 5. The heat exchanger used in this thesis has been specifically designed for the turbofan engines to improve the thermal management of future aircraft power plants. Two different tracer particles; the glass particles and the fluorescent particles have been used in the experiments in order to improve substantially the PIV image quality and further analysing the small-scale structures of the flow. The preliminary application of the PIV technique to this specific heat exchanger geometry in the low speed wind tunnel has been done by using alginate micro particles. The appropriate set-up conditions of the PIV technique have led to obtain the PIV data collection for the incompressible turbulent study on bypass flow over the heat exchanger. Furthermore alginate micro particles containing fluorescein have been found the most efficient alternative as flow seeding in this type of flow.

In future, different configuration of the external gear pump geometry will be analysed and compare with the existing one in order to find out and improve its performance. Alginate particles containing fluorescein will be applied as flow seeding in order to investigate the engine bypass flow heat exchanger in transonic wind tunnel. Furthermore, alginate particles containing fluorescein will be used to study heat and velocity of the experimental flow systems by using PIV/PLIF techniques simultaneously.

CONCLUSIONS

REFERENCES

Adrian RJ, Scattering particle characteristics and their effect on pulsed laser measurements of fluid flow: speckle velocimetry vs particle image velocimetry, Applied Optics, 23; 1690-1691, 1984.

Adrian RJ, An image shifting technique to resolve directional ambiguity in double-pulsed velocimetry, Applied Optics, 25; 3855-3858, 1986.

Adrian RJ, Multi-point optical measurements of simultaneous vectors in unsteady flow: a review, Int J Heat Fluid Flow, 7: 127-145, 1986.

Adrian RJ, Particle imaging techniques for experimental fluid mechanics, Annu Rev Fluid Mech, 23: 261-304, 1991.

Adrian RJ, Particle-imaging techniques for experimental fluid mechanics, Annual Rev Fluid Mech, 23; 261-304, 1991.

Adrian RJ, Twenty years of particle image velocimetry, Exp Fluids, 39: 159-169, 2005.

Adrian RJ, Yao CS, Pulsed laser technique application to liquid and gaseous flows and the scattering power of seed materials, Applied Optics, 24; 44-52, 1985.

Ammourah S, Aroussi A, Vloeberghs M, A PIV study of the cerebrospinal fluid dynamics in a model of the human ventricular system, In: Proceedings of the 12th international symposium on applications of laser techniques to fluid mechanics, Lisbon, 2004.

Anderson MG, Alford WE, Trego ML, Haugland R, Winstanley DK, Cooling systems for use on aircraft, Honeywell International, Inc., Pub. No: US 2008/0314047 A1, 2008.

Angarita-Jaimes D, Ormsby M, Chennaoui M, Angarita-Jaimes N, Towers C, Jones A, Towers D, Optically efficient fluorescent tracers for multi-constituent PIV, Exp Fluids, 45; 623-631, 2008.

REFERENCES

Aslani P, Kennedy RA, Studies on diffusion in alginate gels. I. Effect of cross-linking with calcium or zinc ions on diffusion of acetaminophen. Journal of Controlled Release 42:75-82, 1996.

Baldi S, Hann D, Yianneskis M, On the measurement of turbulence energy dissipation in stirred vessels with PIV techniques, Meas Sci Technol, 7; 1334-1348, 1996.

Baldi S, Yianneskis M, On the quantification of energy dissipation in the impeller stream of a stirred vessel from fluctuating velocity gradient measurements, Chemical Engineering Science, 59; 2659–2671, 2004.

Barker DB, Fourney ME, Measuring fluid velocities with speckle patterns, Optics Letters 1: 135-137, 1977.

Barnhart DH, Adrian RJ, Papen GC, Phase conjugate holographic system for high resolution particle image velocimetry, Appl Opt, 33: 7159-7170, 1994.

Barnhart DH, Chan VSS, Halliwell NA, Coupland JM, Design and construction of the recording camera and interrogation assembly, In: Proceedings International Symposium on Optical Science Engineering and Instrumentation, Paper No. 3783-17, Denver, USA, 1999.

Barnhart DH, Halliwell NA, Coupland JM, Holographic particle image velocimetry: analysis using a conjugate reconstruction geometry, Optics & Laser Technology, 32: 527-533, 2000.

Bennett TJ, Fundamentals of Fluorescein Angiography, http://opsweb.site-ym.com/?FA, 2011.

Borghi M, Milani F, Paltrinieri F, Zardin B, Pressure transients in external gear pumps and motors meshing volumes, In: Proceedings of the SAE Commercial Vehicle Eng. Conf., Washington, DC, 2005.

Borghi M, Milani F, Paltrinieri F, Zardin B, The influence of cavitation and aeration on gear pumps and motors meshing volumes pressures, In: Proceedings of the ASME Int. Mech. Eng. Congr. Expo., Chicago, IL, 2006.

Borghi M, Paltrinieri F, Zardin B, Milani M, External gear pumps and motors bearing blocks design: influence on the volumetric efficiency, In: Proceedings of the 51st Nat. Conf. Fluid Power, 2008.

Brennen CE, Fundamentals of Multiphase Flow, Cambridge University Press, 2005.

Brunn HH, Hot-wire anemometry: principles and signal analysis, Oxfor University Press, 1995.

Bryanston-Cross PJ, The application of PIV (particle image velocimetry) to transonic flow measurements, CH34827-95/0000-53.1, IEEE, 1995.

Bryanston-Cross PJ, Harasgama SP, Towers CE, Judge TR, Towers DP, Hopwood ST, The application of particle image velocimetry in a short duration transonic annular turbine cascade, Journal of Turbomachinery, 114; 504-509, 1992.

Bryanston-Cross PJ, Judge TR, Quan C, Pugh G, Corby N, The application of digital particle image velocimetry (dpiv) to transonic flows, Progress in Aerospace Sciences, 31; 273-290, 1995.

Buchhave P, Particle image velocimetry: status and trends, Experimental Thermal and Fluid Science, 5: 586-604, 1992.

Casoli P, Vacca A, Berta GL, Optimization of relevant design parameters of external gear pumps, In: Proceedings of the 7th JFPS International Symposium on Fluid Power, Toyama, 2008.

Castilla R, Gamez-Montero PJ, Ertürk N, Vernet A, Coussirat M, Codina E, Numerical simulation of turbulent flow in the suction chamber of a gearpump using deforming mesh and mesh replacement, International Journal of Mechanical Sciences, 52; 1334-1342, 2010.

Castilla R, Gamez-Montero PJ, Huguet D, Codina E.Turbulence in internal flows in mini hydraulic components, CIMNE, 241–51, 2005.

REFERENCES

Castilla R, Wojciechowski J, Gamez-Montero PJ, Vernet A, Codina E, Analysis of the turbulence in the suction chamber of an external gear pump using Time Resolved Particle Image Velocimetry, Flow Measurement and Instrumentation, 19; 377–384, 2008.

Chow Y, Uzol O, Katz J, Flow nonuniformities and turbulent "hot spots" due to wake-blade and wake-wake interactions in a multi-stage turbomachine, ASME J Turbomach, 124; 553-563, 2002.

Copenhaver W, Estevadeordal J, Gogineni S, Gorell S, Goss L, DPIV study of near-stall wake-rotor interactions in a transonic compressor, Exp Fluids, 33; 899-908, 2002.

Cornet A, Raimarckers N, Bajusz D, Heat exchange system in a turbomachine, Techspace Aero S.A., Milmort, Belgium, Pub. No: US 2009/0159246 A1, 2009.

Coupland JM, Halliwell JA, Particle image velocimetry: three-dimensional fluid velocity measurements using holographic recording and optical correlation, Appl Opt 31: 1005-1007, 1992.

Day SW, McDaniel JC, PIV Measurements of Flow in a Centrifugal Blood Pump: Steady Flow Journal of Biomechanical Engineering, 127: 244-253, 2005.

Dearn R, The fine art of gear pump selection and operation. World Pumps, 417: 38–40, 2001.

Delafosse A, Collignon ML, Crine M, Toye D, Estimation of the turbulent kinetic energy dissipation rate from 2D-PIV measurements in a vessel stirred by an axial Mixel TTP impeller, Chemical Engineering Science, 66; 1728-1737, 2011.

Deschênes C, Ciocan GD, De Henau V, Flemming F, Huang J, Koller M, Naime FA, Page M, Qian R, Vu T, General overview of the axial T project: a partnership for low head turbine developments, IOP Conf. Series: Earth and Environmental Science, 12; 012043, 2010.

Dierksheide U, Meyer P, Hovestadt T, Hentschel W, Endoscopic 2D-PIV flow field measurements in IC engines, In: Proceedings of 4th international symposium on Particle Image Velocimetry, Paper no:1060, Germany, 2001.

Doolan FN, Coton FN, Galbraith, RAMcD, Measurement of three-dimensional vortices using a hot wire anemometer, AIAA Paper No. 99-3810, 1999.

Ducci A, Yianneskis M, Direct determination of energy dissipation in stirred vessels with two-point LDA, AIChE Journal, 51; 2133-2149, 2005.

Dudderar TD, Meynart R, Simpkins PG, Full-field laser metrology for fluid velocity measurement, Opt Lasers Eng, 9: 163-199, 1988.

Dudderar TD, Simpkins PG, Laser Speckle Photography in a Fluid Medium, Nature, 270; 45-47, 1977.

Eaton M, Keogh PS, and Edge KA, The modelling, prediction, and experimental evaluation of gear pump meshing pressures with particular reference to aero-engine fuel pumps, J Systems and Control Engineering, Proc IMechE, 220: 365-379, 2006.

Edge KA, Keogh PS, Eaton M, Modelling and simulation of pressures within the meshing teeth of gear pumps, In: Proceedings of the Int. Conf. Recent Advances in Aerospace Actuation Systems and Components, Toulouse, France, 2001.

Elovic E, Cooling air cooler for a gas turbofan engine, General electric company, Cincinnati, Ohio, USA, Pub. No: US 004254618, 1981.

Ertürk N, Vernet A, Ferre JA, Castilla R, Codina E, Analysis of the turbulent flow of an external gear pump by time resolved particle image velocimetry, In proceeding: 14th Int. Symp. on applications of laser techniques to fluid mechanics, Lisbon, Portugal, 2008.

Ertürk N, Vernet A, Castilla R, Gamez-Montero PJ, Ferre JA, Experimental analysis of the flow dynamics in the suction chamber of an external gear pump, International Journal of Mechanical Sciences, 53; 135-144, 2011.

Ertürk N, Vernet A, Pallares J, Castilla R, Raush G, Small-scale characteristics and turbulent statistics of the flow in an external gear pump by Time-Resolved PIV, Flow measurement and instrumentation, article submitted, 2012.

REFERENCES

Ertürk N, Vernet A, Uso de alginatos en velocimetría por imágenes de partículas y procedimiento para medir la velocidad de un fluido, Oficina Española de Patentes y Marcas (OEPM), Número de solicitud: P201132029, 2011.

Esquisabel A, Hernández RM, Igartua M, Gascón AR, Calvo B, Pedraz JL, Effect of lecithins on BCG-alginate-PLL microcapsule particle size and stability upon storage, Journal of Microencapsulation, 17:363-72, 2000.

Estevadeordal J, Gogineni S, Goss L Copenhaver W, Gorell S, Study of wake-blade interactions in transonic compressor using flow visualization and DPIV, ASME J Fluids Eng, 124; 166-175, 2002.

Etebari A, Akle B, Farinholt K, Bennett M, Leo D, Vlachos P, The use of active ionic polymers in dynamic skin friction measurements, In: Proceedings of the 2004 ASME heat transfer/fluids engineering summer conference, 2004b.

Etebari A, Carneal J, Vlachos P, On the accuracy of wall shear stress using DPIV, In: Proceedings of the 2004 ASME heat transfer/fluids engineering summer conference, 2004a.

Falfari S, Pelloni P, Setup of a 1D model for simulating dynamic behavior of external gear pumps, SAE Technical Paper, 2007-01-4228, 2007.

Foucaut JM, Stanislas M, Some considerations on the accuracy and frequency response of some derivative filters applied to particle image velocimetry vector fields, Meas Sci Technol, 13; 1058-1071, 2002.

Fouras A, Soria J, Accuracy of out-of-plane vorticity measurements derived from in-plane velocity field data, Exp Fluids, 25; 409-430, 1998.

Gabriele A, Nienow A, Simmons M, Use of angle resolved PIV to estimate local specific energy dissipation rates for up- and down-pumping pitched blade agitators in a stirred tank, Chemical Engineering Science, 64; 126-143, 2009.

Geis T, Rottenkolber G, Dittmann M, Richter B, Dullenkopf K, Wittig S, Endoscopic PIV-measurements in a enclosed rotor–stator system with pre-swirled cooling air, In:

Proceedings of 11th Int. Symp. on Apps. of Laser Tech. to Fluid Mech., Paper no: 26.4, Portugal, 2002.

Grant I, Particle image velocimetry: a review, Proc Instn Mech Engrs, 211: 55-76, 1997.

Grant I, Pan X, Wang X, Stewart N, Correction for viewing angle applied to PIV data obtained in aerodynamic blade vortex interaction studies, Exp Fluids, 18; 95-99, 1994.

Grant I, Smith GH, Liu A, Infield D, Eich T, Particle image velocimetry measurements of the aerodynamics of a wind turbine, In: Proceedings of International congress on instrumentation in aerospace simulation facilities, Rockville, MD, USA, 1991.

Grousson R, Mallick S, Study of the Flow Pattern in a Fluid by Scattered Laser Light, Applied Optics, 16; 2334-2336, 1977.

Hand DP, Entwistle JD, Maier RRJ, Kuhn A, Greated CA, Jones JDC, Fibre optic beam delivery system for high peak power laser PIV illumination, Meas Sci Technol, 10; 239-245, 1999.

Hart DP, The elimination of correlation errors in PIV processing, In: Proceedings of the 9th international symposium on applications of laser techniques to fluid mechanics, Lisbon, Portugal, July, 1998.

Hart DP, PIV error correction, Exp Fluids, 29; 13-22, 2000.

Hart DP, Super-resolution PIV by recursive local-correlation, J Visualization, 10: 1-10, 1999.

Heintz N, Hendrick P, Charlier J, Bajusz D, Raimarckers N, Development and testing of advanced surface coolers for aero engines, In Proceeding: 20th International Society for Air Breathing Engines, Sweden, 2011.

Hill DF, Sharp KV, Adrian RJ, Stereoscopic particle image velocimetry measurements of the flow around a Rushton turbine, Exp Fluids, 29; 478-485, 2000.

Hinze JO, Turbulence, McGraw-Hill, New York, 1975.

REFERENCES

Hjertager LK, Hjertager BH, Deen NG, Solberg T, Measurement of turbulent mixing in a confined wake flow using combined PIV and PLIF, Canadian Journal of Chemical Engineering, 81; 1149-1158, 2003.

Hooke CJ, Kakoullis YP, On-line measurement of film thickness, In: Proceedings of the Conference on Instruments and Computers for Cost Effective Fluid Power Testing, Institution of Mechanical Engineers, Paper C128/79, pp. 51–59, 1979.

Hopkins LM, Kelly JT, Wexler AS, Prasad AK, Particle image velocimetry measurements in complex geometries, Exp in Fluids, 29; 91-95, 2000.

Horvath IA, PIV Data processing by Rabon manual, Rhode Saint Genese, Von Karman Institute, 2011.

Horvath IA, PIV Image Pre-processing by Tücsök manual, Rhode Saint Genese, Von Karman Institute, 2011.

Hou YX, Clemens NT, Dolling DS, Wide-field PIV study of shock induced turbulent boundary layer separation. AIAA J, 441:6–9, 2003.

Houzeaux G, Codina RA, Finite element method for the solution of rotary pumps, Comput Fluids, 36: 667–79, 2007

Huang H, Dabiri D, Gharib M, On errors of digital particle image velocimetry, Meas Sci Technol, 8; 1427-1440, 1997.

Huang KJ, Lian WC, Kinematic flow rate characteristics of external spur gear pumps using an exact closed solution, Mech Mach Theory, 44; 1121-1131, 2009.

Huchet F, Line A, Morchain J, Evaluation of local kinetic energy dissipation rate in the impeller stream of a Rushton turbine by time-resolved PIV, Chemical Engineering Research and Design, 87; 369-376, 2009.

Hunt JCR, Vassilicos JC, Kolmogorov's contributions to the physical and geometrical understanding of small-scale turbulence and recent developments, Proc R Soc Lond, 434: 183-210, 1991.

Hunter WW, Nichols CE, Wind tunnel seeding systems for laser velocimeters, NASA conference publication 2393, NASA, Langley, 1985.

Iliescu MS, Ciocan GD, Avellan F, Analysis of the cavitating draft tube vortex in a Francis turbine using particle image velocimetry measurements in two-phase flow, J Fluids Eng, Vol. 130, issue 2, 021105, 2008.

Ivantysyn J, Ivantysynova M, Hydrostatic Pumps and Motors. New Delhi, India: Academia Books International, 2001.

Iyoi H, Ishimura S, χ - theory in gear geometry. J Mech Transm TASME, 105: 286–90, 1983.

Jin S, Huang P, Park J, Yoo JY, Breuer KS, Near-surface velocimetry using evanescent wave illumination, Exp Fluids, 37; 825-833, 2004.

Katz J, Microscopic particles containing imbedded fluorescent dyes and use thereof in particle image velocimetry, United States patent, Number: 5,124,071, 1992.

Kazushi K, Tetsuo S, Norihumi N, Morio S, Ryusaku Y, Takashi Y, Katsumi M, Hashasen NI, Zasshi G, C.A. V.123, 208665m 55:300-304, 1995.

Keane RD, Adrian RJ, Theory of cross-correlation analysis of PIV images, Applied Scientific Research, 49; 191-215, 1992.

Kim CK, Lee EJ, The controlled release of blue dextran from alginate beads. Int J Pharm, 79:11-19, 1992.

Koc E, Kurban AO, Hooke CJ, An analysis of the lubrication mechanism of the bush-type bearings in high pressure pumps, Tribology International, 30; 553-560, 1997.

Koc E, Hooke CJ, An experimental investigation into the design and performance of hydrostatically loaded floating wear plates in gear pumps, Wear, 209; 184-192, 1997.

REFERENCES

Koike S, Hidemi T, Koichi T, Mitsutomo H, Kenichi T, Goro M, Correction method for particle velocimetry data based on the Stokes Drag Law, AIAA Journal, 45; 2770-2777 , 2007.

Kompenhans J, Höcker R, Application of particle image velocimetry to high speed flows, Particle Image Displacement Velocimetry, von Karman Institute for Fluid Dynamics, pp. 67-84, 1998.

Kresta S, Wood P, The flow field produced by a pitched blade turbine: characterization of the turbulence and estimate of the dissipation rate, Chem Eng Sci, 48: 1761-1774, 1993.

Lai WT, Menon RK, Flow measurements in microchannels using a MicroPIV system, In: Proceedings of the 15th Australasian fluid mechanics conference, Australia, 2004.

Lang H, Mørck T, Woisetschläger J, Stereoscopic particle image velocimetry in a transonic turbine stage, Exp Fluids, 32; 700-709, 2002.

Lang N, Investigation of the supersonic flow field around a delta wing using particle image velocimetry, In: Proceedings of the 10th international symposium on applications of laser techniques to fluid mechanics, Lisbon, 2000.

Lauterborn W, Vogel A, Modern optical techniques in fluid mechanics, Annu Rev Fluid Mech, 16: 223-244, 1984.

Lavoie G, Avallone F, De Gregorio F, Romano GP, Antonia RA, Spatial resolution of PIV for the measurement of turbulence, Exp Fluids, 43; 39-51, 2007.

Lawson NJ, Wu J, Three-dimensional particle image velocimetry: error analysis of stereoscopic techniques, Meas Sci Technol, 8; 897-900, 1997.

Lecordier B, Trinite M, Time resolved PIV measurements for high speed flows, In: Proceedings of the third international work shop on particle image velocimetry, Santa Barbara, CA, 1999.

Lecuona A, Nogueria J, Rodriguez PA, Accuracy and time performance of different schemes of the local field correction PIV technique, Exp Fluids, 33: 743-51, 2002.

Lee GM, Palsson BO, Stability of antibody productivity is improved when hybridoma cells are entrapped in calcium alginate gel beads, Biotechnol Bioeng, 42:1131-35, 1993.

Lim F, Sun AM, Microencapsulated islets as bioartificial endocrine pancreas, Science 210:908-10, 1980.

Linke-Diesinger A, Systems of commercial turbofan engines: an introduction to systems functions, Springer-Verlag, Berlin, 2008.

Liu T, Sullivan JP, Pressure and temperature sensitive paints, Springer, Berlin, 2004.

Liu ZC, Landreth CC, Adrian RJ, Hanratty TJ, High resolution measurement of turbulent structure in a channel with particle image velocimetry, Exp Fluids, 10; 301-312, 1991.

Lourenco L, Krothapalli, A On the accuracy of velocity and vorticity measurements with PIV, Exp Fluids, 18; 421-428, 1995.

Luff JD, Drouillard T, Rompage AM, Linne MA, Hertzberg JR, Experimental uncertainties associated with particle image velocimetry (PIV) based vorticity algorithms, Exp Fluids, 26; 36-54, 1999.

Lundgren TS, Ashurst WT, Area-varying waves on curved vortex tubes with application to vortex breakdown, Journal of Fluid Mechanics, 200; 283-307, 1989.

Manring ND, Kasragadda SB, The theoretical flow ripple of an external gear pump, Trans ASME, J Dyn Syst Meas Control, 125; 396-404, 2003.

Matsumoto S, Kobayashi H, Takashima Y, Production of monodispersed capsules, J Microencapsulation, 3:25-31, 1986.

Mattiason B, Immobilized cells and organelles. Roca Raton FL: CRC Press, 1:3-25, 1983.

McKenna SP, McGillis WR, Performance of digital image velocimetry processing techniques, Exp Fluids, 32; 106-115, 2002.

REFERENCES

McNiel CM, Peltier DW, Reeder MF, Crafton JW, Clean Seeding for Particle Image Velocimetry, In: Proceeding 22nd International Congress Instrumentation in Aerospace Simulation Facilities, 2007.

Mei R, Velocity fidelity of flow tracer particles, Exp Fluids, 22; 1-13, 1996.

Meinhart CD, Wereley ST, Santiago JG, PIV measurements of a microchannel flow, Exp. Fluids, 27; 414-419, 1999.

Melling A and Whitelaw JH, Seeding of gas flows for laser anemometry, DISA Information 15: 5-14, 1973

Melling A, Tracer particles and seeding for particle image velocimetry, Meas Sci Technol, 8; 1406-1416, 1997.

Meselhe EA, Peeva T, Muste MVI, Large scale particle image velocimetry for low velocity and shallow water flows, J Hydrol Eng, 130; 937-940, 2004.

Meyer KE, Velte CM, Ullum T, PIV measurements of flow structures in a spray dryer, In: Proceedings of the 9th international symposium on particle image velocimetry, Japan, 2011.

Meynart R, Digital image processing for speckle flow velocimetry, Review of Scientific Instruments, 53; 110-111, 1982.

Meynart R, Instantaneous velocity field measurements in unsteady gas flow by speckle velocimetry, Applied Optics, 22; 535-540, 1983.

Micheletti S, Baldi S, Yeoh SL, Ducci A, Papadakis G, Lee KC, Yianneskis M, On spatial and temporal variations and estimates of energy dissipation in stirred reactors, Chemical Engineering Research and Design, 82; 1188-1198, 2004.

Monji H, Sato M, Bouncing behavior of rotating cylinder on wall in water, Journal of JSEM, 10; 107-112, 2010.

Moore J, Dry sump pump bubble elimination for hydraulic hybrid vehicle systems, Master thesis in the department of Mechanical engineering, The University of Michigan, 2007.

Mumper RJ, Hoffman AQS, Puolakkainen PA, Bouchard LS, Gombotz WR, Calcium-alginate beads for the oral delivery of transforming growth factor-β_1 (TGF-β_1): stabilization of TGF-β_1 by the addition of polyacrylic acid within acid-treated beads. J. Control. Rel. 30:241-51, 1994.

Nagamura K, Ikejo K, Tutulan FG, Design and performance of gear pumps with a non-involute tooth profile, Proc IMechE, J Eng Manufac, 218; 699-711, 2004.

Naterer GF, Glockner PS, Thiele D, Chomokovski S, Venn G, Richardson G, Surface micro-grooves for near-wall exergy and flow control: application to aircraft intake de-icing, J Micromech Microeng, 15; 501-513, 2005.

Nicolaides D, Honnery D, Soria J, Measurements of velocity and vorticity in grid turbulence using PIV, In: Proceedings of 13th Australasian Fluid Mechanics Conference, Melbourne, Australia, 1998.

Nogueria J, Lecuona A, Rodriguez PA, Data validation, false vectors correction and derived magnitudes calculations on PIV data, Meas Sci Technol, 8: 1493-501, 1997.

Nogueira J, Lecuona A, Rodriguez PA, Local field correction PIV: on the increase of accuracy of digital PIV systems, Exp Fluids, 27; 107-116, 1999.

Nogueria J, Lecuona A, Rodriguez PA, Local field correction PIV, implemented by means of simple algorithms, and multigrid versions, Meas Sci Technol, 12: 1911-21, 2001.

Nogueria J, Lecuona A, Rodriguez PA, Limits on the resolution of correlation PIV iterative methods, Exp Fluids, 39: 305-13, 2005.

Ohmi K, Li HY, Particle-tracking velocimetry with new algorithms, Meas Sci Technol, 11; 603-616, 2000.

REFERENCES

Olver B, Ciampa A, Marrano R, Trepanier R, Lamarre S, Bernard M, Germain P, Turbofan bypass duct air cooled fluid cooler installation, Pratt and Whitney Canada Corp., Pub. No: US 2008/0053059A1, 2008.

Parobek DM, Boyer DL, Clinehens GA, Recent developments in liquid seeding techniques for use with laser velocimetry measurements. AIAA Paper 1986-0769, 14th Aerodynamics testing conference, West Palm Beach FL, 1986.

Pedersen N, Larsen PS, Jacobsen CB, Flow in a Centrifugal Pump Impeller at Design and Off-design Conditions. Part 1: PIV and LDV measurements, Journal of Fluids Engineering, 125: 61-72, 2003.

Pedocchi F, Martin J, García MH, Inexpensive fluorescent particles for large-scale experiments using particle image velocimetry, Exp Fluids, 45; 183-186, 2008.

Pickering CJD, Halliwell NA, Laser speckle photography and particle image velocimetry: photographic film noise, Applied Optics, 23; 2961-2969, 1984.

Poelma C, Westerweel J, Ooms G, Turbulent statistics from optical whole field measurement in particle-laden turbulence, Exp Fluids, 40; 347-363, 2006.

Poncelet D, Production of alginate beads by emulsification/internal gelation, Annals of the New York Academy of Sciences, 944:74-82, 2001.

Poncelet D, De Smet B, Beaulieu C, Huguet ML, Fournier A, Neufeld RJ, Production of alginate beads by emulsification/internal gelation, Part 2, Physicochemistry Appl Microbiol Biotechnol, 43:644-50, 1995.

Poncelet D, Lencki R, Beaulieu C, Halle JP, Neufeld RJ, Fournier A, Production of alginate beads by emulsification/internal gelation I. Methodology, Applied Microbiology & Biotechnology, 38:39-45, 1992.

Prasad AK, Particle image velocimetry, Current Science, 79: 51-60, 2000.

Prasad AK, Stereoscopic particle image velocimetry, Exp Fluids, 29; 103-116, 2000.

Quong D, Neufeld RJ, Skjak-Braek G, Poncelet D, External versus internal source of calcium during the gelation of alginate beads for DNA encapsulation, Biotechnology and Bioengineering, 57:438-46, 1998.

Raffel M, Willert CE, Kompenhans J, Particle Image Velocimetry: a practical guide. ISBN 3-540-63683-8, Springer Verlag, 1998.

Raffel M, Willert CE, Wereley ST, Kompenhans J, Particle image velocimetry: a practical guide, Second edition Springer, Berlin, ISBN: 978354023073, 2007.

Reis CP, Ribeiro AJ, Neufeld RJ, Veiga F, Insulin-loaded alginate nanospheres obtained by emulsification/internal gelation, XII International workshop on bioencapsulation, Servicio editorial Universidad del Pais Vasco, P 251, Vitoria. Spain 2004.

Roquet P, Enhanced design of high pressure gear pumps using environmentally acceptable hydraulic fluids, ECOPUMP, BRITE-EURAM project BE-95- 1046, 1998.

Saarenrinne P, Piirto M, Turbulent kinetic energy dissipation rate estimation from PIV velocity vector fields, Exp Fluids, Suppl: S300-S307, 2000.

Sabroske KR, Seeding materials for use in laser anemometry, AIAA Paper 1993-0006, 1993.

Salib NN, El-Menshawy MA, Ismail AA, Utilization of sodium alginate in drug microencapsulation, Pharm Ind, 40:1230-34, 1978.

Samimy M, Lele SK, Motion of particles with inertia in a compressible free shear layer, Phys Fluids A, 3; 1915-1924, 1991.

Sanders AJ, Papalia J, Fleeter S, Multi-blade row interactions in a transonic axial compressor: Part I – stator particle image velocimetry (PIV) investigations, ASME J Turbomach, 124; 10-18, 2002.

Scarano F, Theory of non-isotropic spatial resolution in PIV, Exp Fluids, 35; 268-277, 2003.

REFERENCES

Scarano F, Oudheusden BW, PIV investigation of a planar supersonic wake flow, 11th international symposium on applications of laser techniques to fluid mechanics, Lisbon Portugal, 2002.

Scarano F, Riethmuller ML, Iterative multigrid approach in PIV image processing with discrete window offset, Exp Fluids, 26; 513-523,1999

Scarano F, Riethmuller ML, WIDIM, Rhode Saint Genese, Belgium, 2000a.

Scarano F, Riethmuller ML, Advances in iterative multigrid PIV image processing, Exp Fluids, Suppl.; 51-60, 2000b.

Schrijer FFJ, Mignoli G, Scarano F, Walpot LMGFM , Experimental capsule afterbody flow investigation, In: Proceedings of the 6th European symposium on aerothermodynamics for space vehicles, 2008.

Schrijer FFJ, Scarano F, Particle slip compensation in steady compressible flows, In: Proceedings of the 7th international symposium on particle image velocimetry, Rome, Italy, 2007.

Schröder A, Geisler R, Staack K, Henning A, Wieneke B, Elsinga GE, Scarano F, Poelma C, Westerweel, Eulerian and lagrangian insights into a turbulent boundary layer flow using time resolved tomographic PIV, New results in numerical and experimental fluid mechanics VII, Notes on numerical fluid mechanics and multidisciplinary design, 112; 307-314, 2010.

Sharp KV, Adrian RJ, PIV study of small-scale flow structure around a Rushton turbine, Fluid mechanics and transport phenomena, 47; 766-778, 2001.

Sharp KV, Kim K, Adrian RJ, Dissipation estimation around a Rushton turbine using particle image velocimetry, In: Proceedings of the 9th International Symposium on Applied Laser Techniques to Fluid Mechanics, 1998.

Sheng J, Meng H, Fox RO, A large eddy PIV method for turbulent dissipation rate estimation, Chemical engineering science, 55; 4423-4434, 2000.

Skjâk-Braek G, Martinsen A, Application of some algal polysaccharides in biotechnology. In: Guiry MD, Blunden G (Eds.), Seaweed Resources in Europe: Uses and Potential, Wiley, Chichester, pp. 219-257, 1991.

Skudarnov PV, Lin CX, Wang MH, Pradeep N, Ebadian MA, Evolution of convection pattern during the solidification process of a binary mixture: effect of initial solutal concentration, International Journal of Heat and Mass Transfer, 45; 5191-5200, 2002.

Spencer A, Hollis D, Correcting for sub-grid filtering effects in particle image velocimetry data, Meas Sci Technol, 16: 2323-35, 2005.

Techet AH, McDonald AK, High speed PIV of breaking waves on both sides of the air-water interface, In: Proceedings of the 6th international symposium on particle image velocimetry, California, USA, 2005.

Tedeschi G, Gouin H, Elena M, Motion of tracer particles in supersonic flows, Exp Fluids, 26; 288-296, 1999.

Tisserant D, Breugelmans FAE, Rotor blade-to blade measurements using particle image velocimetry, ASME J Turbomach, 119; 176-181, 1997.

Tomida H, Mizuo C, Nakamura C, Kiryu S, Imipramine release from Ca-alginate gel beads. Chem. Pharm. Bull. 41:1475-75, 1993.

Towers CE, Bryanston-Cross PJ, Judge TR, Application of particle image velocimetry to large-scale transonic wind tunnels, Optics and Laser Technology, 23; 289-295, 1991.

Tropea C, Yarin AL, Foss JF, Handbook of Experimental Fluid Dynamics, Springer-Verlag, Berlin Heidelberg, pp. 287- 296, 309 – 327, 2007.

Truax BE, Demarest FC, Sommargren GE, Laser doppler velocimeter for velocity and length measurements of moving surfaces, Applied Optics, 23; 67-73, 1984.

Usera G, Vernet A, Ferre JA, Consideration and improvements of the analysis algorithms used for Time Resolved PIV of wall bounded flows, In: Proceedings of the 12th

REFERENCES

international symposium on applications of laser techniques to fluid mechanic, Lisbon, Portugal, 2004.

Uzol O, Chow Y, Katz J, Meneveau, Experimental investigation of unsteady flow field within a two-stage axial turbomachine using particle image velocimetry, ASME J Turbomach, 124; 542-552, 2002.

Veliky IA, Mclean RJC, Immobilized biosystems theory and practice applications, 1st edn. London: Backie and Professional, 67-93, 1994.

Villafañe L, Paniagua G, Kaya M, Bajusz D, Hiernaux S, Development of a transonic wind tunnel to investigate engine bypass flow heat exchangers, Proc. IMechE, Vol. 225, Part G: J. Aerospace Engineering, 8; 902-914, 2011a.

Villafañe L, Yasa T, Paniagua G, Bonfanti G, Development of experimental techniques for the characterization of helicoidal fin arrays in transonic flow conditions, In: Proceedings of the 47th, Joint Propulsion Conference, San Diego, USA, 2011b.

Visser FC, Jonker JB, Investigation of the relative flow in low specific speed model centrifugal pump impellers using sweep-beam PIV, Flow Visualization VII, Begell House Publishers, ISBN 1-56700-036-3, 1995.

Wahab A, Analytical prediction technique for internal leakage in an external gear pump, ASME Turbo Expo 2009: Power for Land, Sea, and Air (GT2009), Paper no: GT2009-59287 pp. 85-92, Orlando, Florida, USA, 2009.

Wakeman TG, Compact air-to air heat exchanger for jet engine application, The United States of America as represented by the Secretary of the Air Force, Washington, D.C., Pub. No: US 004187675, 1980.

Wan LSC, Heng PWS, Chan LW, Development of alginate microcapsules by emulsification, In: Proceedings of the NUS-JSPS Seminar on Recent Developments in Pharmaceutics and Pharmaceutical Technology, pp. 243-255, 1990.

Wan LSC, Chan LW, Heng PWS, Drug encapsulation in alginate microspheres by emulsification, J Microencapsul, 9(3):309-16, 1992.

Wan LSC, Chan LW, Heng PWS, Influence of hydrophile-lipophile balance on alginate microspheres. Int. J. Pharm. 95:77-83, 1993.

Wan LSC, Chan LW, Heng PWS, Surfactant effects on alginate microspheres, Int J Pharm, 103:267-75, 1994.

Wan LSC, Wong TW, Heng PWS, Formation of alginate microspheres produced using emulsification techniques, J Microencapsul, 20(3):424-30, 2003.

Wang S, Sakurai H, Kasarekar A, Numerical modelling and analysis of external gear pumps by applying generalized control volumes, Math Comput Model Dynam Syst, 17; 501-513, 2011.

Wang S, Sakurai H, Kasarekar A, The optimal design in external gear pumps and motors, IEEE/ASME Transactions on Mechatronics, 16; 945-952, 2011.

Weitsman YJ, Elahi M, Effects of fluids on the deformation, strength and durability of polymeric composites: an overview, Mech Time-Depend Mater, 4; 107-126, 2000.

Werely ST, Meinhart CD, Second-order accurate particle image velocimetry, Exp Fluids, 31; 258-268, 2001.

Wernet MP, Application of DPIV to study both steady state and transient turbomachinery flows, Optics & Laser Technology, 32: 497-525, 2000.

Wernet MP, Development of digital particle image velocimetry for use in turbomachinery, Exp Fluids, 28; 97-115, 2000.

Wernet M, Wernet J, Skoch G, Demonstration of a Stabilized Alumina/Ethanol Colloidal Dispersion Technique for Seeding High Temperature Air Flows, In: Proceedings 16th International Congress on Instrumentation for Aerospace Simulation Facilities, Wright-Patterson Air Force Base, 1995.

Westerweel J, Digital particle image velocimetry - theory and application, University Press (Delft), PhD-thesis, 1993.

REFERENCES

Westerweel J, Daribi D, Gharib M, The effect of discrete window offset on the accuracy of cross-correlation analysis of digital PIV recording, Exp Fluids, 23; 20-28, 1997.

Willert C, Stasicki B, Raffel M, Kompenhans J, A digital video camera for application of particle image velocimetry in high-speed flows, SPIE Proceedings Article No. 2546-2519, 1995.

Willert E, Gharib M, Digital particle image velocimetry, Exp Fluids, 10; 181-193, 1991.

Wang S, Mao J, Liu G, Uncertainty of the PIV testing results for gas flow field caused by tracer particles and seeding method, American Institute of Physics, Conf Proc, 914: 148-155, 2007.

Wong CY, Soria J, Characterization of a low Reynolds number turbulent boundary layer using PIV, In: Proceedings of 16th Australasian Fluid Mechanics Conference, Australia, 2007.

Wood G, External gear pumps for accurate and reliable metering duties, World Pumps, 472: 34–6, 2006.

Wulff DL, PIV Measurements in Pumps, In design and analysis of high speed pumps, Educational notes RTO-EN-AVT-143, Paper 5, pp. 5-1 – 5-36, Neuilly-sur-Seine, France, 2006, Available from: http://www.rto.nato.int/abstracts.asp.

Yoon JH, Lee SJ, Stereoscopic PIV measurements of flow behind an isolated low-speed axial-fan, Experimental Thermal and Fluid Science, 28; 791-802, 2004.

Yulong L, Kun L, Fuchun S, Dynamic model of gears with trapped oil and coupled analysis in external spur-gear pump, Applied Mechanics and Materials, 130-134; 610-615, 2011.

Zhang J, Tao B, Katz J, Turbulent flow measurement in a square duct with hybrid holographic PIV, Exp in Fluids, 23; 373-381, 1997.

Zhengliang L, Ying Z, Lufei J, Jinyu J, Qikai Z, Stereoscopic PIV studies on the swirling flow structure in a gas cyclone, Chemical Engineering Science, 61; 4252-4261, 2006.

Zyzman SH, Nordeen CA, McCall JE, United Technologies Corporation, Hartford, CT, Pub. No: US 2008/0016845 A1, 2008.